

Substrate Integrated Waveguide Antenna Applications

A Thesis Submitted to The University

of Kent

For The Degree of Doctor of Philosophy

in Electronic Engineering

By

Liang Wu

August 2015

University of
Kent

Acknowledgements

I would like to take this opportunity to express my deepest appreciation and gratitude to my great supervisor, Dr. Paul Robert Young, for his guidance and encouragement. I would also like to thank my parents for financial support. Also, many thanks indeed to everyone who had helped me during my PhD study, such as Nikos A. Giannakis, Pavlos Sklikas, Temitope Alade, Mohamed Ali Ziai, Anthony Nkansah, Andy Farrel and Yongtian Qiu.

Special thanks to Simon Jack for his fabrication work and help during my PhD study.

Abstract

The research objective of this thesis is to provide a better solution for signal interference and reduce the size of waveguide antenna. The background investigations of different waveguide fabrication technologies and switch control methods are detailed in the introductory part of this thesis. Several novel substrate integrated waveguide (SIW) antennas for different purpose are demonstrated in the body of the thesis. The designs are mainly divided into two kinds.

The first focuses on the switch beam SIW antennas working at 2.4 GHz frequency band. Compared to the corresponding waveguide antennas of multiple-input and multiple-output (MIMO), phased array and switch beam, the proposed SIW antennas have advantages in compact size, easy fabrication and high gain. By DC biasing the surface mounted PIN diodes, the waveguide slots radiate at diode-off state of reverse bias, and are shielded at diode-on state of forward bias. Based on different requirement, the SIW antennas can achieve two-direction, four-direction and six-direction transmission. The gain can be easily changed by extending the size of reflector walls.

The second focuses on reducing the volume of SIW antennas, working at 5 GHz frequency band. A new folded SIW antenna is introduced. By folded the antenna front end part to second layer, the SIW antenna reduces the total length by the size of one-quarter guided wavelength. This folded antenna can radiate either monopole mode or dipole mode, based on the metal surface area. Another two new SIW antennas reduce the total length by directly cutting the front-end part at the slot center. By utilized the intrinsic coupling radiation, the SIW antennas use two half-length slots at different broad-wall plane to achieve 360 degree propagation and wide-band end-fire radiation.

Content

Substrate Integrated Waveguide Antenna Applications	0
Acknowledgements	1
Abstract	2
Chapter 1 Introduction	7
1.1 Applications of microwave spectrum	7
1.2 Current antenna types	10
1.2.1 Waveguide history	10
1.2.2 Planar transmission line	12
1.3 Substrate integrated waveguide (SIW)	14
1.3.1 SIW history background	16
1.3.2 SIW Application and device	22
1.4 Future trend in SIW development.....	24
1.4.1 Fabrication method of Film.....	24
1.4.2 Fabrication method of LTCC / HTCC	25
1.4.3 Fabrication method of silicon.....	27
1.5 Objectives of this thesis research.....	30
1.5.1 Thesis organization	31
Reference	32
Chapter 2 Two radiation directions switching antenna.....	39
2.1 Preliminary work	39
2.1.1 Introduction of switch beam antenna	39
2.1.1 Comparison between PIN diode and the other switches.....	42
2.1.2 PIN diode measurement	47
2.1.3 Overlap preparation.....	57
2.1.4 Waveguide theory of SIW design	59

2.2	Two direction switch antenna.....	69
2.2.1	Antenna geometry	69
2.2.2	1-D results of antenna performance	71
2.2.3	2-D results of near-field range	75
2.2.4	3-D results in Far-field range	82
2.2.5	Conclusion:	91
	Reference	92
Chapter 3	Four directions switch antenna.....	97
3.1.1	Leaky wave design	97
3.1.2	The embryo of four direction antenna idea	99
3.2.1	Four directions switch antenna.....	102
3.2.2	The 1-D results of CST	104
3.2.3	Near-field range 2-D results.....	110
3.2.4	Far-field range measurement results	123
3.2.5	Simulation results of Far-field	129
3.2.5	Conclusion	144
	Reference	145
Chapter 4:	Six directions switch SIW antenna.....	146
4.1	Design idea:.....	149
4.2	The 1-D results:.....	151
4.3	Near-field range 2-D results:.....	155
4.4	Far-field measurement results for single diode open state:.....	157
4.5	The 1-D results of multi-diodes off states.....	161
4.6	2-D near field results of multi diodes off and on states	165
4.7	Far-field measurement results of dual-diode off states	168
4.8	Far-field simulation results of multi-diodes off and on states.....	171
4.9	The others diode-off states of non-designed target:	176
4.10	Further Research	183

4.11 Relationship between reflector extension length and free space wavelength.	186
4.12 Research of diode resistance in off and on states.	188
4.13 Conclusion:	190
Reference.	191
Chapter 5: Substrate Integrated Waveguide (SIW) Antenna minimization designs	192
5.1 Introduction	192
5.2 Whole Folded Antenna	192
5.2.1 Introduction	192
5.2.2 Antenna design	195
5.2.3 Simulation results of 2-D surface current peak	197
5.2.4 Simulation results of E-Field amplitude plot at 2D planes	198
5.2.5 Simulation and measurement results in S1,1	199
5.2.6 Farfield simulation results at 4.976 GHz:	199
5.2.7 Further research the antenna radiation	202
5.3 Two symmetry slots antenna with cutting front-end	204
5.3.1 Introduction	204
5.3.2 Symmetric slots structure and its parameters	204
5.3.3 1D simulation result:	206
5.3.4 Simulation of 2-D results: E-Field plot	207
5.3.5 Simulation of 3-D results: Farfield pattern	212
5.4 Two non-symmetric slots antenna with cutting front-end	214
5.4.1 Antenna structure and its parameters	214
5.4.2 Simulation of 1-D Result:	215
5.4.3 Simulation of 2-D results: E-Field plot	216
5.4.4 Simulation of 3-D results: Farfield pattern	220
5.5 Conclusion	222

References.....	224
Chapter 6: Conclusion and future work	226

Publication:

1. Liang Wu; Andy Farrall; Young, P.R., ‘Substrate Integrated Waveguide Switched Beam Antennas’, *Antennas and Propagation, IEEE Transactions on*, Vol. 63, No. 5, pp. 2301-2305, May 2015.
2. Sanz-Izquierdo B.; Wu, L.; Batchelor, J.C.; Young, P.R., ‘Textile integrated waveguide slot antenna’, *Antennas and Propagation Society International Symposium (APSURSI), 2010, IEEE*, 11-17 July 2010, pp. 1-4.
3. Liang Wu; Izquierdo, B.S.; Young, P.R., ‘Half mode substrate integrated waveguide slot antenna’, *Antennas and Propagation Society International Symposium (APSURSI), 2009, IEEE*, 1-5 June 2009, pp. 1-4.

Chapter 1 Introduction

1.1 Applications of microwave spectrum

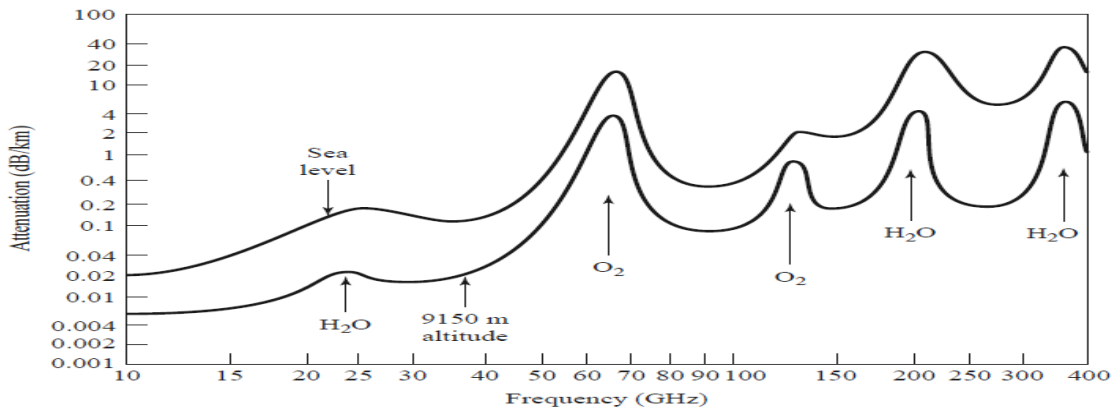


Figure 1-0-1: Average atmospheric attenuation versus frequency (horizontal polarization) [1]

In modern communication, wireless technology plays an important role offering different mobile applications. Although with advantages in mobility, wireless technology in its nature has limitations. For example, even in an open and clear space, outdoor radio propagations still can be vulnerable. Water and oxygen molecules of the atmosphere absorb the energy of electromagnetic wave. Attenuation, therefore, inevitably happens. So the question here is whether the attenuation can be controlled at an acceptable level. The attenuation level mainly depends on the ambient temperature, barometric pressure, and humidity. Crossing the broad frequency spectrum of radio waves and microwaves, the rationales of absorption can be divided into two types, according to the physical states of water molecules. For example, the hydrogen bonds in liquid or solid water can influence the electromagnetic wave absorption, and the rotational transitions of gaseous water molecules also cause absorption by transferring radio waves energy into rotational energy [2]. For similar reason, atmospheric opacity also cause the attenuation of microwave

propagation. According to the Figure 1-0-1, attenuation curves in general tend to rise when the frequencies increase. The minimum attenuation was observed at 10 GHz starting point. And the attenuations peaked at around 22.2, 183.3, and 325.4 GHz [3] because of the H₂O water vapor or called “rain fade”. Also, a considerable increase of attenuation occurred from 30 GHz to 60 GHz due to the molecular oxygen. And for the same reason, another increase was found at the 118.7 GHz.

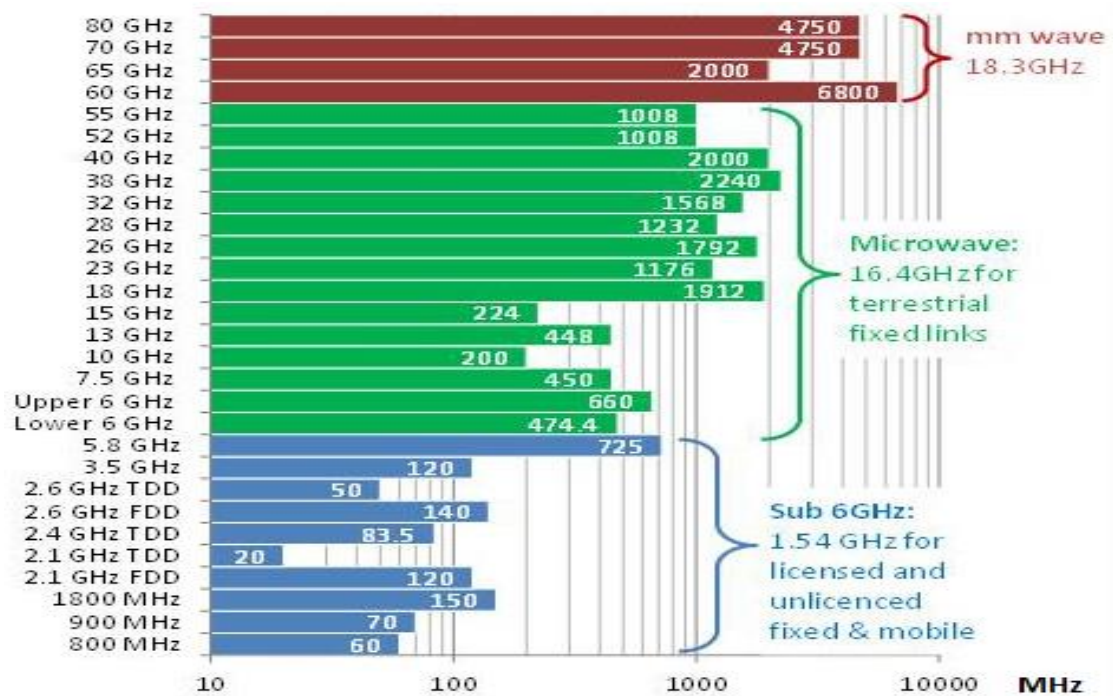


Figure 1-0-2: Total MHz Bandwidth of Upload link and download link in UK [4]

Most of the millimeter wave applications are still in the laboratory stage, due to lack of matching electronic devices, which is further caused by manufacture constraint problems. Generally, the RF systems transmitting millimeter wave are designed with all-in-one integration to reduce the interconnection loss. And some frequencies in this range have been developed for specialized purpose. For example, waves with frequencies at 94 GHz and 140 GHz can be used for the high-resolution detection of passive imaging and active imaging respectively due to the effect of local minimum loss as shown in Figure 1-0-1, [5]. And the 77GHz [6] and 24 GHz [7] can be proposed for the anti-collision sensor radar

in vehicle. The 60 GHz also can be used for indoor wireless data transmission [8] or satellites crosslink communication [9] in space where there is not weather impact and air. The 60 GHz has a wide spectrum over 6 GHz, as shown in Figure 1-0-2. The propagation distance of 60 GHz frequency is limited to an individual room area, due to the weak penetration capacity for concrete wall and obstacle. Another restricting the development of the millimeter wave application is the official license. As the open frequency spectrum in millimeter wave has not yet been unified in different countries, the potential frequency interference could cause legal disputes.

In civil area, the frequency bands widely used are below 10 GHz, such as Wi-Fi based on the IEEE 802.11 specifications, the third and the fourth generation of mobile phone network, and WiMAX based on the 802.16 specifications. It is apparent from the Figure 1-0-2 that the available spectrum bandwidth expands when frequency increases. For the Wi-Fi at 2.4 GHz, its channel bandwidth is merely 83.5 MHz. This explains why the number of subscribers for a particular Wi-Fi is limited to dozens, given the fact that the channels of 20 MHz can be overlapped as shown in Figure 1-0-3. Waves within low frequency band can propagate a relatively long distance, but subject to power limitation [11]. Therefore, Wi-Fi normally is restricted to indoor use, except the 802.11a standard at 5 GHz. Also, as 2.4 GHz band is crowded by many domestic applications, such as microwave oven, wireless door opener, cordless phones and etc [12]. Wi-Fi might be suffer from noise interference.

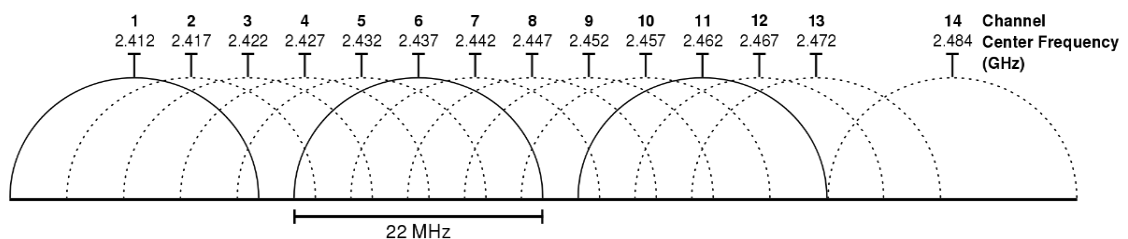


Figure 1-0-3: Wi-Fi (2.4 GHz) band channels overlapping [10]

Compared to 2.4 GHz band, 5GHz band has a wider spectral bandwidth. WiMAX, as a result, can support a larger group of subcarriers than Wi-Fi can do. Though with physical advantages in range coverage, full duplex and supporting quality of service, WiMAX cannot totally replace Wi-Fi. This is because the WiMAX signal has large attenuation when being transmitted into indoor accepters. On the contrary, 2.4 GHz is suitable for indoor use, since 2.4 GHz can penetrate concrete wall and floor. When a Wi-Fi system adopts multiple-input and multiple-output (MIMO) method to increase throughput, the bandwidth gap between Wi-Fi and WiMAX could be greatly narrowed. With different physical characteristics, Wi-Fi and WiMAX are complementary. In the present thesis, the designs introduced and discussed will focus on the 2.4 GHz and 5 GHz band.

1.2 Current antenna types

As the idea of substrate integrated waveguide originates from the combination of waveguide and Microstrip, a brief introduce about the structure and history of these two technologies is set out below.

1.2.1 Waveguide history

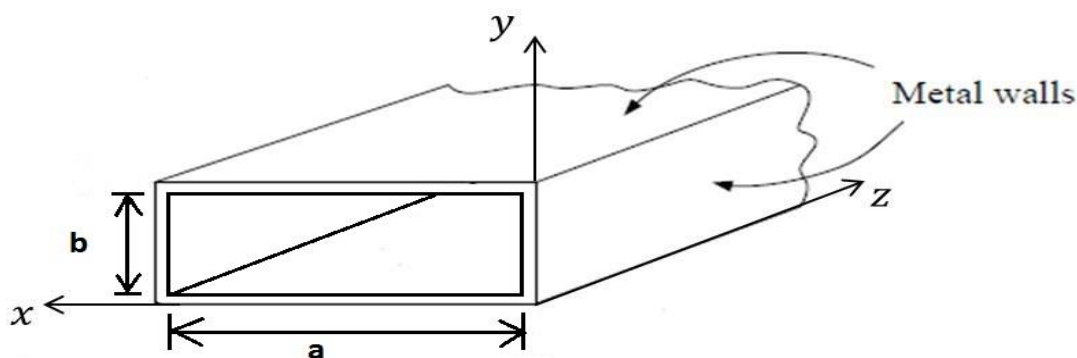


Figure 1-0-4: Rectangular waveguide structure

The width and the height of the rectangular waveguide dimension are represented by letter “a” and “b” respectively, as shown in Figure 1-0-4. Traditionally, the width should be larger than the height. The cross-section of waveguide in arbitrary intersection is shown at an x-y plane. The length of waveguide extends along the z axis. The hollow space in central waveguide can be filled with dielectric material. The waveguide is surrounded by metal walls. Being reflected on the inner surface of the metal, the electromagnetic wave inside the waveguide propagates in a zigzag path. The propagation direction of electromagnetic wave only points toward the z axis. The most frequently used propagation mode in the rectangular waveguides is the transverse electric (TE) mode, in which all electric field components are perpendicular to the propagation direction as shown in Figure 1-0-5. The first TE mode is TE_{10} as shown in Figure 1-0-5. In this mode, only the electric field components on y-axis direction vary. The vertical solid lines in the x-y plane represent the E-field components of y axis. The dash loops inside the waveguide show the magnetic field. The crosses represent E-field components with a downward direction, and the dots represent those with an upward direction.

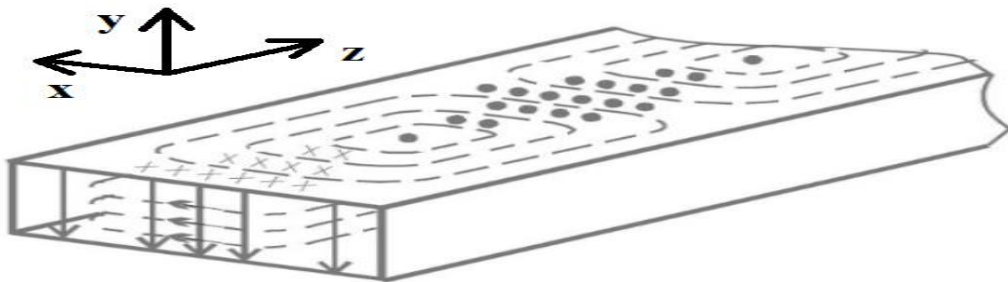


Figure 1-0-5: Electromagnetic field distribution of TE mode

The earliest official record of waveguide shows that Lord Rayleigh [13] is the first founder who built up the prototype of inner conducting hollow pipe by solving the mathematical boundary problem and discovering the transmission mode. However, due to the absence of high frequency source actuator at the time, most frequency bands adopted for laboratory purpose were below the cut-off frequency of bulky tubes [14]. Tests carried out on this

basis, as a result, failed to prove the validity of the guided tube assumption. And the assumption was shelved. Not until 1936, did two American scientists, Barrow [15] and Southworth [16], obtain experimental evidences for the feasibility of waveguide. And later, Bell telephone research group [17] worked out the theoretical proof of waveguide in mathematics. Since then, more and more publication papers proved that the metallic hollow pipe can be used not only as enclosed transmission line of electromagnetic wave but also as an antenna radiator. Detailed analysis of waveguide property and characteristic has been achieved during 1940s. Specifically, Watson's work [18] on the resonant slot of rectangular waveguide, has made a profound contribution to the waveguide formula derivation. And since 1950s, the proven formula has been widely used in waveguide structures with different fabrication technologies.

1.2.2 Planar transmission line

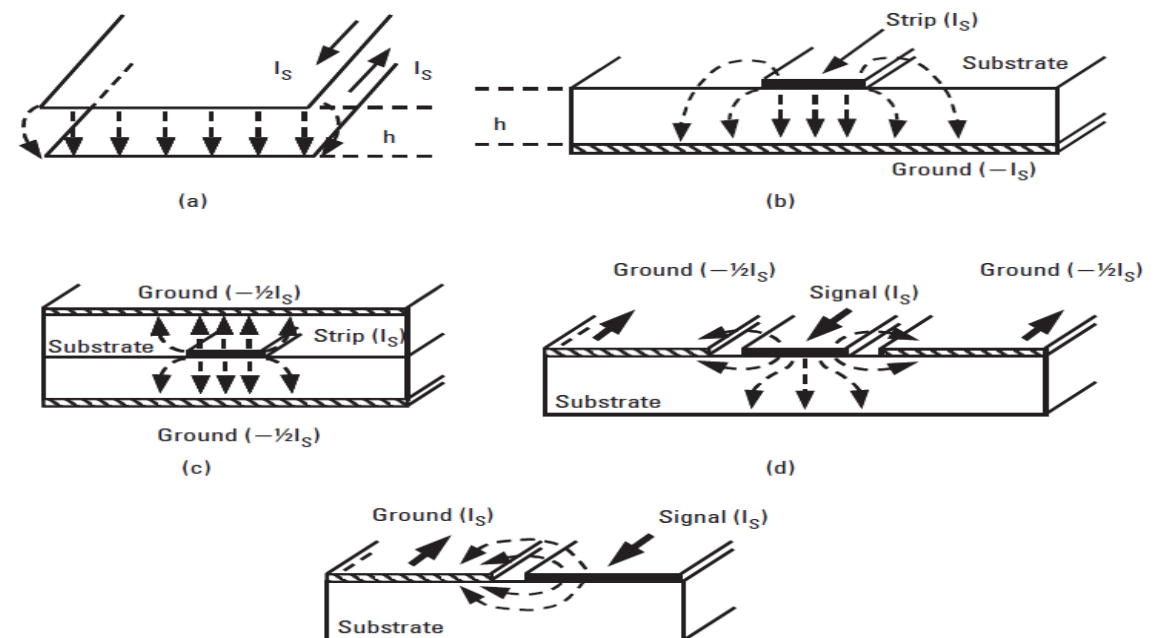


Figure 1-0-6: planar transmission lines and propagation E-field plots [19] (a) parallel-plate, (b) Microstrip, (c) stripline, (d) coplanar waveguide, and (e) slot line

Accompanied with the development of printed circuit board (PCB) manufacture technology since 1950s, planar printed transmission lines have been introduced, such as Microstrip, stripline, slotline, and coplanar waveguide as shown in Figure 1-0-6,. Although these transmission lines originally were merely used for on-board electrically connecting, gradually various other circuit functions derived. For example, these transmission lines can work as power divider, filter, antenna, and coupler. All these circuit functions can be easily realized by etching surface metal into specific pattern. Furthermore, these planar transmission lines can be integrated into one single board sharing the same dielectric layer. Therefore, planar printed transmission lines have advantages in volume, little-weight, simplified design, and low-cost manufacture. But the disadvantages are obvious. Usually, the planar transmission designs form uncoated metal lines directly on a substrate. The conducting metal surface, in such a circumstance, is exposed to air. The conduction, therefore, suffers from serious radiation leak as shown in Figure 1-0-6, loss, coupling and interference. Also, the power capacity is limited in this kind of transmission lines.

The advantages of traditional rectangular waveguide exactly redeem the shortcomings of planar printed transmission lines. As the rectangular waveguide is enclosed by a thick metal wall, all the signal propagation takes place inside the waveguide. Therefore, rectangular waveguides have the benefits of considerably reduced loss and leakage, high quality factor, cross-talk free, and high power handling capacity. Although by filling dielectric material, the size of a waveguide can be reduced, the volume of a dielectric waveguide, nevertheless, is larger than the Microstrip counterpart. As a result, traditional waveguides have inherent vice, such as cumbersome size, costly and slow processing. Furthermore, when a metallic waveguide need to be assembled with other circuit components, the integration process could be complicated and inefficient.

1.3 Substrate integrated waveguide (SIW)

In building a complete RF system, both planar printed transmission lines and traditional waveguides encounter the same integration problem. Active components, passive components, and transmission components, usually, are made by different manufacturing methods and with different interfaces, thus extra losses are incurred during the insertion, transition, and transmission processes. As a consequence, the ideal design performance for each system components cannot be achieved. In order to optimize the system integration, a novel guided structure called substrate integrated waveguide (SIW) has been put forward, as shown in Figure 1-0-7 (a). Moreover, the transmission lines formed by the SIW not only have the favorable physical characteristic of planar printed transmission lines, but also possess the excellent performance of solid waveguide.

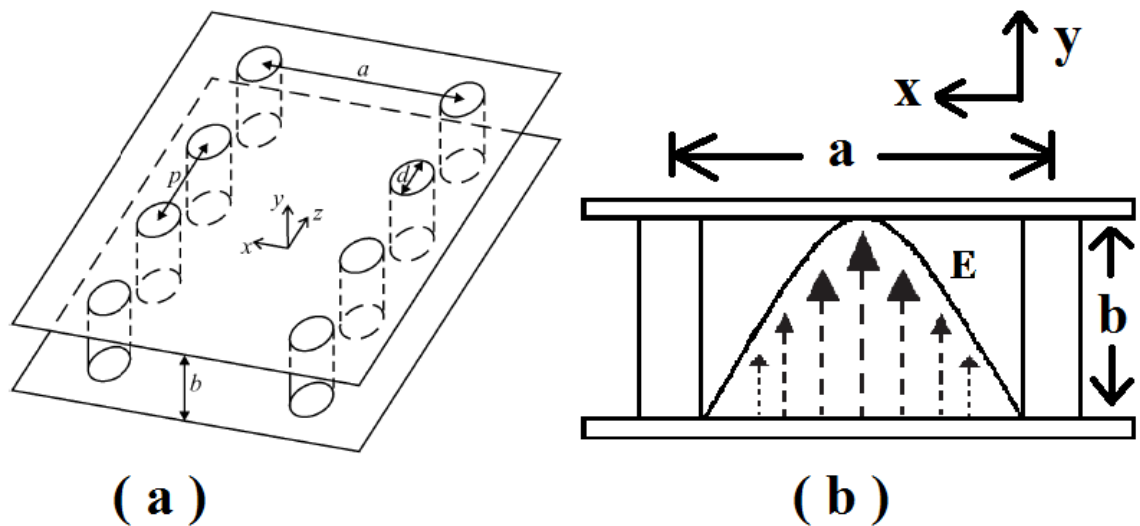


Figure 1-0-7: (a) SIW structure of perspective view [20], and (b) Fundamental mode of SIW in cross-section view

Essentially, the structure of SIW is similar to a rectangular dielectric-filled waveguide structure. By adopting the PCB fabrication method of Microstrip, SIW, however, scales down original height to the thickness of PCB. The PCB substrate, in this sense, can be regarded as the inner-filled dielectric of a waveguide. The two copper sheets of PCB are equivalent to the two metallic broad walls of waveguide. And the two rows of electroplated via holes, which drilling through the PCB, replace the narrow walls of waveguide. Therefore, the copper sheets and via holes form a current loop in the sectional view, which is similar to the cross-section case of traditional solid metal waveguide. In addition, all these via holes are drilled in equal distance, and the regular interval between each pair of adjacent current loops is filled with dielectric material. The interval between adjacent loops is in inverse proportion to the density of via holes. So that, the arrangement of via holes in PCB can form a complete dielectric-filled waveguide.

Similar to the propagation characteristic in bulky waveguide, the compressed electromagnetic wave in SIW also moves forwards along a zigzag route between the two rows of via holes by being reflected. Therefore, each SIW has a specific lowest transmission frequency. And the wavelength of the cut-off frequency should be in proportion to the width of the particular SIW. As the thickness of PCB is quite thin, the height “b” of SIW usually is less than 2 mm. Moreover, the arrangement of via holes is dense, which means distance “p” between two posts is small and the post diameter “d” is small as well. Therefore, SIW has negligible loss and small attenuation. It is to be noted here that the most distinguishing mark of SIW is the current distribution on via holes. The surface current on a traditional waveguide can flow towards to any direction. But the current on via holes surface is limited to vertical direction. As individual via holes are discrete, the side wall current cannot flow longitudinally across the regular intervals. Therefore, the propagation in SIW can only perform TE_{m0} modes of traditional rectangular waveguide, in which the E-field is perpendicular to the propagation direction and will not

change across the Y-axis. Thus, the first mode of SIW is the TE_{10} mode, as shown in Figure 1-0-7 (b).

1.3.1 SIW history background

The metalized via holes, though, have been widely used in PCB manufacture long ago for reducing the coupling between electronic elements. The idea of via holes waveguide was first purposed by Shigeki in 1994 [21]. The development of SIW post-holes wall is limited to the accuracy of electromagnetic field computation, which further depends on the numerical analysis method and computer processing capability available at the time. Instead to explain the algorithm of post-holes wall, the following description will briefly introduce the milestones in the history of metal post wall development.

The application of band-pass waveguide filter has been developed for a long time, especially the method of conducting post insertion. Besides the evanescent mode adopted by combline filter, the propagation mode is the primary concern of filter works. During that time, Marcuvitz has summarized various experimental cases and practical analysis data in this topic [22]. One common design is the inductive post, which is made up by paralleling incident E-field of fundamental mode or higher-order mode to the single or multiple perfect electrical conductor (PEC) posts. The inserting depth of posts is alterable. For example, posts can be partly inserted into or penetrate through the waveguide from the broad wall, as shown in Figure 1-0-8 and Figure 1-0-9. As the input wave is hindered by the post insertion, the incident wave is the source inducing current on the surface of post. Therefore, the scattering field and equivalent circuit of post become the main research aspect.

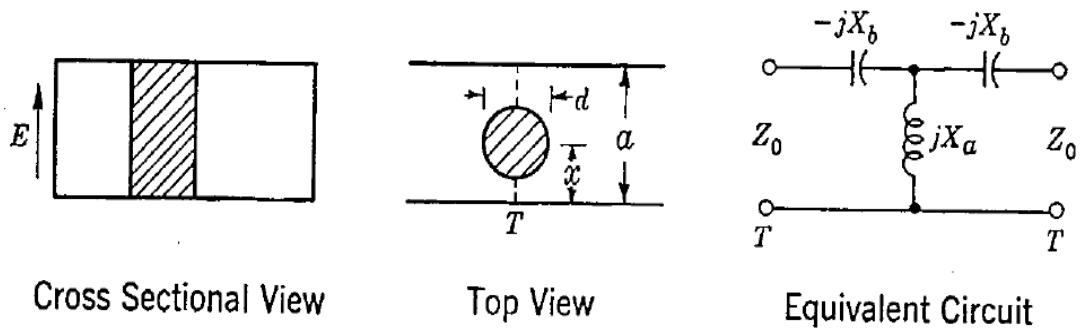


Figure 1-0-8: Metal post full insertion [22]

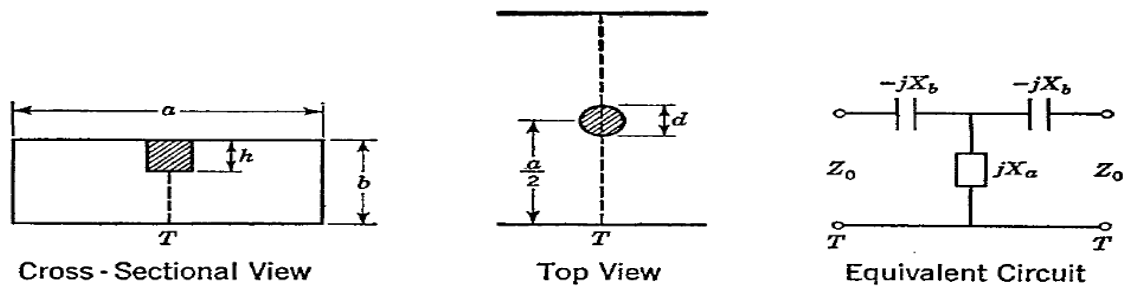


Figure 1-0-9: Metal post partial insertion [22]

Bradshaw [23] put forward some improved expressions to calculate the scattering field of partially inserted thin post, which give a tentative idea to the case of total insertion. As the filter structure mentioned in Bradshaw's paper has a gap between the post end and the ground, the induced current on the post surface is not constant, which is more complex than the current in the total insertion case. Previous researches of waveguide filter mainly focus on the small post insertion, Leviatan [24], in this case, published a paper to analyze the case of single large post by using the Method of Moments (MOM) [25] with boundary condition. In early papers, each post was just represented by a surface current. The innovation of Leviatan's paper is that in the calculation process, the large post was substituted by finite set of non-singular thin surface currents, which can be expressed by Fourier series, as shown in Figure 1-0-10. The direction of each thin current is in accordance with the longitudinal axis of post. The current changes circumferentially. By being substituted in the Kummer's transformation, the modified Green's function, which

is used for calculating single thin current under different mode, can be expressed into a fast converging series. Thus, the scattering field of a large post is derived. And the result can be further used to calculate the scattering matrix of single large post model. This theoretical calculation of MOM shows that the values of the final data not only are consistent with Marcuvitz's results, but also extend the curves of Marcuvitz results to the case of large post. Later, based on the work of Leviatan, Li [26] extended the improved converging solution procedure to the case of multiple posts array, which achieves the same accuracy as single post does.

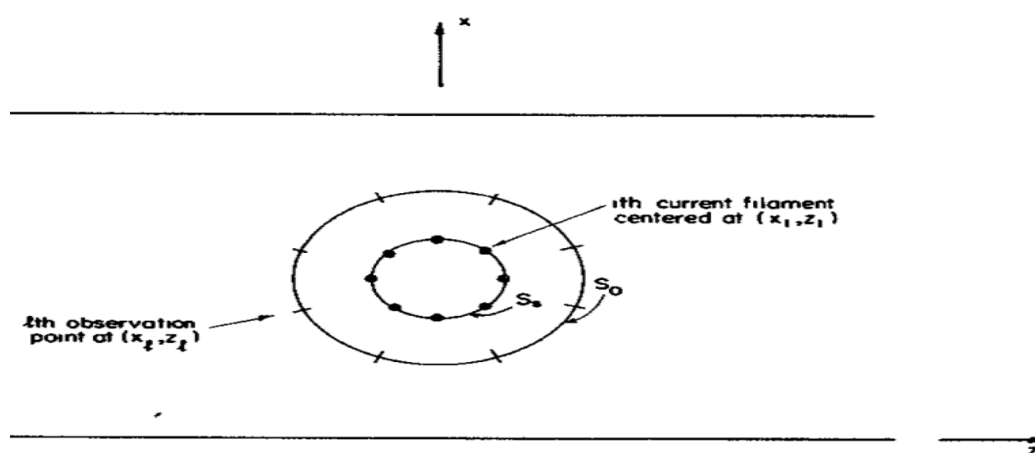


Figure 1-0-10 : multiple surface current filaments to replace metal post [24]

Previously, as the numerical methods available were not precise enough, the design of filter structure mainly depended on measured results. The measured results, however, were affected by measurement errors and uncertain tolerance range. A breakthrough progress has been achieved by Abele [27] who in the first time solved the mathematical convergence problems for the arrays of regular post. Later, Collin [28] worked out the convergence problems in similar manner, which offers an optional solution. In 1998, Ando and Hirokawa designed a novel PCB structure of waveguide antenna in the form of via metalized post array [29]. In this design, the volume of waveguide was greatly reduced by let the parallel-plate antenna and the feed structure share the same grounded planar dielectric substrate. As shown in the Figure 1-0-11, the waveguide is fabricated by drilling

relatively high-density via holes array directly in the dielectric material. The copper-plated holes replace traditional thick metal wall. As the manufacture procedure is relatively simple, this new waveguide structure has advantages in cost, fabrication, and volume.

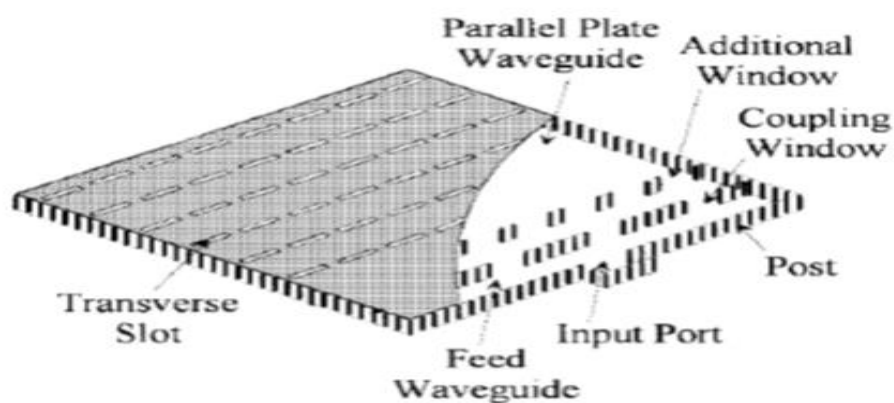


Figure 1-0-11 : Fabricated structure of waveguide [29]

Based on Leviatan's moment method [29] for single inductive metal post model and the Auda's calculation treatment [30] for arbitrary shape, the research team of Professor Ando analyzed the practical performance of post array and calculated the propagation constant of electromagnetic wave inside this post structure. For a given PEC wall equivalent width a_e , as shown in Figure 1-0-13, the effective waveguide width a_f of posts array is in proportion to the diameter of posts and the periodic interval of posts arrangement. As shown in the Figure 1-0-12, the waveguide width of metalized holes a_f gradually decreases when the interval between holes increases. However, as the interval increases, transmission energy leakage increases, the equivalent effective traditional waveguide width a_e , as a result, increases as well. When the interval is equal to or lesser than twice the length of holes diameter, the attenuation can be neglected.

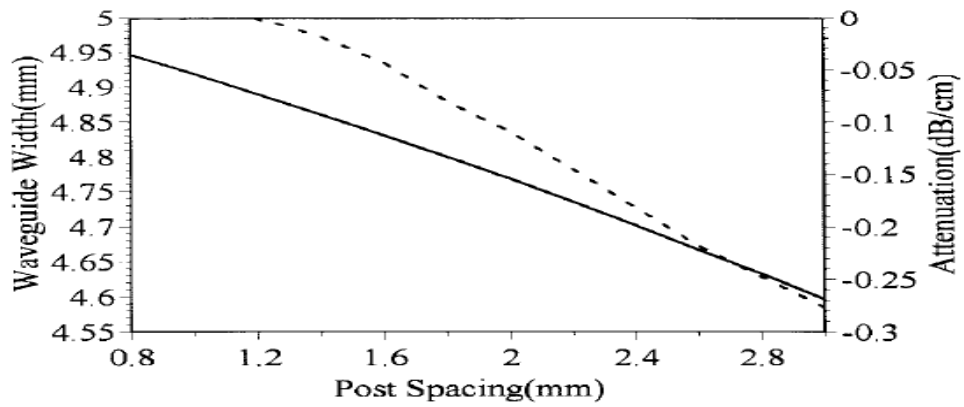


Figure 1-0-12: Solid line is waveguide width of post array, dash line is attenuation coefficient [29]

Although the design of Hirokawa got desirable experimental results, the numerical analysis method applied, as shown in Figure 1-0-13, has limitations in calculation. Specifically, this method can only be used for a rough initial approximation for the transmission wave propagating inside the non-radiation feed waveguide region. As the two rows of posts are the boundaries between inner waveguide and outer space, the thin current density on the inner surface of a post is different from the one on the outer surface. Therefore, the geometry discretization under boundary conditions need to be solved out. As the feed arrangement used in Hirokawa paper is only suitable for parallel-plate array of large area size, a simple structure of Microstrip-feed-waveguide for single antenna plate was proposed by Tzuang [31] in 2000. By using photolithography fabrication procedure of Printed Circuit Board (PCB), Tzuang integrated a Microstrip feedline into a via-post waveguide. So that the feedline and the antenna are on the same board sharing common substrate and ground. Based on the works of Hirokawa and Tzuang, Ke Wu proposed a new planar Substrate Integrated Waveguide (SIW) in 2001, which is the structure adopted in the present thesis. Since then, the standard SIW configuration is finalized with the top and bottom broad walls covered by PCB copper sheet, and both sides of narrow walls formed by metalized post-wall.

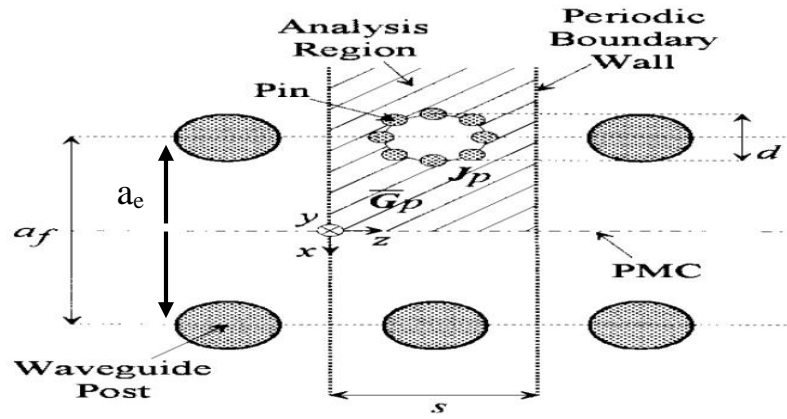


Figure 1-0-13: Surface current filament analysis method [29]

Since 2000, the operating speed of personal computer processor has been accelerated dramatically, which is fast enough to deal with the heavy iterated simulation. Therefore, numerous computer-aided design (CAD) software are available to accurately solve the complicated calculation of hybrid electromagnetic field. All the simulations of designs in the present thesis were worked out by Computer Simulation Technology AG (CST). Based on the full-wave method, the Finite-difference time-domain (FDTD) solver in CST serves to analyze the electromagnetic field propagation characteristic of SIW model. The advantage of the full-wave method is that all electromagnetic field components will be taken into account, such as H_x , H_y , H_z , E_x , E_y , E_z . Moreover, under the full-wave model, the time derivative terms of Maxwell's equation, which represent interactions between E and B fields, have a definite range, instead of being arbitrarily set at zero. Hence, the full wave analysis can fully consider all potential situations. However, FDTD solver requires high-end computers and can be time consuming.

1.3.2 SIW Application and device

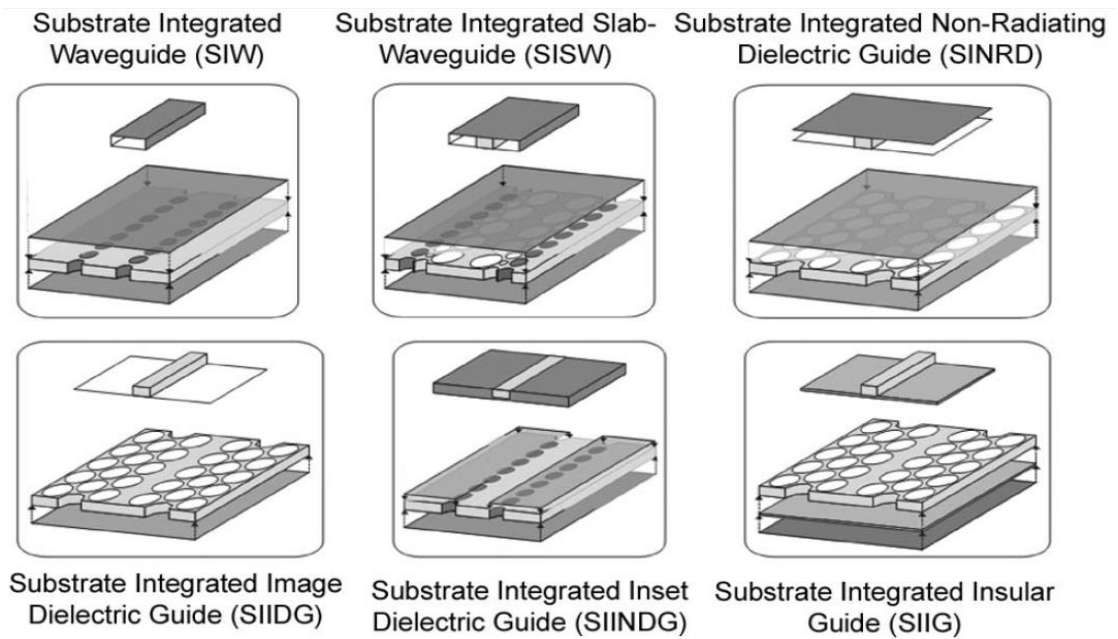


Figure 1-0-14: equivalent planar structures corresponding to each 3-D prototype [32]

In order to transform solid devices into planar structures, some derivative designs for SIW structure were developed. Dielectric transmission lines in nonplanar forms were transformed into corresponding planar structures, as shown in Figure 1-0-14, such as substrate integrated non-radiative dielectric (SINRD) [33], substrate integrated inset dielectric guide (SIINDG) [34], substrate integrated slab waveguide (SISW) [35], substrate integrated insular guide (SIIG) [36][37], substrate integrated image dielectric guide (SIIDG) [38] [39], and substrate integrated ridge waveguide (SIRW) [40][41]. A common characteristic of these new planar designs is that the large holes in regular arrangement are not for via fence purpose. The hollow nonmetal large holes in substrate adjust the effective relative permittivity of the substrate between the dielectric permittivity and vacuum permittivity. All these planar designs can be fabricated in one circuit board as parts of a substrate by a one-step process. Using the same dielectric material, these new designs as transitions can efficiently connect different interfaces in a broad frequency range. Moreover, as the electromagnetic field propagation is bounded inside the dielectric

material, these planar designs have advantages in isolation and loss reduction. As a result, above new structures increase the range of alternative dielectric transmission line models, which enhances the integration capability of the SIW.

The SIW not only realize the same function as solid waveguides do, but also can achieve some system functions of RF front-end circuitry, such as power amplifier [42], mixer [43], power divider [44], balun [45], phase shifters [46], magic-T [47], directional couplers [48], and circulators [49]. As one of the necessary active devices in RF circuit is the oscillator, the oscillator for planar SIW attracts much attention. In general, there are three kinds of SIW oscillators. The first type is the feedback oscillator [50], which applies the same circuit scheme of conventional electronic counterpart. The feedback type still consists of amplifier, feedback loop and SIW cavity. The second type is the reflection oscillator [51]. In order to control frequency in a better way, the active devices are mounted on SIW. The third type is the push-push oscillator [52], which uses two outputs to oscillate out of phase mode. The major research interests about SIW passive devices focus on the filters. The configurations of filter can be divided into three types. The first type is the cavity resonator filter formed by metalizing via holes [53]. The second type is the inductive via structure filter formed by inserting metalized via holes at specific locations [54]. The third type is compact folded structure filter [55], whose length is reduced. Compared to the designs of components in traditional circuit system, the designs of SIW devices are simple and direct. This is because the design work of SIW devices is simplified from a traditional solid design to a two-dimensional design. As the visible side walls in SIW can be used as reference, additional via holes can be precisely inserted at target points. Moreover, As SIW devices are in planar form, all these designs can be either integrated in one single board or vertically stacked together.

1.4 Future trend in SIW development

Except for the PCB application, the SIW configuration as a part of RF front-end circuit can be used in the other fabrication technologies which will be introduced as following.

1.4.1 Fabrication method of Film

Experiencing half century development, thick and thin film technologies have been used in photovoltaic cell, multilayer circuits, different scales integration circuits and etc. As one of the most important application of film technology, sensors have been widely applied in many fields, such as in automobile, aerospace, industrial production, medical science, and military [56]. The credit for such a wide application must go to the reliability of the film technology and the stable performance of films. Both the thick and thin film are fabricated in a layer-by-layer structure. Intuitively, the difference between the thick and thin film is the thickness. With a thickness of micrometer level, films are thick; and with a thickness of nanometer level, films are thin. However, the thick and thin films, technically, are distinguished by the deposition methods employed in processing. Thick films are screen-printed, and thin films are vacuum-deposited [57].

Thick films first appear in 1950s as a substitute of printed circuit board [58]. During that time, thick film is an immature auxiliary technology. Since the performance and resolution of conducting line have been greatly improved, a breakthrough in the development of thick film has been achieved in 1960s by making the fabrication process come true on an industrial scale. The realization of integrated circuit in 1960s established a sound

theoretical basis for later circuit designs. Since then, different active and passive circuit components, together with fabrication technologies, have been applied in high density circuit packing. In 1965, the manufacturer and researchers set out to study films in nanometers for the demand of precision machining. As the production process of traditional thick film is cumbersome and inefficient, in 1986 Hibridas Groups, proposed a remarkable new method to cut the fabrication procedure and cost, which is called photoimageable thick-film technology [59]. This technology has been extensively used in millimeter wave applications over a broad frequency range, such as Microstrip line from 2GHz to 10 GHz [60], Metal-Pipe Rectangular Waveguides (MPRWGs) from 60 to 90 GHz [61], and waveguide filter at W band and F band [62]. Since 1990s, thin film, as the mainstream, has reached nanometer level and been used in coating processes for various applications. However, for the RF application, thick films are the most widely used auxiliary material, due to the cost advantage of thick films.

1.4.2 Fabrication method of LTCC / HTCC

For military purpose, ceramic material was for the first-time used for insulating fundamental substrate in radio communication equipment in 1940s [63]. LTCC and HTCC technologies as a result emerged. In the late 1940s and 1950s, the booming post-war electronic market boosted the development of modern planar printed circuitry [64], which remarkably reduced the volume and heaviness of electronic equipment by replacing conventional bulky electronic components with a planar circuit board. Co-fired ceramics, at the time, were widely applied to manufacturing innovation. The embryonic form of LTCC and HTCC first emerged at the production of IBM computer chip board with multiple layers in 1960s. In 1980s, the current concept of LTCC first appeared, and was used by Hughes and DuPont [65] in the production of military radar chip. During the past

20 years, LTCC and HTCC technologies have enjoyed a high-speed development [66]. More and more sophisticated three-dimensional LTCC structures have been integrated with active and passive components in MCM package [67], and widely utilized in all fields of microelectronics applications. The difference between HTCC and LTCC is sintering temperature. HTCC is fired and molded with a temperature range between 1500 and 1600 degree Celsius; and the LTCC is with a temperature range between 850 and 1050 degree Celsius [63]. The specific temperature limit depends on the material properties of selected conductors and substrates which further lies with the specific function of applications.

HTCC are mainly applied to leading-edge products, such as military hardware, artificial satellites and medical devices. Since the working description in these top-end fields requires a high reliability of equipment even in hostile environments. HTCC has a chance to demonstrate advantages in firmness and refractoriness [68]. However, as HTCC normally used in high temperature environment, available matching conducting materials suffer from low conductivity. Also, passive components cannot be embedded inside the HTCC layers. Moreover, the manufacture process of HTCC is complex and incompatible with thick film technology. With cost advantage over both HTCC and traditional thick film, LTCC is widely used in commercial products. The conducting materials of LTCC, which can be used in transmission lines or antennas [63], has a better conductivity than the lossy metals in HTCC do. Compared to the loss tangent of dielectric in FR4, the one of LTCC is lower. LTCC, thus, has an outstanding performance in RF electronic system, and is commonly applied to the extra high frequency GHz-band applications [69]. Furthermore, the thermal conductivity of LTCC is significantly better than that of PCBs [69]. Compared to the traditional thru-hole connection, the surface mount devices (SMD) in PCB can reduce the whole circuit volume and simplify the bonding process. However, by innovating embedment building, LTCC can do a better job than PCB in reducing volume, soldering and electromagnetic interference. The printed resistors, inductors,

capacitors, and chips, can be buried into the layers of LTCC model or hollow area in LTCC sheet. Alternately, the passive components and circuit can be integrated on the surface of LTCC model. So that, the LTCC model, in fact, employs a three-dimensional design. Since for each layer of LTCC the thickness is negligible, there is not an upper limit in the number of layers that can be added to a design. Even though PCB also can form multi-layer substrates, in practice, the number of layers is restricted to a few [70]. By assembling an adequate number of layers, LTCC can imitate the structure of PCB [71]. Moreover, LTCC can be applied to many other SIW applications, such as transition [72], antenna feed [73], and filter [74]. Especially for filters, LTCC has advantage in stacking. Nevertheless, LTCC mainly has two shortcomings which restrict its machining precision. One problem is that ceramic tapes inevitably shrink during the firing process. Another problem is that the machining error of LTCC metal cannot be managed within few micrometers [75].

1.4.3 Fabrication method of silicon

Because a massive number of transmitter/receiver (T/R) elements needed to be fixed in the array, the hybrid microwave integrated circuit (MIC) shows deficiencies in lossy interconnection, complicated system configuration, and cumbersome volume. By contrast, monolithic microwave integrated circuit (MMIC) based on very-large-scale-integration (VLSI) process, can offer reliable large RF array system at a compact size, and, thus, is suitable for cost-effective batch production. As MMIC aims to assemble all the transmission lines, passive components and active components on one single IC substrate, semiconductor technology makes building the RF system on one chip possible. So that the MMIC can reduce both the volume and weight of RF system without degradation.

However, MMIC has disadvantages. For example, post-fabrication tuning and passive component rework are not allowed by MMIC, the production procedure of MMIC is complex and time consuming, and the passive components are low quality factor and restrict power. As the machining precision of MMIC is high, CMOS semiconductor technology is a competitive candidate for the RF system design supporting up to Terahertz frequency band. Although the III-V family semiconductors have superior performance over the others, the exorbitant manufacturing cost limits the promotion of III-V technology in civilian market. Indium phosphide (InP) and GaAs though have been used for many years, these materials remain expensive. In recent years, Bipolar Complementary Metal Oxide Semiconductor (BiCMOS) has been proposed as a compromise solution. With a relatively low production cost, BiCMOS has the advantages of both bipolar junction transistor and the CMOS transistor. The most frequently used semiconductor material is silicon. With a low cost, silicon BiCMOS are suitable for mass production. But the RF performance of silicon substrate is unsatisfactory, due to the high loss and low resistivity [76]. In order to solve this problem, Silicon-Germanium (SiGe) material has been introduced, based on the same silicon fabrication procedure. Compared to silicon, this new material has better performance yet low cost. As the base bandgap potential of SiGe transistor can be turned down from 1.12 eV of Si to 0.66 eV of Ge, the carriers' density and gain can be raised [77]. Moreover, the Ge dopant increases the frequency sensitivity. Hence, SiGe is a desirable choice for RF system. And silicon and SiGe become mainstream materials, as showed in Figure 1-0-15.

Recently, a SIW structure based on silicon substrate has been proposed [78]. In this paper, benzocyclobutene (BCB) polymer is used as the SIW substrate material. By filling up the uneven trenches, BCB polymer can form a relatively smooth dielectric surface. Moreover,

BCB polymer has a low dissipation. In addition, the relative permittivity of BCB polymer, 2.65, is close to the permittivity of the frequently-used dielectric. The metal components of this SIW are made with gold. Verified by measurement, SIW based on silicon fabrication method can successfully work at millimeter frequency band. By using BCB polymer as the middle layer between passive components and silicon dielectric, silicon material loss can be greatly reduced to an acceptable level. This is a major stride forward of silicon application in SIW.

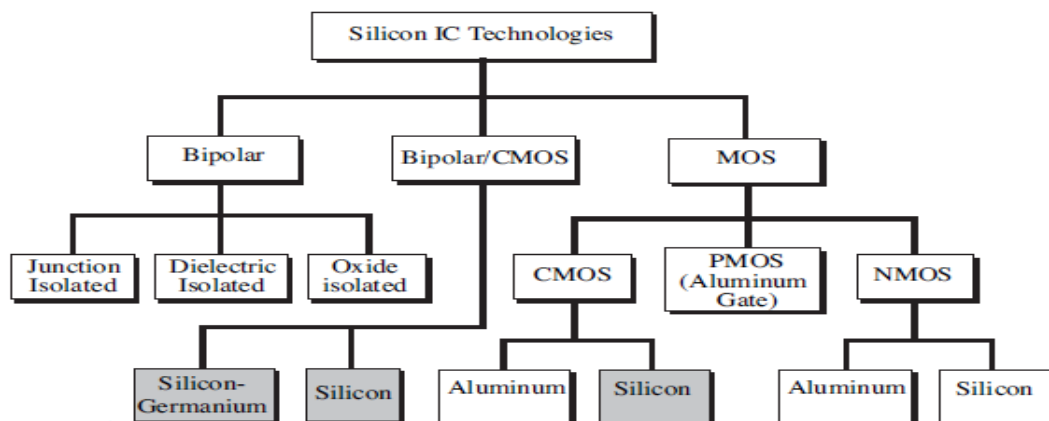


Figure 1-0-15: Classification of Silicon Technology [79]

Although the above LTCC, thin-film, and silicon fabrication methods have superiority over traditional PCB method, these fabrication technologies, in practice, cannot be widely used. This is because only a few companies and laboratories is able to carry out this sophisticated machining procedures. The difficulty in fabrication and the requirement in accuracy, therefore, limit the output rate of final products. As a result, these fabrication methods are expensive. By using Duroid material, the PCB substrates not only reduce dielectric loss but also possess precise dielectric constant. So that, the PCB can reliably fabricate antenna at gigahertz frequency band. Since PCB technology do not need expensive investment for machine and working condition, the PCB is widely supported by many factories around the world. Therefore, the PCB has advantages in low cost,

simple fabrication process, and rich experience. In the present thesis, all the designs are built upon the PCB technology.

1.5 Objectives of this thesis research

As 2.4 GHz and 5 GHz band are free and have been approved by many countries, researches in the present thesis will base on these two frequency bands. Furthermore, the fabrication requirement of PCB in these two frequency bands can be satisfied by the production technology of university workshop. And the measurement equipment in laboratory can fully support designs of these two frequency bands. Therefore, the first research objective of the present thesis is to seek better solutions for current 2.4 GHz and 5 GHz antenna. As these two frequency bands have been developed over 10 years in various application areas, the signal interference among different wireless products has become the major issue. Current solutions mainly can be classified into two types. One is the hardware solution which increases radiation gain by adding antennas, such as the electrical phased array and the beamforming antenna array. Another is the software solution which seeks to enhance the signal analysis capability of RF system. Both methods, however, are expensive. Therefore, the present thesis try to use a low-cost design, the SIW antenna, to realize the switch-beam function. The most attractive advantage of this SIW switch-beam antenna is to reuse the frequency channel in any direction at 360 degree by a single antenna. Moreover, this new antenna can easily be upgraded to an antenna array to increase gain. In regard of gain, SIW switch antenna outperforms any other planar printed design, such as Microstrip switch array. The second research objective is to find out different ways to downsize SIW antenna.

1.5.1 Thesis organization

In Chapter 2, we introduce the switching two radiation directions waveguide antenna with PIN diodes control. Also in this chapter, we will demonstrate the background research of the design.

In Chapter 3, we introduce the switching four radiation directions waveguide antenna. Also in this chapter, we will prove that the reflector wall can affect radiation gain. This suggests that the gain can be managed in accordance with the requirement of application.

In Chapter 4, we introduce the switching six radiation directions waveguide antenna. In this chapter, an important feature of this antenna is that this antenna generates radiation by coupling E-fields, so that can cover a relatively large range. Also, compared to the planar radiation range of simple switching antennas, the radiation E-field of this antenna can steer to cover half sphere space. Restricted by time, we do not perform the eight radiation directions and waveguide antenna array. We leave this for future research.

In Chapter 5, we introduce some single-radiation-direction antennas. The purpose of these designs is to use a simple antenna structure to realize different radiation directions. This idea is based on the characteristic of intrinsic coupling E-fields.

In the Chapter 6, we summarize the progress of current research, and discuss future work.

Reference

- [1] David M. Pozar (2011), *Microwave Engineering*, 4th edn., United States of America: Wiley.
- [2] Wikipedia contributors (5 August 2015), “Electromagnetic absorption by water”, [Online]. Available: https://en.wikipedia.org/w/index.php?title=Electromagnetic_absorption_by_water&oldid=674662461 (Accessed: 5th April 2014).
- [3] T. Koryu Ishii (1995), *Handbook of Microwave Technology. Volume 2, Applications*, San Diego: Academic Press
- [4] Julius Robson (2012), “*Backhaul bandwidth across the spectrum*”, [Online]. Available: <http://cbl.com/infocast/backhaul-bandwidth-across-spectrum> (Accessed: 12th May 2014).
- [5] Jeffrey A. Nanzer (2012), “*Microwave and Millimeter-wave Remote Sensing for Security Applications*”, Norwood, MA: Artech House.
- [6] Hartmann, M. ; Wagner, C. ; Seemann, K. ; Platz, J. ; Jager, H. ; Weigel, R., “A Low-Power Low-Noise Single-Chip Receiver Front-End for Automotive Radar at 77 GHz in Silicon-Germanium Bipolar Technology”, in *Proc. IEEE Radio Frequency Integrated Circuits (RFIC) Symposium 2007 IEEE*, Honolulu, HI, Jun. 2007, pp. 149-152.
- [7] V. Cojocaru, H. Kurata, D. Humphrey, B. Clarke, T. Yokoyama, V. Napijalo, T. Young, and T. Adachi, “A 24 GHz Low-Cost, Long-Range, Narrow-Band, Monopulse Radar Front End System for Automotive ACC Applications”, in *IEEE MTT-S International Microwave Symposium (IMS) Digest*, Honolulu, USA, June 2007, pp. 1327--1330.
- [8] P. Smulders, “Exploiting the 60 GHz band for local wireless multimedia access: Prospects and future directions”, *IEEE Communications Magazine*, no. 1, Jan. 2002, pp. 140-147.
- [9] Choung, Y. H., “V-band crosslink antenna”, in *Antenna and Propagation Society International Symposium 2005 IEEE*, 2005, Vol. 3A, pp. 387-390.
- [10] Wikipedia, the free encyclopedia (2015), “*List of WLAN channels*”, [Online]. Available at: http://en.wikipedia.org/wiki/List_of_WLAN_channels (Accessed: 17th April 2014).
- [11] Souransu Banerji, Rahul Singha Chowdhury, “Wi-Fi & WiMAX: A Comparative Study”, *Indian Journal of Engineering*, Vol.2, No. 5, 2013.

- [12] Bradley Mitchell “Is 5 GHz Wi-Fi Network Hardware Better than 2.4 GHz?” [Online]. Available: <http://compnetworking.about.com/od/wirelessfaqs/f/5ghz-gear.htm> (Accessed: 5th June 2014)
- [13] Lord Rayleigh, “On the Passage of Electric Waves through Tubes, or the Vibrations of Dielectric Cylinders”, in *Phil. Mag.*, Vol. 43, pp. 125, 1897.
- [14] Houldin, J.E., “Wave guides”, *Students' Quarterly Journal*, Vol.10, No.39, 1940.
- [15] Barrow W. L., “Transmission of Electromagnetic Waves in Hollow Tubes of Metal”, *Proc. I.R.E.*, Vol. 24, No.10 , 1936, pp. 1298.
- [16] Southworth, G.C., “Hyper-frequency wave guides — General considerations and experimental results”, *The Bell System Technical Journal*, Vol. 15, No.2, pp. 284-309, 1936.
- [17] Carson, John R.; Mead, Sallie P.; Schelkunoff, S.A., “Hyper-Frequency Wave Guides—Mathematical Theory”, *The Bell System Technical Journal*, Vol. 15, No. 2, pp. 310-333, 1936.
- [18] Watson, W. H., “Resonant Slots”, *J. IEE*, Vol.93, part IIIA, pp.747-777, 1946.
- [19] Eric Holzman (2006) *Essentials of RF and Microwave Grounding* , Norwood, MA: Artech House Publishers, pp. 57
- [20] D. Deslandes and K.Wu, “Accurate modeling, wave mechanisms, and design considerations of a substrate integrated waveguide”, *IEEE Trans. Microwave Theory Tech.*, vol. 54, pp. 2516-2526, June 2006.
- [21] Shigeki, F., “Waveguide line,” (in Japanese) *Japan Patent* 06-53 711, Feb. 25, 1994
- [22] N. Marcuvitz, Ed., *Waveguide Handbook*, M.I.T. Rad. Lab. Ser., vol. 10. New York: McGraw-Hill, 1951, pp. 257-262, 271-272, 285-286.
- [23] J. A. Bradshaw, “Scattering from a Round Metal Post and Gap”, *IEEE trans. on Microwave Theory and Tech.*, vol. 21, No. 5 pp. 313-322, May 1973.
- [24] Y. Leviatan, P. G. Li, A. T. Adams, and J. Perini, “Single-post inductive obstacle in rectangular waveguide,” *IEEE Trans. Microwave Theory Tech.*, vol. MTT-31, pp. 806-812, Oct. 1983.
- [25] R. F. Harrington, *Field Computation by Moment Methods*, ser. IEEE Press/OUP Electromagnetic Wave Theory. Piscataway, NJ: IEEE Press, 1993.
- [26] P. Li, A. Adams, Y. Leviatan, and J. Perini, “Multiple-post inductive obstacles in rectangular

- waveguide,” *IEEE Trans. Microwave Theory Tech.*, vol. MTT-32, no. 4, pp. 365-373, Apr. 1984.
- [27] T. A. Abele, “inductive post arrays in rectangular waveguide”, *The Bell system technical Journal*, Vol. 57, No.3, March 1978.
- [28] R. E. Collin, *Field Theory of Guided Waves*, 2nd ed., New York: Wiley-IEEE Press, 1990, pp. 591-594.
- [29] J. Hirokawa, and M. Ando, “Single-layer Feed Waveguide Consisting of Posts for Plane TEM Wave Excitation in Parallel Plates,” *IEEE Trans. Antennas Propagate*, vol. 46, no. 5, pp. 625-630, May 1998.
- [30] H. Auda and R. F. Harrington, “Inductive posts and diaphragms of arbitrary shape and number in a rectangular waveguide,” *IEEE Trans. Microwave Theory Tech.*, vol. MTT-32, pp. 606–613, June 1984.
- [31] C.-K. C. Tzuang, K.-C. Chen, C.-J. Lee, C.-C. Ho, and H.-S. Wu, “H-plane mode conversion and application in printed microwave integrated circuit,” in *Proc. 30th Europ. Microw. Conf.*, Oct. 2000, pp. 1-4.
- [32] Wu, K., Cheng, Y.J., Djerafi, T., Hong, W.: “Substrate-integrated millimeter-wave and terahertz antenna technology”. *IEEE Proc.* Vol.100 No.7, pp. 2219-2232, 2012.
- [33] Cassivi, Y. , Ke Wu, “Substrate integrated NRD (SINRD) guide in high dielectric constant substrate for millimetre wave circuits and systems”, *Microwave Symposium Digest, 2004 IEEE MTT-S International*, Vol. 3, 2004, pp. 1639 -1642.
- [34] Kumud Ranjan Jha, Ghanshyam Singh, *Terahertz Planar Antennas for Next Generation Communication*, Switzerland: Springer, 2014.
- [35] Bozzi, M. , Dominic Deslandes, Paolo Arcioni, Luca Perregrini, Ke Wu , Giuseppe Conciauro, “Efficient analysis and experimental verification of substrate-integrated slab waveguides for wideband microwave applications”, *International Journal of RF and Microwave Computer-Aided Engineering*, Vol. 15, No. 3, pp. 296-306, 2005.
- [36] A. Patrovsky and K. Wu, “Substrate integrated image guide (SIIG) - A planar dielectric waveguide technology for millimeter-wave applications”, *IEEE Trans. Microw. Theory Tech.*, vol. 54, no. 6, pt. 2, pp. 2872–2879, Jun. 2006.
- [37] A. Patrovsky and K. Wu, “94-GHz broadband transition from coplanar waveguide to substrate integrated image guide (SIIG)”, *Proc. IEEE Int. Microw. Symp.*, 2007, pp. 1551-1554.

- [38] A. Petosa, A. Ittipiboon and S. Thirakoune. "Perforated dielectric resonator antennas", *Electronics Letters*, Vol. 38, No. 24. 21", pp. 1493-1495, Nov. 2002.
- [39] K. Wu, D. Deslandes, and Y. Cassivi, "The substrate integrated circuits---A new concept for high-frequency electronics and optoelectronics," in *Proc. 6th Int. Conf. Telecommun. Modern Satellite Cable Broadcast Service*, Oct. 2003, vol. 1, pp. 3-5.
- [40] Che, W. Li, C. Zhang, D. Chow, Y.L., "Investigations on propagation and the band broadening effect of ridged rectangular waveguide integrated in a multilayer dielectric substrate", *Microwaves, Antennas & Propagation, IET*, Vol. 4, No. 6 , pp. 674-684, 2010.
- [41] Bozzi, M. Winkler, S.A. Wu, K., "Broadband and compact ridge substrate-integrated waveguides", *Microwaves, Antennas & Propagation, IET*, Vol. 4, No.11, pp. 1965-1973, 2010.
- [42] Zhebin Wang, Adhikari, Sulav, Dousset, David, Chan-Wang Park, Ke Wu, "Substrate integrated waveguide (SIW) power amplifier using CBCPW-to-SIW transition for matching network", *Microwave Symposium Digest (MTT), 2012 IEEE MTT-S International*, 2012, pp. 1-3.
- [43] Ji-Xin Chen, Wei Hong, Zhang-Cheng Hao, Hao Li, Ke Wu, "Development of a low cost microwave mixer using a broad-band substrate integrated waveguide (SIW) coupler", *Microwave and Wireless Components Letters, IEEE*, Vol. 16, No. 2, pp. 84-86, 2006.
- [44] Hao, Zhangcheng, Wei Hong, Hao Li, Hua Zhang, Ke Wu, "Multiway broadband substrate integrated waveguide (SIW) power divider", *Antennas and Propagation Society International Symposium, 2005 IEEE*, Vol.1A, 2005, pp. 639- 642.
- [45] Zhen-Yu Zhang, Ke Wu, "A Broadband Substrate Integrated Waveguide (SIW) Planar Balun", *Microwave and Wireless Components Letters, IEEE*, Vol. 17, No. 12, pp. 843-845, 2007.
- [46] Ali, A., Fonseca, N.J.G., Coccetti, F., Aubert, H., "Analysis and design of a compact SIW-based multi-layer wideband phase shifter for Ku-band applications", *Antennas and Propagation Society International Symposium (APSURSI), 2010 IEEE* , 2010, pp. 1 - 4.
- [47] Zhu, F., Hong, W., Chen, J.-X., Wu, K., "Design and Implementation of a Broadband Substrate Integrated Waveguide Magic-T", *Microwave and Wireless Components Letters, IEEE*, Vol. 22, No. 12, pp. 630 – 632, 2012.

- [48] Ali, A.; Aubert, H.; Fonseca, N.; Coccetti, F., "Wideband two-layer SIW coupler: design and experiment," *Electron. Lett.*, Vol. 45, No.13, pp. 687-689, 2009.
- [49] D'Orazio, W., Wu, K., Helszajn, J., "A substrate integrated waveguide degree-2 circulator", *Microwave and Wireless Components Letters, IEEE*, Vol. 14, No. 5, pp. 207 – 209, 2004.
- [50] Cassivi, Y, and K. Wu, "Low Cost Microwave Oscillator Using Substrate Integrated Waveguide Cavity," *IEEE Microwave Wireless Comp. Lett.*, Vol. 13, No. 2, pp.48-50, 2003.
- [51] Fan Fan He, Ke Wu, Wei Hong, Liang Han, Xiao Ping Chen, "A Low Phase-Noise VCO Using an Electronically Tunable Substrate Integrated Waveguide Resonator," *IEEE Trans. Microwave Theory Tech.*, Vol. 58, No. 12, pp. 3452-3458, 2010.
- [52] Georgiadis, A., Via, S.; Collado, A.; Mira, F., "Push-Push Oscillator Design Based on a Substrate Integrated Waveguide (SIW) Resonator," *39th European Microwave Conference 2009*, Rome, Italy, Sept. 29-Oct. 1, 2009, pp.1231-1234.
- [53] Xiao Ping Chen, Wei Hong, Cui, T., Chen, Jixin, Ke Wu, "Substrate Integrated Waveguide (SIW) Linear Phase Filter," *IEEE Microwave Wireless Comp. Lett.*, Vol. 15, No.11, pp.787-789, 2005.
- [54] Deslandes, D., and K. Wu, "Single-Substrate Integration Technique of Planar Circuits and Waveguide Filters," *IEEE Trans. Microwave Theory Tech.*, Vol. 51, No.2, pp.593-596, 2003.
- [55] Lin-Sheng Wu, Junfa Mao, Wen-Yan Yin, "Compact quasi-elliptic bandpass filter based on folded ridge substrate integrated waveguide (FRSIW)", *Microwave Conference Proceedings (APMC), 2012 Asia-Pacific*, 2012, pp. 385-387.
- [56] S. Mergui, "Advances in Materials for Sensors," invited paper, *NATO ASI Series, High Technology*, Vol 2, May 23-25, 1994, pp. 239-259.
- [57] "Thick and Thin Film Technology", [Online]. Available: http://www.srmuniv.ac.in/downloads/thick_and_thin_film_technology.doc, [Accessed 23rd May 2014]
- [58] Hanneke Van Doorn, "Thick Film Sensors, Handbook of sensors and actuators volume 1", The Netherlands: Elsevier science B.V., 26 Aug 1994. pp. 3.
- [59] J. Minalgienė, V. Baltrushaitis, S. Muckett, "Very Fine Line Photoimageable Thick Film Technology Developed at Hibridas", *Microelectronics International*, Vol. 11, No. 2, 1994, pp.25 – 30.

- [60] Muckett, S.; Minalgene, J.; "Hibridas' photoimageable thick film process and materials for microwave and sensor component applications" *IEMT/IMC Symposium, 2nd*, 15-17 April, 1998, pp. 154,160.
- [61] M. S. Aftanasar, P. R. Young, I. D. Robertson, J. Minalgene, and S. Lucyszyn, "Photoimageable thick-film millimeter-wave metal-pipe rectangular waveguides," *Electron. Lett.*, vol. 37, no. 18, pp. 1122-1123, Aug. 2001.
- [62] M. S. Aftanasar, P. R. Young, and I. D. Robertson, "Rectangular waveguide filters using photoimageable thick-film processing," in *Proc. 32nd Eur. Microwave Conf.*, Milan, Italy, Sep. 2002.
- [63] Fred D. Barlow III, Aicha Elshabini, "*Ceramic Interconnect Technology Handbook*", Florida: CRC Press, January 24, 2007, pp. 194, 237
- [64] Cleo Brunetti, and Roger W. Curtis, *Printed Circuit Techniques, National Bureau of Standards Circular 468*, Washington: United States Department of Commerce, November 15, 1947.
- [65] M. Prudenziati, and J Hormadaly, *Printed Films: Materials Science and Applications in Sensors, Electronics and Photonics*, Cambridge: Woodhead Publishing, September 13, 2012, pp. 134.
- [66] S. Annas. "Advances in low temperature co-fired ceramic (LTCC) for ever increasing microelectronic applications", *IEEE Elect. Comp. Tech. Conf.*, 2003, pp.1691-1693.
- [67] Sarmad Al-Taei, David Haigh, and George Passiopoulos, "Multilayer Ceramic Integrated Circuits (MCICs) Technology and PassiveCircuit Design", *Proceedings of the London Communication Symposium 2001, 6th Annual London Conference on Communications*, 10-11 September 2001, pp.139-142.
- [68] "*High and Low Temperature Cofired Multilayer Ceramics (HTCC and LTCC)*", [Online]. Available: <http://www.schott.com/epackaging/english/download/schott-htcc-ltcc-datasheet-2013-08-eng.pdf>, [Accessed 5th May 2014].
- [69] Yoshihiko Imanaka, *Multilayered Low Temperature Cofired Ceramics (LTCC) Technology*, Boston: Springer Science and Business Media, Inc., January 10, 2005, pp. 9-10.
- [70] "*WHAT IS THE LTCC?*", [Online]. Available: http://www.ltcc-consulting.com/What_is_the_LTCC, [Accessed 5th May 2014]
- [71] Hao Li, Wei Hong, Tie Jun Cui, Ke Wu, Yu Lin Zhang, Li Yan, "Propagation characteristics of substrate

- integrated waveguide based on LTCC”, *Microwave Symposium Digest, 2003 IEEE MTT-S International*, Vol. 3, No. 3, 2003, pp. 2045-2048.
- [72] Tsung-Hsun Yang, Chi-Feng Chen, Huang Ting-Yi, Wang Chun-Long, Wu Ruey-Beei, “A 60GHz LTCC transition between microstrip line and substrate integrated waveguide”, *Microwave Conference Proceedings, 2005. APMC 2005. Asia-Pacific Conference Proceedings*, Vol. 1, 2005, pp. 4.
- [73] Bunea A.-C., Neculoiu D., Lahti M., Vaha-Heikkila T., “94 GHz substrate integrated waveguide fed antenna in LTCC technology”, *2012 IEEE Asia-Pacific Conference on Antennas and Propagation (APCAP)*, 2012, pp. 283-284.
- [74] Huang Ting-Yi, Shen Tze-Min, Chen Bo-Jiun, Chien Hung-Yi, Wu Ruey-Beei, “Design of miniaturized vertically stacked SIW filters in LTCC”, *Microwave Conference, 2009. EuMC 2009. European*, 2009, pp. 413 - 416.
- [75] Jong-Hoon Lee, and Manos M. Tentzeris, *Three-Dimensional Integration and Modeling: A Revolution in RF and Wireless Packaging*, Synthesis Lectures on Computational Electromagnetics, Morgan & Claypool Publishers, 2008, pp. 7.
- [76] Robertson I.D., Luczyn S., *RFIC and MMIC Design and Technology*, 2nd edn., London: The Institution of Engineering and Technology, 2001, pp. 97.
- [77] Senapati, B., Maiti, C. K., “RF Amplifiers Using SiGe-HBTs”, *International conference, Communications, computers and devices ICCCD*, 2000, pp. 127-132.
- [78] Ik-Jae Hyeon ; Woo-Young Park ; Sungjoon Lim ; Chang-Wook Baek, “Millimeter-wave filter using novel micromachined substrate integrated waveguide structure with embedded silicon vias in BCB dielectrics”, *Solid-State Sensors, Actuators and Microsystems Conference (TRANSDUCERS), 2011 16th International*, 2011, pp. 2482-2485.
- [79] Phillip E. Allen and Douglas R. Holberg, *CMOS Analog Circuit Design*, 2nd edn., New York: Oxford University Press, USA, February 7, 2002, pp. 19.

Chapter 2 Two radiation directions switching antenna

2.1 Preliminary work

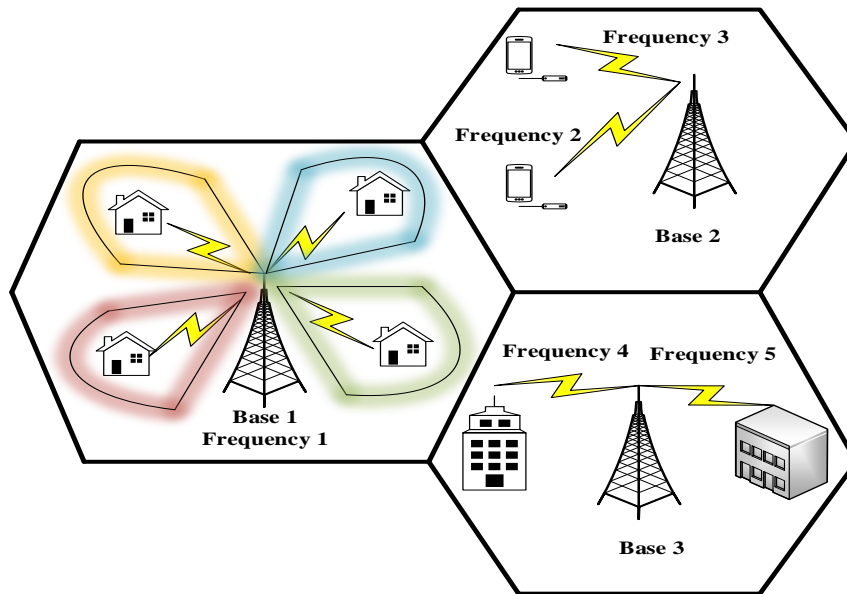


Figure 2-0-1: point-to-point directional wireless communication

2.1.1 Introduction of switch beam antenna

Wi-Fi as a fundamental technique is used in many portable devices, such as mobile phones, tablet computers, and notebooks. But the multipath fading, both in indoor and outdoor environments, has caused serious problems. For example, transmission speed would be dropped down, signal interference happens, and frequency channel resource would be strained. The MIMO application is one of the popular solutions, because directional and reconfigurable antennas can increase the overall signal power received, and reuse the same frequency channels. But, the frequency resource limitation still exists, especially, between

neighbor cellular transmitting stations. Another conventional solution is the phased array. By using phase shifters to control the phase of each antenna, phased array is capable of wide-range scanning. However, phased array has obvious disadvantages in complicated interconnection of feeding network, large power consumption, and energy inefficiency. Some improvements have been adopted in phased array, such as the $n \times n$ Butler matrices made by SIW [1]. Though this method makes phased array system simpler than before, the phased array, all the same, is a sophisticated and cumbersome system, compared with the switch-beam antenna.

As shown in Figure 2-0-1, the directional switched beam antenna is a promising technique to solve the problems of multipath fading, band congestion, and inefficient energy utilization by diversifying space, using adaptive algorithm, controlling beamforming, and reusing frequency[2][3]. Because of involving many antennas to connect transceiver devices, phased array and MIMO system are bulky. In contrast, switch SIW antenna, though is an integration of many antennas, have a size and a feeding equivalent to those of a single antenna. So that switch antenna can solve both the front-end downsizing issue and the back-end interconnection issue. Moreover, because the phased array with electronical steering is a high-end design. The prohibitive cost make phased array uncompetitive in civil market. For the MIMO system, many antennas need to be installed on a large platform, which can be costly as well. With advantages in low cost, small volume, low-weight, isolation, and high production, switch SIW antenna is an economical solution. In addition, SIW designs have been applied to many back-end devices, such as phase shifter, coupler, filter, and resonator. So that, the SIW structure has another advantage in integrating radio system. Though with competitive advantage in price and fabrication, Microstrip antenna array suffer from severe spurious interference, low gain, cross talk coupling, and poor radiation efficiency.

The beam pattern diversity antennas have been mentioned by some researchers, such as Ming-Iu Lai [4], Carl B. Dietrich, Jr [5] and Nguyen Viet Anh [6]. Ming-Iu Lai [4] purposed a switched-beam antenna with 8 directions. But there are two defects. The first problem is the inefficient gain. In this design, PIN diodes were mounted on the antenna surface and the lossy FR4 substrate to achieve a compact size of antenna. The gain was sacrificed with a maximum value at only 2.1 dBi. The second problem is the asymmetric radiation pattern. The main beams in opposite directions are asymmetrical which is caused by the coaxial cable, control lines and batteries locating under the antenna. Because this design has not taken the biasing circuit of PIN diodes into account during simulations. The paper of Carl B. Dietrich, Jr [5] offered a prototype of diversity configurable antenna. All of the farfield pattern mentioned in this paper, however, are asymmetrical and suffer from significant distortion. In the paper of Nguyen Viet Anh [6], the MIMO antenna proposed is with a large size, as four input ports are necessary. Moreover, most of the radiation efficiency results in that paper are unfavorable, which usually around 50 percentage of efficiency. Switched beam based on single antenna structure is an attractive solution, which has been proved to be feasible in dipole antenna with PIN diodes control [7] and active metallic photonic band-gap materials (AMPBG) [8]. However, this kind of designs needs many switches to control a series of radiation elements. Ngamjanyaporn [9] proposed a better solution for radiation controlling, which integrates the physical characteristics of PIN diode working state into patch radiation resistance condition. The major shortcoming of this 8-PIN-diode design is that the radiation is limited to two directions. Based on the working mechanism of Ngamjanyaporn [9], the present thesis purposes three types of single waveguide antennas with two-direction, four-direction and six-direction switching beams respectively and longitudinal slots. The main advantage of these novel designs is that by controlling the intrinsic radiation property of slots, the directional switched beams have a 360-degree coverage. As PIN diodes are directly mounted in the center of slot, these diodes, essentially, work as integrated components of

slot. For the 4- and 6-direction designs, since the pointing angle of each beam is less than 90 degrees, radiations are highly directional. Therefore, the same frequency can be reused in other directions.

In this chapter, a 2-direction switch beam SIW antenna with PIN diodes control is proposed for WLAN application. The theoretical basis of SIW antenna design is developed from conventional rectangular waveguide. For designing the 2-direction switch antenna, extensive preparatory researches have been undertaken. And based on detailed comparisons among switches from different categories, PIN diode has been chosen.

2.1.1 Comparison between PIN diode and the other switches

The RF signal transmission can be controlled by the switch, called relay. Relays mainly can be divided into three types, as Electromechanical Relays (EMR), Microelectromechanical System (MEMS) Relays and Solid-State Relays (SSR) [10]. More than 90 percent of PCB circuits use electromechanical relays [11]. In comparison with solid-state relays, PCB mounted EMR relays have greater power handling capability, higher breakdown voltage and firmer packaging. Obviously, the disadvantages of EMR are bulky volume, long switching time, large actuation voltage, large power consumption and no application for high frequency [12]. Moreover, the lifespan of EMR can be shortened by internal contact wear caused by rapid frequency, high load, and large voltage and current [13].

Solid state relay (SSR) based on semiconductor technology is second widely used in the civil market with a market share of around 10 percent [11]. The attractive characteristics

of SSR are high reliability and long service life [14]. Just as the name indicates, SSR do not have moving mechanical parts which might cause failure, wear and inefficiency. Moreover, since components in SSR do not need to move, SSR consume less power than EMR do. SSR can be further divided into two types, as PIN diode and Field Effect Transistor (FET), respectively. Generally, FET are made by Gallium Arsenide (GaAs), Gallium Nitride (GaN), or silicon [15]. The distinguishing feature of FET is that FET can be perfectly integrated with semiconductor circuits, as both of them adopt the same fabrication technology and substrate material. So that, compared to other relays, FET relays have a much smaller volume and footprint. The operation mechanism of FET is shown in Figure 2-0-2. When there is a forward bias between the source terminal and the gate terminal, the FET is turned on having a current transmission with positive input voltage. When there is a reverse bias, the pathway of current between the source terminal and the drain terminal would be totally blocked by the depletion layer, as the negative input voltage would enlarge the area of depletion layer. So that, by managing voltage biases, FET can be switched on and off. Therefore, the FET have advantages in switching speed and isolation.

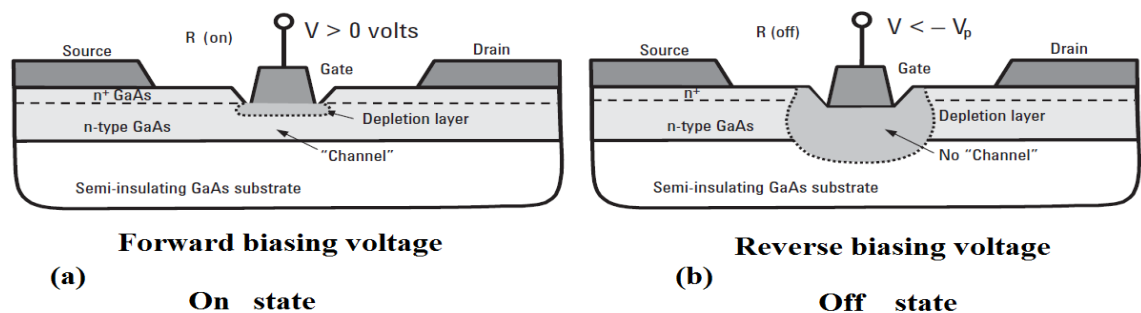


Figure 2-0-2: the working principle of FET [16]

PIN diode relays have similar performance and characteristics with FET relay, as the working mechanisms of them are essentially the same. Therefore, compared to electromechanical relays (EMR), solid-state relays (SSR) have characteristics of no sparking, no bounce and no sound during switching [17]. Relative to the voltage control

in FET, the PIN diode is controlled by the direct current (DC) bias. Obviously, PIN diode relays use more power than FET relays do. As a substitute of EMR, PIN diodes are widely used in the PCB design via the surface mount technology (SMT). As SIW antennas are produced under the PCB technology, the PIN diode is the most competitive candidate for switching designs, which will be studied further in the next section.

In 1979, Microelectromechanical systems (MEMS), or called Micro Systems Technology (MST) was introduced [18], which makes integration of all mechanical sensors, actuators and electrical devices into microscale structure possible [19]. MEMS has been widely used in many applications, such as printers, game controllers, cameras, projectors, digital watches, mobile phones and vehicles [20]. Compared to electromechanical switches and solid state switches, MEMS switches has the broadest working frequency range and the smallest working power. There are three production methods for radio frequency (RF) MEMS: bulk micromachining, surface micromachining, and LIGA [21]. LIGA is a German acronym for Lithographie, Galvanik, and Abformung, which mean lithography, electroforming, and molding, respectively [22]. The most frequently used method is surface micromachining. Actuators with different working mechanisms are available to MEMS, such as optical actuators [23], mercury-droplet actuators [24], piezoelectric actuators [25], electrothermal actuators [26], magnetostatic actuators [27], electromagnetic actuators [28] and electrostatic actuators [29]. Most RF MEMS employ electrostatic ones. RF MEMS include series switches and shunt switches in circuit. Normally, the shunt switches work at millimeter wave frequency band [30], and the series switches work at lower frequency range. The moving parts of MEMS can be classified as cantilevers, bridges and membranes. The membrane can be regarded as a closed form bridge with a fixed circumference. Generally, MEMS switches consist a suspending metal actuator and an electrode controller. As showed in Figure 2-0-3, the cantilever is of the series switch type. When the beam is pendent over the Microstrip contact in off state, the

circuit path of RF signal is interrupted, and the circuit is switched off. When the beam touches the Microstrip contact, the circuit is complete. Also as showed in Figure 2-0-4, the bridge is of the shunt switch type. When the bridge suspends, the circuit works. The bridge is used for cross connection between the two grounds of Coplanar Waveguide (CPW). When the bridge falls down to the central transmission line of CPW, the circuit is shorted. Compared with solid state switch, MEMS has a better isolation performance, as on-state RF signal will not be transferred into the external-controlled direct current (DC) bias loop.

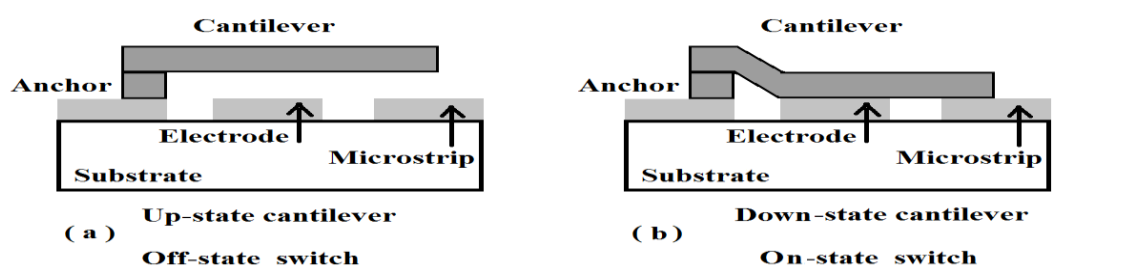


Figure 2-0-3: Cantilever working mechanism [31]

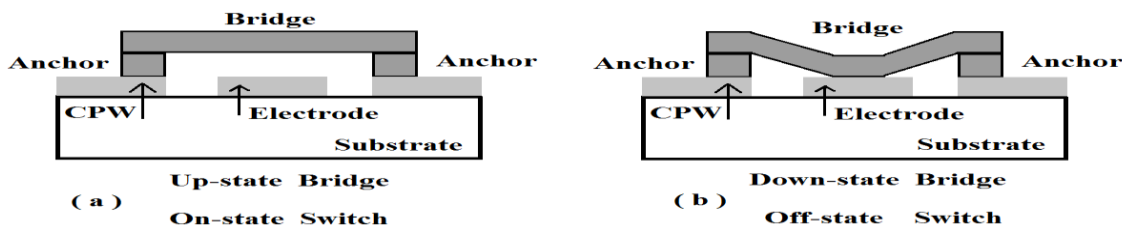


Figure 2-0-4: Bridge working mechanism [31]

RF MEMS switches, however, have some defects. Since all of the cantilevers, electrodes, Microstrips and bridges are extremely thin, these delicate devices have a high risk of deformation, corrosion, fracture, and arcing [32]. The surface adhesion force can cause the contact and flexible beam to be stuck together. Moreover, as MEMS switch works with high voltage bias, the strong electric field in down state can cause a high charge density in dielectric material, which leads to stiction as well. Compared to solid state switches, MEMS switches have a lower power consumption, but a higher actuating

voltage. Furthermore, the structure of MEMS switch is more complex than solid state switch. Only few companies are able to design and produce MEMS in mass scale. The air gap of MEMS switch is susceptible to the high voltage. Even without bias voltage, the thin air gap cannot withstand strong RF signal, and MEMS switches can be automatically turned on. As MEMS switch is vulnerable to any unexpectedly change, rigorous packaging and clean environment are required. Based on the mature semiconductor technology, the cost of a naked MEMS device is low. But the packaging of MEMS costs a lot. Therefore, the final products of MEMS switch do not has price advantage over solid state switches. Since MEMS switches use a high bias voltage to control the mechanical movement of parts, both the lifespan and speed of MEMS switches cannot reach the standards of solid state switches. Also, MEMS switches have a common intrinsic defect which is hysteresis.

A comparison of Electromechanical Relays (EMR), Microelectromechanical System (MEMS), and Solid-State Relays (SSR) is showed in Figure 2-0-5. To take the design condition of SIW antenna into account, PIN diodes have advantage in integrating with PCB technology, and show a better performance than EMR products. MEMS switches are not employed by the designs in this thesis for three reasons. Firstly, MEMS are too small to be mounted on SIW antenna slots. Secondly, because of mass production, PIN diodes have cost advantage over MEMS switches. Finally, PIN diodes have a faster switch speed and longer working life than MEMS switches. Therefore, PIN diodes are chosen for SIW antenna design.

Characteristic	MMR	GaAs FET	PIN diode	EMR PCB	EMR SMA
Size	Small	Very small	Small	Medium	Large
Resistance	0.5Ω	1-5Ω	1-5Ω	0.1Ω	0.5Ω
Switching Power	2W CW	0.5W CW	5W CW	10W CW	35W CW
Breakdown Voltage	Low	Low	Varies	High	High
Speed	0.5-200μs	10-100ns	10-100ns	0.8-10ms	1-40ms
Life Cycle	100 million+	Billion	Billion	0.5-5 million	0.1-2 million
Frequency	Up to 70GHz	Up to 4GHz	Up to 20GHz	Up to 5GHz	Up to 40GHz
Ins. Loss max (dB)	0.25	0.5	0.5	0.4	0.1
Isolation min (dB)	40	30	30	40	80
3rd Order Harmonics	Very good	Poor	Poor	Good	Very good
Power Consumption	Very low	Low	Low	Medium	High
Drive Voltage	5V, 28V, 48V	3V, 5V	3V, 5V	5V, 12V	12V, 28V
Integration Capability	Very good	Very good	Very good	Average	Difficult
Cost – SPDT type	8.00-20.00\$	0.50-4.50\$	0.90-8.00\$	0.85-12.00\$	38-90\$

Figure 2-0-5: Comparison of different switches [33]

2.1.2 PIN diode measurement

Unidirectional current features PIN diode, which is suitable for switch control. With a forward bias, PIN diode works like a short circuit. The majority electrons in negatively doped N-region and the majority holes in positively doped P-region simultaneously flow into the high resistance I-region, and form an internal E-field. And the direction of this internal E-field is consistent with the external applied negative voltage. Moreover, the areas of depletion regions at the junctions of PIN diode are reduced by the forward bias. So that the internal E-field reinforces the flow of charges and weakens the resistance of I-region. With a reverse bias, PIN diode works like an open-circuit. By connecting the positive and negative poles of applied voltage to the N-region and P-region of PIN diode respectively, all the majority charge carriers accumulate at the terminals of opposite polarity. So that the majority charge carriers in both regions will not flow to I-region. The free charges of external applied voltage, as a result, cannot flow through the PIN diode. For an effective SIW antenna slot control, the resistance range of PIN diode must match to the characteristics of slot radiation. When PIN diode is reverse bias in an open-circuit

state, antenna slots are switched to radiate; by contrast, when PIN diode is forward bias in a short-circuit state, antenna slots are switched to be shielded, as shown in Figure 2-0-6.

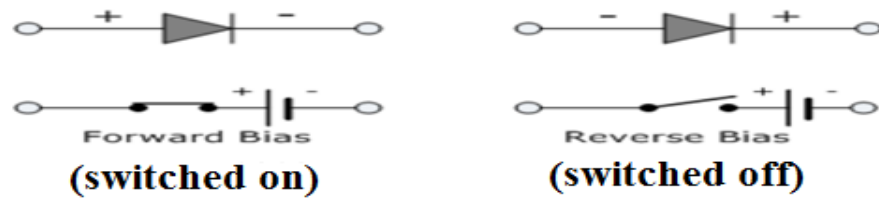


Figure 2-0-6: different PIN diode switch states correspond to different bias circuit

Top view dimensions	Side view dimensions	Foot print

Table 2-0-1: PIN diode specification, Unit: mm

The present thesis employs the BAR64-02V PIN diode made by Infineon Company. Detailed information about the PIN diode is showed in Table 2-0-1. For an effective design, the width of antenna slots should not be greater than the length of PIN diode. Therefore, in determining the width of slots, two factors need to be taken into consideration: the length of PIN diode and the etching errors. As the error scope of etching can be limited to ± 0.1 mm, given the length of the PIN diodes selected is $1.35 \text{ mm} \pm 0.1 \text{ mm}$ as shown in Table 2-0-1, the slot width of all the designs proposed in this thesis is uniformly confined within 1.3 mm. The specification of this PIN diode model declares a RF working range between 1 MHz and 6 GHz. However, the measured results at 2.4 GHz are unsatisfied. Thus, in order to make sure whether the diode can reach the minimum requirement of the proposed designs, further tests are necessary.

The measurements are performed on a Microstrip-line platform by soldering the diode to the two ends of a broken Microstrip line, as shown by the partial enlarged view of ‘TS’ block in Figure 2-0-9. The following measurement results are provided by Dr. Young. The ideal values of reflection coefficient and transmission coefficient are 0 and 1, respectively. Figure 2-0-7 shows phasor magnitude curves with different S-parameters. For all S-parameters, a common feature is that noise increases with frequency. Specifically, significant noise interferences of transmission coefficient S1,2 and S2,1 begin at 2 GHz frequency. The minimum values of reflection coefficient S1,1 and S2,2 are observed at 1.9GHz which are slightly above 0. Furthermore, in order to find out a desirable reference plane, the phase at Microstrip through lines are measured, as shown in Figure 2-0-8. As the two Microstrip through lines bring in additional noise and phase, the rapidly changing phase in Figure 2-0-8 increases loss. A de-embedded measurement, as shown in Figure 2-0-9, is used to eliminate the effect of phase variation. By adding two blocks of negative de-embedding lines on each side of the TS block, the phase at the Microstrip lines can be maintained at zero.

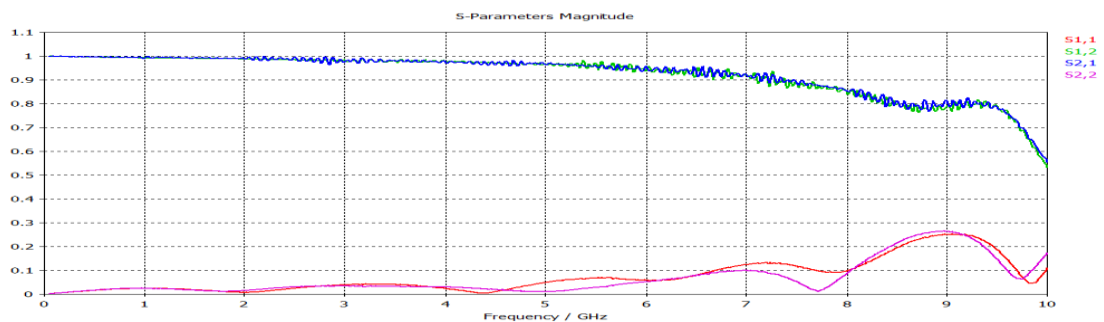


Figure 2-0-7: Measurement results of S-parameters for the testing diode

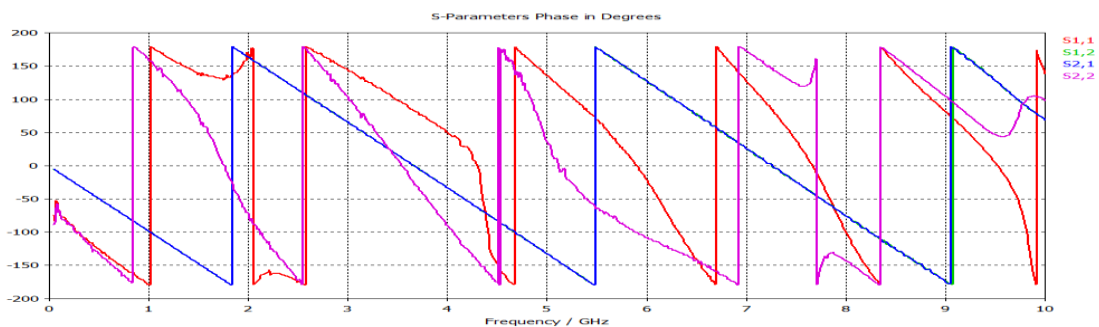


Figure 2-0-8: measured phase of through line in degrees

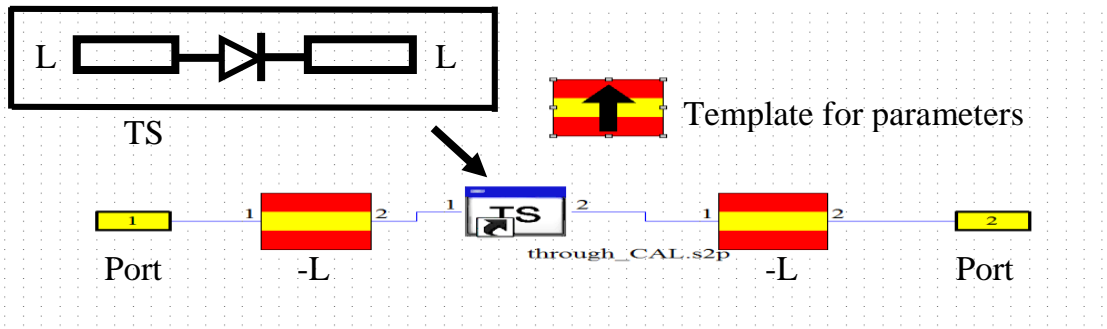
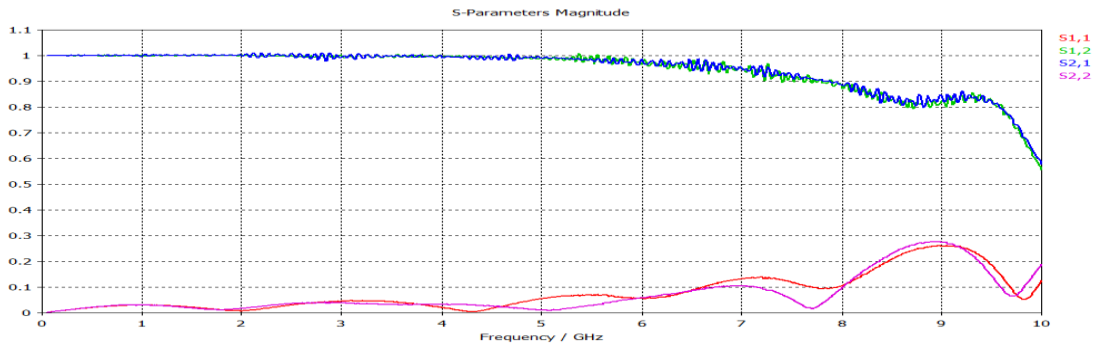
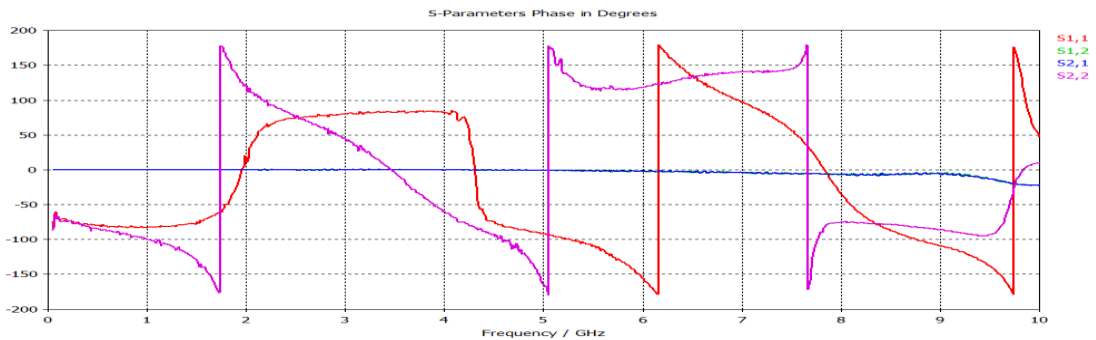


Figure 2-0-9: The circuit of de-embedded measurement in CST



(a)



(b)

Figure 2-10: (a) S-parameters measurement with de-embedding lines, (b) phase measurement with de-embedding lines.

Compared with the measurement results in Figure 2-0-7, the results of transmission coefficient $S_{2,1}$ and $S_{1,2}$ in Figure 2-10 (a) have been significantly improved, and the starting point of degradation is postponed to 5 GHz from the original 2 GHz. Although these ripples are small fluctuations between 2 GHz and 3 GHz as shown in Figure 2-10 (a), the insertion loss of PIN diode is tolerable. Therefore, the extra loss caused by the test

platform is successfully eliminated by adding negative length ($-L$) de-embedding lines. The measurement results of reflection coefficient $S_{1,1}$ and $S_{2,2}$ in Figure 2-10 (a) still remain the same as those in Figure 2-0-7. Compared with Figure 2-0-8, all the phase curves in Figure 2-10 (b) have been significantly improved. Especially, when frequency is below 5 GHz, the phase curves of transmission coefficient remain at zero, which reconfirms the effectiveness of loss offset.

Parameter extraction method:

The s-parameters of a series impedance Z are given by

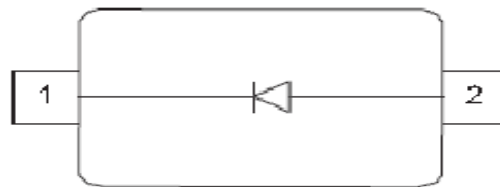
$$\begin{pmatrix} S_{1,1} & S_{1,2} \\ S_{2,1} & S_{2,2} \end{pmatrix} = \frac{1}{2Z_0 + Z} \begin{pmatrix} Z & 2Z_0 \\ 2Z_0 & Z \end{pmatrix}$$

$$\text{Obviously, } S_{1,1} = \frac{Z}{2Z_0 + Z} \quad S_{2,1} = \frac{2Z_0}{2Z_0 + Z}$$

$$\text{Solving for } Z \text{ yields: } Z = \frac{2S_{11}Z_0}{1 - S_{11}} \quad \text{Or} \quad Z = \frac{2Z_0(1 - S_{21})}{S_{21}}$$

with similar expressions for $S_{2,2}$ and $S_{1,2}$.

The known Z_0 is the characteristic impedance of the transmission line. The unknown $S_{1,1}$ and $S_{2,1}$ can be obtained by measurements. The insertion loss measurement of $S_{2,1}$ are less sensitive to the small mismatches in transition, compared with the measurements of $S_{1,1}$. Therefore, the expression using $S_{2,1}$ might be more accurate than the one using $S_{1,1}$. This has been proved in Figure 2-10 (b).



SC79 type package

Schematic 2-1: Schematic diagram of internal PIN diode package

The diode impedance also can be represented in a circuit analysis way. As shown in Schematic 2-1, the PIN diode is connected to the package terminals by wires. Regardless of whether the PIN diode is biased or not, the wire, theoretically, will produce the same inductance L in each state. With forward bias, the PIN diode shows the characteristics of resistor; while with reverse bias, the PIN diode shows the characteristics of both resistor and capacitor. The whole package can be considered as a single PIN diode. Further analyses are showed as follow.

Biased state:

Under forward bias, a PIN diode is in biased state. The diode in biased state can be represented by an inductor and a resistor in series, as $Z = R + j\omega L$

Since, Z can be derived from S-parameters, then R and L can be calculated as follow:

$$R = \text{Re}(Z) \quad \text{and} \quad L = \frac{1}{\omega} \text{Im}(Z)$$

Unbiased state:

Under reverse bias, a PIN diode is in unbiased state. In unbiased state, the diode can be represented by an inductor L in series with a parallel combination of a large resistor R and a capacitor C . The diode impedance is shown as follow:

$$Z = j\omega L + \frac{R}{1 + j\omega CR}$$

Which can also be expressed as:
$$Z = \frac{R}{1 + (\omega CR)^2} + j\omega L - j \frac{\omega CR^2}{1 + (\omega CR)^2}$$

According to the data sheet of PIN diode, C is 0.6 pF and R is 3000 Ω , so $(\omega CR)^2$ equals to 3198 at 5 GHz and 128 at 1 GHz. We therefore can assume that $(\omega CR)^2$ is significantly larger than 1. Thus, we can approximate Z by

$$Z = \frac{1}{(\omega C)^2 R} + j\omega L - j \frac{1}{\omega C}$$

Hence,

$$\text{Re}(Z) = \frac{1}{(\omega C)^2 R} = Z - j\omega L + j \frac{1}{\omega C}$$

$$\text{Im}(Z) = \omega L - \frac{1}{\omega C} = \left(Z - \frac{1}{(\omega C)^2 R} \right) \frac{1}{j}$$

As R can drop significantly with frequency, the assumption that $(\omega CR)^2 \gg 1$ might be invalid. Nevertheless, using the approximated Z to calculate C and R at low frequency level is acceptable. Expression are given as follow:

$$C = \frac{1}{\omega(\omega L - \text{Im}(Z))} \quad \text{and} \quad R = \frac{1}{(\omega C)^2 \text{Re}(Z)}$$

The measurement results of BAR6402 PIN diode with 9V and 3V forward biases and a reverse bias are presented as follow.

De-embedded BAR6402 diode with 9V forward bias:

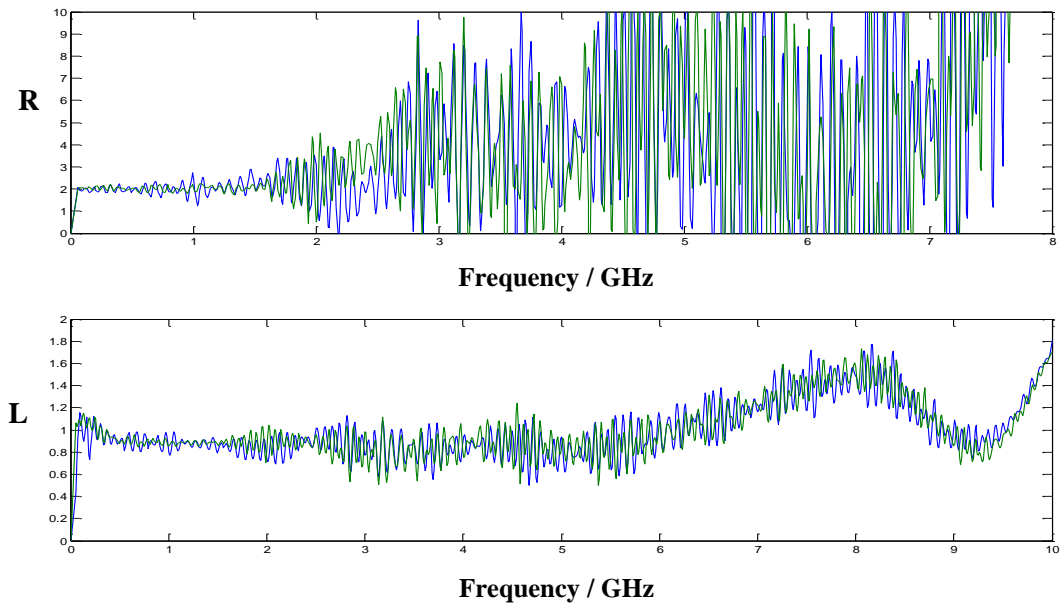


Figure 2-0-11: De-embedded diode with 9V forward bias

As shown in Figure 2-0-11, the upper graph shows the resistance R of diode in ohms versus to frequency F; and the bottom graph shows the inductance L of diode in nH versus to the frequency F. As the measurements of R and L are subject to RF noise interference, the mean value of R and L are adopted. As can be seen, below 7 GHz, the mean values of R fluctuate between 2 and 6 ohms; and L remains at around 0.9nH.

De-embedded BAR6402 diode with 3V forward bias:

As shown in Figure 2-0-12, the upper graph shows the resistance R of diode in ohms versus to the frequency F; and the bottom graph shows the inductance L of diode in nH versus to the frequency F. As can be seen, the average value of R is in the range between 5 and 8 ohms at around 2.4 GHz; and the average value of L is approximate to 0.9nH.

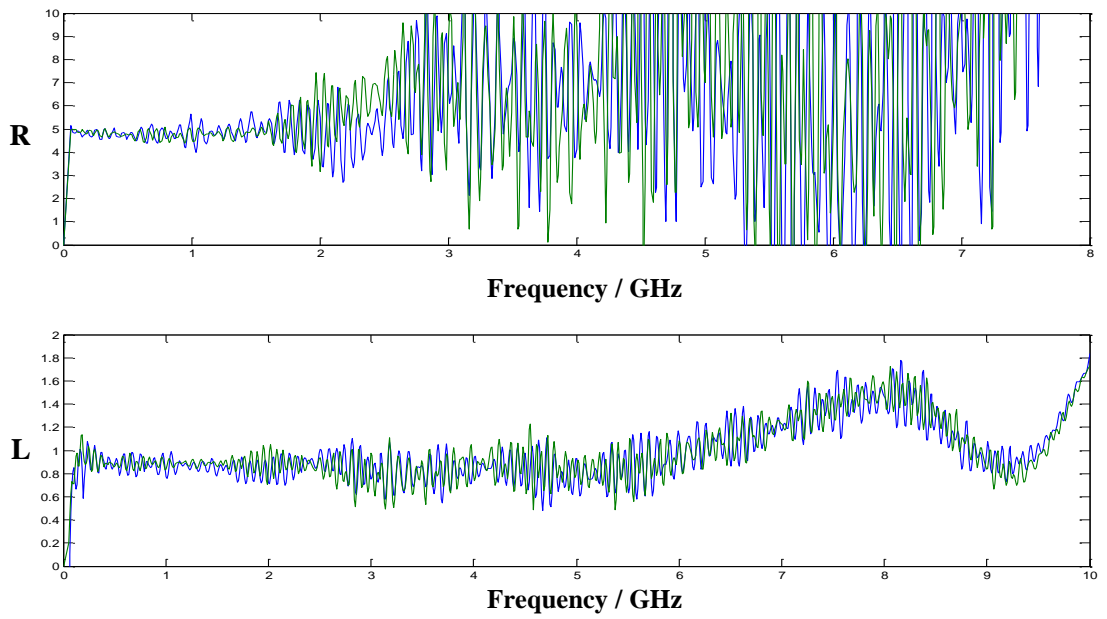


Figure 2-0-12: De-embedded diode with 3V forward bias

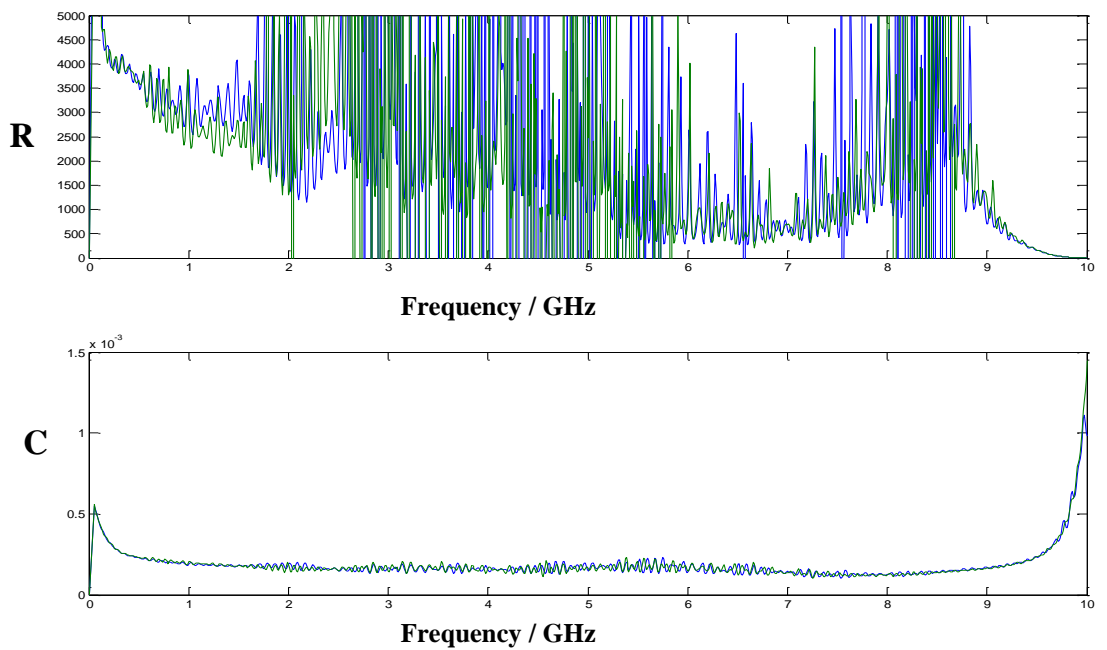


Figure 2-0-13: De-embedded BAR6402 diode in unbiased state

De-embedded BAR6402 diode in unbiased state:

As shown in Figure 2-0-13, the upper graph shows the resistance R of diode in ohms versus to the frequency F; and the bottom graph shows the capacitance C in nF versus to

the frequency F . Since the inductance is a constant, the L measured in previous cases is used here for cancelling out the reactance. Given L equals to 0.9 nH, the resistance R drops from 5000 ohms to 1500 ohms between 2 GHz and 5 GHz, and the capacitance keeps at around 0.2 pF.

To summarize the measurement results, the inductance L is 0.9 nH and the capacitance C is 0.2 pF. As the inductance L is caused by the package parasitic which is shown in Schematic 2-1, both unbiased and biased states are in series with the intrinsic inductance L . As the capacitance in specification is 0.17 pF, which is close to the measured value 0.2 pF, the proposed antenna design will use a capacitance with 0.17 pF for diode in reverse bias. The resistance of diode fluctuates between 2 and 8 ohms at forward bias, and between 2000 and 5000 ohms at reverse bias. Therefore, the diode is represented by the following parameters in the simulation setting:

1. In unbiased state, the diode is represented by a 3000 -ohm resistance R_r in parallel with a 0.17 -pF capacitance C , as shown in (a)

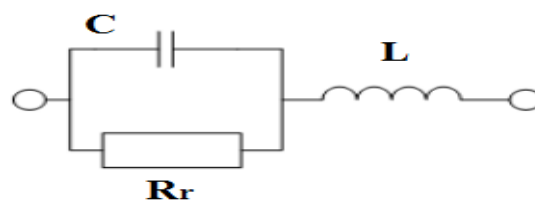


Diagram 2-0-1: equivalent circuit diagram of unbiased state

2. In biased state, the diode is represented by a 2 -ohm resistance R_f .

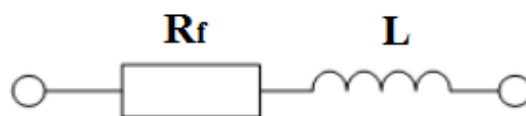


Diagram 2-2: equivalent circuit diagram of biased state

Power supply for PIN diode:

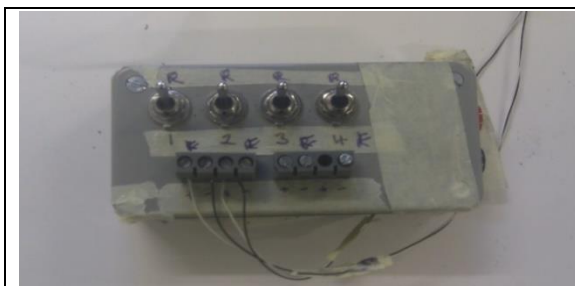


Figure 2-0-14: Switch box

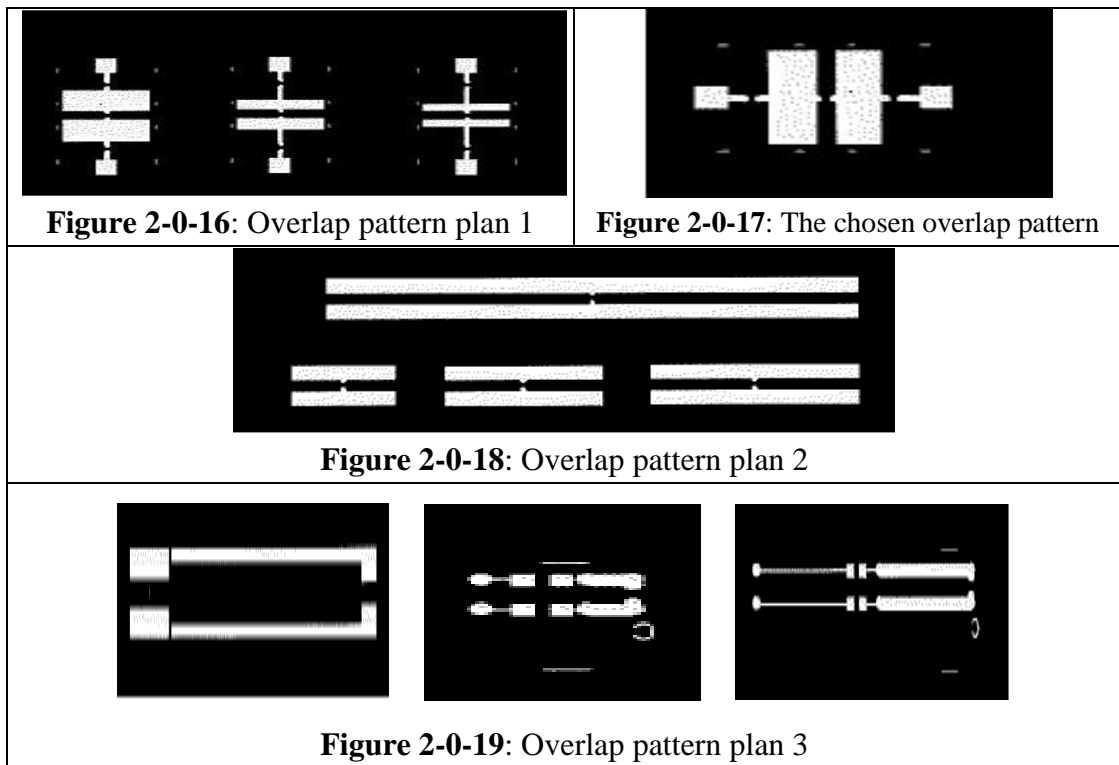


Figure 2-0-15: Battery

The switch box showed in Figure 2-0-14 will be used in the proposed switch antenna designs. The power is supplied by a series of three 9V batteries as shown in Figure 2-0-15, which provide 27-voltage in reverse bias and 10 mA in forward bias. In order to provide the required current, the batteries need to be in series with a 10 K resistance.

2.1.3 Overlap preparation

Since an overlay film is affixed on the metal surface of waveguide with double-sided adhesive tape, further tests about the overlap film are performed. The film as mentioned above consists two layers: the upper one is copper, and the bottom one is dielectric. The adhesive tape used is made of Polyimide material with a relative permittivity between 2.78 and 3.48. Also, 0.8 μH inductors are used to shield the noise caused by the long wires of DC power supply. Bound by the budget, we use the existing inductor chokes in laboratory, which have a working frequency below 1 GHz. On each slot there is an overlap; and on each overlap, a PIN diode is soldered in the center, and on each side of the PIN diode, one inductor and one wire are soldered, as shown in Figure 2-0-20.



As the overlap film need to be etched for devices mounting, the overlap circuit pattern is important and worthy of study. The final choice is made after testing ten candidate options. The circuit patterns, shown in Figure 2-0-16, Figure 2-0-18 and Figure 2-0-19, are some of the alternative options. The pattern show in Figure 2-0-17 is chosen, as this overlap pattern has the minimum coupling effect with antenna slot. The coupling effect between overlap and slot can be found by a direct measurement of the reflection coefficient $S_{1,1}$. The cause of coupling is that the radiation not only transmits to outer space, but also penetrates into the capacitive tape under the overlap. As the relative permittivity of the tape and the waveguide substrate dielectric are close, the radiation wave tends to propagate into the tape. Furthermore, as the overlap has a thin metal layer on top surface, the radiation E-field will be guided along this overlap top metal, and then extend to DC wires. This guided wave will produce an interfering frequency mode which is very close to the working frequency 2.4 GHz. As all the overlap can potentially produce unexpected resonant frequency mode, the selection criterion of overlap pattern is to choose the one with the minimum frequency interference. The overlap pattern showed in Figure 2-0-17

will be used in all proposed switch antenna designs. The two metal pads soldering with the PIN diode have capacitive effect. As shown in Figure 2-0-20, each capacitive pad has a layout area of $8 \times 3.2 \text{ mm}^2$ for supplying a 17 pF capacitance to cancel out unexpected inductance. And on each side of the PIN diode, there is another $2.1 \times 1.9 \text{ mm}^2$ pad for 0.6nH inductor connection and wires bonding. The above-mentioned overlap pattern will be used in all proposed switch antenna design.

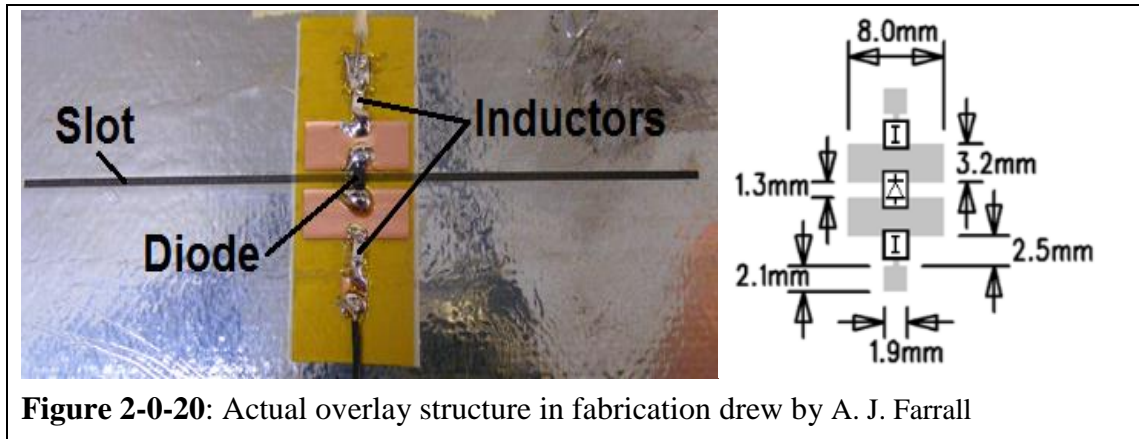


Figure 2-0-20: Actual overlay structure in fabrication drew by A. J. Farrall

2.1.4 Waveguide theory of SIW design

Since SIW is developed on the base of traditional waveguide, the traditional waveguide theories can be applied to SIW. In the textbooks of elementary electromagnetism, such as in Jeffrey [34] and Wheeler [35] editions, waveguide structure is introduced by a dual-wire transmission line. As shown in Figure 2-0-21, on each cross section, the dual-wire transmission line can be bypassed by connecting two sides of each wire with two metal lines, which are a quarter wavelength long and with a short-circuit terminal. This is to say that, in each cross-section plane, there are two half-cycle bypasses which vary the phase 180 degrees. Therefore, the dual-wire transmission line with bypass keeps the transmission amplitude in each cross-section plane constant. A series of such bypass cross-

section planes form a rectangular waveguide. This waveguide configuration interpretation hints a phase difference between the top and the bottom planes. Moreover, as the width of waveguide broad wall is half-wavelength long, the broad wall also has 180-degree phase difference. Therefore, the two broad surfaces of waveguide can be divided into four regions, as shown in Figure 2-0-22. Each pair of diagonal regions are in-phase. But regions in adjacent position are anti-phase. For example, if region 1 and region 3 both have a positive phase, region 2 and region 4 would have a negative phase.



Figure 2-0-21: Waveguide formed by two wires transmission line [36]

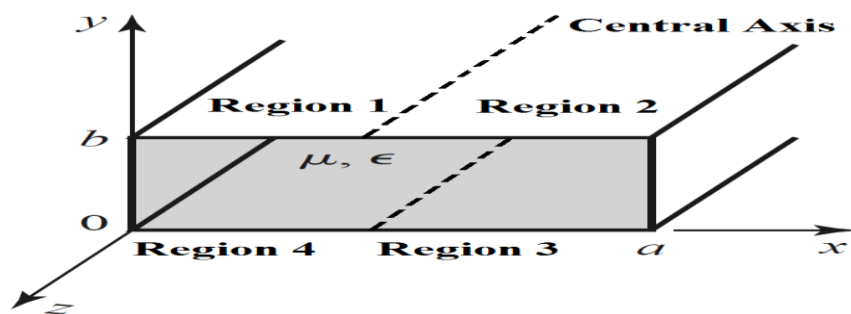


Figure 2-0-22: waveguide phase division in 4 regions

The surface current density \mathbf{K} as an auxiliary method can be used to analyze phase. When the \mathbf{K} directions of slot regions are the same, the radiations of slots will be in-phase, vice versus. The \mathbf{K} is defined as:

$$\mathbf{K} = \hat{\mathbf{a}}_n \times \mathbf{H} \quad [37] \quad \text{where } \hat{\mathbf{a}}_n \text{ is the unit normal vector on waveguide surface.}$$

For waveguide antenna application, TE₁₀ mode has the largest power to radiate. Based on the H-field components in TE₁₀ mode as shown in Figure 1-0-5, the **K** direction not only can distinguish the phase difference in these four regions, but also can indicate the polarization of radiation E field as shown in Figure 2-0-23. Only when the waveguide slot is perpendicular to surface current density **K**, the surface current will be perturbed, which makes the slots radiate. The input electric field of waveguide in the fundamental mode TE₁₀ is:

$$\vec{E} = -2E_0 \sin \frac{m\pi x}{a} \sin(\omega t - \frac{2\pi z}{\lambda_g}) \hat{a}_y \quad [38]$$

Where E₀ is the constant amplitude of E-field; λ_g is the guided wavelength; ‘x’ is the variable at X axis, which is with a range of the waveguide width ‘a’; ‘z’ is the variable at Z axis, which is the wave propagation direction inside waveguide; ‘m’ is mode number. The incident E-field only varies along the X axis, and shows in half cycle of sinusoidal wave.

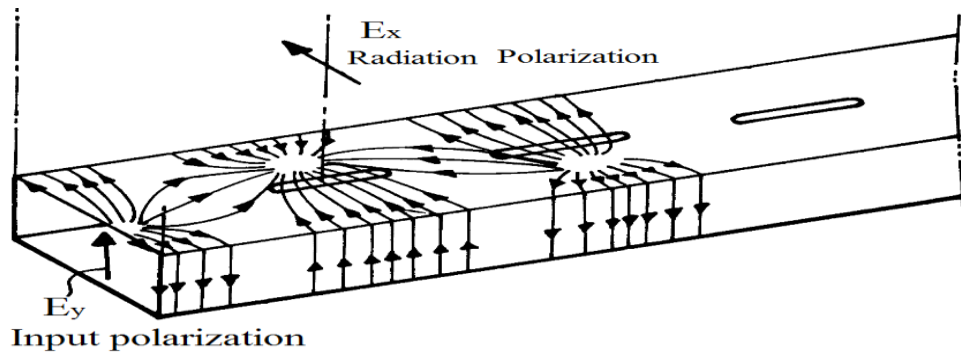


Figure 2-0-23: waveguide surface current distribution

When the front end output port of waveguide antenna is short-circuited, the longitudinal slots offsetting from broad wall central line will radiate at specific position. According to the transmission line theory, when the longitudinal slot center locates one quarter wavelength away from the waveguide front end, the overlapped E-fields between the front end reflection E-field and the input E-field will reach the maximum intensity at the slot

center. Based on the fundamental mode, the transmission line theory and the Babinet's principle, Stevenson [39] used Green function to deduce the longitudinal slot characteristic and presented the slot by a shunt conductance which is normalized by the characteristic admittance. As the Stevenson theory is a representative work of equivalent circuit method, Silver rewrote the longitudinal slot formula into an engineering form, which is shown as following.

$$g = \frac{G}{Y} = g_1 \sin^2 \left(\frac{\pi x}{a} \right) \quad [40] \quad \text{Where } g_1 = 2.09 \frac{\lambda_g a}{\lambda b} \cos^2 \frac{\lambda \pi}{2\lambda_g} \quad [40]$$

Where x represents the offset from the central axis to the waveguide edge.

Therefore, the E-field radiates along the slot in half cycle of sinusoidal wave. Stevenson theory only works accurately in traditional rectangular waveguides, both hollow and dielectric filled ones. The reason is that the height 'b' of traditional waveguide is sufficiently large, compared with the height of substrate integrated waveguide (SIW). So that, the radiation field in the slot of traditional rectangular waveguide, though, is composed by unperturbed incident field and perturbed field surrounding at the slot edge, the unperturbed incident field holds a dominant position over the other. However, in the SIW, perturbed field takes the dominant position, which produces modes other than the incident TE₁₀ mode. As shown in Figure 2-0-24, the SIW structure causes unique radiating feature in slot. Compared with traditional rectangular waveguide, SIW has a thinner metal layer, and a greater aspect ratio between height and width, and replaces narrow side walls with metal-plated via holes. The SIW with metal-plated via posts has three more constitutive parameters than the traditional bulky waveguide, respectively, the distance between the centers of adjacent posts represented by 'p', the air gap between adjacent post surfaces represented by 's' and the diameter of metal post represented by 'd', as shown in Figure 2-0-24.

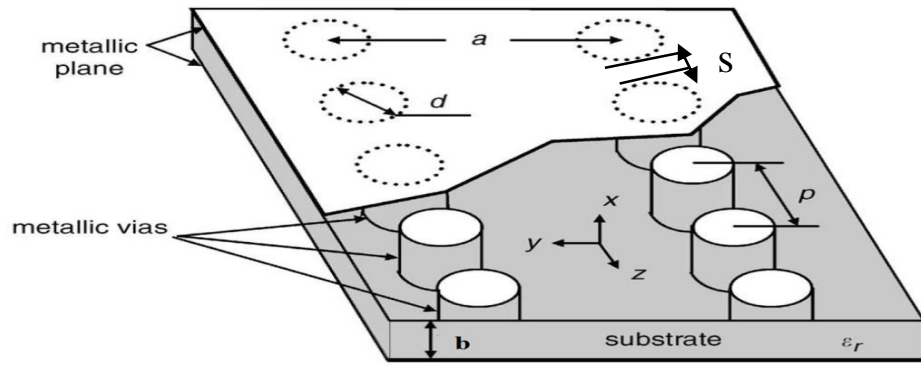


Figure 2-0-24: Geometry of substrate integrated waveguide [41]

The potential leakage problem of SIW relates to the parameters of ‘p’, ‘s’ ‘b’ and ‘d’. As found in Hirokawa [42] paper, the effective width ‘a’ of SIW is inversely proportional to the via post interval ‘p’. To increase interval ‘p’ will cause a greater electromagnetic wave diffusion to outer space. According to the Figure 1-0-12, when ‘p’ is 1mm, the attenuation will be around 0.05 dB/cm. The air gap ‘s’ also directly relates to the electromagnetic wave leakage [43]. As shown in Figure 2-0-25, when the air gap ‘s’ is larger than 0.5 mm, the leakage loss will accelerate. So that, the practical maximum value of ‘s’, based on the equation of $s = (p-d)$, is defined at 0.5 mm. Although to increase diameter ‘d’ can reduce the air gap ‘s’, this practice has been proved to be infeasible [44]. The experimental evidence shows that attenuation constant increases in proportion to the diameter dimension. The empirical rule is let p equal to 2d. Once the ‘s’ and ‘p’ are set at 0.5 mm and 1mm, respectively, the ‘d’ shall be 0.5 mm. All the proposed SIW designs in this thesis will use the above three values for via post setting.

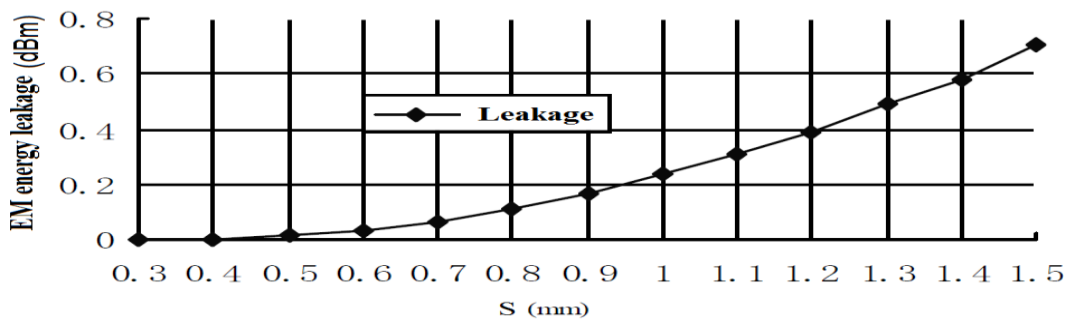


Figure 2-0-25: Power loss calculated by scattering parameters [43]

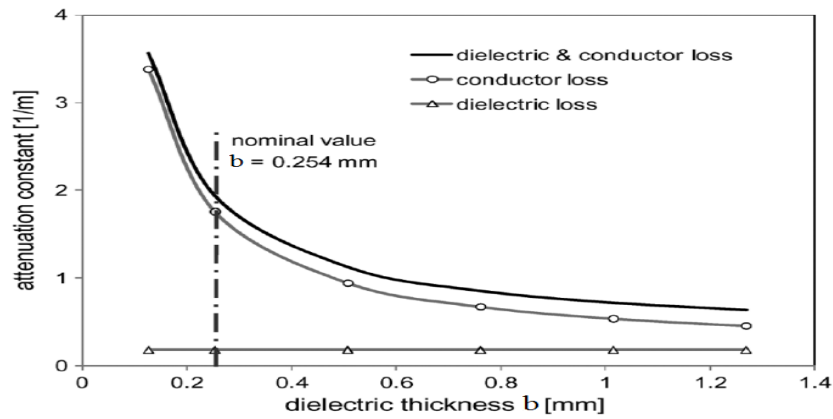


Figure 2-0-26: the relation between thickness b and attenuation constant [45]

On one hand, the height ‘ b ’ of SIW should be kept very small, otherwise higher-order modes will vary along the via post surface and radiate to outer space. On the other hand, ‘ b ’ should not be too small. This is because SIW simultaneously suffers from radiation leakage loss, ohmic loss and dielectric loss [46]. As the height ‘ b ’ is inversely proportional to the attenuation constant as shown in Figure 2-0-26 [45], a small ‘ b ’ will cause a large attenuation loss. Therefore, there is a trade-off in deciding the dimension of ‘ b ’. Duroid PCB laminate with a thickness of 1.575 mm is chosen. Also the dielectric loss relates to the intrinsic property of substrate material. The higher the permittivity is, the greater the dielectric loss will be [47]. Moreover, substrates with high permittivity will guide the electromagnetic field to propagate towards to dielectric. A great proportion of electromagnetic field energy retains in the substrate, and the radiation efficiency, as a result, degrades. Taking all these factors into consideration, all the proposed SIW antenna designs in this thesis will choose the PCB substrate with a relative permittivity of 2.2.

The S-parameter performance, such as return loss, is affected by the width ‘ a ’ of SIW, which in turn depends on the post diameter ‘ d ’ and post interval ‘ p ’. Only in odd mode transmission, can SIW with an appropriate structure have the working principle and the physical property the same as the corresponding conventional waveguide. Therefore, the

width ‘a’ of SIW, like the traditional waveguide width ‘w’, can be used to calculate the proper size of SIW and other relative waveguide characteristics. The following four calculation formulas demonstrate the relationships between ‘a’ and ‘w’.

$$\text{Equation (2-0-1) : } a = \frac{2w}{\pi} \cot^{-1} \left(\frac{\pi p}{4w} \ln \frac{p}{2d} \right) \quad [48]$$

$$\text{Equation (2-0-2) : } a = w + \frac{d^2}{0.95p} \quad [49]$$

$$\text{Equation (2-0-3) : } w = a - 1.08 \frac{d^2}{p} + 0.1 \frac{d^2}{a} \quad [44]$$

$$\text{Equation (2-0-4) : } a = w = \frac{c}{2f_c \sqrt{\epsilon_r} \cos \theta} \quad [50]$$

Equation (2-0-1) [48] provides a theoretical analysis of the narrow side walls between SIW and traditional metallic waveguide. This width calculation of SIW is deduced from the surface impedance of via posts, ‘a’, as a result, is mainly determined by the factor of ‘p/2d’. As the side walls of traditional waveguide are formed by Perfect Electric Conductor (PEC), the surface impedance of PEC side walls should be naught. Therefore, when d=p/2, the SIW width ‘a’ equals to the width of traditional waveguide ‘w’. This suggests that in a specific frequency band, the surface impedance of the via posts can approximate to zero. When d< p/2 as shown in Figure 2-0-27 (a), the SIW width ‘a’ is smaller than the width of traditional waveguide ‘w’, which means that the via posts are working like an inductive wall. When d> p/2 as shown in Figure 2-0-27 (b), the SIW width ‘a’ is larger than the width of traditional waveguide ‘w’, which means that the via posts are working like a capacitive wall. Figure 2-0-27 [48] shows the top views of electromagnetic field distribution in H plane and the above-mentioned side wall positions. The dash line and the solid line represent the via posts of SIW and the side wall of traditional waveguide, respectively. To keep the propagation field of SIW the same as that of traditional waveguide, the location of SIW via posts wall is determined by ‘d’, ‘p’, or ‘s’. Therefore, the SIW via posts design in this thesis is based on the equation, d= p/2.

Equation (2-0-2) [49], is derived from the cut-off frequency formula. This equation only works at TE₁₀ mode under the conditions that $d/b > 1/4$, 'b' is fixed at 1.5mm and 'p' is small. Obviously, the SIW width 'a' is slightly larger than the width of equivalent traditional waveguide 'w', and the difference should be within the range of 'd'.

Under the restrictions of $d/p > 1/3$ and $d/a < 1/5$, Equation (2-0-3) [44] includes the factor 'd/w' to reduce the deviation of attenuation constant. This equation, as a result, is considered to be more precise than Equation (2-0-2). As the dimension 'p' \ll 'a' in Equation (2-0-3), the width 'w' of equivalent traditional waveguide is also smaller than corresponding 'a' of SIW. However, the calculation of this equation is inconvenient, as 'a' need to be solved out in a denominator of quadratic function.

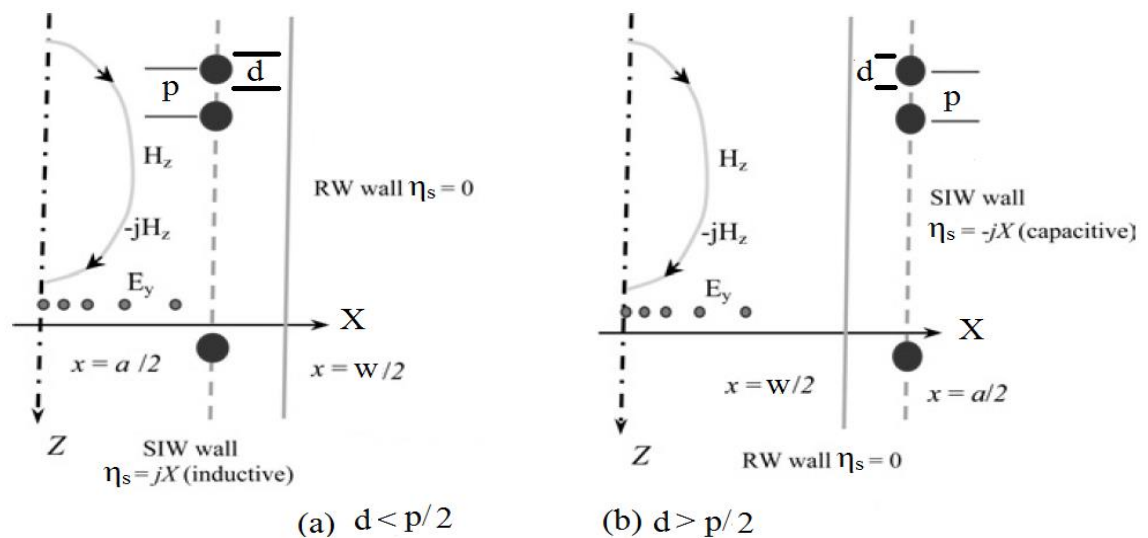


Figure 2-0-27: Equivalent waveguide width corresponding to SIW vias size [48]

Under the premises that $d/a < 1/8$, $d/p > 2/5$ and the interval of via posts is small, Equation (2-0-4) [50] is suitable for the case that the widths of SIW and traditional waveguide are equal. Based on the SIW width 'a', the intrinsic waveguide characteristics, such as the

cutoff frequency, working frequency range, guided wavelength, dispersion characteristics and propagation constant, can be derived. As shown in Figure 2-0-28 [44], in SIW, waves propagate in a zigzag path with an incident angle $\cos\theta$, which is identical to the case of traditional metallic waveguide if omitting the leakage of higher frequencies in the air gap 's'. As the calculation of Equation (2-0-4) is easy and fast, all the SIW structures in this thesis will use this equation to do rough calculations of input TE_{10} mode at preliminary stage.

Equation (2-0-5):
$$\cos \theta = \frac{n\lambda_g}{2a} \quad [50]$$

Where 'n' is mode order and ' λ_g ' is the guided wavelength.

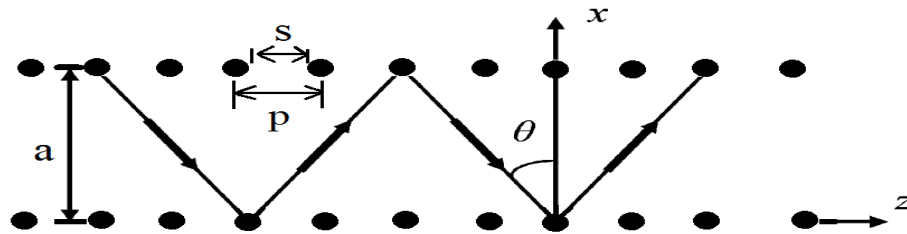


Figure 2-0-28: TE_{n0} mode propagation in zigzag path [44]

As shown in Equation (2-0-5), the guided wavelength is inversely proportional to the angle θ . The larger the angle θ is, the smaller the wavelength will be [51]. When angle θ is 0, waveguide stops propagating, which means the cutoff frequency is reached. Once SIW width 'a' is determined, SIW can be connected to a 50Ω Microstrip input port by a transition. Generally, there are two kinds of SIW transitions. One is coplanar waveguide (CPW) [52] as shown in Table 2-0-2 (a), the other is Microstrip line [54] as shown in Table 2-0-2 (b). As both the signal feed line and ground are on the same plane, the CPW transition is suitable for the thick SIW substrate and high dielectric constant substrate. For forming a CPW transition, a pair of feedline slots with two transition slots need to be etched on the substrate. Therefore, CPW feedline requires a higher fabrication precision

than Microstrip feedline. Moreover, compared with Microstrip line, CPW has a larger radiation leakage loss, which will weaken the SIW slot radiation.

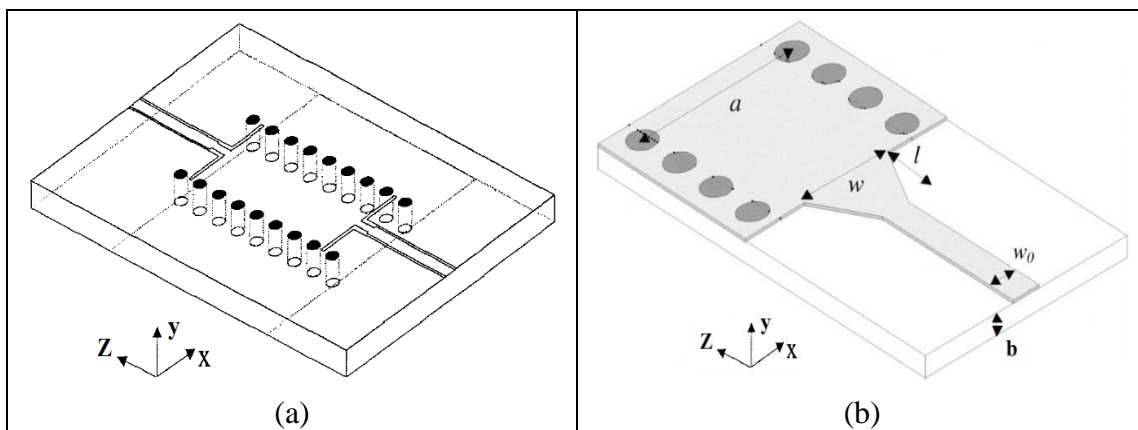


Table 2-0-2: (a) Coplanar transition [52], (b) Microstrip transition [53]

For the thin substrate, the fringing field loss of Microstrip line is tolerable. As the SIW designs in this thesis use the PCB laminate with a thickness of 1.575 mm, the Microstrip transition is selected. The advantage of Microstrip transition is that the input transversal E-field of SIW is similar to the E-field distribution inside the Microstrip line substrate, as shown in Figure 2-0-29. Therefore, the substrates of Microstrip transition and SIW can be integrated into one single plane.

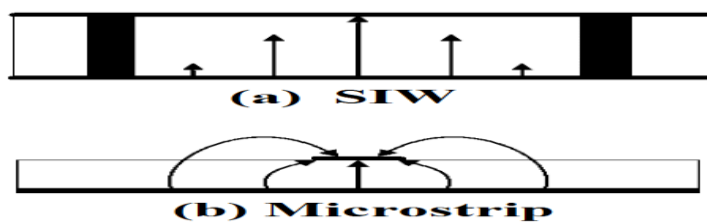


Figure 2-0-29: Transverse E field in SIW and Microstrip

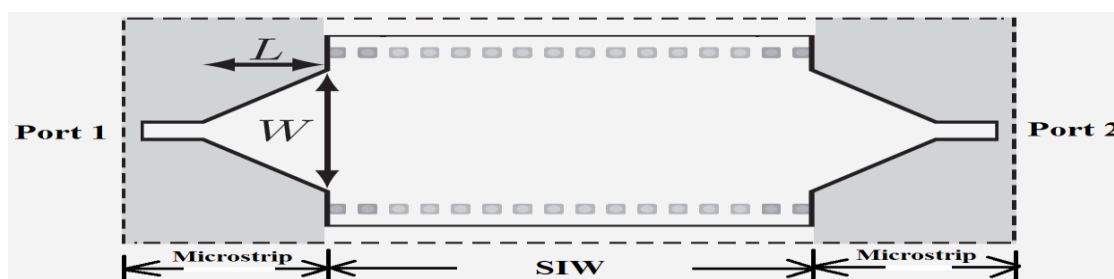


Figure 2-0-30: Two ports network for transition match [55]

The Microstrip transition consists of a 50-ohm rectangular Microstrip line and a taper transition. As the structure of Microstrip transition is simple, the optimal dimension of taper can be work out by directly tuning the width 'W' and length 'L' of taper in simulation. Also, the two-port network model in simulation is built up by connecting two back-to-back Microstrip transitions to the two terminals of SIW, as shown in Figure 2-0-30. When $S_{1,1}$ is below -20 dB and $S_{2,1}$ approaches to zero, the transition bandwidth is defined by the $S_{1,1}$. The Microstrip transition has a wider bandwidth than CPW transition.

2.2 Two direction switch antenna

The purpose of building a two-direction switch SIW antenna is to research whether PIN diodes can be used to control slots in different planes. One application of the two-direction switch-beam antenna is the point-to-point wireless bridge for backhaul.

2.2.1 Antenna geometry

Figure 2-0-31 and Figure 2-0-32 show the topside and underside of the antenna, respectively. As the switching DC power wires have potential risk of guiding RF signal and can cause unwanted leaky radiation, these wires are stuck at the two sides of waveguide by yellow tapes. Figure 2-0-33 shows the drawing dimensions of the antenna fabricated. These dimensions are set for the convenience of fitting to the reference point which is fixed. Table 2-0-3 shows the value of all antenna parameters in simulation.

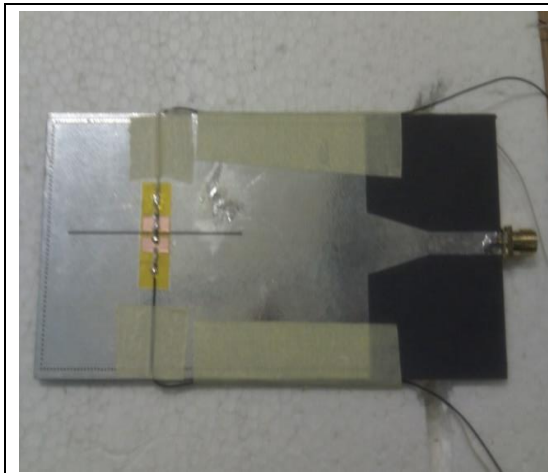


Figure 2-0-31: Top view of antenna

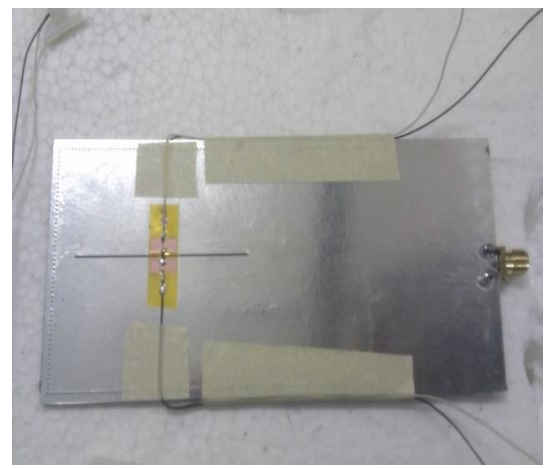


Figure 2-0-32: Bottom-view of antenna

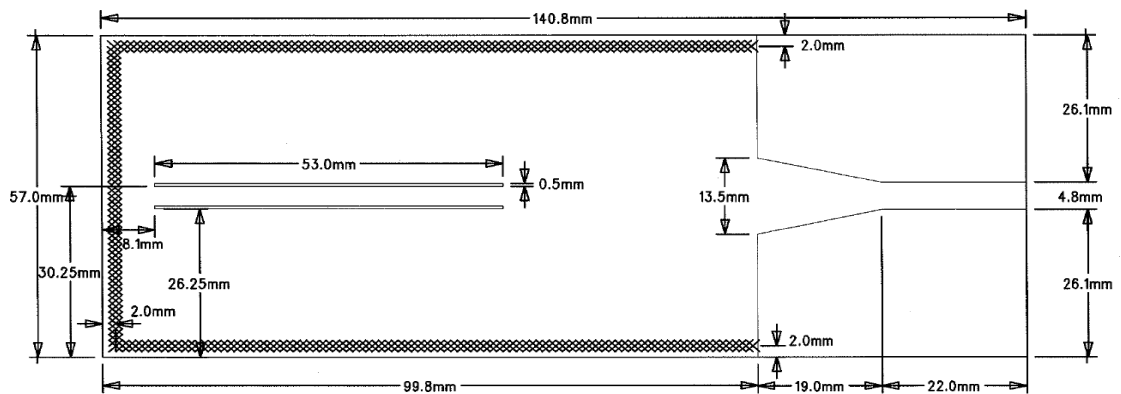


Figure 2-0-33 : Fabrication dimensions of two directions antenna drawn by A. Farrel

Parameters	Length / mm	Description
L	97.8	Length of waveguide antenna part= $r*3$
a	53	Waveguide width
b	1.575	Thickness of waveguide substrate
T	0.07	Thickness of surface copper
Ls	53	Slot length
r	32.6	One quarter lambda wavelength
ext	2	PEC wall width
i	4.75	Input port width
n	19	Length of Taper
u	13.5	Width of Taper
f	22	Length of Microstrip feedline
w	0.5	Slot width
x	2	Offset of slot position from central line of waveguide to edge

Table 2-0-3: Parameters of 2-direction Antenna

2.2.2 1-D results of antenna performance

As the performance of single diode off state is the key measuring object, the $S_{1,1}$ of diode 1 and diode 2 will be measured individually. The $S_{1,1}$ simulation results in Figure 2-0-34 and Figure 2-0-35 have nearly identical return losses and bandwidths. Both slots have an identical response frequency at 2.433GHz.

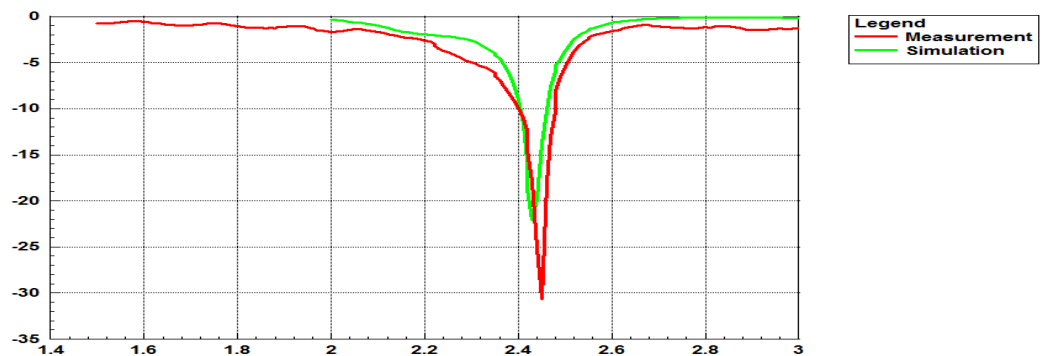


Figure 2-0-34: $S_{1,1}$ curve of top slot diode switched off

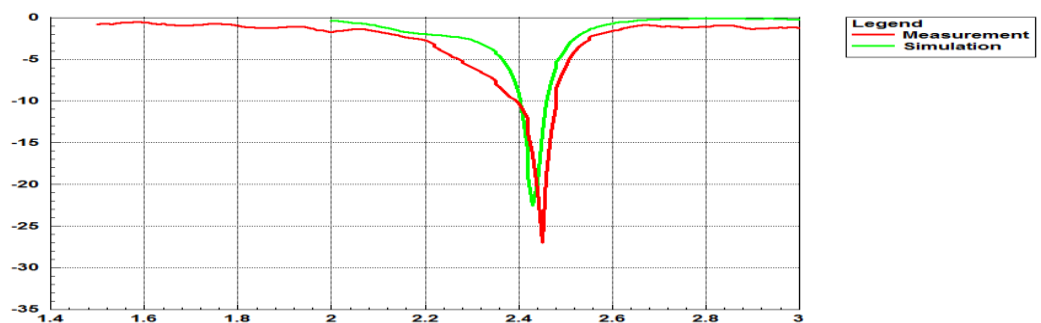


Figure 2-0-35: $S_{1,1}$ curve of bottom slot diode switched off

But, the actual measurement results of $S_{1,1}$ are better than the simulation outcomes in both reflection coefficient and bandwidth. And the actual response frequency of both diode 1 and diode 2 states are kept at 2.450 GHz which is very close to the simulation frequency. Usually, the $S_{1,1}$ curve of traditional waveguide antenna in the absence of diode-mounting is symmetric to the resonant frequency center point. But, within the frequency range between 2.100 GHz and 2.400 GHz, the $S_{1,1}$ results from both

measurement and simulation have asymmetric low return loss values, which suggests that there are some power responding in slot between this frequency range. This can be caused by the overlap mounting. The detailed results of the two diode states are listed in Table 2-0-4. The S_{1,1} values of simulation and measurement are all below -20dB, which means that less than 1% of the power reflects back to the input port from the antenna. The bandwidth is counted when return loss is below -10 dB. Therefore, the bandwidths in Figure 2-0-34 and Figure 2-0-35 all reach the minimum requirement of 50 MHz. The measurement values of bandwidth are greater than the simulation results.

Top diode 1 off state	Simulation results	Measurement results
S_{1,1} Return loss	-23.25 dB	-30.71 dB
Working frequency	2.433 GHz	2.45 GHz
Bandwidth	56.4 MHz	80.5 MHz
Bottom diode 2 off state	Simulation results	Measurement results
S_{1,1} Return loss	-23.75 dB	-27 dB
Working frequency	2.433 GHz	2.45 GHz
Bandwidth	57.1 MHz	90 MHz

Table 2-0-4: S_{1,1} results of simulation and measurement in diode 1 and diode 2 off-state

Table 2-0-4 shows that slot 2 performs a bit better than slot 1. The reason is that the metal surface areas in the top and bottom broad walls are different, though these two slots are identical. This phenomenon will be further analyzed in the following near-field and far-field results. Figure 2-0-36 shows the S_{1,1} results of all-diode off state. Both the simulation and the measurement have a good response at 1.900 GHz, which is lower than the working frequency of single diode. This is because the impedance in all-diode off state is different from the impedance in single-diode state. Therefore, all-diode off-state antenna needs to reduce the slot length to keep the working frequency at 2.433 GHz. Table 2-0-5 shows the comparison of the three S_{1,1} results at different frequencies. It is clear that the working frequencies of all-diode off-state and single-diode off-state will not interfere with each other. Figure 2-0-37 shows the results of all-diode on-state. The simulation results

along the whole frequency spectrum are all less than -0.4dB. But the minimum measured value of S_{1,1} is -2.139 dB at 2.410 GHz as shown in Table 2-0-6. The measurement results are slightly worse than the simulation results at -1.9 dB. This is because the actual resistance of diodes in short-circuit state is larger than the design value, 2 ohms. These graphs of reflection coefficient prove that the diodes are all working well in different states. The measurement results are very close to the simulation ones. Therefore, the simulation results can be used to do further analysis and explain the antenna working mechanism.

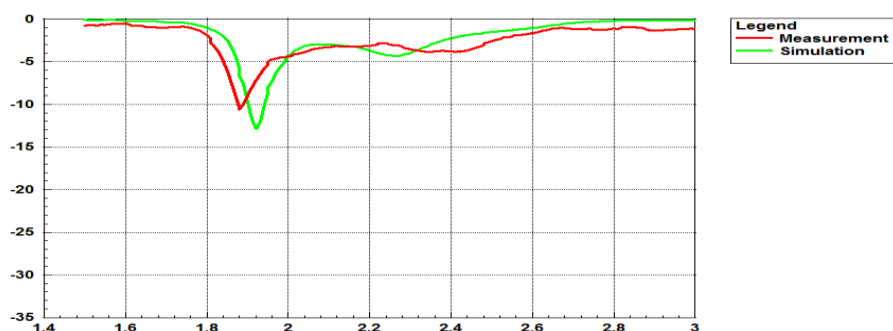


Figure 2-0-36: All-diode switched off

All diodes switched off	Simulation results	Measurement results
1st return loss / frequency	-12.912 dB at 1.920 GHz	-10.663 dB at 1.884 GHz
Bandwidth	41MHz	18MHz
2nd return loss / frequency	-4.133dB at 2.267GHz	-3.839dB at 2.406GHz
Bandwidth	-	-
3rd return loss / frequency	-1.950dB at 2.433 GHz	-3.771dB at 2.433 GHz
Bandwidth	-	-

Table 2-0-5: S_{1,1} of simulation and measurement in all diodes off-state

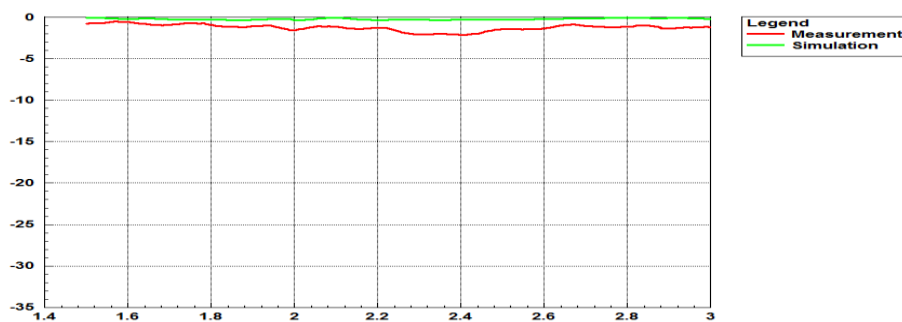


Figure 2-0-37: All-diode switched on

All diodes switched on	Simulation results	Measurement results
1 st return loss / frequency	-0.344 dB at 2.315 GHz	-2.139 dB at 2.410 GHz
Bandwidth	-	-
2 nd return loss / frequency	-0.341 dB at 1.863 GHz	-1.212 dB at 1.876 GHz
Bandwidth	-	-
3 rd return loss / frequency	-0.294 dB at 2.433 GHz	-2.026 dB at 2.433 GHz
Bandwidth	-	-

Table 2-0-6: S1,1 of simulation and measurement in all diodes on-state

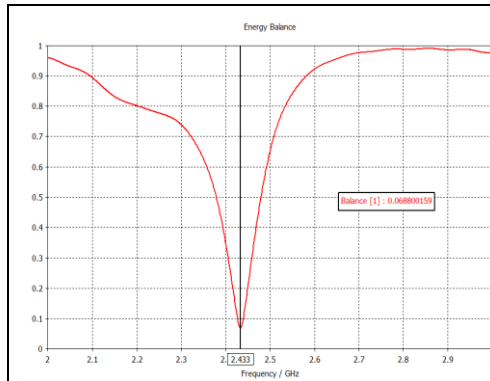


Figure 2-0-38: Energy Balance of top slot 1

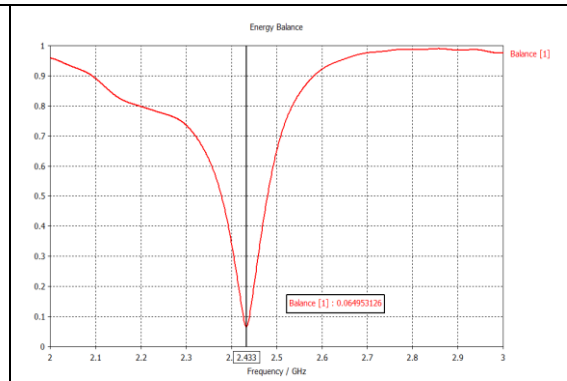


Figure 2-0-39: Energy Balance of Bottom slot 2

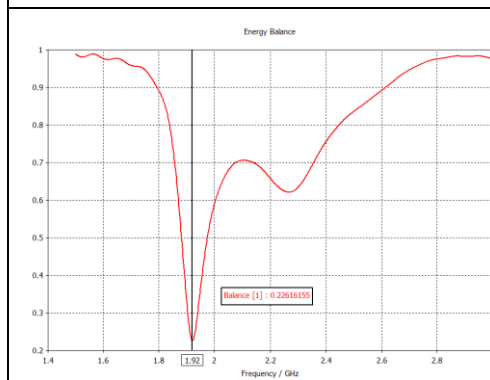


Figure 2-0-40: Energy balance of all diodes on

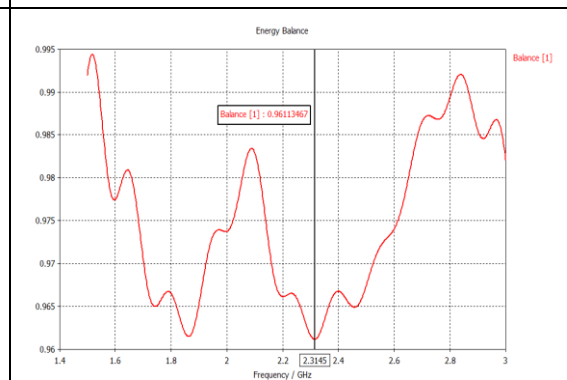


Figure 2-0-41: Energy balance of all diodes off

Figure 2-0-38 and Figure 2-0-39 show the energy balance simulation results of diode 1 off-state and the diode 2 off-state, respectively. Both two states have over 93 percent of the energy radiating to the outer space. And less than 10% of the energy leaks between 2.1 GHz and 2.3 GHz. This leakage should be caused by the short-circuited diode. Figure 2-0-40 shows the energy balance of all-diode off-state. There are two troughs in the graph, one is 0.621 at 2.267 GHz, and another is 0.226 at 1.92 GHz. The record low 0.226 means that 77 percent of the energy leaves without turning back. Figure 2-0-41 shows the energy balance of all-diode on-state. The lowest value of radiating energy in Figure 2-0-41 is

0.961 at 2.315 GHz, which means that almost 4% of the energy leaks out from the slots. At 2.433 GHz, the energy balance is 0.967 which means around 3.3% of the energy leaks.

2.2.3 2-D results of near-field range

The following section will show the E-field distribution in near field scope at three different cut-planes. The near field region is $R < 0.62\sqrt{D^3/\lambda}$, where R is the distance from antenna, λ is the wavelength in air, and D is the largest dimension of antenna. Although near field energy do not contribute to farfield propagation, near field pattern can show the surface scattering interference of antenna. Moreover, as the radiation mechanism of waveguide is based on the perturbed field of slot, E-field distribution surrounding the slots need to be analyzed. To contrast, the radiation of dipole antenna depends on the surface current distribution.

Figure 2-0-42 and Figure 2-0-43 show the coordinates of XOZ cut-plane. The location of diode 1 at the (x,y,z) coordinate is (32.60, 28.50, 1.65); The location of diode 2 at (x,y,z) coordinate is (32.60, 24.50, -0.07). Figure 2-0-44 shows the diode 1 off state. The maximum E-field with a value of 26335.7 V/m offset at the slot 1 outer edge, but not at the slot center, because of the mild coupling between the waveguide top surface traveling wave and the input signal surface wave of Microstrip transition. This coupling will cause uneven distribution of the induced charges on the two long sides of the slot. This is an intrinsic problem of Microstrip structure, which can be solved by adding a metal reflector perpendicular to the top plane. Although part of the Microstrip E-field is exposed in air, most of the E-field in this part is transmitted into antenna. Only a negligible amount of the energy leaks from Microstrip.

Figure 2-0-45 shows the diode 2 off state. The pattern shown in Figure 2-0-45 is nearly identical to the one in Figure 2-0-44, except the coupling caused by Microstrip. As being connected to the ground of the Microstrip, slot 2 does not have coupling effect. Therefore, the maximum E-field appears at the center of the slot. The slot 2 has a stronger radiation intensity than slot 1, because the ground has a larger metal surface area which causes more surface current around the slot 2.

Figure 2-0-46 and Figure 2-0-47 show all-diode off state at different frequencies. As both slots have identical radiation pattern, only the cut-plane of slot 1 is shown. For each slot, the maximum E-field locates at the slots center, because these two slots share internal energy and external surface coupling wave equally. As the slots in Figure 2-0-46 have better impedance match at 1.92 GHz, the E-field observed at 1.92 GHz is stronger than the one at 2.433 GHz, shown in Figure 2-0-47.

Figure 2-0-48 and Figure 2-0-49 show all-diode on state at 2.315GHz and 2.433 GHz, respectively. Both two figures show very small leakage at the slots. The peak E-field all locate at the inner center of the waveguide, which means that most of the energy is confined in waveguide. The higher-order mode in the slots shown in Figure 2-0-49 proves that the short-circuited diode can work at 2.433 GHz. Although the Microstrip feedlines of both figures have significant leakage, these leakages mainly exist in near field. As the XOZ cut-planes in all-diode on state cannot fully demonstrate the E-field at slots, another cut-plane will be introduced to analyze the slot leakage E-field.

XOZ cut-plane position at the Y axis

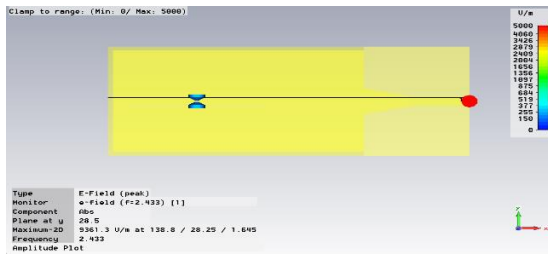


Figure 2-0-42: diode 1 center at Y axis 28.5 mm

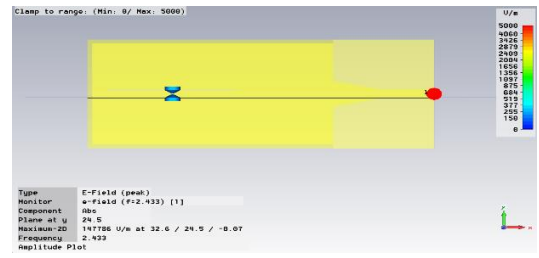


Figure 2-0-43: Diode2 center at Y axis 24.5 mm

Diode 1 switched off

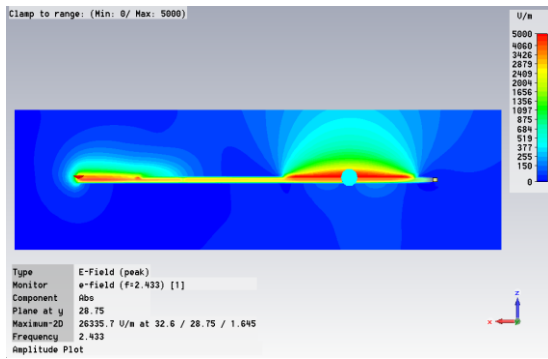


Figure 2-0-44: XOZ plane of top slot diode 1 off

Diode 2 switched off

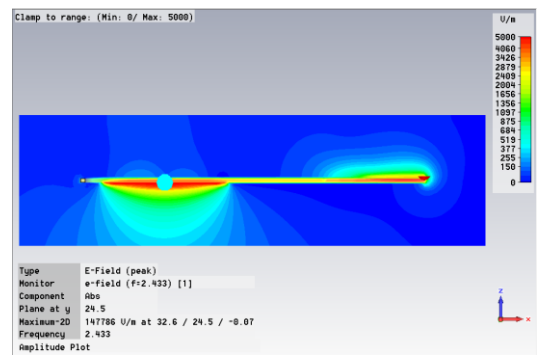


Figure 2-0-45: XOZ plane of bottom slot diode 2 off

All diodes switched off

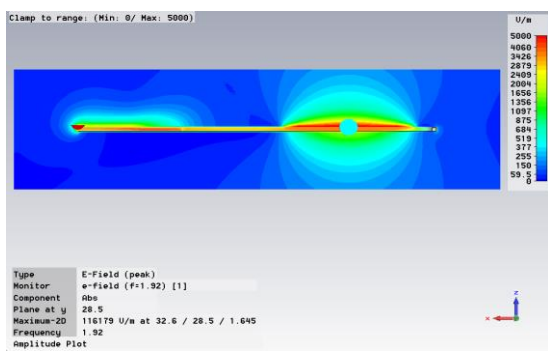


Figure 2-0-46: XOZ at D1 center when 1.92 GHz

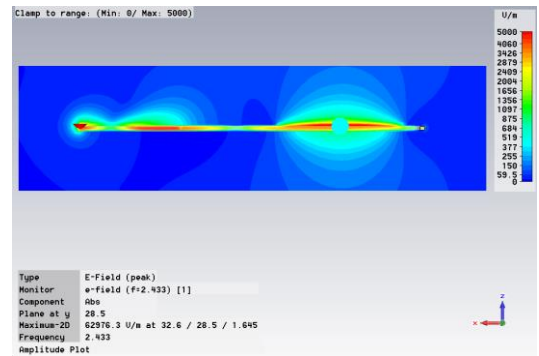


Figure 2-0-47: XOZ at D1 center when 2.433 GHz

All diodes switched-on

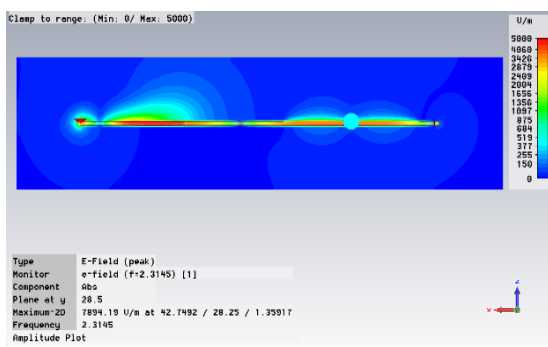


Figure 2-0-48: Diode 1 center plane at 2.315GHz

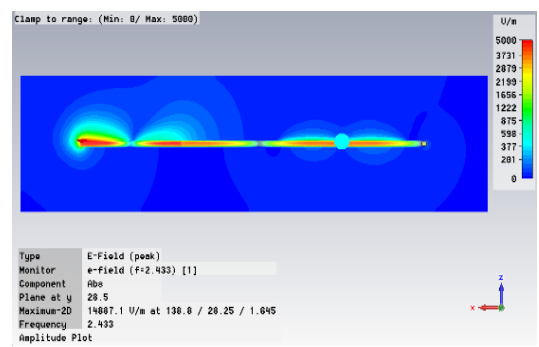


Figure 2-0-49: Diode 1 center plane at 2.433GHz

Figure 2-0-50 (a) shows the YOZ cut-plane located at the X axis where $X=32.6$ mm. Figure 2-0-50 (b) shows the schematic drawing of working diode in diode 1 off state. Figure 2-0-51 and Figure 2-0-52 show the radiation E-fields of the top slot and the bottom slot at YOZ cut-plane, respectively. The bottom slot has a larger radiation intensity than top slot. This is because the metal surface areas are different between the top plane and the bottom plane of waveguide. As the feed line at top plane consists of a taper transition and a 50 ohm rectangular Microstrip line, the ground plane obviously has a larger metal surface area than top plane. Moreover, the backward component of top slot radiation is coupled with the fringing field of Microstrip feed line, which will store the coupling E-field energy in near field range. But the bottom slot radiation will not have these problems, due to the uniform plane. However, the graphs of the two single-diode off states all show obvious scattering E-field at the waveguide edge. Figure 2-0-53 shows the E-field distribution of all-diode off state. The maximum E-field intensity locates at the top slot, which is different to the case of single diode. The reason is that the shunt impedance of two diodes has a better match at top slot. As within the waveguide the E-fields of the two radiation slots are in phase, the coupling fields inside the waveguide can reduce the effect caused by the difference in surface metal areas. Moreover, the surface radiation E-fields of the two slots in Figure 2-0-53 are in-phase only around the slots surface, but anti-phase at the two edges of the waveguide. Figure 2-0-54 shows the E-field distribution of all-diode on state. This graph show that only negligible leaky waves of higher-order mode escape from the waveguide surface. And the maximum E-field locates inside the waveguide. Therefore, the diodes in on state can have an effect similar to a short circuit.

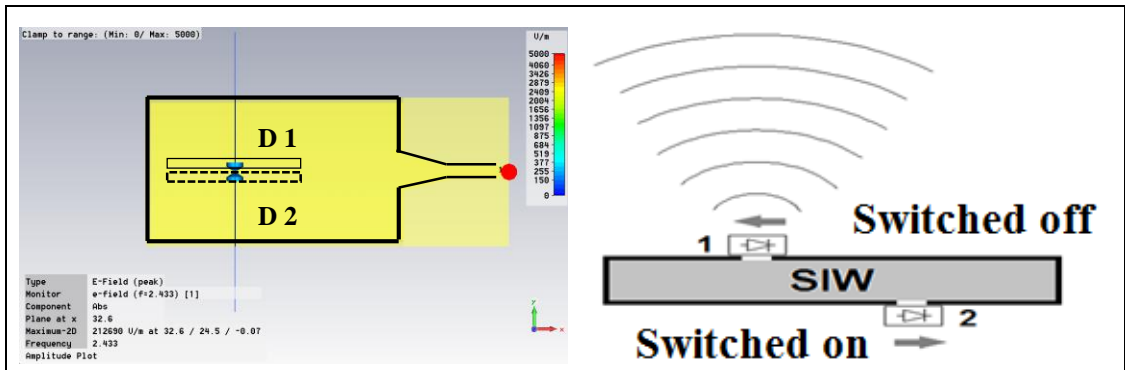


Figure 2-0-50: (a) YOZ plane at X axis 32.6 mm, (b) diode states schematic drawing by A. Farrel

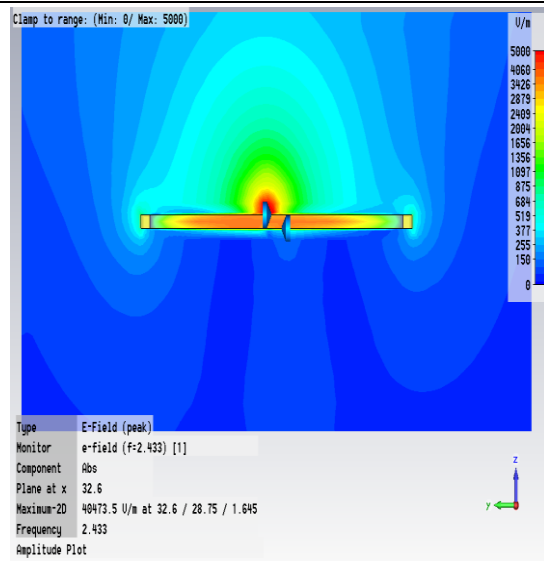


Figure 2-0-51: Top Diode 1 off state at 2.433 GHz

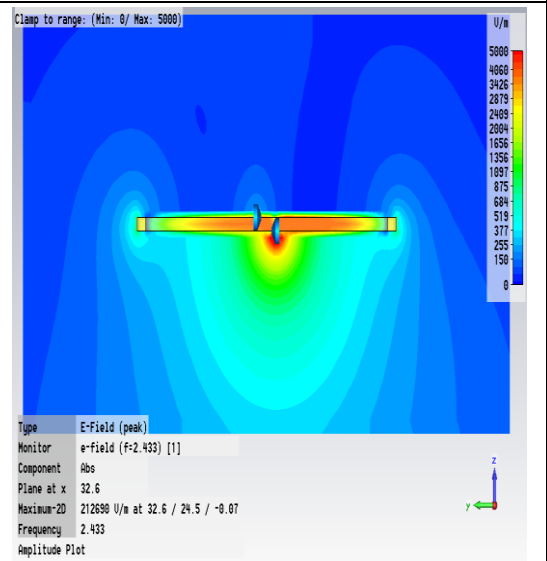


Figure 2-0-52: Bottom Diode 2 off at 2.433 GHz

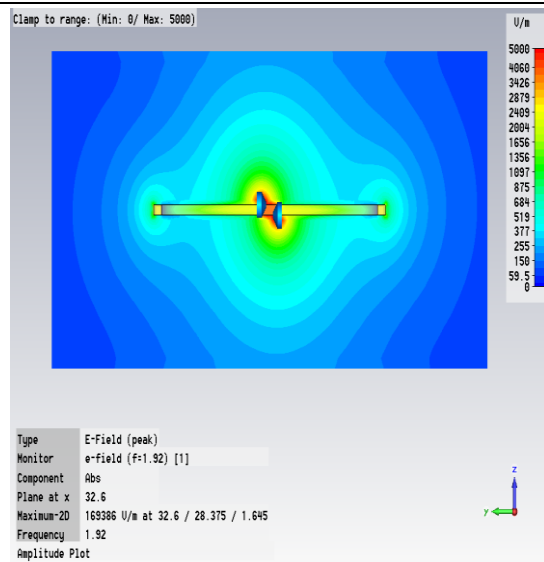


Figure 2-0-53: all-diode off at 1.92 GHz in YOZ

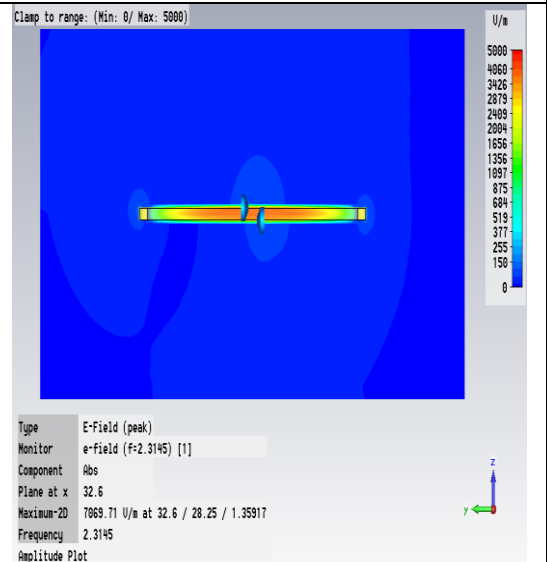


Figure 2-0-54: all-diode on at 2.315 GHz in YOZ

For observing the E-field on the waveguide broad wall, the XOY cut-plane is introduced. Figure 2-0-55 shows the XOY cut-plane above the waveguide top surface. Figure 2-0-56 shows the XOY cut-plane beneath the waveguide bottom surface. Both XOY cut-planes have a 1mm distance from the waveguide surface. Figure 2-0-57 and Figure 2-0-58 show the radiation E-field of the top slot and bottom slot in XOY planes, respectively. These two graphs show that the slots have the same E-field distribution at the antenna part. But at the feedline part, only the top plane has E-field distribution at the Microstrip transition section. The common feature in these two graphs is that the radiation E-field trends to the two corners of antenna front end. This tendency is mainly caused by the forward guided wave transmitting from waveguide interior. As slot is offset from the central line of waveguide, the distance from slot to the two edges of waveguide are different. As a result, the E-field strength at the two sides of the slot are unbalanced. And the shorter distance side will have a stronger E-field distribution. Figure 2-0-57 shows that the E-field along the two edges of the waveguide slightly trends backward to the input port. So that, this graph proves that surface waves of radiation and Microstrip outer E-field part couple together. As the radiation patterns of all-diode off state and single-diode off state are similar, the E-field pattern of all-diode off state in XOY plane will not be repeated here. Figure 2-0-59 and Figure 2-0-60 show the E-field distribution of the top and the bottom planes at all-diode on state at 2.315 GHz. As the short-circuit effect of diodes restrains the fundamental mode from properly resonating at slots, these two graphs show the leaky wave radiation caused by higher-order mode. The leaky wave decrease significantly after leaving the slots edges.

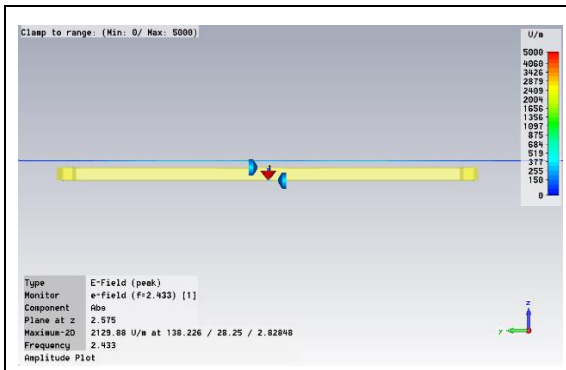


Figure 2-0-55: XOY plane when Z= 2.575 mm

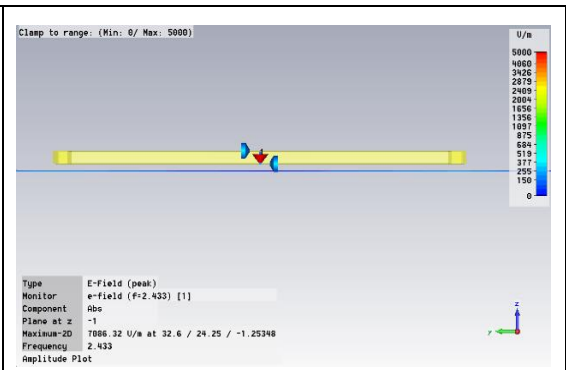


Figure 2-0-56: XOY plane when Z= -1 mm

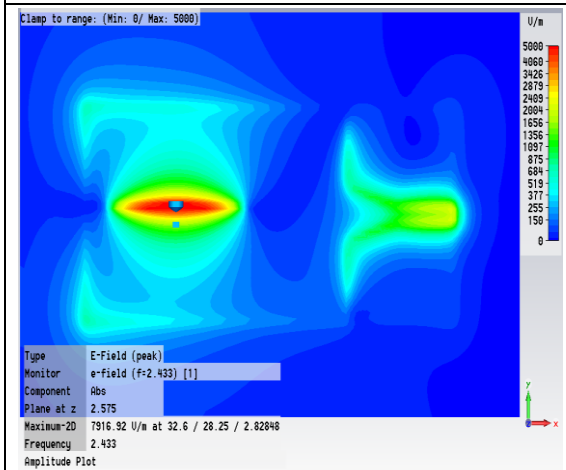


Figure 2-0-57: Diode 1 off at 2.433 GHz

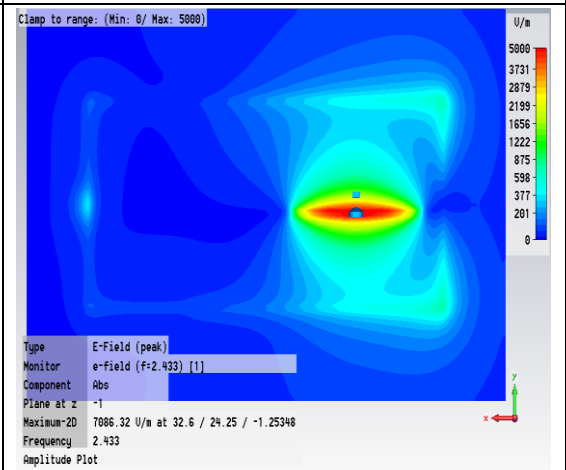


Figure 2-0-58: Diode 2 off at 2.433 GHz

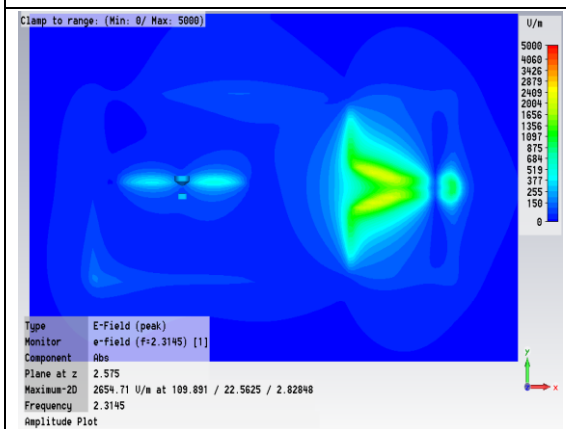


Figure 2-0-59: top plane of all-diode on

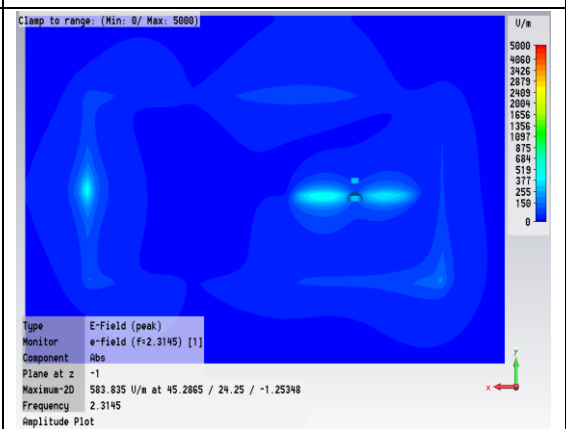


Figure 2-0-60: bottom plane of all-diode on

2.2.4 3-D results in Far-field range

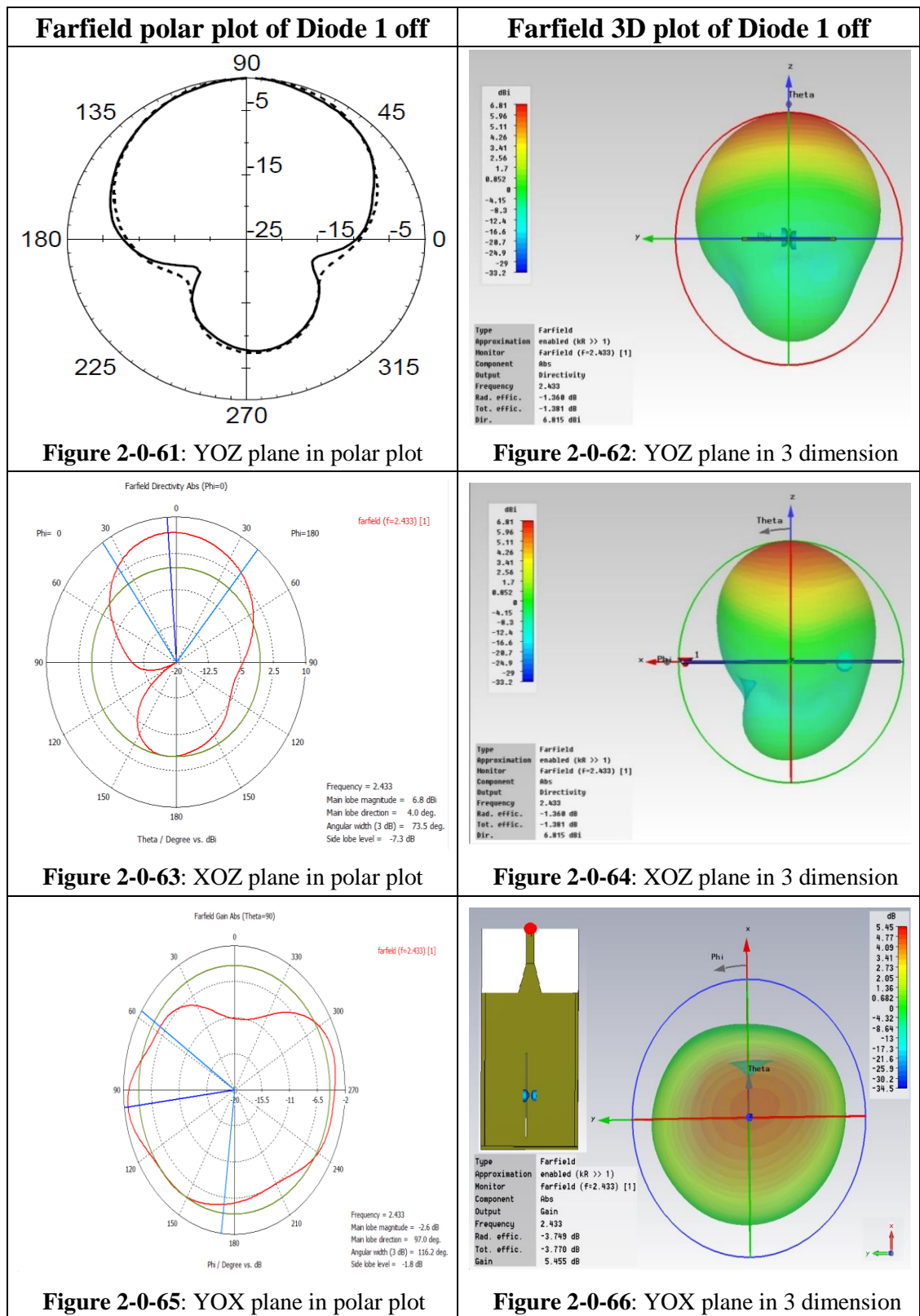


Figure 2-0-61 to Figure 2-0-66 show the far-field results of diode 1 off-state. The three-dimensional far-field pattern shown in Figure 2-0-62 is at a YOZ plane. The radiation efficiency and total efficiency are -1.360 dB and -1.381 dB, respectively. As the difference between these two efficiency value is only 0.021 dB, the loss of impedance mismatch is low, which has been proven by the corresponding $S_{1,1}$ result. Figure 2-0-61 shows the far-field E-plane with polar plot in a YOX plane, where the dash line and the solid line represent the simulation result and measurement result, respectively. The simulation gain is 5.455 dBi, which is higher than that of the quarter-wavelength monopole antenna. The measurement gain is 5.2 dBi, and the measurement pattern matches with the simulation pattern. The main lobe direction offsets 2 degree from the normal line, because the E-field strengths are difference at the two sides of radiation slot. As showed in Figure 2-0-51, compared with the right edge, the left-edge of waveguide has a larger scattering field guided into the bottom plane. Therefore, on the right side of the slot more E-field energy can be radiated. As the side lobe level is -7.3 dB, the side lobe is -1.845 dB. As the radiation of top slot is anti-phase with the leaky wave of ground slot, these two E-fields cancel each other out at both sides of waveguide. So that the farfield pattern at the ground plane of waveguide shrinks sharply. Figure 2-0-64 shows the 3D far-field pattern in a XOZ plane, and Figure 2-0-63 shows the corresponding polar plot. The main lobe direction in Figure 2-0-63 shows a 4 degree deviation toward input port. The leaky wave of bottom slot also has a backward tendency. As shown in Figure 2-0-44, the radiation E-field couples backward with the fringing field of Microstrip transition. Moreover, Figure 2-0-57 shows that in front of the antenna, the dominant radiation E-field in XOY plane is in-phase with the weak leaky wave of slot 2. As a result, these two waves combine together, diffract into ground plane and move towards to input port under the influence of radiation E-field. The 3dB angular width in XOZ plane as shown in Figure 2-0-63 is 73.5 degree, which is 27.6 degree smaller than the one shown in YOZ plane in Figure 2-0-61. This is because in the radiation E-field, the Y-axis component is larger than the X-axis component. The

side lobe level in XOZ plane as shown in Figure 2-0-63 still is 7.3 dB, which is the same as the result in YOZ plane shown in Figure 2-0-61. The 3D far-field pattern shown in Figure 2-0-66 demonstrates the 3 dB beamwidth scope of main lobe. Figure 2-0-66 shows that the far-field peak does not locate at the exact center, but slightly trends towards the input port, which proves the main lobe directions in Figure 2-0-63 and Figure 2-0-64. Figure 2-0-65, as the corresponding polar plot of Figure 2-0-66, shows the bottom half of the farfield by taking the top surface of the waveguide as the cut-plane. Figure 2-0-65 also shows that the local E-field main direction in XOY plane has a 7 degree forward deviation from the Y-axis. The reason is showed in Figure 2-0-57, where the propagation trends to waveguide edge. The shorter the lateral distance from slot to waveguide edge is, the more intensive the radiation would be. Moreover, Figure 2-0-65 have two lobes at 60 degree and 300 degree, respectively. This is because the backward E-field component is guided along both edges of the waveguide.

Figure 2-0-67 to Figure 2-0-72 show the far-field results of diode 2 off-state. Figure 2-0-68 shows the 3D far-field pattern in YOZ plane. The radiation efficiency and total efficiency in Figure 2-0-68 are -1.357 dB and -1.376 dB, respectively, which have a difference of 0.019 dB. Compared with the 0.021 dB difference of slot 1 shown in Figure 2-0-62, the efficiency difference of slot 2 is smaller. Thus, slot 2 has a slightly better impedance matching than slot 1, which can be proved by Table 2-0-4. Figure 2-0-67 shows the corresponding polar plot of Figure 2-0-68, where the dash line and solid line represent the simulation result and measurement result, respectively. Both lines have similar shape. The simulation gain is 5.490 dBi, which is slightly greater than the one in slot 1. This is because the metal surface area of ground plane is a slightly larger than that of the top plane. But the measurement gain is 4.7 dBi, which is 14% less than the simulation one. The reason of the reduction is that the additional loss and reactance caused by overlap and mounting devices increase the forward state resistance of diode 1 and decreases the reverse state

resistance of diode 2. The main lobe direction in Figure 2-0-67 has a 2 degree deviation from the normal line, which is the same as the one in slot 1. The reason is shown in Figure 2-0-51 and Figure 2-0-52. As both slots have in-phase radiations, the left-edge scattering field of waveguide in both slots is larger than the right edge one. So that both the radiations of two slots incline to the right. The back lobe patterns shown in Figure 2-0-67 and Figure 2-0-61 are different. This is because these back lobes consists of different elements. The back lobe in Figure 2-0-61 mainly consists of leaky wave from slot 2. But, the back lobe in Figure 2-0-67 mainly consists of the coupling E-fields of slot 1 leaky wave and Microstrip fringing field. Compared with the simulation pattern, the measured back lobe in Figure 2-0-67 shrinks, as a great proportion of the radiation energy has diffracted into the top plane and reduced the area of the coupling E-fields. This is another reason causing the low measurement gain in slot 2. Figure 2-0-69 and Figure 2-0-70 show the XOZ plane far-field in 3D pattern and polar plot, respectively. The 3 dB angular width in Figure 2-0-69 is 71 degree, which is 2.5 degree less than the one of slot 1 in Figure 2-0-63. This is because the waveguide ground plane has a larger metal surface area to reflect the radiation E-field of slot 2. Figure 2-0-72 shows the three-dimensional 3 dB beamwidth scope. Figure 2-0-71 is the corresponding polar plot of Figure 2-0-72. The local main lobe direction of slot 1 and 2 in XOY plane, as shown in the figures, are almost the same. Figure 2-0-58 explains why the local main lobe in Figure 2-0-71 is at the edge of waveguide, but not at the front end. As the E_y of radiation not only is a dominant component but also is in-phase with the leaky wave of slot 1, the radiation tends to be guided along the Y axis and move towards waveguide edges. As the width of waveguide is limited, the radiation cannot be totally reflected, and part of the E-fields are continuously guided by the two edges of the waveguide to move towards the front end. But, E-fields at the front end will not contribute to the farfield, as these guided E-fields are anti-phase at the edge of front-end.

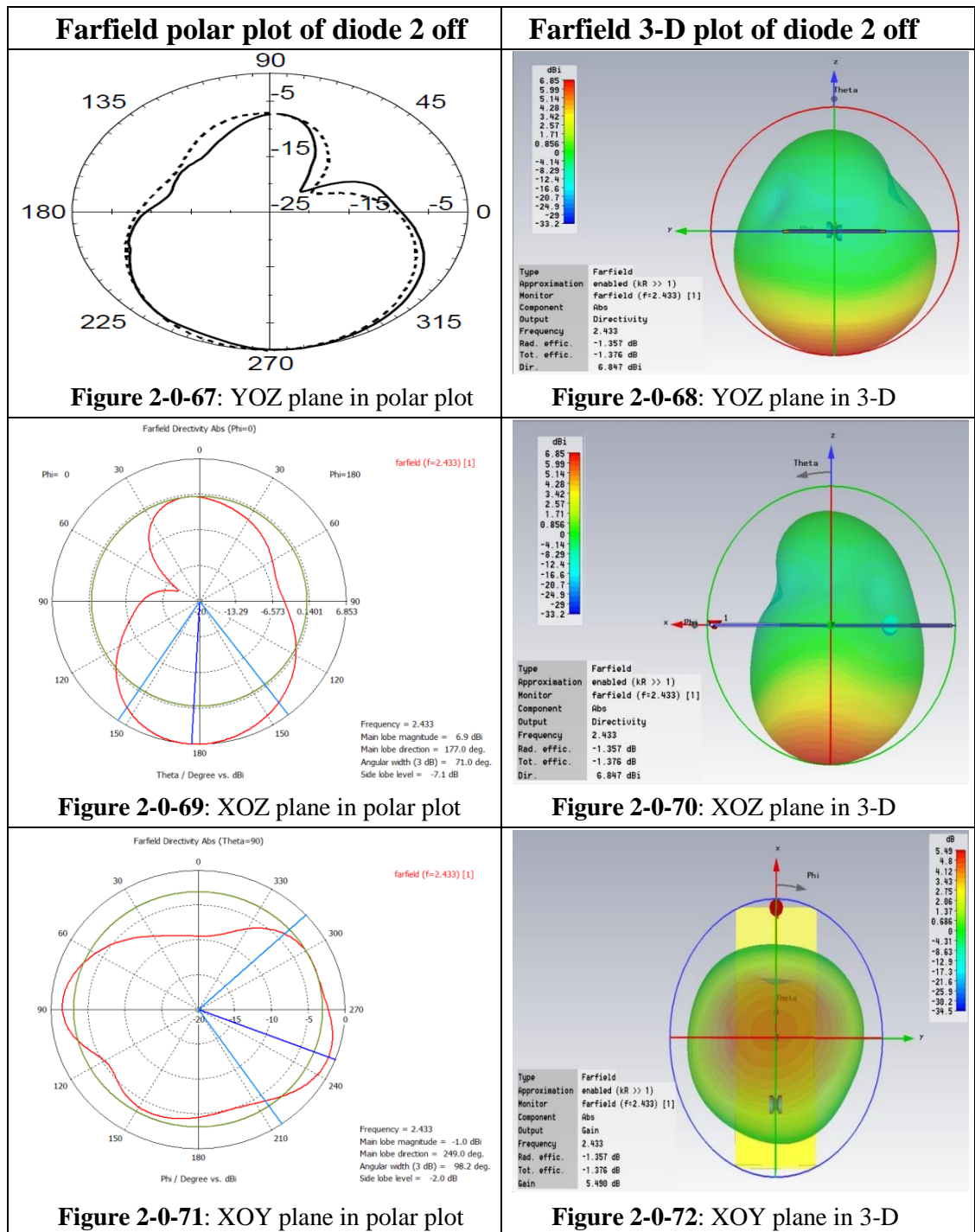


Figure 2-0-73 to Figure 2-0-78 show the far-field results of all-diode off-state working at 1.920 GHz. Figure 2-0-74 shows the 3D E-plane far-field pattern in YOZ plane, for which the radiation efficiency and total efficiency are -1.578 dB and -1.806 dB, respectively. These efficiency results are worse than the results found in the single-slot radiations, because the slots impedance for this state has not been optimized. The gain in Figure 2-0-74 is 3.296 dB, which is 2 dB less than the gain in single-slot radiations. Figure 2-0-73

shows the corresponding polar plot of Figure 2-0-74. The radiation patterns of both slots in Figure 2-0-73 are symmetric about the horizontal plane. The 3 dB angular width in Figure 2-0-73 is 86.8 degree, which is worse than the single-slot radiation results. This angular width proves again the mismatch of slots impedance. Figure 2-0-76 shows the three-dimensional 3 dB beamwidth pattern in XOY plane. As shown by the figure, the main lobe peak locates at the center-back of antenna. Figure 2-0-75 shows the corresponding polar plot of Figure 2-0-76. As the cut-plane of the polar plot is close to waveguide surface, this polar plot is affected by the near field. The local main lobe direction in Figure 2-0-75 shows an obvious tendency to the front side, because the off-peak E_y component of the mismatched slot can be easily guided along the waveguide edge. Therefore, the E_y components is merged into the E_x components to form an enhanced E_x components which is the vector sum of E_y and E_x . And the enhanced E_x components at both sides of waveguide not only propagate to the front end of antenna but also to the input port. As both slots are in-phase radiation, the E-field distribution at both planes are the same. Moreover, as the radiation of slot 1 is the main lobe, the surface E-field distribution is mainly determined by slot 1. Due to the unequal E_y at the two sides of the slot 1, Figure 2-0-75 shows that the side lobe locates at 270 degree and the back lobe locates at 40 degree instead of 0 degree. Figure 2-0-78 shows the 3D far-field pattern in XOZ plane. The main lobes from both slots in Figure 2-0-78 are nearly identical. Figure 2-0-77 shows the polar plot of XOZ plane. The main lobe direction in Figure 2-0-77 has a 6-degree deviation from the normal line, which means that the main lobe is slightly backward to the input port. The reason is that the fringing field of Microstrip couples with the radiation E-field of waveguide top slot, as shown in Figure 2-0-44. The 3 dB angular width is 77.8 degree in Figure 2-0-77, which is larger than the corresponding results of single-diode off-state. As the E_y components is merged into the E_x components at both sides of waveguide, the

radiation intensity of longitudinal component is enhanced. So that the beam width in Figure 2-0-77 is increased.

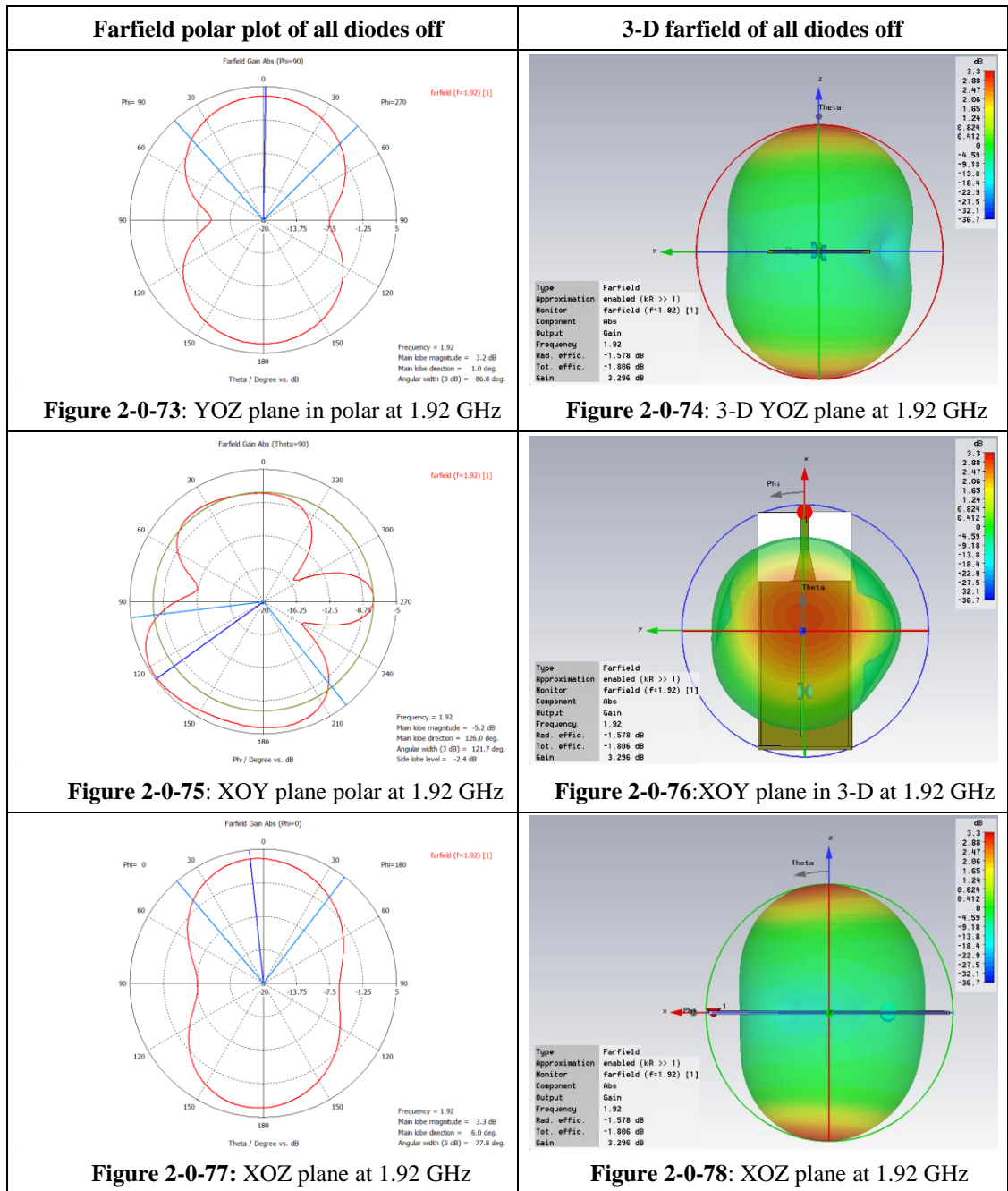


Figure 2-0-80 shows the three-dimensional far-field pattern in the YOZ plane when the antenna is working at all-diode on-state at 2.315 GHz. As 2.315 GHz is the largest response frequency at this state, the diodes working at 2.433 GHz will have a better short-circuit performance if the farfield results at 2.315 GHz reach the minimum design

requirement. In Figure 2-0-80, the radiation efficiency and total efficiency are -2.039 dB and -13.22 dB, respectively. As the difference between total efficiency and radiation efficiency is around 11 dB, the loss caused by the mismatch between antenna and feedline is very high, which, in turn, reduces the radiation efficiency. The gain value is 2.941 dBi, which is the smallest result among the four switch states in this two-direction antenna. But, this gain is caused by the fringing field of Microstrip feedline at higher-order mode, instead of the leakage of slots. Figure 2-0-79 shows the corresponding YOZ plane polar plot of Figure 2-0-80. The main lobe direction in Figure 2-0-79 has a 4-degree deviation from the normal line. The 3 dB angular width of this main lobe is 95.6 degree. Figure 2-0-82 shows the three-dimensional far-field pattern of the XOY plane. The far-field pattern in Figure 2-0-82 clearly shows two main lobes, which are caused by the leakage of the slots at higher-order mode. Therefore, the TE_{10} mode of slot is successfully suppressed by the short-circuited diodes. Figure 2-0-81 shows the corresponding polar plot of Figure 2-0-82. In Figure 2-0-81, the far-field direction locates at 138 degree, which means the leaky E-field of XOY plane slowly attenuates in that direction.

Figure 2-0-84 shows the three-dimensional far-field pattern in XOZ plane. Two main lobes of higher-order mode point to different directions, one trends to backward, another trends to forward. As the fringing field of Microstrip feedline couples with the leaky wave of top slot, the leaky E-field of slot 1 is stronger than that of slot 2. Moreover, Figure 2-0-48 and Figure 2-0-59 can prove that these radiation E-fields are leaky waves which only escape from the uncovered part of slots. Figure 2-0-83 shows the corresponding polar plot of Figure 2-0-84. The main lobe in Figure 2-0-83 locates at the peak of the forward leaky E-field. The leaky E-field of slot 2 only has a small intensity level. So that the leaky far-field at the top plane mainly is enhanced by the fringing field at the Microstrip transition region.

Farfield polar plot of all diodes on

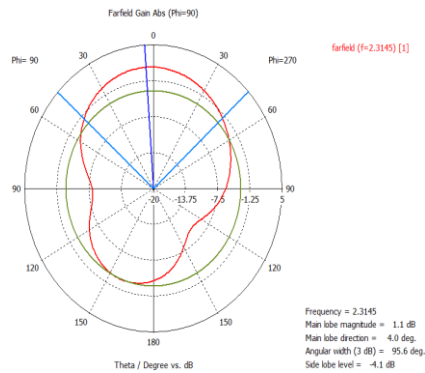


Figure 2-0-79: YOZ plane in polar at 2.315 GHz

3D farfield of all diodes on

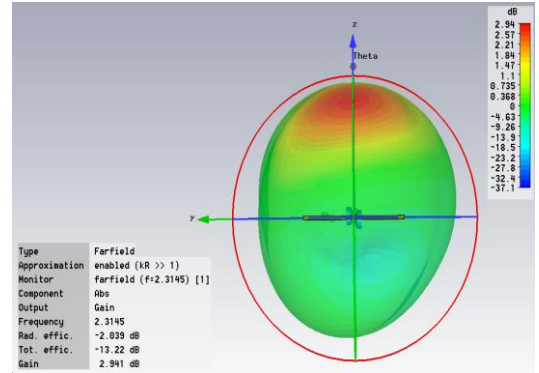


Figure 2-0-80: YOZ plane in 3D at 2.315 GHz

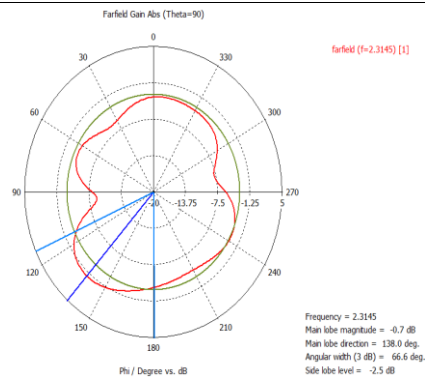


Figure 2-0-81: YOX plane in polar at 2.315 GHz

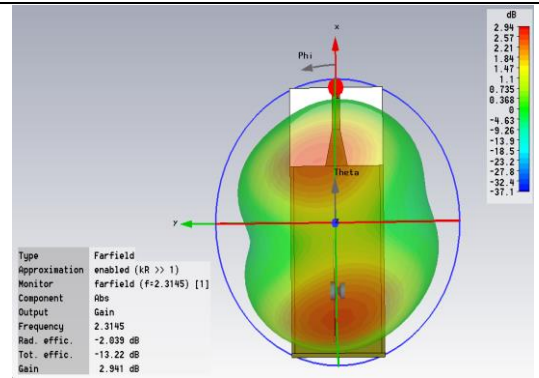


Figure 2-0-82: YOX plane in 3D at 2.315 GHz

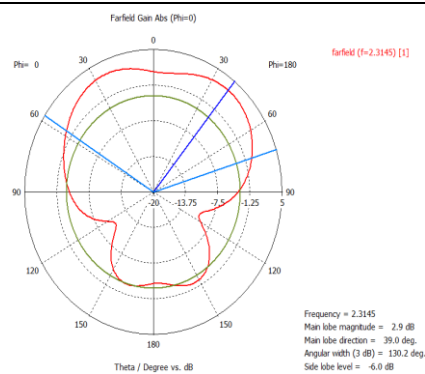


Figure 2-0-83: XOZ plane in polar at 2.315 GHz

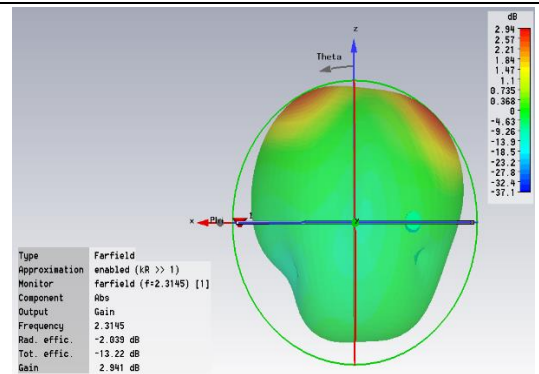


Figure 2-0-84: XOZ plane in 3D at 2.315 GHz

2.2.5 Conclusion:

In this chapter, the suitable overlap and PIN diode have been selected by carrying out measurements and comparative analyses. This chapter used a two-direction antenna to prove the feasibility of using PIN diode as switch control at 2.4 GHz. The antenna has been modeled by CST simulation and successfully tested by measurement. The graphs shown in Figure 2-0-61 to Figure 2-0-66 provide the far-field results of diode 1 off-state. Under this state, the antenna is able to work at the design requirements. The graphs in Figure 2-0-67 to Figure 2-0-72 show that contrast to diode 1, diode 2 off-state has an opposite far-field pattern. The main lobe patterns of the two single-diode off states are symmetric about the waveguide plane, and both of the main lobes have a 7 dB side lobe level. Therefore, the two-direction switch antenna with three working states allows selections in radiation directions. Although the all-diode off-state is not an intended design, this working state still has an acceptable radiation result, as shown in Figure 2-0-73 to Figure 2-0-78. This two-direction antenna can be used in wireless bridge application, such as radio repeater, which can significantly extend the propagation distance. Besides the switch antenna design, we have also done the PIN diodes research in frequency tuning application. The resonance frequency of all-diode off-state can be tuned up from 1.9 GHz to 2.4 GHz by adding two diodes on each slot. But, the thesis will not show this results, as the test data remain fragmentary. The graphs in Figure 2-0-79 to Figure 2-0-84 show that the fundamental resonance mode has been totally suppressed. The antenna working at all-diode on-state reaches the design requirements. Being forward bias, the diodes will work like a short-circuited conducting path, and will no longer perturb the surface current and inner resonance mode of the waveguide.

Reference

- [1] Fan Fan He, Ke Wu, Wei Hong, Liang Han and Xiao-Ping Chen. Low-cost 60-GHz smart antenna receiver subsystem based on substrate integrated waveguide technology. *IEEE Trans. Microw. Theory Techn.*, vol. 60, no.4, pp. 1156-1165, 2012.
- [2] M. Chryssomallis, "Smart antennas," *IEEE Magazine Antennas Propag.* , vol. 42, pp. 129-136, 2000.
- [3] J. H. Winters, "Smart antennas for wireless systems," *IEEE Pers. Commun.* , vol. 5, pp. 23-27, 1998.
- [4] Ming-Iu Lai, Tjung-Yu Wu, Jung-Chin Hsieh, Chun-Hsiung Wang and Shyh-Kang Jeng , "Compact Switched-Beam Antenna Employing a Four-Element Slot Antenna Array for Digital Home Applications", *IEEE Trans. Antennas Propag.*, vol. 56, no. 9, pp. 2929-2936, Sep. 2008.
- [5] Carl B. Dietrich, Jr., Kai Dietze, J. Randall Nealy, and Warren L. Stutzman "Spatial, Polarization, and Pattern Diversity for Wireless Handheld Terminals" *IEEE Trans. Antennas Propag.*, vol. 49, no. 9, pp. 1271-1281, Sep. 2001.
- [6] Nguyen Viet Anh, and Park Seoong Ook, "Compact Switched and Reconfigurable 4-ports beam Antenna Array for MIMO applications", *2011 IEEE MTT-S International Microwave Workshop Series on Intelligent Radio for Future Personal Terminals (IMWS-IRFPT)*, 2011, pp. 1-3.
- [7] A. Edalati and T. A. Denidni, "Frequency Selective Surfaces for Beam-Switching Applications," *IEEE Trans. Antennas Propag.*, vol. 61, no.1, pp. 195-200, 2013.
- [8] G. Poilasne, P. Pouliguen, K. Mahdjoubi, L. Desclos and C. Terret, "Active metallic photonic band-gap materials (MPBG): experimental results on beam shaper," *IEEE Trans. Antennas Propag.*, vol. 48, no.1, pp. 117-119, 2000.
- [9] P. Ngamjanyaporn and M. Krariksh, "Switched-beam single patch antenna," *IEEE Electron. Lett.*, vol. 38, no.1 , pp. 7-8, 2002.
- [10] Zlatoljub D. Milosavljevic , "RF MEMS Switches", *Microwave Review*, pp 1-2, June 2004.
- [11] Thurai Vinay, Dinesh Sood, Zuraini Dahari, "Mems Electromagnetic Micro Relays Overview and Design Considerations", *IJUM Engineering Journal*, vol. 6, no. 2, pp. 47-60, 2012.

- [12] Paul Smart, (2004). “*Electromechanical Relays*”, lecture notes distributed in Mechatronics ECE 5320 Assignment#1: PPT slides for sensors and actuators 2004 at Utah State University, [Online]. Available: http://mechatronics.ece.usu.edu/ece5320/Schedule/hw01-2004/paul_smart_a.ppt, [Accessed: 14th June 2014].
- [13] IXYS integrated circuits division (2014). “*Advantages of Solid-State Relays Over Electro-Mechanical Relays*”, Application Note: AN-145, pp. 6, [Online]. Available: [http://www.ixysic.com/home/pdfs.nsf/www/AN-145.pdf/\\$file/AN-145.pdf](http://www.ixysic.com/home/pdfs.nsf/www/AN-145.pdf/$file/AN-145.pdf), [Accessed: 25 July 2014].
- [14] Solid State Optronics (2015). “*Solid State Relays vs. Electromechanical Relays*”, Application Notes, [Online]. Available: <http://www.ssousa.com/appnote040.asp>, [Accessed: 27 July 2014].
- [15] Peter Bacon, Drew Fischer and Ruan Lourens, (2014) “Overview of RF Switch Technology and Applications”, *Microwave Journal frequency matters*, [Online]. Available: <http://www.microwavejournal.com/articles/print/22557-overview-of-rf-switch-technology-and-applications> [Accessed: 4 April 2014].
- [16] Agilent Technologies, Inc. (2009) “*Understanding RF/Microwave Solid State Switches and their Applications*”, Application Note, [Online]. Available: <http://cp.literature.agilent.com/litweb/pdf/5989-7618EN.pdf>, [Accessed: 26 July 2014].
- [17] “*Solid-state relay*”, Wikipedia article, (2014), [Online]. Available: http://en.wikipedia.org/wiki/Solid-state_relay, [Accessed: 31 December 2014].
- [18] Nadim Maluf, Kirt Williams, *An Introduction to MEMS Engineering*, 2nd edn., Norwood: Artech House, Inc. 2004.
- [19] K. E. Peterson, “Micromechanical membrane switches on silicon,” *IBM J. Res. Develop.*, vol. 23, no. 4, pp. 376-385, July 1979.
- [20] Lindroos V., Tilli M., Lehto A., Motooka T., S. Franssila, M. Paulasto-Krockel, Veli-Matti Airaksinen *Handbook of Silicon Based MEMS Materials and Technologies*, Burlington, MA: William Andrew, 2010.
- [21] C. A. Desmond and P. Abolghasem, “Applications of Wafer Bonding to Non-Electronic Microstructures,” in *Proceedings of the 4th International Symposium on Semiconductor Wafer Bonding*,

- 1997, pp. 95-105.
- [22] William N. Sharpe, *Springer Handbook of Experimental Solid Mechanics*, Würzburg: Springer, 2008.
- [23] Tze-Wei Yeow, Law, K.L.E., Goldenberg, A., "MEMS optical switches", *IEEE Communications Magazine*, Vol. 39, No. 11, pp. 158-163, 2001.
- [24] Simon, J. , Saffer, S., Kim, J.Y., "A liquid-filled microrelay with a moving mercury microdrop", *Journal of Microelectromechanical Systems*, Vol. 6, No. 3, pp. 208-216, 1997.
- [25] Gross, S.J. , Zhang, Q.Q., Trolier-McKinstry, S. ,Tadigadapa, S. , Jackson, T.N., "RF MEMS piezoelectric switch", *Device Research Conference 2003* , 2003, pp. 99-100.
- [26] J. Qiu, J. Lang, A. Slocum, and R. Strumpler, "A high-current electrothermal bistable MEMS relay," in *Proc. IEEE Micro Electro Mechanical Systems 2003, Kyoto, Japan*, Jan. 19-23, 2003, pp. 64-67.
- [27] J. A. Wright, Y.-C. Tai, and G. Lilienthal, "A magnetostatic MEMS switch for DC brushless motor commutation," *Proceedings: Solid-State Sensor and Actuator Workshop 1998, Hilton Head Island, South Carolina*, 1998, pp. 304-307.
- [28] Bendong Liu, Desheng Li, Xiaobo Yang, Xiang Li, "Design and Fabrication of a Micro Electromagnetic Actuator", *Nano/Micro Engineered and Molecular Systems, 2006. NEMS '06. 1st IEEE International Conference on*, 2006, pp. 353-356.
- [29] J. J. Yao, S. T. Park, R. Anderson, and J. DeNatale, "A low power/low voltage electrostatic actuator for RF MEMS applications", in *Solid-State and Actuator Workshop, Hilton Head*, June 2000, pp. 246-249.
- [30] R. Sorrentino, and Giovanni Bianchi, *Microwave and RF Engineering*, Singapore: Wiley, 2010.
- [31] A. R. Jha, *MEMS and Nanotechnology-based Sensors and Devices for Communications Medical and Aerospace Application*, United States: CRC Press, 2008.
- [32] Allyson L. Hartzell, Mark G. da Silva, Herbert Shea, *MEMS Reliability (MEMS Reference Shelf)*, New York: Springer, 2010.
- [33] T. Campbell, "MEMS Switch Technology Approaches the "Ideal Switch"", *Applied Microwave & Wireless*, Vol. 13, No. 5, pp. 100-107, May 2001.
- [34] Jeffrey S. Beasley and Gary M. Miller, *Modern Electronic Communication*, 8th Edition, Upper Saddle

- River, United States of America: Prentice Hall, 2004.
- [35] Gershon J. Wheeler, *Introduction to Microwaves*, Englewood Cliffs, United States of America: Prentice-Hall Inc., 1963.
- [36] Christian Wolff, “Waveguides”, [Online]. Available: <http://www.radartutorial.eu/03.linetheory/Waveguides.en.html#abs1> [Accessed: 1 June 2014].
- [37] Matthew N. O. Sadiku, *Elements of Electromagnetics*, Second Edition, Fort Worth, United States of America: Harcourt Brace College Publishers, 1994.
- [38] Nannapaneni Narayana Rao, *Elements of Engineering Electromagnetics*, 6th Edition, Upper Saddle River, United States of America: Prentice Hall Inc, 2004.
- [39] Stevenson, A.F., “Theory of Slots in Rectangular Wave-Guides”, *Journal of Applied Physics*, vol. 19, no. 1, pp. 24-38, 1948.
- [40] Samuel Silver, Hubert M. James, *Microwave Antenna Theory and Design*, London, UK: Peter Peregrinus Ltd., 1984.
- [41] Yan, L. , Hong, W. , Wu, K. , Cui, T.J., “Investigations on the propagation characteristics of the substrate integrated waveguide based on the method of lines”, *Microwaves, Antennas and Propagation, IEE Proceedings* , vol. 152, no. 1, pp. 35 – 42, 2005.
- [42] J. Hirokawa, and M. Ando, “Single-layer Feed Waveguide Consisting of Posts for Plane TEM Wave Excitation in Parallel Plates,” *IEEE Trans. Antennas Propagat.*, vol. 46, no. 5, pp. 625-630, May 1998.
- [43] Sheng Zhang Zhang, Zhi Yuan Yu, Can Li, Jian Hua Deng, “Electromagnetic energy leakage characteristics of substrate integrated waveguide”, *Microwave Conference Proceedings, 2005. APMC 2005. Asia-Pacific Conference Proceedings* , 2005, vol. 2.
- [44] Feng Xu, Ke Wu, “Guided-wave and leakage characteristics of substrate integrated waveguide”, *Microwave Theory and Techniques, IEEE Transactions on* , vol. 53, no: 1, pp. 66-73, 2005.
- [45] Bozzi, M. , Perregrini, L., Ke Wu, “Modeling of Conductor, Dielectric, and Radiation Losses in Substrate Integrated Waveguide by the Boundary Integral-Resonant Mode Expansion Method”, *Microwave Theory and Techniques, IEEE Transactions on*, vol. 56, no. 12 (2), pp.3153-3161, 2008.
- [46] Bozzi, M. , Pasian, M., Perregrini, L., Ke Wu , “On the losses in substrate integrated waveguides”.

Microwave Conference, 2007. European, 2007, pp.384-387.

- [47] C. Yeh, and F. Shimabukuro, *The Essence of Dielectric Waveguides*, New York: Springer, 2010.
- [48] Che, W., Deng, K., Wang, D., Chow, Y.L., “Analytical equivalence between substrate-integrated waveguide and rectangular waveguide”, *Microwaves, Antennas & Propagation, IET*, vol. 2, no: 1, pp. 35-41, 2008.
- [49] Cassivi, Y., Perregrini, L., Arcioni, P., Bressan, M., Wu, K., Conciauro, G., “Dispersion characteristics of substrate integrated rectangular waveguide”, *Microwave and Wireless Components Letters, IEEE*, vol. 12, no. 9, pp. 333-335, 2002.
- [50] David M. Pozar, *Microwave Engineering*, 4th edn., United States of America: Wiley, 2011.
- [51] Notaros, Branislav M., *Electromagnetics*, New Jersey: Prentice Hall, 2011.
- [52] Deslandes, D., and K. Wu, “Integrated transition of coplanar to rectangular waveguides,” *IEEE MTT-S International Microwave Symposium Digest (IMS 2001)*, Baltimore, MD, June 5-10, 2001, pp. 619-622.
- [53] Deslandes, D., “Design equations for tapered microstrip-to-Substrate Integrated Waveguide transitions”, *Microwave Symposium Digest (MTT), 2010 IEEE MTT-S International*, 2010, pp. 1.
- [54] Deslandes, D., and K. Wu, “Integrated microstrip and rectangular waveguide in planar form,” *IEEE Microwave Wireless Comp. Lett.*, Vol. 11, No. 2, pp. 68-70, 2001.
- [55] Miralles, E., Esteban, H., Bachiller, C., Belenguier, A., Boria, V.E., “Improvement for the design equations for tapered Microstrip-to-Substrate Integrated Waveguide transitions”, *Electromagnetics in Advanced Applications (ICEAA), 2011 International Conference on*, 2011, pp. 652-655.

Chapter 3 Four directions switch antenna

In this chapter, a 4-direction switch-beam SIW antenna with PIN diodes control is proposed for the WLAN application. The E-field polarization in this kind of the antenna coincides with the vertical elevation plane. The proposed antenna is anticipated to have a higher gain than the dipole antenna, and can generate a symmetric radiation pattern. Other advantages of this new design include compact structure and low cost. Also, by controlling the propagation direction, one particular frequency can be reused in different directions.

3.1.1 Leaky wave design

The PIN diode switch control with DC bias has been proved to be practicable in the two-direction antenna. For further research, this chapter will try to improve the slot performance. Waveguides usually have two kinds of propagation, which are the leaky wave for radiation antenna and the guided wave for transmission line. Given the slot width is restrictive, this new switch antenna will use leaky wave to increase the bandwidth. As only the homogeneous wave is of our interest, the wave vector is used as an auxiliary parameter to analyze the characteristics of leaky wave. Usually, the wave number is simply the magnitude of wave vector. However, the complex wave number corresponds to the propagation constant in complex conjugation relation. This is, the real part of the propagation constant γ relates to the imaginary part of the complex wave number, and the imaginary part of the propagation constant γ relates to the real part of the complex wave number [4].

$$\text{Re}(\gamma) = \text{Im}(\tilde{k}) = |\alpha|/2$$

$$\text{Im}(\gamma) = \text{Re}(\tilde{k}) = \beta$$

To simplify the writing, the imaginary part of the complex wave number is represented by k_y , since only the radiation component in Y-axis direction is of interest. The wave number in air is shown by the following equation and Figure 3-0-1

$$k_0^2 = \beta^2 + k_y^2$$

$$\text{Where } \beta = \sqrt{\epsilon_r k_0^2 - \left(\frac{\pi}{a}\right)^2}, \quad k_0 = \frac{\omega}{c}$$

$$\text{Hence, } k_y = \sqrt{k_0^2 - \beta^2}$$

Where λ_g is the wavelength in dielectric, ω is angular frequency, and c is the light speed.

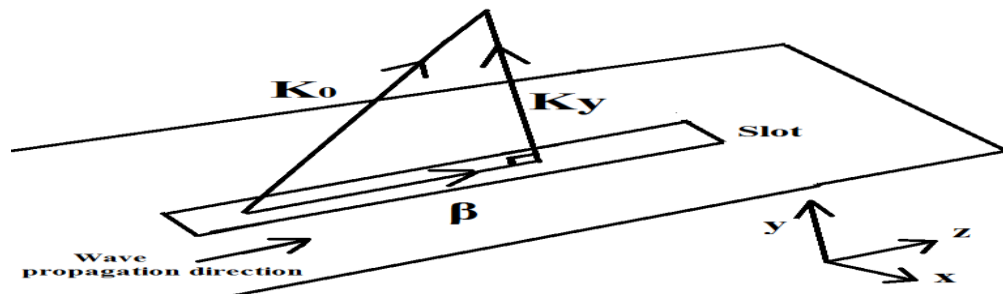
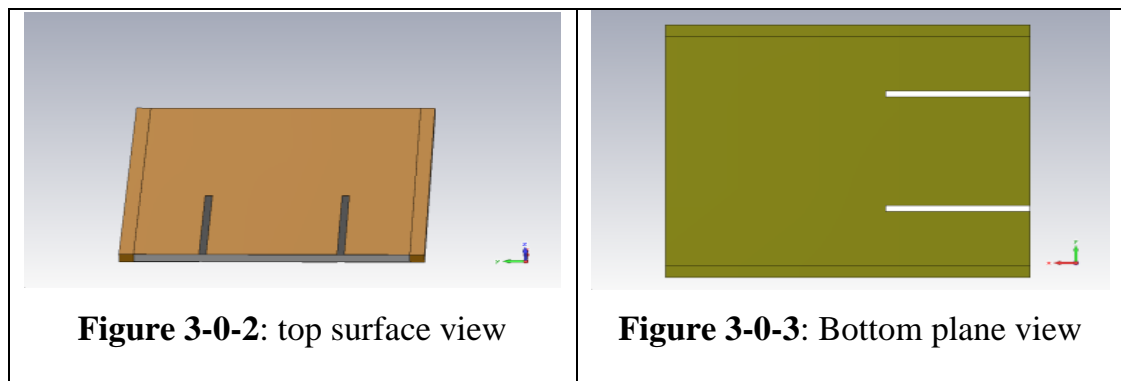


Figure 3-0-1: wave number components

When $\beta < k_0$, k_y is a real number. The periodic function of leaky wave in Y axis direction $e^{ik_y y}$ can be displayed as an image of sinusoidal wave, which represents the radiation of leaky wave from slot. When $\beta > k_0$, k_y is an imaginary number. In order to separate the imaginary unit and real number, k_y is replaced by $i\alpha$. So that, the periodic function of leaky wave in Y axis direction $e^{-\alpha y}$ is shown as an image of a recession curve, which means the rapid attenuation of propagation wave in air.

3.1.2 The embryo of four direction antenna idea



The following design aims to build a four-slot antenna with intrinsic radiation-coupling. The structure of this dual-side coupling antenna is showed in Figure 3-0-2 and Figure 3-0-3. On each waveguide broad wall there are two parallel slots which are symmetric to the waveguide central line. Slots on different planes are also vertically symmetric. These four slots are with a length about one-quarter guided wavelength. And the antenna front end is open.

The reflection coefficient $S_{1,1}$ of the antenna, as showed in Figure 3-0-4, is -22.191 dB at 5.808 GHz and the bandwidth at -10 dB is 69.441 MHz. The operating principle of coupling is showed in Figure 3-0-5. As there is a 180-degree difference between phases of the waveguide top plane and bottom plane, the vertically symmetric slots are anti-phase on the waveguide surface, but in-phase at the edge of waveguide. Moreover, the phases of the slots on the same plane have a 180-degree difference, which means that anti-phase radiations at the central line of broad wall will cancel out each other. As these four slots are symmetric and identical in size, the coupling E-fields at the two sides of the waveguide are equivalent. Although the waveguide does not have a reflector wall at the central line, these two coupling E-fields can radiate outward in opposite directions.

The far-field results are showed in Figure 3-0-6 to Figure 3-0-11. Figure 3-0-6 shows the three dimension (3D) far-field pattern in YOZ plane. The radiation efficiency and total efficiency are -0.054 dB and -0.082 dB, respectively. These high efficiencies suggest that nearly all of the incident energy has been radiated into outer space. Figure 3-0-7 shows the corresponding polar plot of Figure 3-0-6. The main lobe direction in Figure 3-0-7 points to 90 degree, which means that the radiation direction parallels to the horizontal plane of waveguide. The 3 dB angular width is 105.4 degree. The advantage of this antenna is that the coupling E-fields realize directional radiation without reflector wall. Figure 3-0-8 shows the 3D far-field pattern in XOY plane. The two main lobes in this pattern locate exactly at the two sides of the waveguide. Figure 3-0-9 shows the corresponding polar plot of the Figure 3-0-8. Two side lobes are found in Figure 3-0-9. One has a forward direction, another has a backward direction. Figure 3-0-10 shows the part of three-dimensional main lobe pattern which is not less than 3 dB angular width. The ellipse main lobe with a peak locating at the horizontal plane proves the existence of E-field coupling. Figure 3-0-11, as the polar plot of Figure 3-0-10, shows a very weak E-field at the waveguide front end.

Taking advantage of the characteristic of coupling E-fields, the four-slot antenna can realize six-direction, or eight-direction propagation by inputting TE_{20} mode. For research purpose, two additional reflector walls will be installed on the four-direction antenna along the central line of the waveguide. The original coupling E-field is expected to remain the same. The four direction antenna results will be introduced as follow.

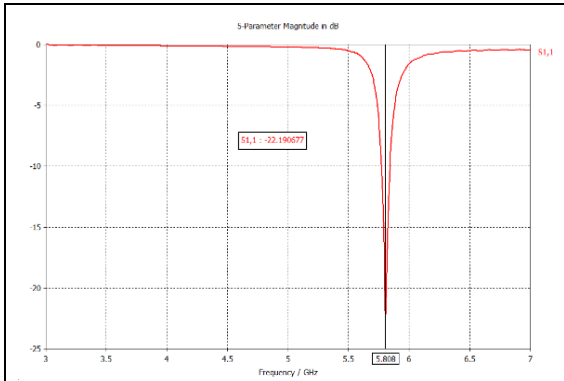


Figure 3-0-4: S1,1 result

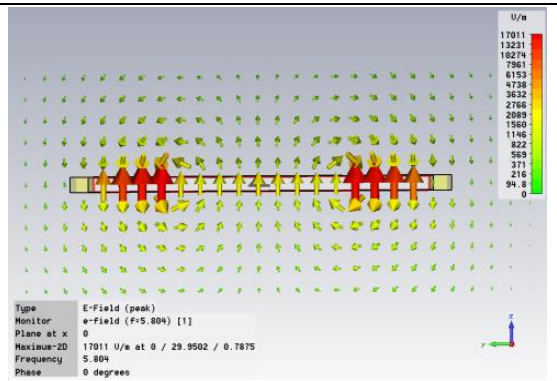


Figure 3-0-5: YOZ plane E-field in arrow

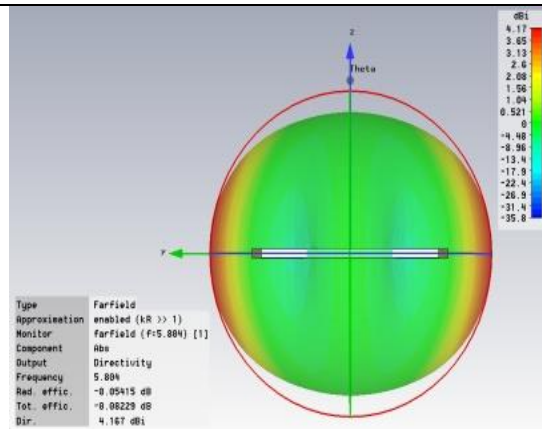


Figure 3-0-6: YOZ plane Far-field 3 D plot

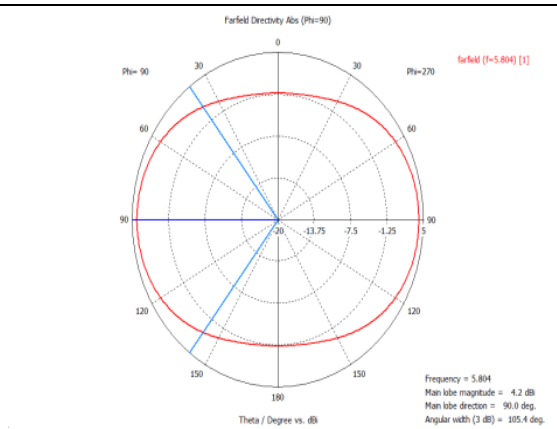


Figure 3-0-7: YOZ plane polar plot

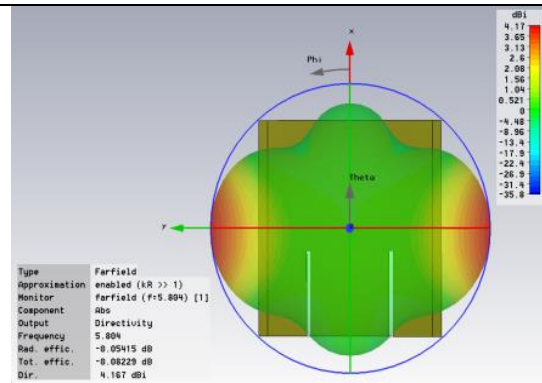


Figure 3-0-8: XOY plane 3D far-field

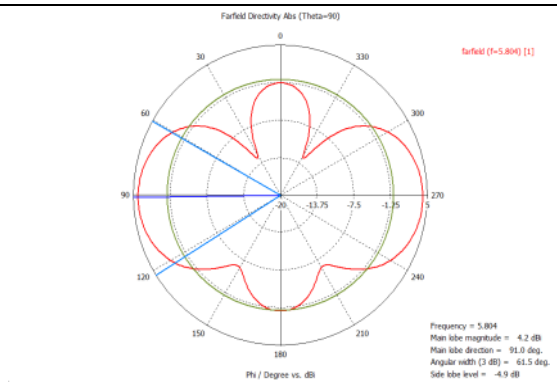


Figure 3-0-9: XOY plane polar plot

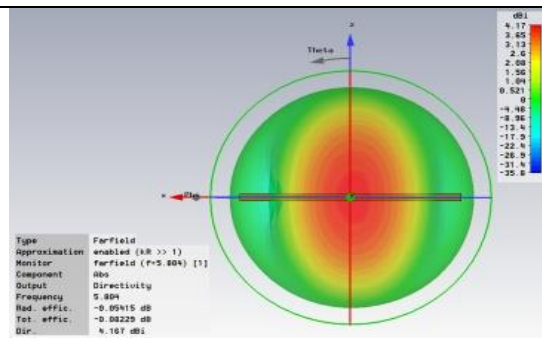


Figure 3-0-10: XOZ plane 3 D far-field

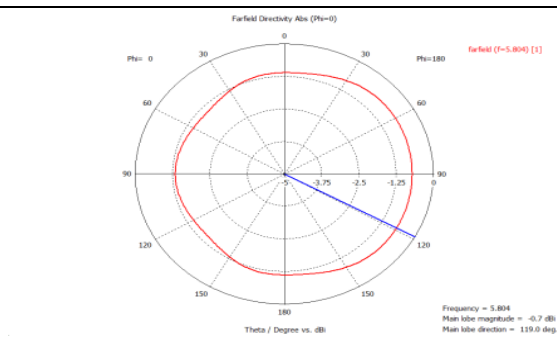


Figure 3-0-11: XOZ plane polar plot

3.2.1 Four directions switch antenna

Figure 3-0-12 and Figure 3-0-13 show the top plane and the bottom plane of the 4-direction antenna, respectively. The red dot represents the signal input port, and the blue dots represent the PIN diode switches. Figure 3-0-14 shows the positions of the four diodes in a front end view after rotating the antenna 90 degrees to the left. Therefore, the top plane of waveguide is at the left-hand side, and the bottom plane is at the right-hand side. Since the radiation space has been divided off by the two reflector walls and the waveguide broad wall, as shown in Figure 3-0-14, each slot has a separate radiation area.

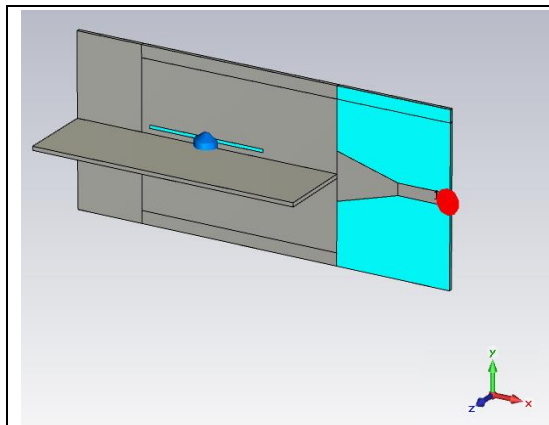


Figure 3-0-12: Top view in YOX plane

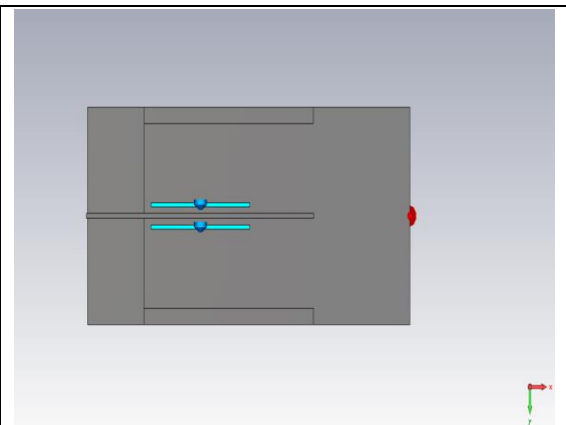


Figure 3-0-13: Bottom view in YOX plane

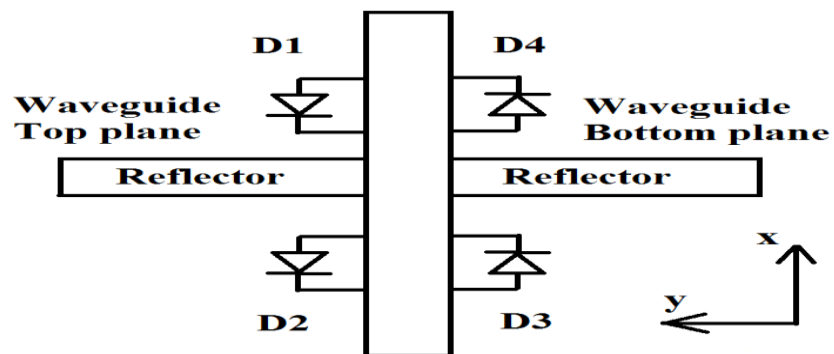


Figure 3-0-14: Front end view in YOZ plane by rotate antenna 90 degree

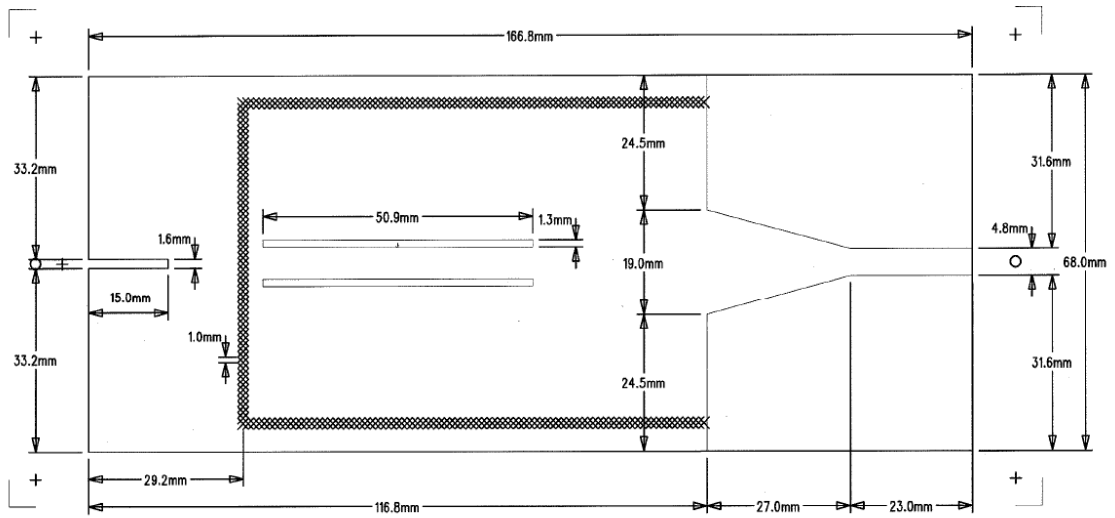


Figure 3-0-15: Fabrication sizes of 4 direction antenna drawn by A. Farrel

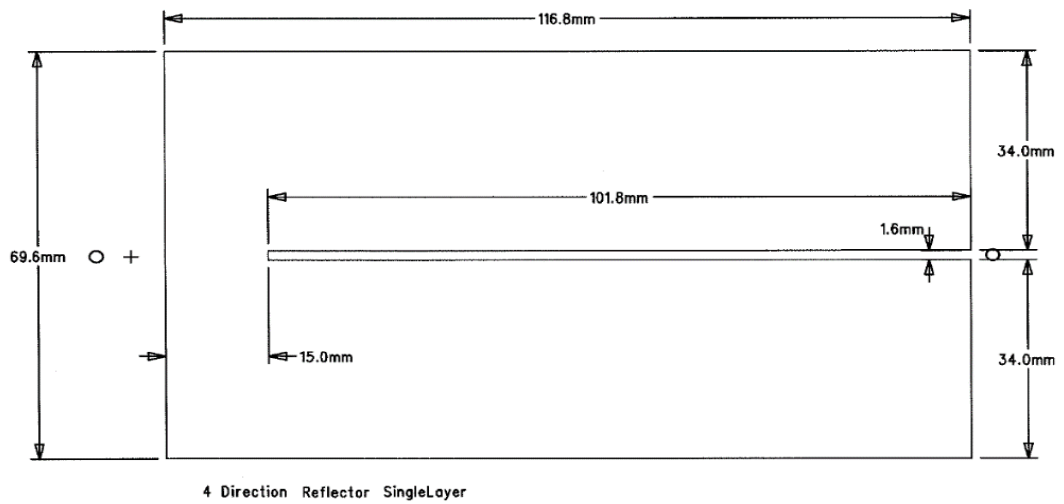


Figure 3-0-16: Fabricated reflector size of 4-direction antenna drawn by A. Farrel

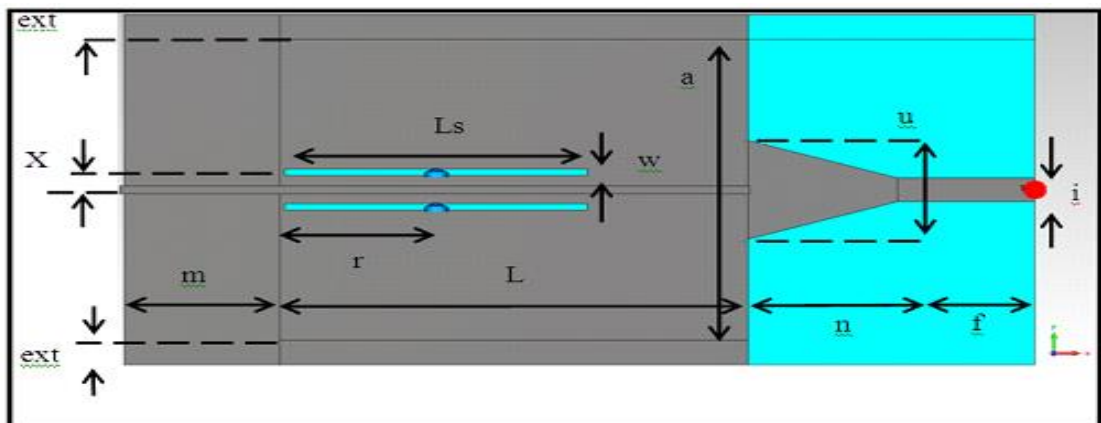


Figure 3-0-17: XOY plane top view of antenna and simulation structure parameters

Parameters	Length /Unit: mm	Description
L	87.6	Length of waveguide antenna part= $r*3$
a	58	Waveguide width
b	1.575	Thickness of waveguide substrate
T	0.07	Thickness of surface copper
Ls	50.9	Slot length
r	29.2	One quarter lambda wavelength
ext	5	PEC wall width
i	4.75	Input port width
n	27	Length of Taper
u	19	Width of Taper
f	23	Length of Microstrip feedline
w	1.3	Slot width
m	29.2	Front PEC extension $L-r*2$
x	3.5	Slot offset position from waveguide central line to edge

Table 3-0-1: Parameters of simulation structure

Figure 3-0-15 and Figure 3-0-16 show the fabrication real sizes of the antenna and the reflector wall. The real sizes are set according to the simulation model. Figure 3-0-17 shows the parameters of antenna model in simulation, and Table 3-0-1 shows the value of each parameter. The working mechanism of the 4-direction switch antenna is that when one of the four diodes is in reverse bias, the rest of the diodes will be in forward bias. This is, at any time only one slot will radiate, other slots will be shielded.

3.2.2 The 1-D results of CST

Figure 3-0-18 and Figure 3-0-19 show the comparisons of reflection coefficient $S_{1,1}$ in measurement and simulation for diode 1 off-state and diode 2 off-state, respectively. Although both of the $S_{1,1}$ measurement results are below -20 dB, the measurement curves all have two undesired modes working at the frequencies below 2.4 GHz. Table 3-0-2

shows the detailed results of these two single-diode off states. As shown in the table, both measurement results are observed at the center frequency 2.48 GHz. And the bandwidths of these two states are all over 50 MHz.

Figure 3-0-20 and Figure 3-0-21 show the comparisons of S_{1,1} results in measurement and simulation for diode 3 and diode 4, respectively. The measurement S_{1,1} results of diode 3 and diode 4 state are all slightly below -20 dB, which mean that the reflection signal is less than 1% of the input signal. Again, both two graphs have two undesired frequency modes responding below 2.4 GHz. By comparing the measurement S_{1,1} results of the four slots, slot 2, slot 3 and slot 4 all have a similar S_{1,1} value at around -20 dB, only the S_{1,1} of slot 1 reached -40 dB. This is because the parasitic effects of the bias network and overlap can slightly affect the impedance matching of slots. These additional switch circuit placements caused by manual error in antenna assembling are uncontrollable. Table 3-0-3 shows the detailed results of diode 3 and diode 4 off states. Both of slot 3 and slot 4 responded at the center frequency 2.47 GHz which is 10 MHz lower than the response frequencies of the top-plane slots. Slot 1 and slot 4 at the left side of waveguide both have a 68 MHz bandwidth, and share a similar noise curve. Slot 2 and slot 3 at the right side of the waveguide both have a 57 MHz bandwidth and the same noise curve. As the reflector walls confine the coupling E-fields of radiation and leaky wave, the DC wires and overlays only affect the coupling interaction between the vertically symmetric slots. Therefore, the vertical pair of slots have similar performance. In practice, the noise frequencies below 2.4 GHz can be filtered out by the backend RF block circuit. Therefore, all of these four reflection coefficient S_{1,1} results can reach the design requirement.

Figure 3-0-22 and Figure 3-0-23 show the S_{1,1} results of dual-diode off states, where diode 1 and diode 4 are set as a pair and diode 2 and diode 3 are set as a pair, respectively. As the low-cost inductors cannot fully filter out the noise, both graphs have a noticeable noise at 2.2 GHz, which is caused by the intrinsic problem of inductors. As the DC bias wires for remote control are over 70 centimeters long, these wires increase the noise level. Therefore, the length of wires should be minimized. This solution will also be proved to be feasible in the six-direction antenna design, of which the noise decreased 4 dB by reducing the wire length to 50 cm. But, this solution will cause difficulty in the antenna installation during the measurement process. When absorber is mounted behind the antenna, the tense wires can easily be broken at the overlay solder joints. Table 3-0-4 shows the detailed results of these two off states. The S_{1,1} of diodes 1 and 4 off state is -12.36 dB, which is smaller than the -14.42 dB of diodes 2 and 3 off state. The reason is that the actual impedances of slot 2 and slot 3 are equal, which is suitable for coupling radiation. Table 3-0-4 shows that two dual-diode states have the same response frequency at 2.5 GHz and bandwidth about 40 MHz. Figure 3-0-24 shows that both simulation and measurement have two response frequencies in all-diode off-state. As shown in Table 3-0-5, the first mode of measurement is -14.2 dB at 1.8 GHz with a 64 MHz bandwidth at -10 dB, which means that the impedances of slots match at 1.8 GHz. The measurement S_{1,1} result of all-diode on-state in Figure 3-0-25 suggests that there is a noise caused by the wires with a value of -6.5 dB at 2.28 GHz. The fluctuated S_{1,1} curve trends upward to -2 dB from 2.4 GHz to 2.5 GHz. Table 3-0-6 shows that the S_{1,1} is -2.7 dB at the sample frequency 2.433 GHz, which is the working frequency of single diode off state. Therefore, the amount of leakage in all-diode on-state is within the design required tolerance.

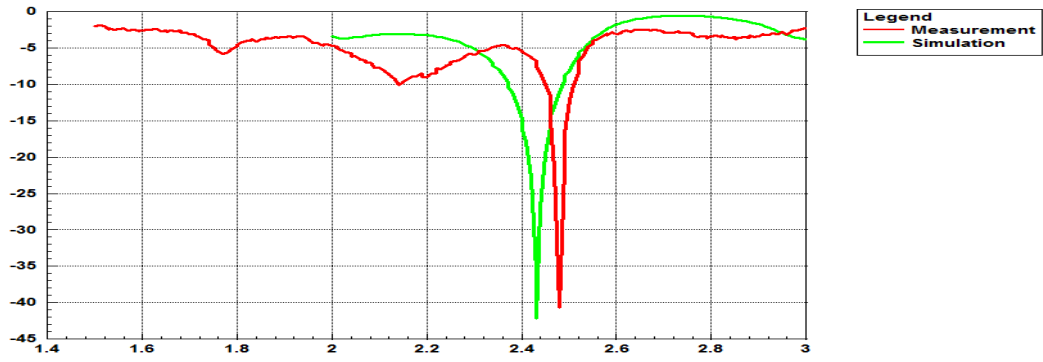


Figure 3-0-18: S1,1 of top surface diode 1 off

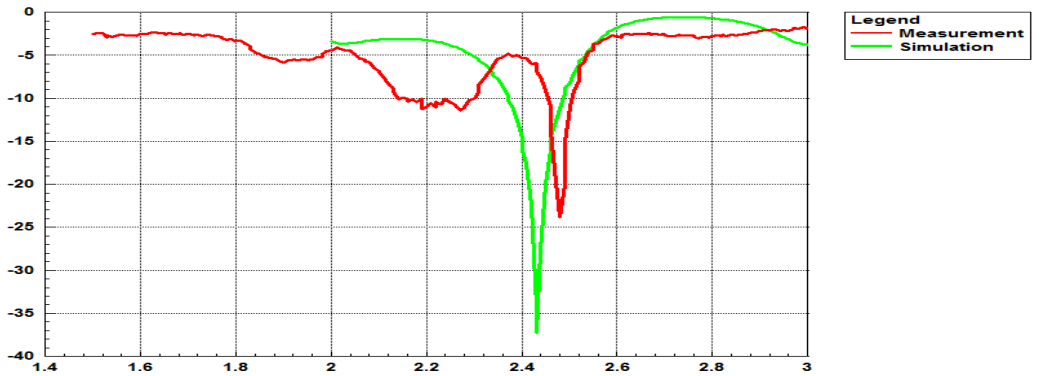


Figure 3-0-19: S1,1 of top surface diode 2 off

Diode 1 switched off	Simulation results	Measurement results
Reflection coefficient S1,1	-42.20 dB at 2.433 GHz	-40.73 dB at 2.48 GHz
Bandwidth	114.69 MHz	68 MHz
Diode 2 switched off	Simulation results	Measurement results
Reflection coefficient S1,1	-42.52 dB at 2.433 GHz	-24.83 dB at 2.48 GHz
Bandwidth	113.66 MHz	57 MHz

Table 3-0-2: S1,1 results of diode 1 and diode 2 off-state

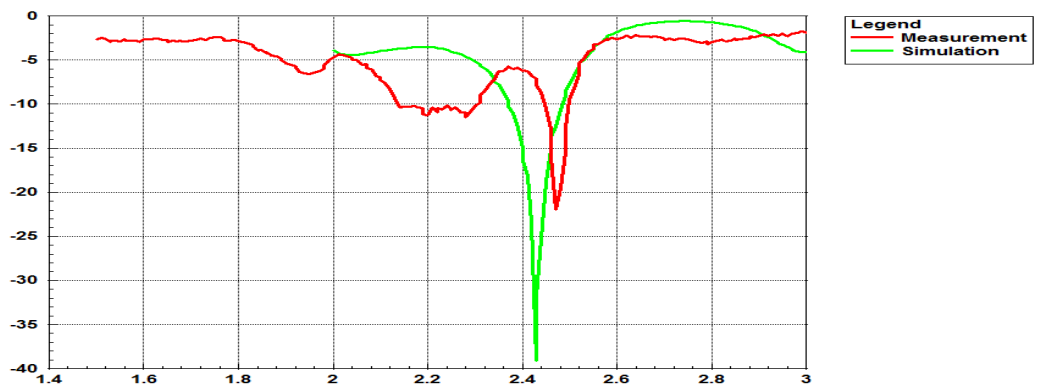


Figure 3-0-20: S1,1 of bottom surface diode 3 off

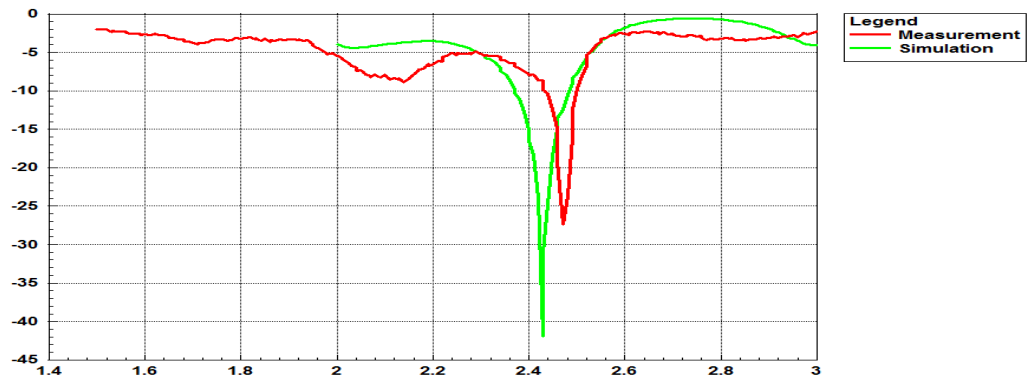


Figure 3-0-21: S1,1 of bottom surface diode 4 off

Diode 3 switched off	Simulation results	Measurement results
Reflection coefficient	-39.10 dB at 2.431 GHz	-21.95 dB at 2.47 GHz
Bandwidth	110.91 MHz	57 MHz
Diode 4 switched off	Simulation results	Measurement results
Reflection coefficient	-41.92dB at 2.431GHz	-27.41 dB at 2.47 GHz
Bandwidth	110.76 MHz	68 MHz

Table 3-0-3: S1,1 of diode 3 and diode 4 switched off

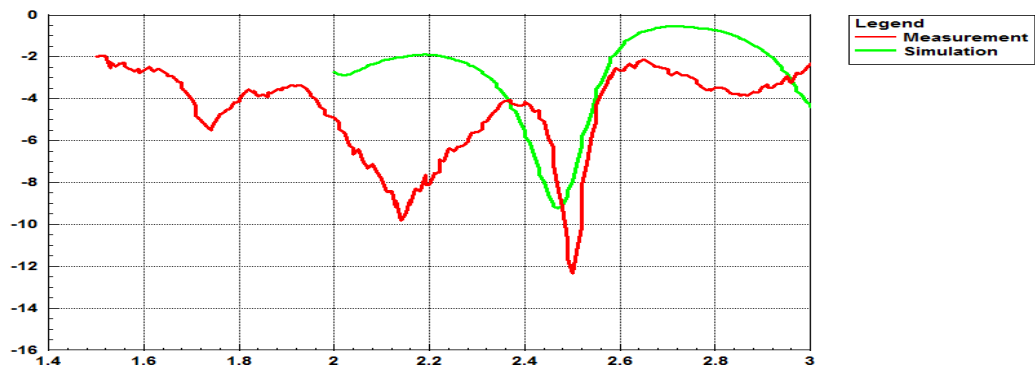


Figure 3-0-22: S1,1 of both diode 1 and diode 4 off

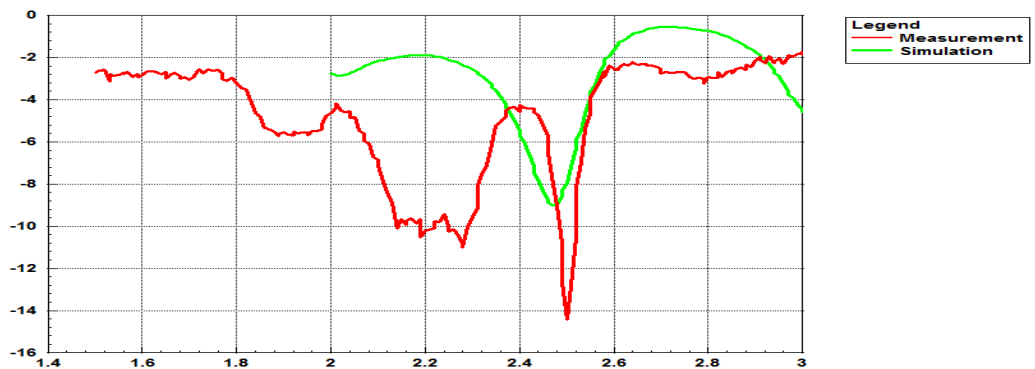


Figure 3-0-23: S1,1 of both diode 2 and diode 3 off

Diodes 1 & 4 switched off	Simulation results	Measurement results
Reflection coefficient	-9.24 dB at 2.472 GHz	-12.36 dB at 2.5 GHz
Bandwidth	0 MHz at -10 dB standard	40 MHz
Diodes 2& 3 switched off	Simulation results	Measurement results
Reflection coefficient	-9.03 dB at 2.473 GHz	-14.42 dB at 2.5 GHz
Bandwidth	0 MHz at -10 dB standard	40 MHz

Table 3-0-4: S1,1 of both two diodes switch-off

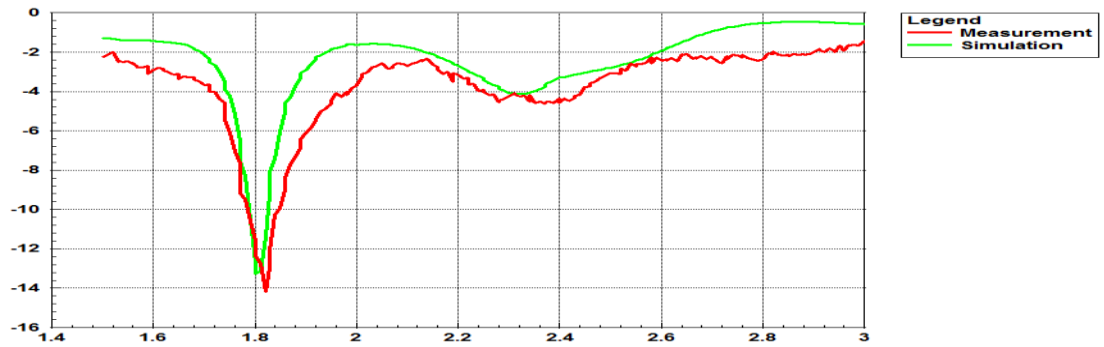


Figure 3-0-24: S1,1 of all diodes switched-off

All diodes switched-off	Simulation results	Measurement results
1st reflection coefficient / frequency	-13.280 dB at 1.806 GHz	-14.192 dB at 1.818GHz
Bandwidth	38.583 MHz	63.75 MHz
2 nd reflection coefficient / frequency	-4.132 dB at 2.322GHz	-4.607 dB at 2.365 GHz
3 rd reflection coefficient / frequency	- 3.084dB at 2.433GHz	- 4.223dB at 2.433GHz

Table 3-0-5: S1,1 results of all diodes switched-off

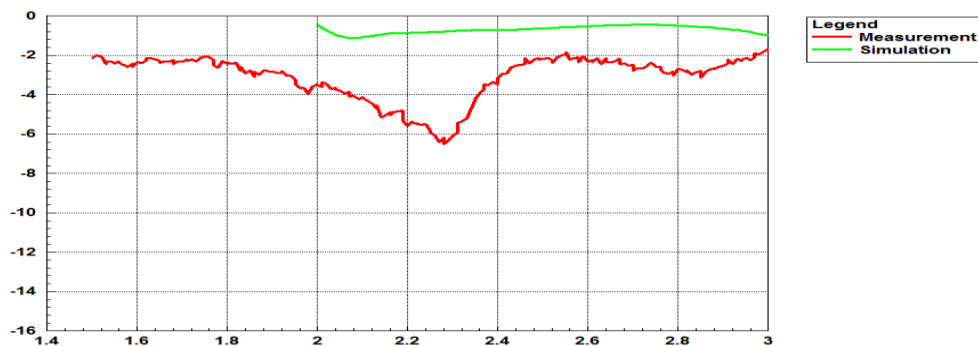


Figure 3-0-25: S1,1 of all diodes switched-on

All diodes switched-on	Simulation results	Measurement results
1st reflection coefficient / frequency	-1.110dB at 2.097 GHz	-6.510 dB at 2.280 GHz
2 nd reflection coefficient / frequency	-0.691 dB at 2.433 GHz	-2.657 dB at 2.433 GHz

Table 3-0-6: S1,1 results of all diodes switched-on

3.2.3 Near-field range 2-D results

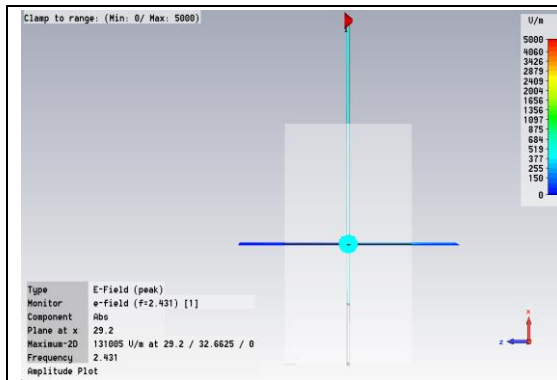


Figure 3-0-26: YOZ plane at X axis 29.2 mm

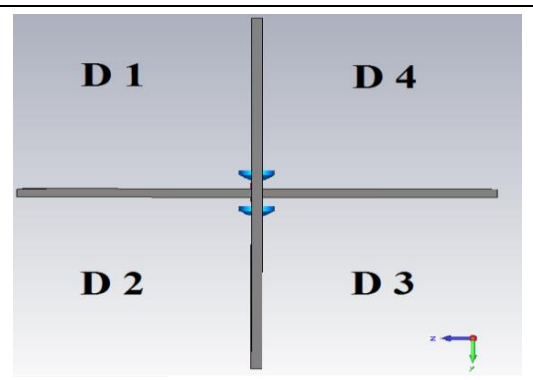


Figure 3-0-27: Diodes position in YOZ plane

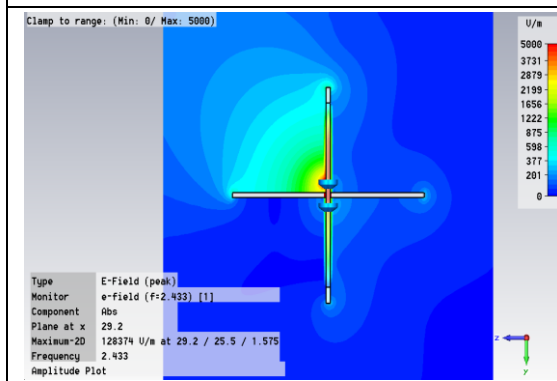


Figure 3-0-28: Diode 1 switched off

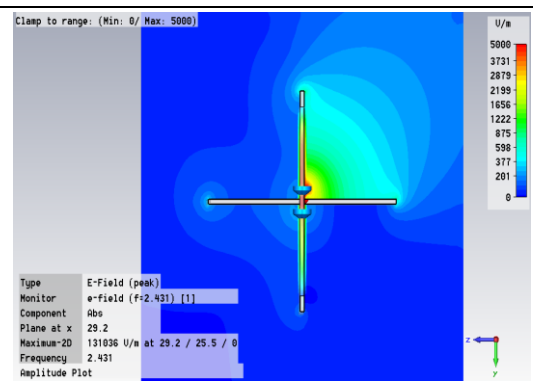


Figure 3-0-29: Diode 4 switched off

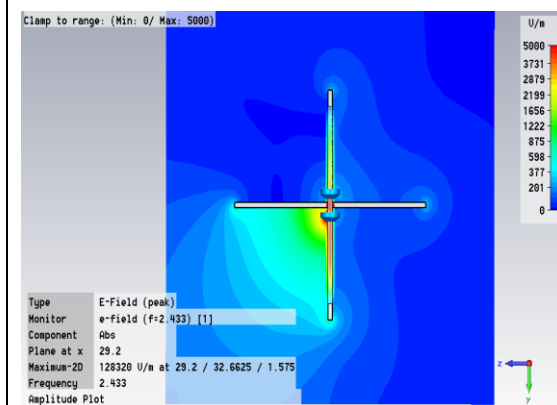


Figure 3-0-30: Diode 2 switched off

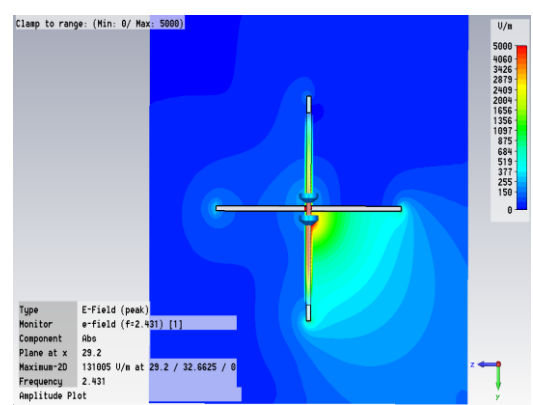


Figure 3-0-31: Diode 3 switched off

As the reflection coefficient $S_{1,1}$ results of measurement are essentially in agreement with the simulation ones, this antenna model can be further analyzed in 2D near field simulation. Figure 3-0-26 shows the YOZ cut-plane located at 29.2 mm along the X axis, where is the slot center. To facilitate understanding, Figure 3-0-27 shows the position of diodes in a YOZ cut-plane. Figure 3-0-28 and Figure 3-0-30 show the E-field distributions of

waveguide top-plane slots in YOZ cut-plane. Both graphs have symmetric pattern and the same maximum E-field magnitude. Since the working principles of the top-plane slots are the same, in order to simplify the interpretation, only the working principle of diode 1 will be introduced here. In Figure 3-0-28, the diffraction from the slot 1 region spreads across the other three regions. For the slot 4 region, the diffraction is the major component of E-field, and leaky wave is the minor component. The slot 4 has a medium level leaky wave. As the diffraction is only in-phase superimposition with leaky wave at the outer part of slot 3 region, the leaky wave dominates the E-field in slot 3 region. Therefore, slot 3 has the largest leaky wave. As short-circuited slot 3 and open-circuited slot 1 are in a diagonal, slot 3 locates at the back lobe of slot 1. Although the slot 3 region has a significant scattering, the scattering only dissipates energy in near field range, and does not contribute to farfield radiation. The diffraction in slot 2 region is anti-phase with the leaky wave. Slot 2 region has the smallest leaky wave.

Figure 3-0-29 and Figure 3-0-31 show the E-field distributions of slot 4 and slot 3 in YOZ cut-plane, respectively. The radiation E-fields of the bottom slots are slightly larger than those of top slots. The two graphs of the bottom slots are identical and symmetric. The diode 4 switch-open state in Figure 3-0-29 is used to explain the working principle of bottom slots. In Figure 3-0-29, the coupling E field in the slot 1 region consists of major diffraction and minor leaky wave. The slot 1 has a leaky wave at medium level. The E-field in the slot 2 region is a superposition of minor diffraction and major leaky wave. The slot 2, as a result, has the largest leaky wave. In the slot 3 region only leaky wave appears, as the diffraction and leaky wave are anti-phase within the region. The slot 3 has the smallest leaky wave. In summary, for a shielded slot, the strength of leaky wave is determined by its position relative to the radiating slot. Specifically, the shielded slot in a diagonal position to the radiating slot has the strongest leaky wave; the shielded slot beneath the radiating slot has the medium leaky wave; and the shielded slot on the same

plane with the radiating slot has the weakest leaky wave. Figure 3-0-32 and Figure 3-0-33 show the E-field distributions of dual-diode off states. One common feature of these two graphs is that the coupling radiations all trend to the waveguide top plane, as top slots have a more intensive E-field than bottom slots. But, the attenuation of radiation in bottom slot region is slower than the one in top slot region, as the waveguide ground has a larger metal surface area to converge E-field. Therefore, the coupled leaky waves from short-circuited diodes also trend to the waveguide top plane. Both graphs have strong diffraction at the edges of the top and bottom reflectors, which means that radiation E-fields also disperses backward.

Figure 3-0-34 shows the E-field distribution of all-diode off state at 2.433 GHz, which is the working frequency of single diode off-state. In this graph, the two coupling E-fields at both sides of the waveguide trend toward to the waveguide top plane as well. As slots on the same plane of the waveguide are anti-phase with each other, there are obvious scattering phenomena at the edges of top and bottom reflectors. Because the slots impedance are mismatched at 2.433 GHz, the E-field intensity of all-diode off is clearly smaller than those of single-diode off states. Figure 3-0-35 shows the E-field distribution of all-diode on-state at 2.433 GHz in YOZ cut-plane. Although this graph has leaky waves at all of the four slots, the magnitude of leaky wave in on state is very small relative to those in the off states. The maximum E-field in Figure 3-0-35 is merely one-twentieth of the E-field strength in single diode off states at 2.433 GHz. The leaky waves in Figure 3-0-35 are only guided along the metal surface of waveguide and reflector walls. Therefore, these leaky waves are confined within the four slots regions. The leaky wave energy of four slots is mainly stored in near field range.

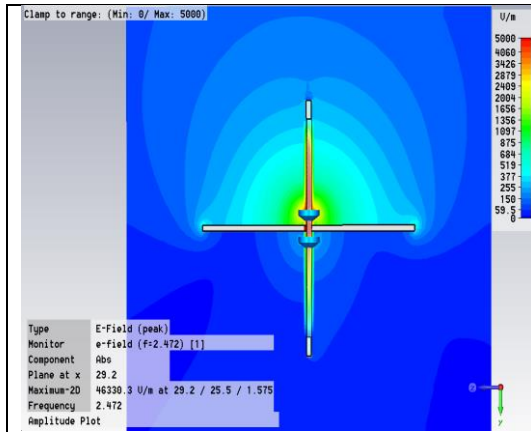


Figure 3-0-32: Diodes 1 & 4 off

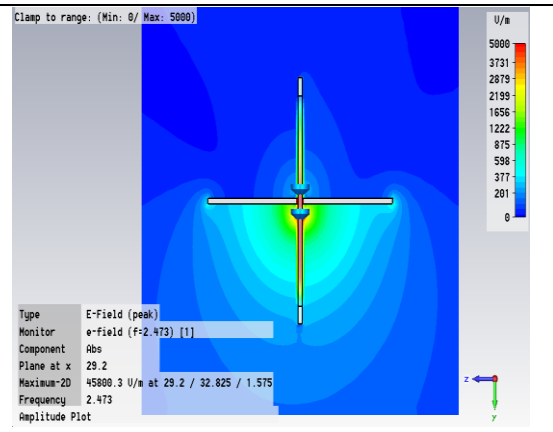


Figure 3-0-33: Diodes 2 & 3 off

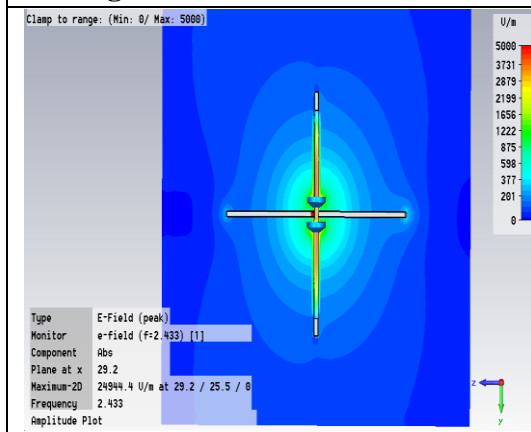


Figure 3-0-34: All diodes off at 2.433 GHz

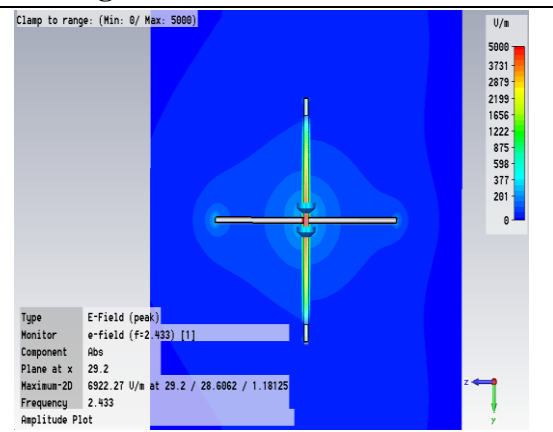


Figure 3-0-35: All diodes on at 2.433 GHz

XOZ plane position at the center of slots 1&4

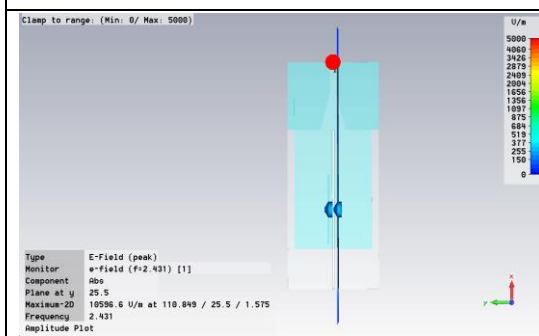


Figure 3-0-36: D1&D4 center at Y axis 25.5 mm

XOZ plane position at the center of slots 2&3

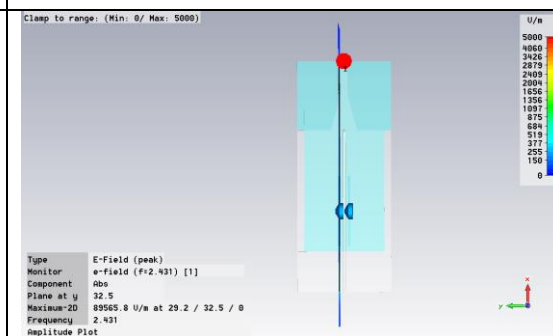


Figure 3-0-37: D2&D3 center at Y axis 32.5 mm

As the YOZ cut-plane only displays the part of the E-field components of slot, the XOZ cut-plane is introduced. Figure 3-0-36 and Figure 3-0-37 show the XOZ cut-planes at 25.5 mm and 32.5 mm on Y axis, respectively, which are longitudinal central cross sections of slots.

Figure 3-0-38 and Figure 3-0-39 are the XOZ cut-planes of radiative slot 1 and short-circuit slot 2 in diode 1 off state, respectively. Figure 3-0-40 and Figure 3-0-41 show the short-circuited slot 1 and radiative slot 2 in diode 2 off state, respectively. As the E-field distributions in these two states are nearly identical, only the single diode 1 off state will be discussed here. Slot 1 radiation in Figure 3-0-38 is guided towards to the two corners along the edge of top reflector. Although the diffraction at back corner couples with Microstrip fringing field, the radiation still can be guided towards to the front corner of top reflector. Therefore, the diffraction mainly appears at the front corner of bottom reflector. Slot 4 has leaky wave of higher-order mode, which can couple with diffraction at the front corner of bottom reflector. The diffraction in Figure 3-0-39 also gathers at the two corners of top reflector in slot 2 region. The leaky wave of slot 2 is anti-phase with the diffraction around the top reflector wall. But the leaky wave of slot 3 couples with diffraction at the front corner of bottom reflector. As the leaky waves in the slot 3 region and slot 4 region are in-phase with the diffraction, Figure 3-0-38 and show how the leaky waves couple with diffraction at the front corner of bottom reflector.

Figure 3-0-42 and Figure 3-0-43 show two ZOY cut-planes of diode 3 off-state. Figure 3-0-44 and Figure 3-0-45 show the corresponding cut-planes of diode 4 off-state. The E-field patterns in these four graphs are identical and symmetric, but these E-field patterns are slightly different from the ones of the top-plane diodes off states. To simplify the explanation, only diode 3 off state will be analyzed. In the slot 3 region, the radiation E-field with an unbalanced distribution mainly gathers at the front corner as shown in Figure 3-0-43. As the bottom radiation is not affected by Microstrip fringing field, the guided waves on the bottom reflector exhibit the original forward tendency of the input TE_{10} mode. As shown in Figure 3-0-42 and Figure 3-0-43, the leaky waves of slot 1 and slot 2 are in-phase with diffraction at the front corner of top reflector. The scattering intensity at the edge of top reflector in slot 2 region is larger than the one in slot 1 region. Both

graphs show that there is a weak diffraction coupling with fringing field at the back corner of top reflector. As the outer space fringing field is an intrinsic characteristic of Microstrip, this coupling is a common feature of all these four single diode off states. Although the bottom reflector in Figure 3-0-42 has a strong scattering E-field, the leaky wave of slot 4 does not couple with the scattering E-field. Therefore, leaky wave is anti-phase with scattering in slot 4 region.

Figure 3-0-46 and Figure 3-0-47 show two ZOY cut-planes of dual diode 1 and 4 off-state. Figure 3-0-48 and Figure 3-0-49 show the corresponding planes of dual-diode 2 and 3 off-state. These four graphs have symmetric patterns. The common feature of these graphs is that for each vertical pair of slots, the maximum E-field always locates at the waveguide top-plane slot. Therefore, the main lobe direction of coupling radiation is in the waveguide top slot region. Since the graphs of the vertical pair of slots are the same, only the dual-diode 1 and 4 off-state will be discussed here. Both Figure 3-0-46 and Figure 3-0-47 show that the largest scattering appears at the back corner of top reflector. This is because the Microstrip fringing field attracts the radiation backward component of slot 1. Without affecting by the fringing field, the radiation E-field in the slot 4 region has a relatively balanced distribution as shown in Figure 3-0-46. In Figure 3-0-47, the leaky waves of slot 2 and slot 3 do not couple with diffraction at the center of the respective reflector edge, which means that leaky waves are anti-phase with diffraction at slot 2 region and slot 3 region.

Figure 3-0-50 and Figure 3-0-51 show the XOZ cut-planes of all-diode off-state. The sample frequency is kept consistent at 2.433 GHz for comparing the performances of different diode states. These two graphs are totally identical and symmetric with the reflector wall. Because of the mismatched impedance, the radiation intensity of all-diode

off-state is only around one-fifth of the E-field intensity of single diode off-states. The inefficient radiations of top slots trend backward due to coupling with the fringing field. Therefore, the back corner of top reflector has a large scattering E-field. Without the fringing field impact, the surface guided wave on the bottom reflector trends to the front corner. A typical feature of all-diode off-state is that the radiation is significantly affected by the Microstrip feedline due to the impedance mismatching between antenna and feedline.

Figure 3-0-52 and Figure 3-0-53 show the ZOY cut-planes of all-diode on-state at 2.433 GHz. Both graphs show that all of the four slots have leaky wave at higher order mode. Moreover, the maximum E-field of all-diode on-state always locates in the bottom slots. The maximum strength of leaky E-field in all-diode on-state merely equals to 35% of the E-field strength observed in all-diode off-state, or is less than 8% of the values obtained in single-diode off states. Furthermore, the Microstrip fringing field is guided along the reflector edge from the back corner. And the scattering E-fields in the other three corners of reflectors are negligible.

ZOX cut-plane of diode 1 off state

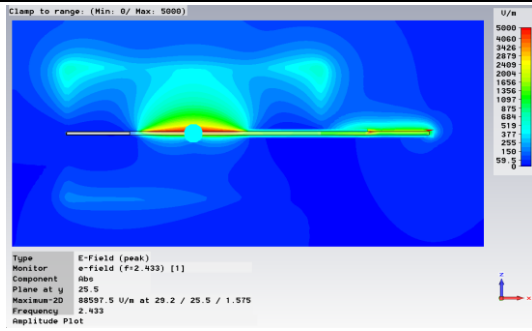


Figure 3-0-38: Diode 1 of at Y=25.5mm

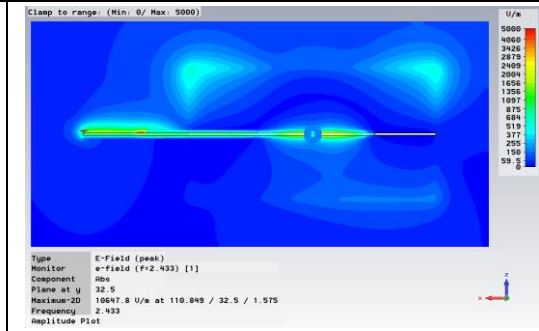


Figure 3-0-39: Diode 1 off at Y=32.5mm

ZOX cut-plane of diode 2 off-state

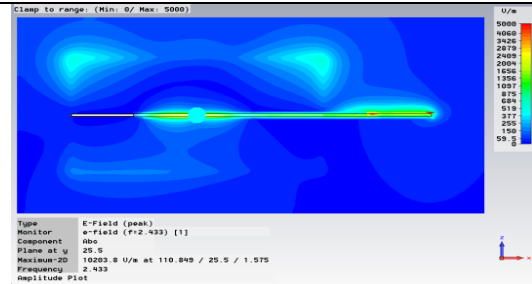


Figure 3-0-40: Diode 2 off at Y=25.5mm

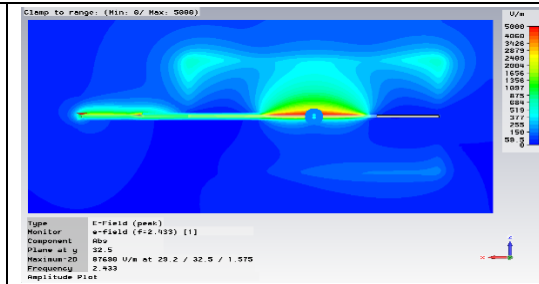


Figure 3-0-41: Diode 2 off at Y=32.5mm

ZOX cut-plane of diode 3 off state

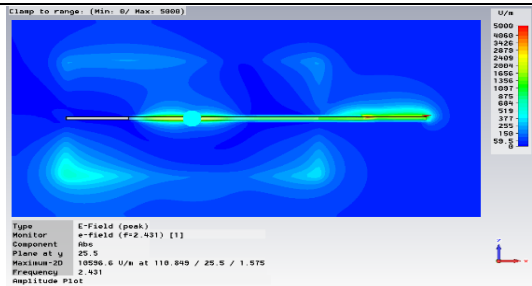


Figure 3-0-42: Diode 3 off at Y=25.5mm

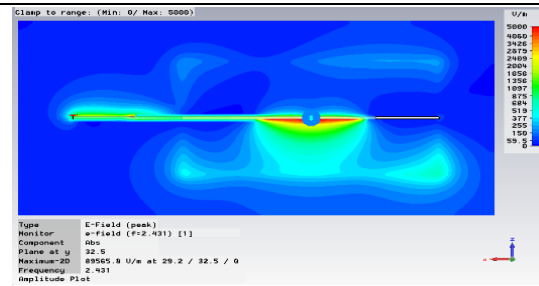


Figure 3-0-43: Diode 3 off at Y=32.5mm

ZOX cut-plane of diode 4 off state

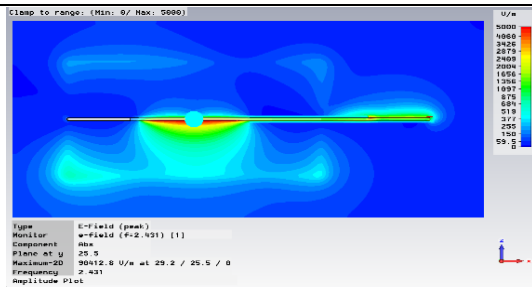


Figure 3-0-44: Diode 4 off at Y=25.5mm

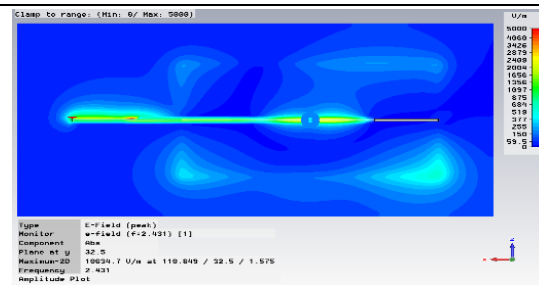


Figure 3-0-45: Diode 4 off at Y=32.5mm

ZOX cut-plane of diodes 1 and 4 off state

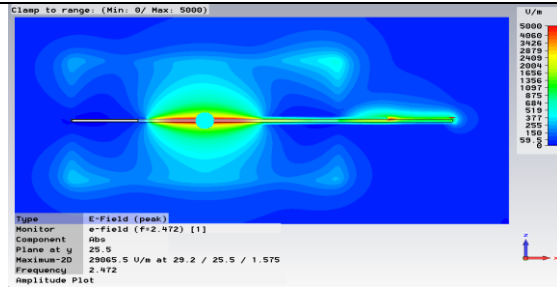


Figure 3-0-46: Diodes 1&4 off at Y=25.5mm

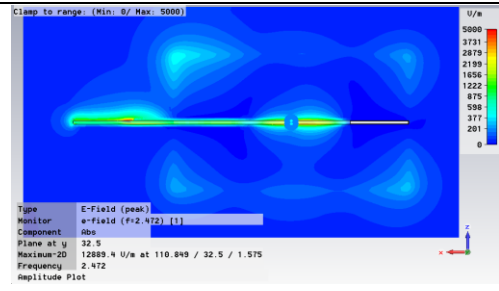


Figure 3-0-47: Diodes 1&4 off at Y=32.5mm

ZOX cut-plane of diodes 2 and 3 switch-open state

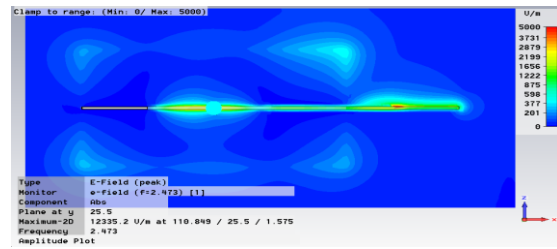


Figure 3-0-48: Diodes 2&3 off at Y=25.5 mm

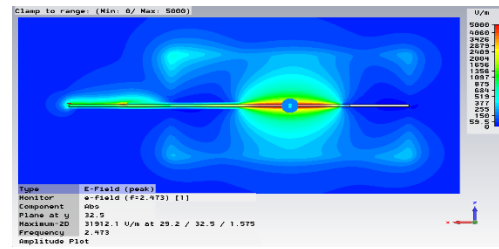


Figure 3-0-49: Diodes 2&3 off at Y=32.5mm

ZOX cut-plane of all diodes off-state

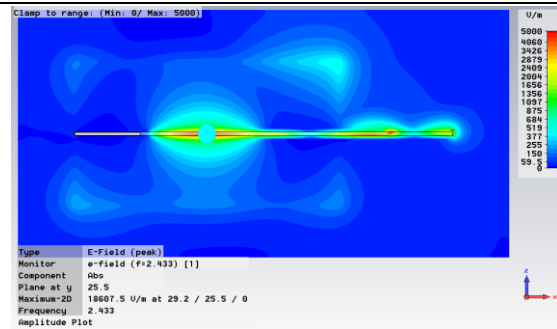


Figure 3-0-50: All diodes off at Y=25.5 mm

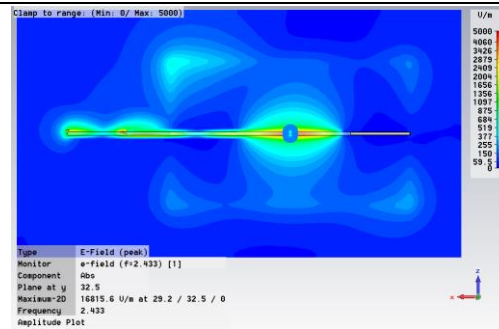


Figure 3-0-51: All diodes off Y=32.5mm

ZOX cut-plane of all diodes on-state

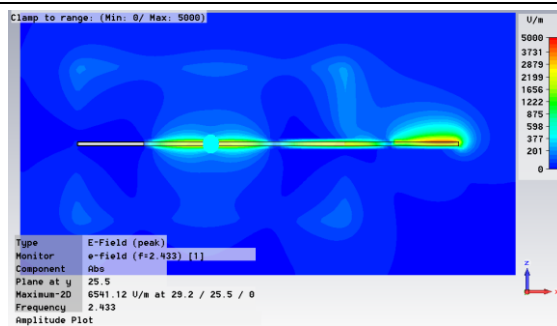


Figure 3-0-52: All diodes on at Y=25.5 mm

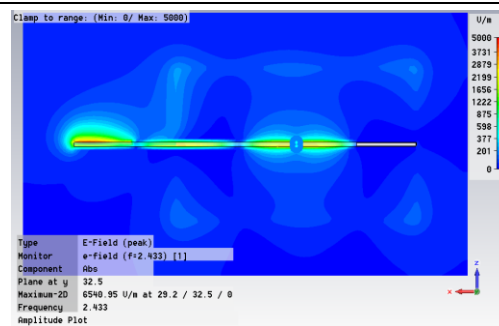


Figure 3-0-53: All diodes on at Y=32.5mm

Figure 3-0-54 and Figure 3-0-55 show the XOY cut-planes locating at $Z=2.575\text{mm}$ for top-plane and $Z= -1\text{mm}$ for bottom-plane, respectively. Figure 3-0-56 and Figure 2-0-58 show the off states of diode 1 and diode 2 in XOY cut-planes, respectively. Since both graphs are totally the same and symmetric with the top reflector, only Figure 3-0-56 will be analyzed. In slot 1 region, there is a strong scattering E-field covering the whole waveguide edge and the front corner as shown in Figure 3-0-56. But the radiation in slot 1 obviously trends to the back corner of waveguide. This phenomenon again proves that the radiation couples with the Microstrip fringing field at the boundary between antenna and feedline. Although the diffraction in slot 2 region spreads along waveguide edge towards to the front corner, the leaky wave in slot 2 does not couple with diffraction. Therefore, the leaky wave and diffraction are anti-phase at the slot 2 region. Figure 3-0-57 and Figure 2-0-59 show the off states of diode 3 and diode 4 in XOY planes, respectively. The E-field distribution of both graphs are similar to those of the top slots. Contrast to top slots, bottom slots are not interfered by the fringing field, so the graphs of bottom slots have intensive scatterings at the two front corners of waveguide and negligible guided waves at the back corners of waveguide. But the radiation in bottom slot region also trends to backward, as the large ground area of feedline guides the radiation towards to input port side. The common feature of the four single-diode off states is that the leaky wave of shielded slot at the same plane with radiation slot is always anti-phase with the diffraction.

Figure 3-0-60 and Figure 3-0-61 show the XOY cut-planes of dual-diode 1 and 4 off-state. Dual-diode 2 and 3 off-state shares the same E-field distribution with dual-diode 1 and 4 off-state, as shown in Figure 3-0-62 and Figure 3-0-63. These four graphs are symmetric with reflector walls. A regular pattern in these four graphs is that both the radiations in top slots slightly incline to the input port side, whereas both the radiations in bottom slots slightly trend forward to the front corner. Furthermore, the leaky waves of the two short-circuited slots are anti-phase with the diffraction. But the leaky waves of the

two short-circuited slots are in-phase with each other at the opposite side of the radiation main lobe. Therefore, the back lobe is enhanced, which is larger than the ones of single diode off states.

Figure 3-0-64 and Figure 3-0-65 show two XOY cut-planes of all-diode off-state at 2.433 GHz. Figure 3-0-64 shows that the radiations of top slots trend backward to the input port side; whereas, Figure 3-0-65 shows that the radiations of bottom slots trend forward to the front corners. Compared with the radiations in single-diode and dual-diode off states, the radiation in all-diode off-state obviously has a weaker E-field and a smaller distribution area on the waveguide surface. The maximum E-field strength of the state is only half to the E-field intensity of single diode off states, as mismatching impedance causes input energy to dissipate at feedline in the form of higher-order mode as showed in Figure 3-0-64. Therefore, the reflection loss is large. Furthermore, the mismatching impedance also causes uneven radiation strength between top and bottom slots. The radiation E-field strength of top slots is over 25% less than the bottom slots ones. Figure 3-0-66 and Figure 3-0-67 show the XOY cut-planes of all-diode on-state at 2.433 GHz. The leaky wave strength of the four slots in this state is only one-fourth of the radiation strength in all-diode off-state, or is less than 14% of the radiation intensity of single-diode off-state. Furthermore, the E-field strength of feedline in this state is 30% higher than the one of all-diode off-state. Although the taper transition in Figure 3-0-66 shows a scattering phenomenon, the leaky waves and scattering E-fields actually do not contribute to farfield radiation.

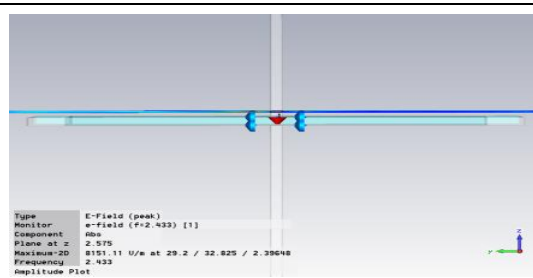


Figure 3-0-54:XYO cut-plane at 2.4 mm of Z axis

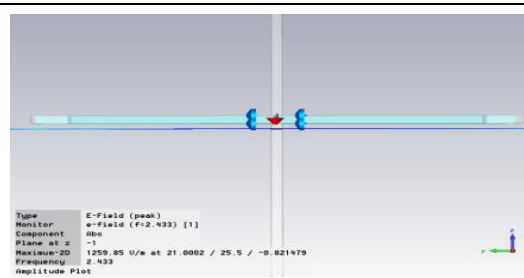


Figure 3-0-55:XYO plane at -0.8 mm of Z axis

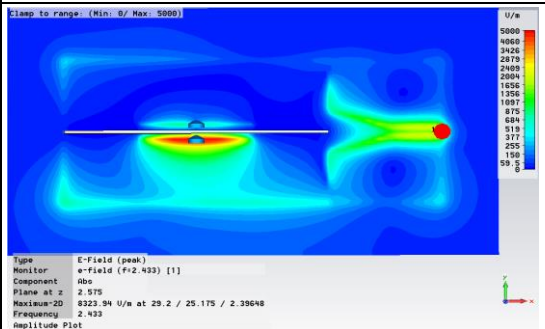


Figure 3-0-56: Top YOX plane of diode 1 off

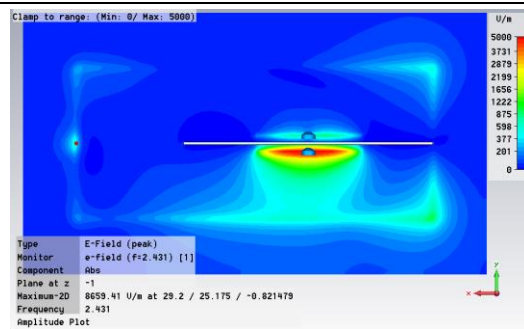


Figure 3-0-57:Bottom YOX plane of diode 4 off

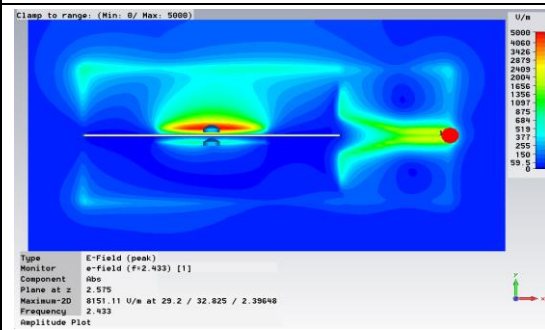


Figure 3-0-58: Top YOX plane diode 2 off

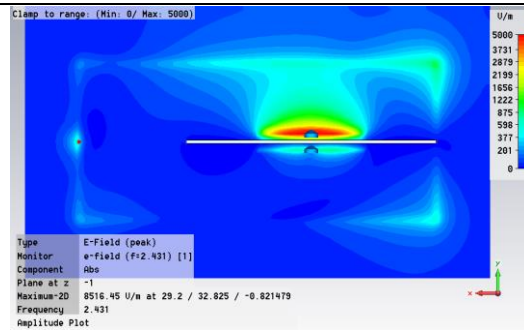


Figure 3-0-59:Bottom YOX plane diode 3 off

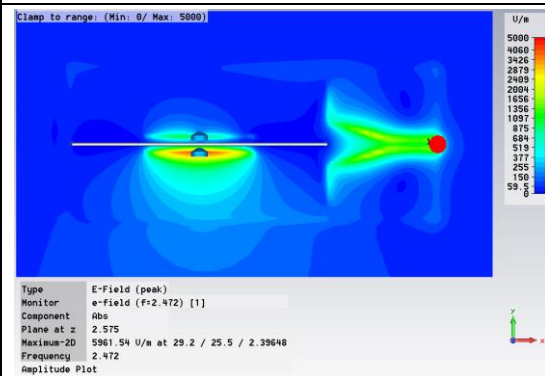


Figure 3-0-60: Top view of diodes 1 & 4 off

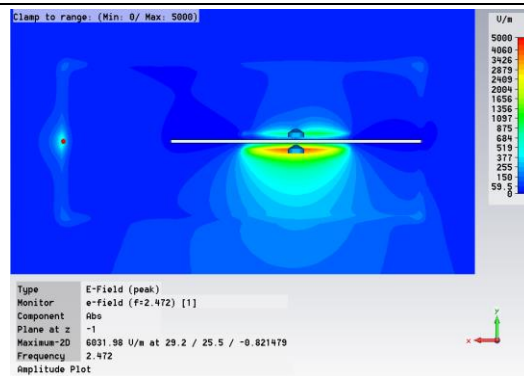


Figure 3-0-61:Bottom view of diodes 1 & 4 off

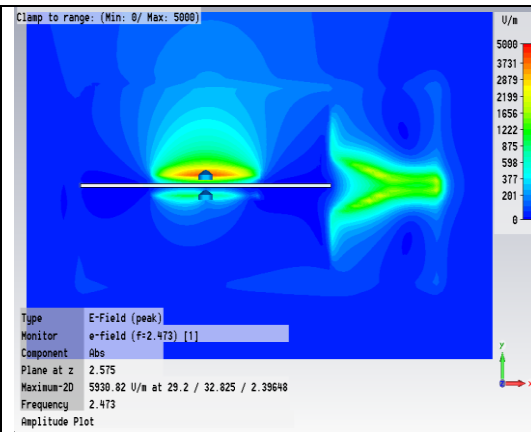


Figure 3-0-62: Top view of diodes 2 & 3 off

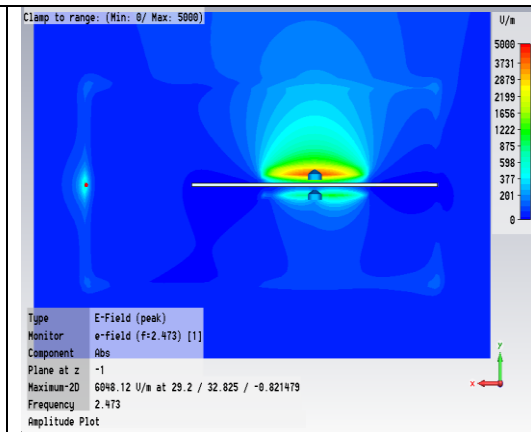


Figure 3-0-63: Bottom view of diodes 2 & 3 off

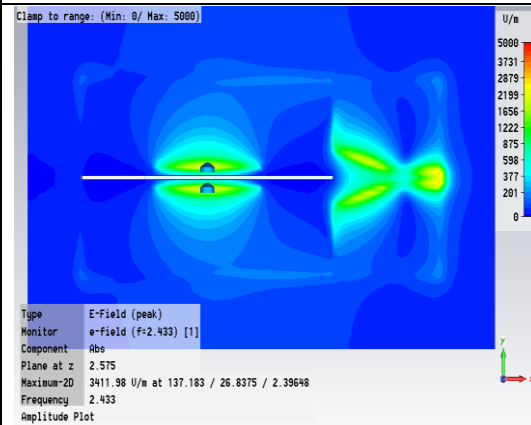


Figure 3-0-64: Top view of all diodes off

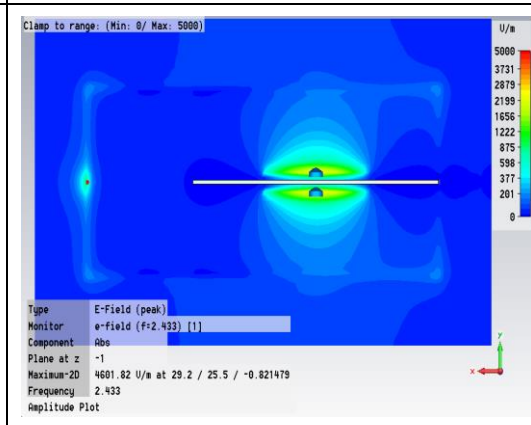


Figure 3-0-65: Bottom view of all diodes off

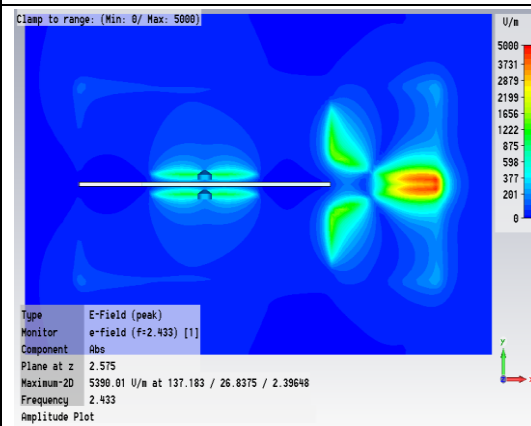


Figure 3-0-66: Top view of all diodes on

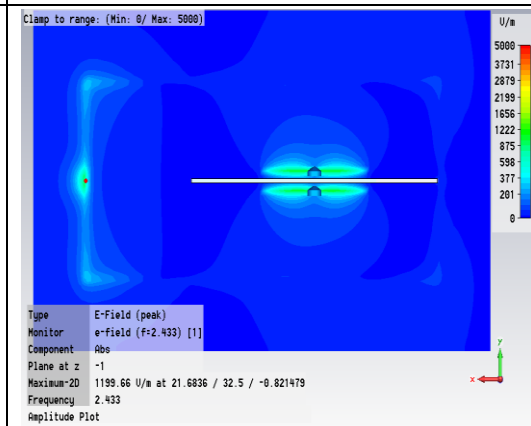


Figure 3-0-67: Bottom view all diodes on

3.2.4 Far-field range measurement results

The comparison graphs in Figure 3-0-68 to Figure 3-0-75 show the far field results of different diode states in YOZ plane. In the graphs, all measurement results are consistent with the simulations. The small differences between measurement and simulation are mainly caused by the inherent unstable performances of diodes. The wires and the overlap parasitic effects will also affect the far-field. As half of the overlap circuits is bended and pasted on the vertical reflector wall, and the manual installations of overlaps cannot guarantee a precise positioning, the performances of diodes are affected. These unpredictable factors of diodes produce variable results, and mutually influence the radiation coupling between the vertical pair of slots. But these fabrication errors are tolerable. The side lobe levels shown in Figure 3-0-68 to Figure 3-0-73 are all lower than -6 dB. Table 3-0-7 summarizes the measurement gains. Within the error tolerance, the measurement gains of all the slots are around 5dB, except for the one of slot 2 which is 4.5 dB. This is because diode 2 in reverse bias cannot reach 3000 ohms. These gains can be further improved by extending both the width of antenna and the height of reflector. Overall, the measurement results reach the design requirement.

As shown in Figure 3-0-71, the slot 4 has a similar radiation pattern with slot 1, only the radiation mechanism of slot 1 will be discussed here. Figure 3-0-68 shows the far field results of diode 1 off state. The main lobe directions in measurement and simulation are 132 degree and 134 degree, respectively. The measurement side lobe in slot 4 region is slightly smaller than simulation one. Therefore, the short-circuited diode 4 achieves the design resistance, 2 ohms. The measurement diffraction at slot 4 region is larger than the one obtained in simulation. However, the measurement side lobe in slot 2 region is 2 dB stronger than simulation ones, and merges with the back lobe in slot 3 region. The short-

circuited diode 2, as a result, must be over 2 ohms. The measurement back lobe in slot 3 region is 1.5 dB smaller than the simulation result. Overall, the directions of side lobes in measurements are the same with results in the simulation. As shown in Figure 3-0-70, the slot 3 has a similar radiation pattern with slot 2, only the radiation mechanism of slot 2 will be discussed here. Figure 3-0-69 shows the far field results of diode 2 off state. The main lobe directions of measurement and simulation are the same, which all locate at the 226 degree. In slot 1 region, the measurement side lobe strength is 2dB larger than the simulation one, as the resistance of short-circuited diode 1 is over 2 ohms. The measurement back lobe strength is 1.5 dB larger than the simulation one, as the resistance of short-circuited diode 4 is also over 2 ohms. As shown in Figure 3-0-69, the measurement pattern, in general, is consistent with the simulation one, including the directions of side lobes and back lobe.

As shown in Figure 3-0-72, the dual-diode 1 and 4 off-state has the same farfield pattern with the dual-diode 2 and diode 3 off-state, thus only the radiation mechanism of dual-diode 2 and 3 off-state will be discussed here. The direction of measurement main lobe, as shown in Figure 3-0-73, has a 10 degree difference to the simulation result. As the reverse diode 2 has a larger resistance than the reverse diode 3, the measurement pattern trends to the slot 2 region. Furthermore, in the slot 4 region, the measurement diffraction is 2 dB larger than the simulation result. This increased diffraction means that, in actual practice, more E-field from the slot 3 region is conducted into the slot 4 region. The measurement back lobe in Figure 3-0-73 is 2 dB larger than the simulation result, as the resistances of the short-circuited diode 1 and diode 4 are larger than 2 ohms. Moreover, the back lobe trends to the slot 1 region, as the resistance of diode 1 is larger than the one of diode 4. Therefore, slot 1 has a larger leaky wave. Figure 3-0-74 shows the far field results of all-diode off-state. The patterns of simulation and measurement are nearly the same. Both patterns are symmetric about reflectors. As the coupling of Microstrip fringing

field and radiation E-field enhances the strength of the E-field on the top reflector, the attenuation level at top reflector is -26 dB, whereas the one at bottom reflector is -40 dB. Therefore, the attenuation on top reflector is smaller than the one on bottom reflector. As the coupling E-fields of slot 1 and slot 4 are stronger than the coupling E-fields of slot 2 and slot 3, the E-fields from slot 1 region and slot 4 region diffract into the slot 2 region and slot 3 region. Therefore, the attenuation mainly happens on the reflector surface inside the slot 2 region and the slot 3 region.

Figure 3-0-75 shows the far field results of all-diode on-state. The patterns of measurement and simulation are quite similar, which all consist of three lobes. The lobe at the 180 degree is caused by the Microstrip fringing field, which is 2 dB smaller than the prediction given by simulation. Slot 3 has the largest leaky wave, which is 5 dB stronger than the fringing field. Slot 4 has the second largest leaky wave. As the ground plane has a larger metal surface area than the top plane, the leaky waves in bottoms slots are stronger than those in top slots.

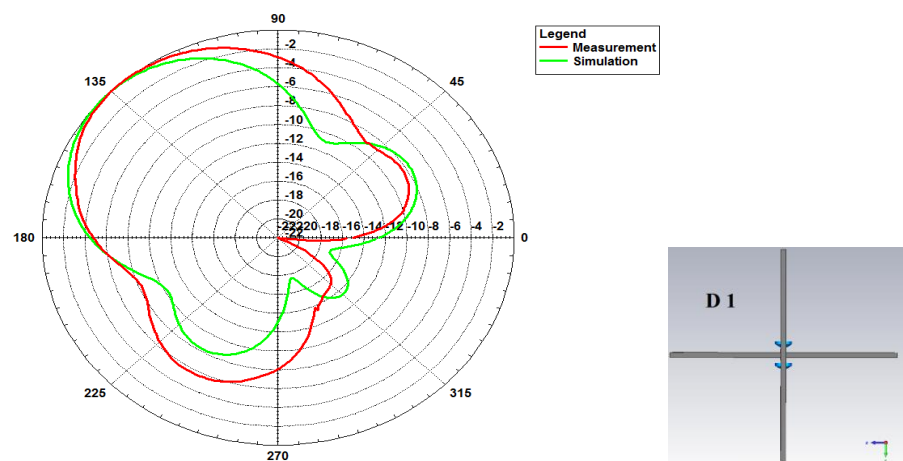


Figure 3-0-68: Far-field measurement of diode 1 off-state

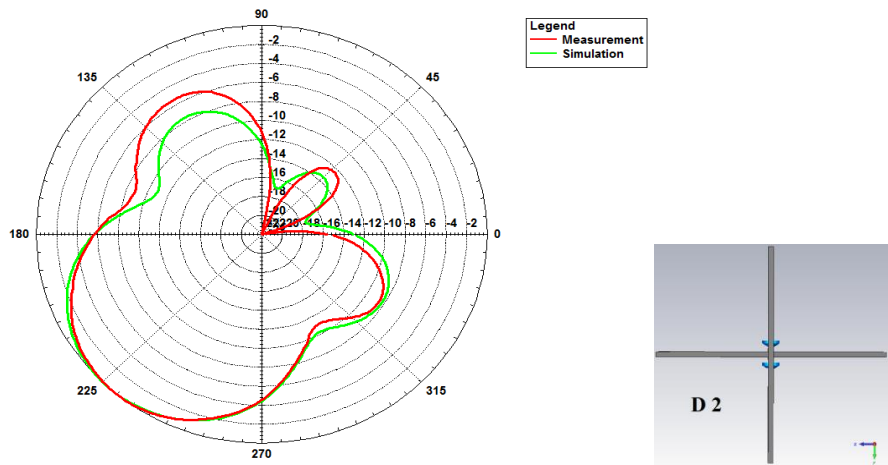


Figure 3-0-69: Far-field measurement of diode 2 off-state

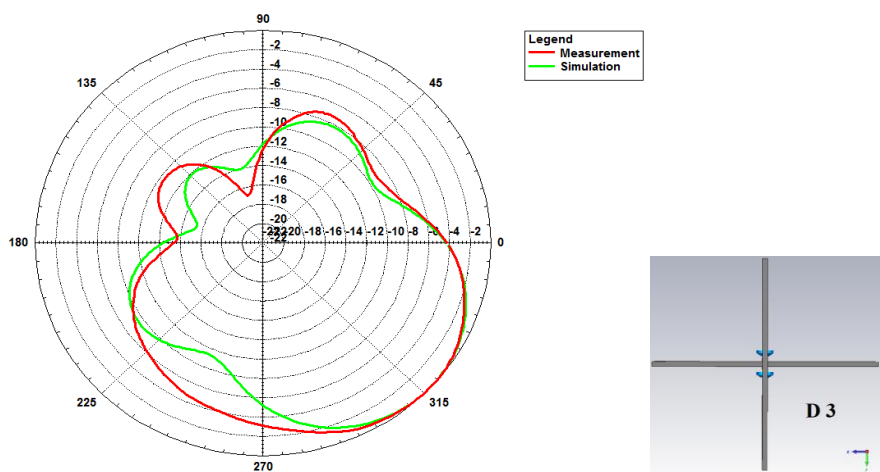


Figure 3-0-70: Far-field measurement of diode 3 off-state

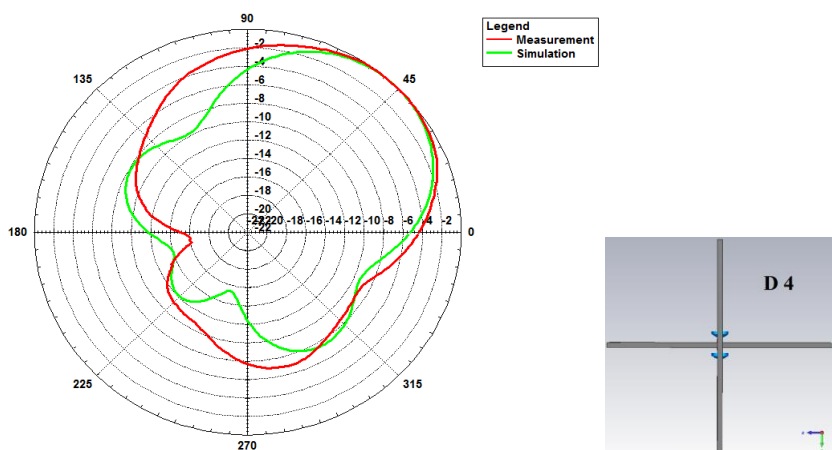


Figure 3-0-71: Far-field measurement of diode 4 off-state

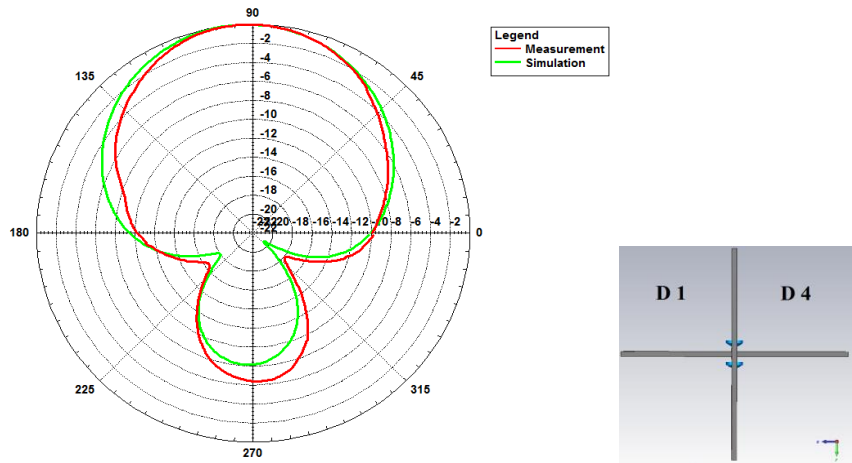


Figure 3-0-72: Far-field measurement of diode 1 & 4 off-state

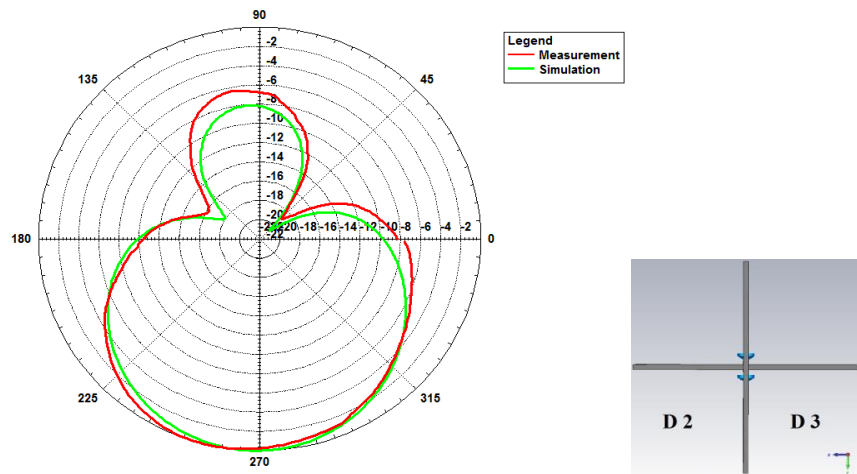


Figure 3-0-73: Far-field measurement of diode 2 & 3 off-state

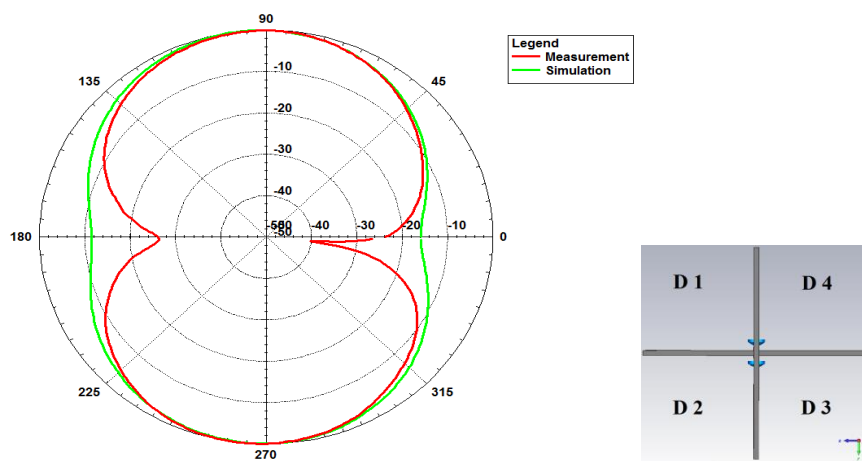


Figure 3-0-74: Far-field measurement of all-diode off-state

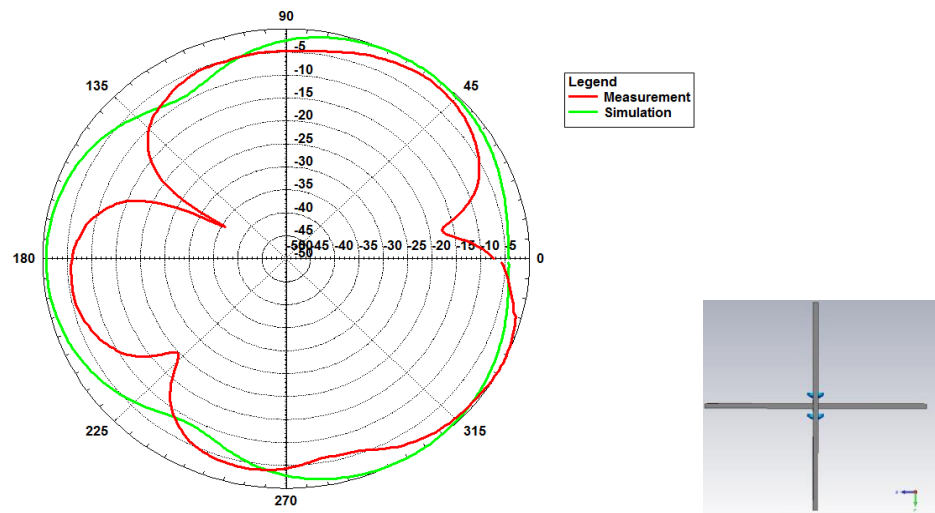
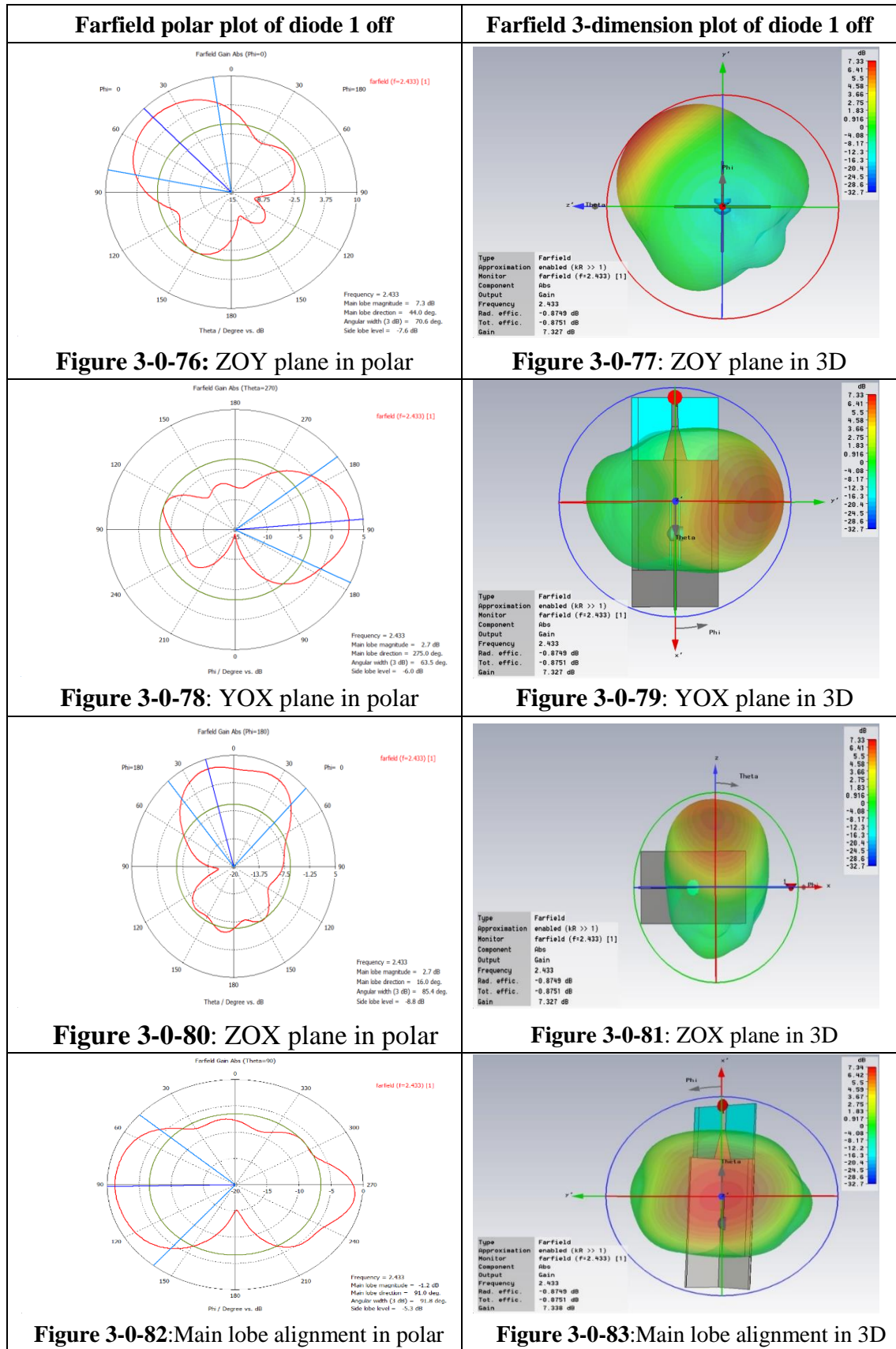


Figure 3-0-75: Far-field measurement of all-diode on-state

Single diode off state	Slot 1	Slot 2	Slot 3	Slot 4
Ideal simulation without overlap	7.3 dB at 2.43 GHz	7.3 dB at 2.43 GHz	7.1 dB at 2.43 GHz	7.1 dB at 2.43 GHz
Simulation Gain with overlap	6.5 dB at 2.43 GHz	6.5 dB at 2.43 GHz	6.2 dB at 2.43 GHz	6.2 dB at 2.43 GHz
Measurement Gain	5.5 dB at 2.48 GHz	4.5 dB at 2.48 GHz	5.4 dB at 2.47 GHz	5.2 dB at 2.47 GHz

Table 3-0-7: Gain measurement for single diode off-state

3.2.5 Simulation results of Far-field



As the simulation results are highly consistent with the measurement results, the further detail analysis of farfield can be carried out by simulation. For speeding up the simulation, all the antenna models are simplified by removing the overlap. As the farfield results of top-plane diode off states are identical, the following analysis will only focus on the diode 1 off state.

Figure 3-0-76 to Figure 3-0-83 show the farfield results of diode 1 off state in different cut-planes. The ideal gain of slot 1 radiation is 7.327 dBi without reacting with overlaps and wires. The radiation efficiency and the total efficiency are -0.8749 dB and -0.8751 dB, respectively. These efficiency values mean that over 80% of the incident power is radiated from slot 1 to outer space. Figure 3-0-77 shows the three dimensional farfield pattern in ZOY plane. Figure 3-0-76 shows the corresponding polar plot, which is an E-plane radiation pattern. The direction of main lobe in Figure 3-0-76 is 44 degree, which is 1 degree deviating from the prediction, 45 degree. As slots are all slightly offset from the waveguide central line, on a particular YOZ cut-plane of slots, the conducting distance from the slot to the edge of reflector is longer than the one from the slot to the edge of waveguide. The longer the distance is, the more the radiation can be reflected. Furthermore, Figure 3-0-38 and Figure 3-0-39 show that diffraction and leaky wave are anti-phase in slot 2 region, which cancel out each other at the center of the top reflector edge. Only the two corners of the top reflector have scattering E-field. But, Figure 3-0-56 shows that diffraction and leaky wave are in-phase in slot 4 region, which couple along the whole waveguide edge. The radiation has a potential tendency to trend to the slot 4 region. As a result, the main lobe direction of slot 1 slightly deviates 1 degree to the waveguide plane. As shown in Figure 3-0-76, the 3dB angular width is 70.6 degree. The gain is inversely proportional to the 3dB beam width. A large 3dB angular width will decrease the gain. Therefore, the balance between 3dB beam width and gain depends on the practical application requirement. The side lobe level shown in Figure 3-0-76 is -7.6dB,

which is determined by the size of reflection area. The larger the reflection area is, the lower back lobe will be. The maximum side lobe in Figure 3-0-76 locates at slot 2 region. The side lobe in slot 4 region is slightly smaller than the one in slot 2 region. These two side lobes all consist of leaky waves and diffraction. The diffraction is the predominant component of side lobes when short-circuited diodes are ideally working at 2 ohms. The diffraction intensities are different between slot 2 region and slot 4 region. The back lobe of slot 3 region in Figure 3-0-76 also relates to the diffraction as well. The back lobe is -13 dB lower than the main lobe.

Figure **3-0-79** shows that the main lobe slightly deviates towards to the waveguide front end. The radiation E-field only diffracts at the two corners of the top reflector and is null at the center of the top reflector edge. The concave pattern in slot 2 region proves that the leaky wave and diffraction in this region are anti-phase, and cancel out each other. This finding is in agreement with the E-field distributions in Figure 3-0-38 and Figure **3-0-39**. Figure 3-0-81 shows that the main lobe also trends to the waveguide front end. The radiation E-field diffracting into slot 4 region trends backward to the input port side. This backward E-field distribution is proved by Figure 3-0-56 and Figure 3-0-57. The main lobe diffraction in slot 4 region is larger than the one in slot 2 region as shown in Figure **3-0-79** and Figure **3-0-81**. This has also been proved in Figure 3-0-38 and Figure 3-0-56.

The polar plot in Figure **3-0-78** shows the far-field pattern at the waveguide plane. The cutting line of this YOX plane is the horizontal blue line of X-axis shown in Figure **3-0-81**. The direction of local main lobe has a 5-degree deviation towards to the input port side. The reason of the deviation is shown in Figure 3-0-56. Coupling with the Microstrip fringing field, the radiation E-field is guided backward along the edge of waveguide. The polar plot in Figure **3-0-80** shows the far-field pattern at the reflector plane. The

cutting line of this polar plot is the green line of X-axis shown in Figure 3-0-79. The direction of local main lobe is 16 degree forward, as the radiation E-field on the top reflector trends to the front corner. The local main lobes in Figure 3-0-78 and Figure 3-0-80 are both 2.7 dB, which means that the intensities of diffractions towards adjacent slot regions are equal. The 3 dB angular width shown in Figure 3-0-78 is smaller than the one in Figure 3-0-80. As the side lobe level in Figure 3-0-78 is smaller than the one in Figure 3-0-80, the diffraction at the waveguide edge of slot 2 region is larger than the one at the bottom reflector. Therefore, Figure 3-0-78 and Figure 3-0-80 once again prove that the maximum side lobe locates at the slot 2 region.

The coordinate system in Figure 3-0-82 and Figure 3-0-83 is aligned with the main lobe, which is different from the above-mentioned orthogonal coordinate. As these two graphs are only used to show the partial pattern of main lobe, both the graphs do not adopt far-field parameters. With a 3D pattern, Figure 3-0-83 shows that the shape of main lobe within 3 dB beamwidth is slightly asymmetric. Figure 3-0-82 shows the outlines of two diffractions, where the diffraction at 91 degree towards slot 4 region and the diffraction at 267 degree towards slot 2 region.

The far-field results of bottom slots are similar to the top slot ones. The following content will focus on the difference. As showed in Figure 3-0-93 and Figure 3-0-101, the gains of slot 3 and slot 4 are around 7.155 dB, which are slightly smaller than the top slots results. This is because the unified slot length is adjusted to match with the top slots impedance. Extending to the feedline ground, the bottom plane has a larger metal area than the top plane, the impedance of bottom slots, as a result, are slightly different from the one of top slots. The mismatched impedance can cause the bottom radiations to spread out around slightly. Therefore, in ZOY plane, the 3 dB angular width of bottom radiations

is 1.4 degree larger than the one of top radiations. And, in YOX plane, the 3 dB angular width of bottom radiations shown in Figure 3-0-94 and Figure 3-0-102 are 5.3 degree larger than the top slots ones shown in Figure 3-0-78 and Figure 3-0-86. The radiation efficiency and the total efficiency of bottom radiations are -0.9280 dB and -0.9283 dB respectively, which means that around 81% of the energy is sent out. The efficiencies among the four slots only have a 0.1dB difference. Figure 3-0-96 and Figure 3-0-104 show that the side lobe level in ZOY cut-plane is 1.6 dB smaller than the result of top slots. This is because when the bottom slots are radiating, the Microstrip fringing field only enhance the side lobe on the waveguide top plane. In Figure 3-0-98 and Figure 3-0-106, the outline patterns of main lobe are rounded at both sides, which means that the diffraction distribution at the bottom reflector edge and the waveguide bottom plane edge are similar. But the intensity of diffraction E-field on the bottom reflector edge is slightly larger than the one on the bottom waveguide edge.

Farfield polar plot of diode 2 off

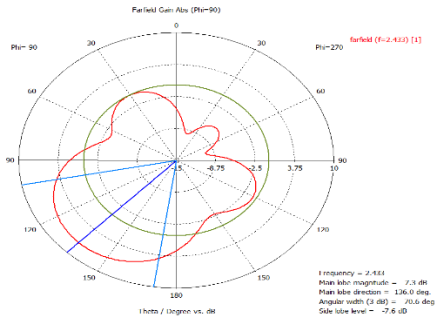


Figure 3-0-84: ZOY plane in polar

Farfield 3-dimension plot of diode 2 off

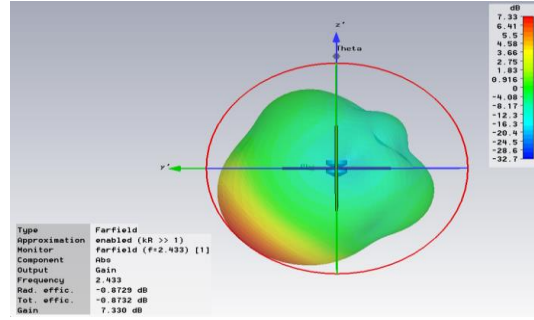


Figure 3-0-85: ZOY plane in 3D

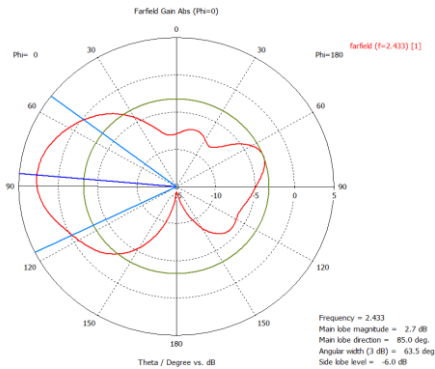


Figure 3-0-86: YOX plane in polar

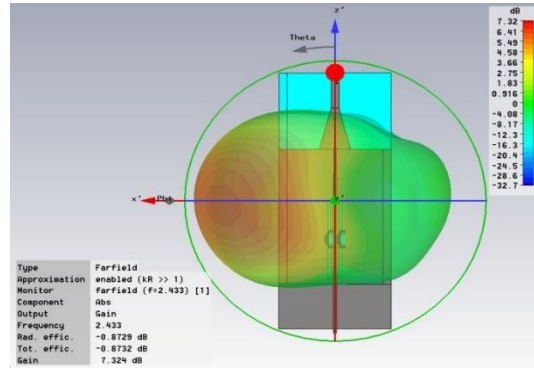


Figure 3-0-87: YOX plane in 3D

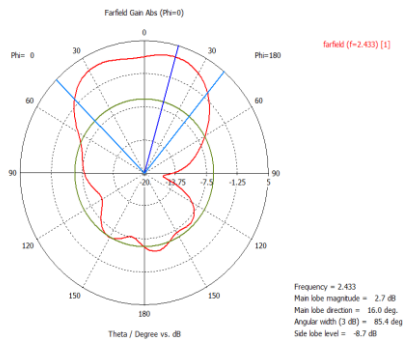


Figure 3-0-88: ZOX plane in polar

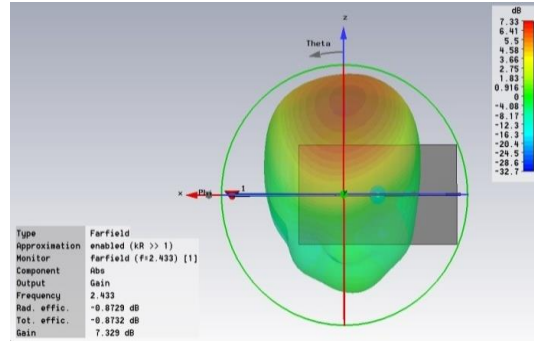


Figure 3-0-89: ZOX plane in 3D

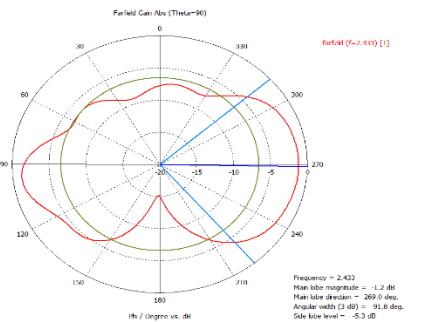


Figure 3-0-90: Main lobe alignment in polar

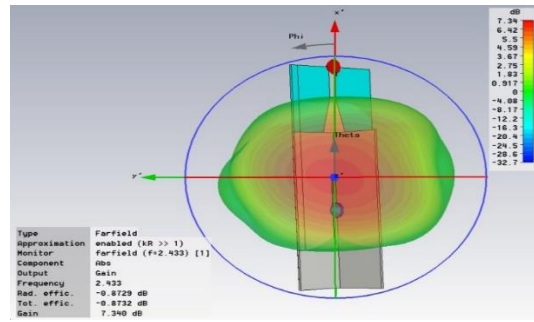


Figure 3-0-91: Main lobe alignment in 3D

Farfield polar plot of diode 3 off

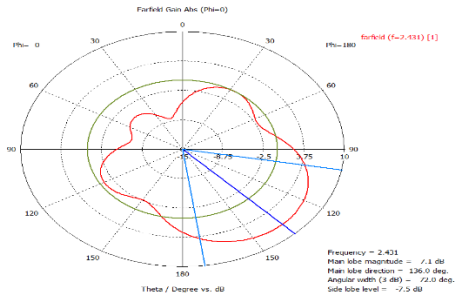


Figure 3-0-92: ZOY plane in polar

Farfield 3-dimension plot of diode 3 off

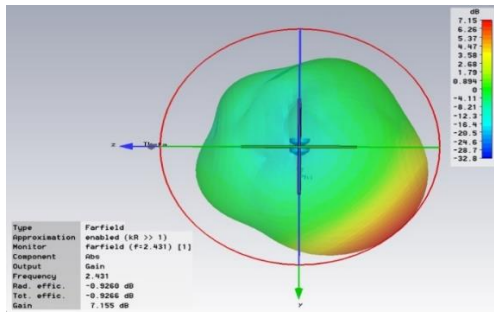


Figure 3-0-93: ZOY plane in 3D

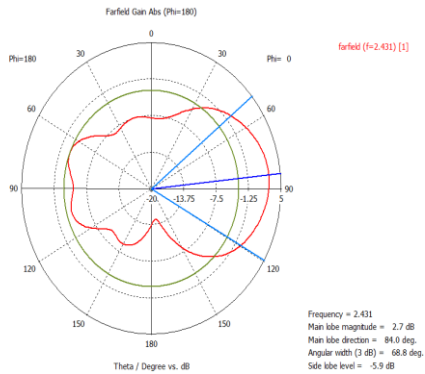


Figure 3-0-94: YOX plane in polar

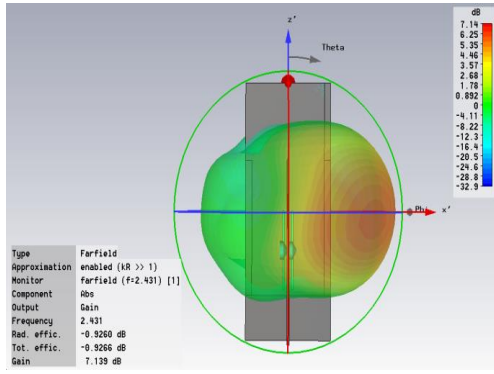


Figure 3-0-95: YOX plane in 3D

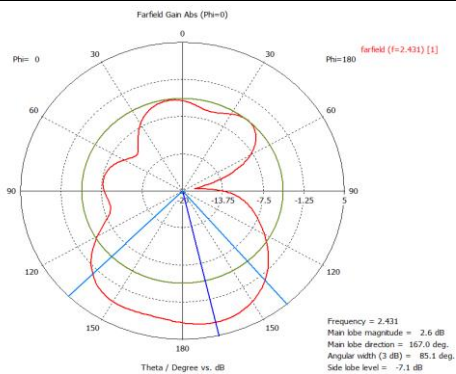


Figure 3-0-96: ZOX plane in polar

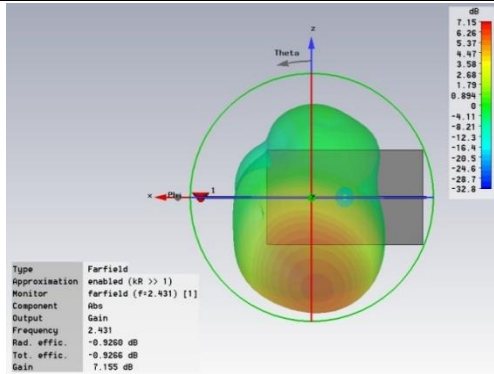


Figure 3-0-97: ZOX plane in 3D

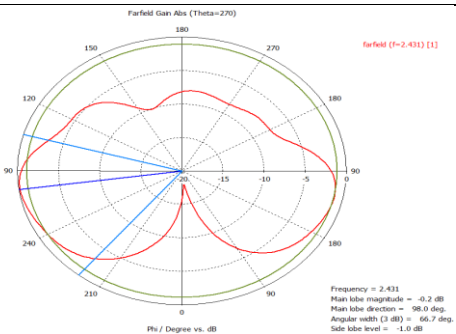


Figure 3-0-98: Main lobe alignment in polar

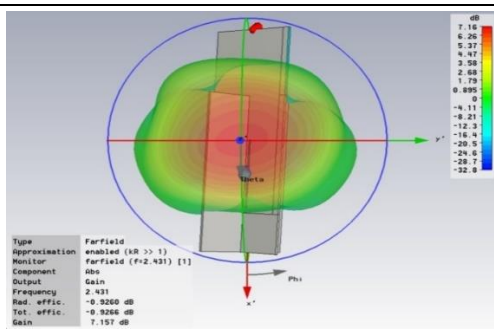


Figure 3-0-99: Main lobe alignment in 3D

Farfield polar plot of diode 4 off

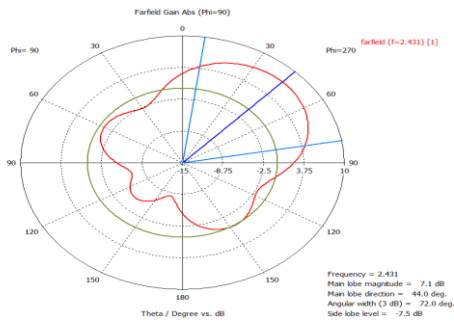


Figure 3-0-100: ZOY plane in polar

Farfield 3-dimension plot of diode 4 off

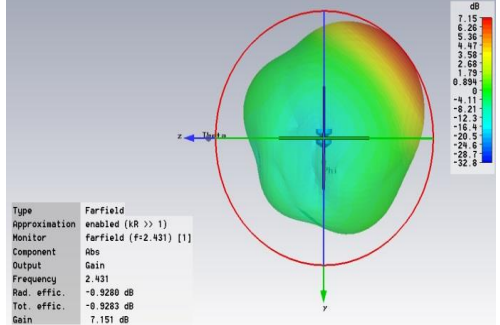


Figure 3-0-101: ZOY plane in 3D

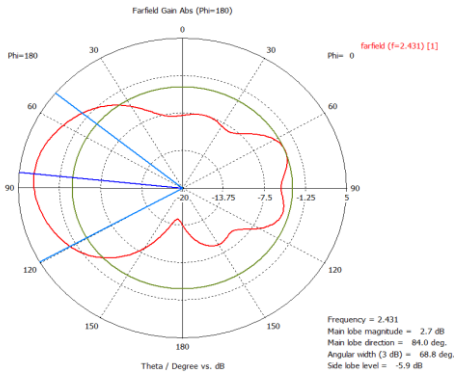


Figure 3-0-102: YOX plane in polar

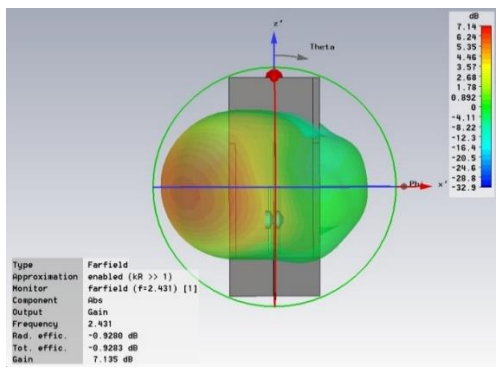


Figure 3-0-103: YOX plane in 3D

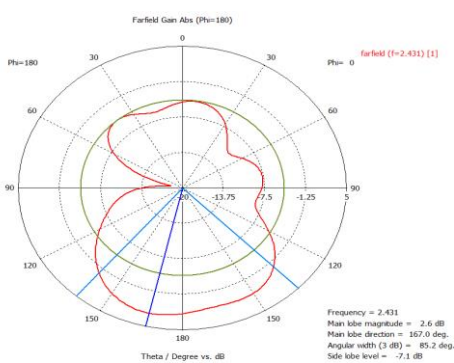


Figure 3-0-104: ZOX plane in polar

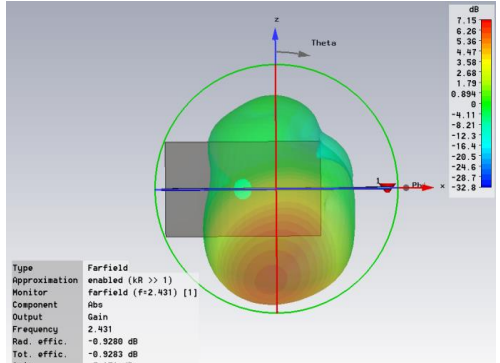


Figure 3-0-105: ZOX plane in 3D

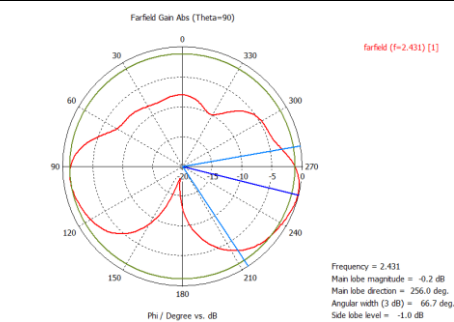


Figure 3-0-106: Main lobe alignment in polar

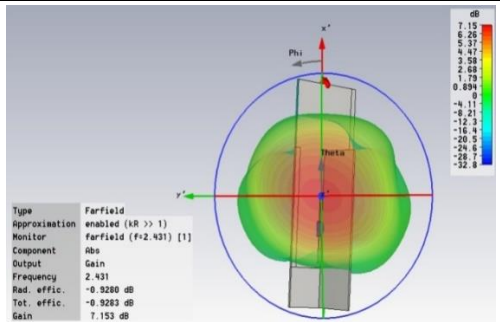


Figure 3-0-107: Main lobe alignment in 3D

The far-field results of dual-diode 1 and 4 off-state are shown in Figure 3-0-108 to Figure 3-0-113. The two dual-diode off states not only have symmetric far-field patterns, but also have identical farfield results. Therefore, only the dual-diode 1 and 4 off-state will be analyzed here. As shown in Figure 3-0-109, the radiation efficiency and the total efficiency are -0.9346 dB and -1.486 dB, respectively, which in linear scale are 0.807 and 0.71, respectively. The radiation efficiency of dual-diode state is similar to those of single-diode off states, but the total efficiency of dual-diode off-state is 0.5 dB less than those of single-diode off states. This is because the impedance of slots in dual-diode off states is mismatched. Therefore, the gain, as shown in Figure 3-0-108, is 6.242 dB, which is 1 dB less than the result of single slot radiation. Compared with the results of single diode off-state in ZOY plane, the main lobes of dual-diode off-state has a broader 3 dB angular width (beamwidth) and a larger side lobe level. This beamwidth is broadened by the coupling radiations from slot 1 and slot 4. As the waveguide planes of slot 1 and slot 4 have intensive guided surface waves towards the edge, the diffraction at reflectors decreases. If the waveguide edges were extended, the beamwidth would be reduced and the radiations of the two slots would be separated. The main lobe direction shown in Figure 3-0-108 has a 3-degree deviation trending to slot 1 region. As, in single-diode off-state, the gain of slot 1 is larger than the one of slot 4, the dominant component of this coupling radiations is from slot 1. The ZOY plane result in Figure 3-0-46 proves the maximum E-field locates in slot 1. Moreover, Figure 3-0-109 shows that the main lobe in slot 4 region attenuates more quickly than the one in slot 1 region. Therefore, the peak of main lobe is in slot 1 region. In addition, the diffraction at the edge of top reflector is larger than the one at the edge of bottom reflector. Although, in near field range, the leaky wave of slot 3 is slightly larger than the one of slot 2, a major part of the back lobe locates at slot 2 region. The back lobe shown in Figure 3-0-108 is formed by the diffraction and the coupling leaky waves from slot 2 and slot 3.

Figure 3-0-111 shows a 3D far-field pattern in YOX plane. Figure 3-0-110 shows the corresponding polar plot. In Figure 3-0-110, the main lobe direction has a 2-degree deviation backwards to the input port. The reason as showed in Figure 3-0-60, is that the Microstrip fringing field couples with the radiation component at the waveguide surface. As the waveguide top plane, compared with the bottom plane, has a smaller metal surface area, the 3 dB beamwidth of slot 1 radiation is 5.3 dB smaller than the one of slot 4 radiation in YOX plane. The beamwidth of dual-slot 1 and 4 radiation as shown in Figure 3-0-110 is 64.6 degree, which is 1 degree larger than the beamwidth of slot 1 radiation. Since the main lobe locates in slot 1 region, the beamwidth of the dual-slot radiation is similar to the beamwidth of slot 1 radiation. Therefore, the beamwidth of dual-slot radiation is similar to the beamwidth of the individual slot radiation, given this individual slot locates in the same region as the main lobe of the dual-slot radiation. Furthermore, the beamwidth in Figure 3-0-110 once again proves that the main lobe consists of coupling E-fields from slot 1 and slot 4, but is not a simple superimposition of E-fields. The gain and side lobe level in Figure 3-0-110 are identical to the ones in Figure 3-0-108. Figure 3-0-113 shows a 3D far-field pattern in ZOX plane. In this graph, the peak of main lobe mainly locates at slot 1 region and slightly trends to the input port side. The polar plot in Figure 3-0-112 shows the far-field pattern at the reflector plane. The cutting line of this ZOX plane is the vertical green line as shown in Figure 3-0-111. The direction of the largest local lobe in Figure 3-0-112 points to the back corner of top reflector. The reason is that the strong coupling fields, consisting of the Microstrip fringing field and diffraction, gather at the back corner of top reflector, as shown in Figure 3-0-46 and Figure 3-0-47. Figure 3-0-112 also shows that each of the other three corners of reflectors has a lobe, as the diffractions locate at all of the four corners of reflectors. The coupling of Microstrip fringing field and backward radiation component shown in Figure 3-0-112 produces a small lobe at 90 degree, which is the taper transition region.

Diodes 1&4 off-state farfield polar plot

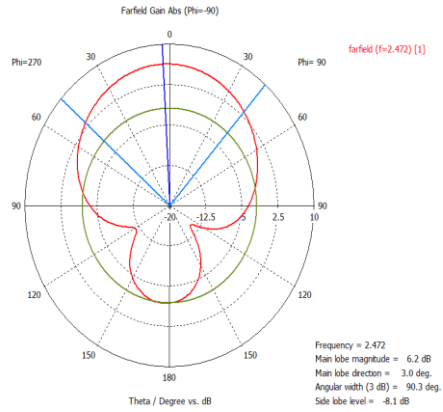


Figure 3-0-108: ZOY plane in polar

Diodes 1&4 off-state 3-dimension pattern

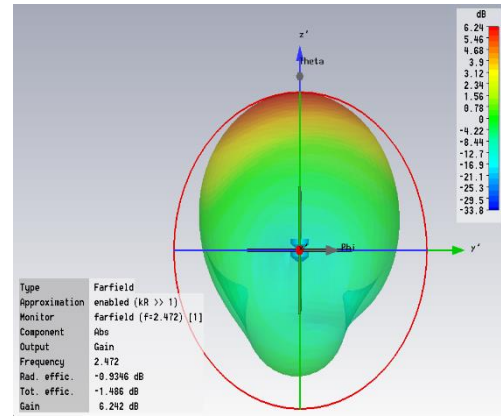


Figure 3-0-109: ZOY plane in 3-D

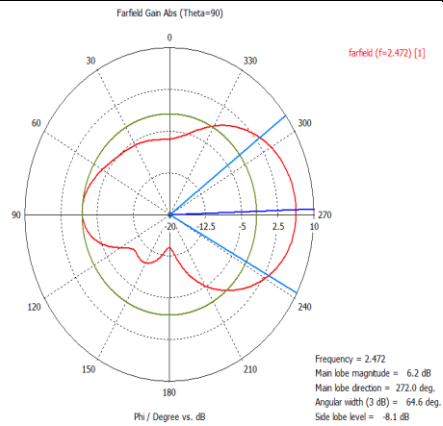


Figure 3-0-110: YOX plane in polar

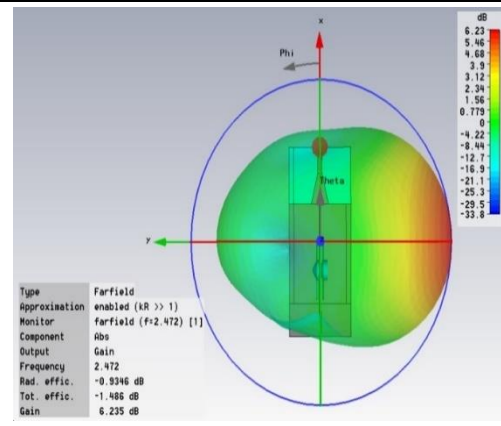


Figure 3-0-111: YOX plane in 3-D

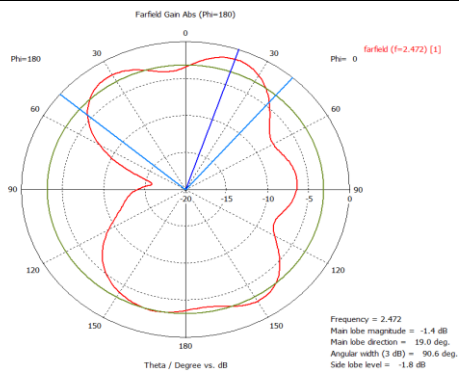


Figure 3-0-112: ZOX plane in polar

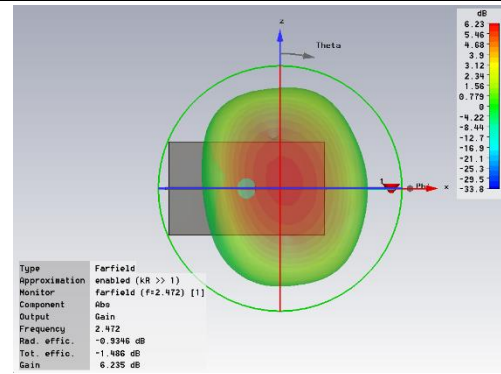


Figure 3-0-113: ZOX plane in 3-D

Diode 2 & 3 off-state farfield polar plot

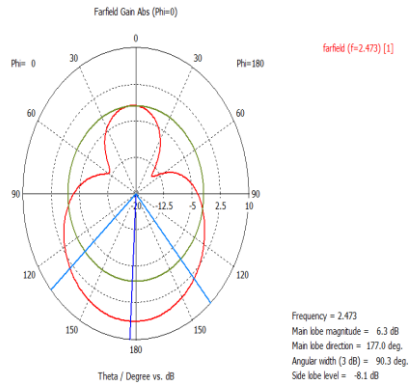


Figure 3-0-114: ZOY plane in polar

Diode 2&3 off-state 3-dimension pattern

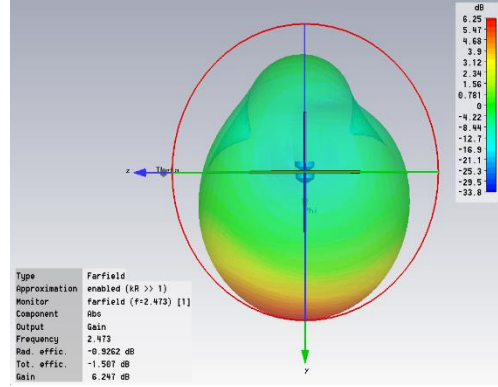


Figure 3-0-115: ZOY plane in 3-D

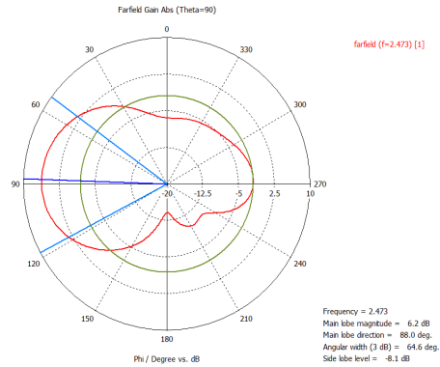


Figure 3-0-116: YOX plane in polar

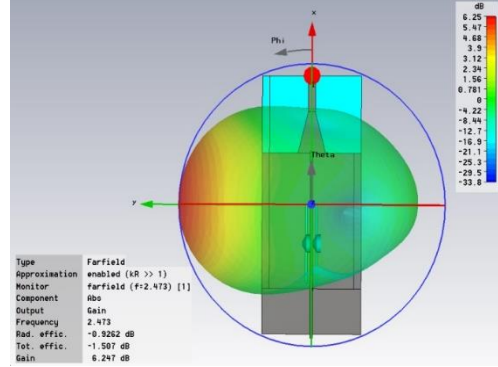


Figure 3-0-117: YOX plane in 3-D

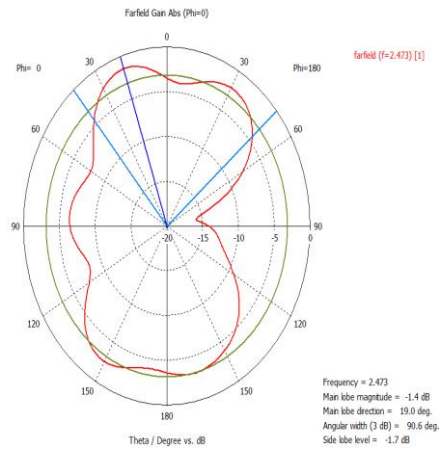


Figure 3-0-118: ZOX plane in polar

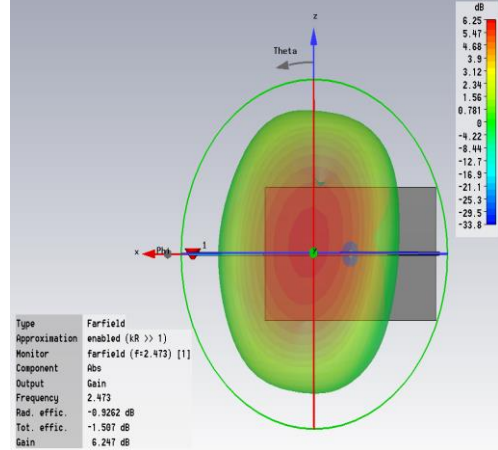


Figure 3-0-119: ZOX plane in 3-D

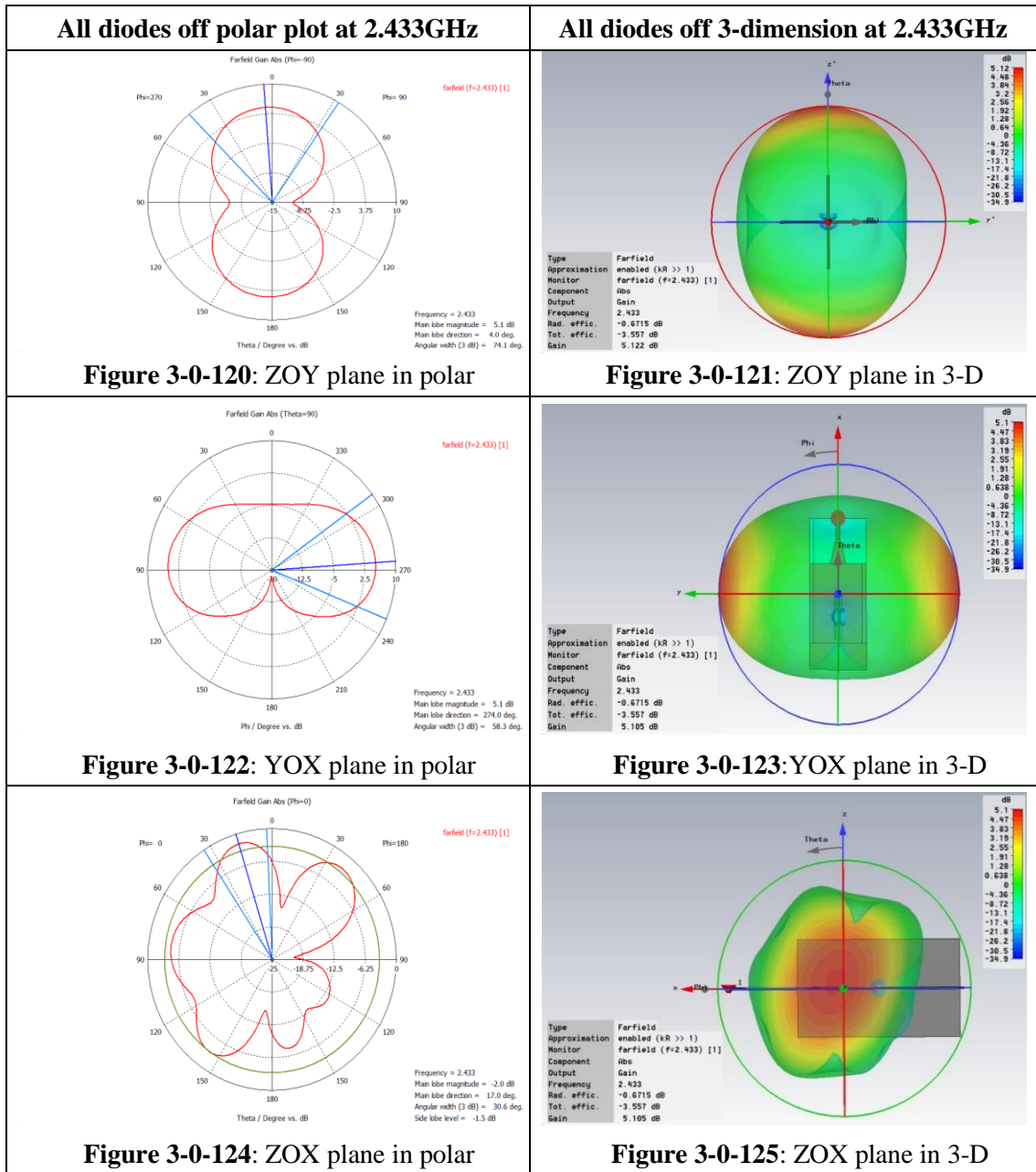


Figure 3-0-120 to Figure 3-0-125 show the farfield results of all-diode off-state at 2.433 GHz. In Figure 3-0-121, the radiation efficiency and the total efficiency are -0.6715 dB and -3.557 dB, respectively. Both efficiency results drop down, especially the total efficiency, as the reflection coefficient S_{1,1} at 2.433 GHz is only -4.223 dB. The mismatched impedance of slots coupled with the unsuitable slot length causes a sharp decrease in the total efficiency. The gain shown in Figure 3-0-121 is 5.122 dB. Even though the previous 2D near-field results show that the maximum E-field is at bottom slots, the bottom slots radiations are guided into the top slots regions because of the in-

phase coupling. Therefore, the direction of farfield main lobe shown in Figure 3-0-120 has a 4-degree deviation towards slot 1 region. In Figure 3-0-122 the farfield null only appears at the antenna front-end, as the Microstrip fringing field mitigates the far-field attenuation at antenna back-end. The direction of local main lobe shown in Figure 3-0-122 has a 4-degree deviation towards input port. The reason, as showed in Figure 3-0-64, is that the backward component of radiation couples with the fringing field. Moreover, as the 3 dB angular width shown in Figure 3-0-120 and Figure 3-0-122 are 74.1 degree and 58.3 degree respectively, the main lobe peak of ZO plane as shown in Figure 3-0-125 is oval in shape, and locates backward at top slot region. Figure 3-0-125 shows the location of main lobe peak, which is in top slot region and slightly offset to input port side. Figure 3-0-124 shows the corresponding polar plot of Figure 3-0-125. The largest side lobe in Figure 3-0-124 locates at the back corner of top reflector, as the fringing field of feed line couples with the scattering E-field at the back corner of the top reflector, as shown in Figure 3-0-51. The smallest side lobe is on the front corner of bottom reflector, which only consists of scattering E-field without being affected by the fringing field. The side lobe at around 85 degree is caused by the fringing field of feed line. Compared with the fringing field in other diode-off states, the fringing field in all-diode off-state is larger because of impedance mismatching. Therefore, the feed line in Figure 3-0-124 has higher-order mode radiation. Figure 3-0-126 to Figure 3-0-131 show the farfield results of all-diode on-state at 2.433 GHz. Figure 3-0-127 clearly shows that all slots do not radiate. The -1.7 dB main lobe in Figure 3-0-126 and the -0.2 dB main lobe in Figure 3-0-128 all suggests that there is not a radiation, but only a leakage. Figure 3-0-129 and Figure 3-0-131 show that the only radiation remaining is from the fringing field of feed line. The fringing field of higher-order mode propagates on the feed line, and couples with the diffraction on the back corner of top reflector. Figure 3-0-130 proves that a strong fringing field can cause the farfield. Overall, the farfield results at 2.433 GHz reach the slot short-circuit requirement, as none of the slots radiates, except the fringing field radiating backward.

All Diodes on polar plot at 2.433GHz

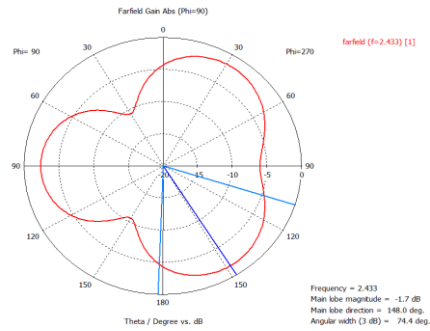


Figure 3-0-126: ZOY plane in polar

All Diodes on 3-dimension at 2.433GHz

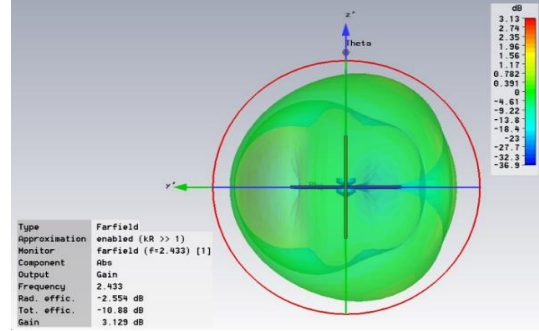


Figure 3-0-127: ZOY plane in 3D

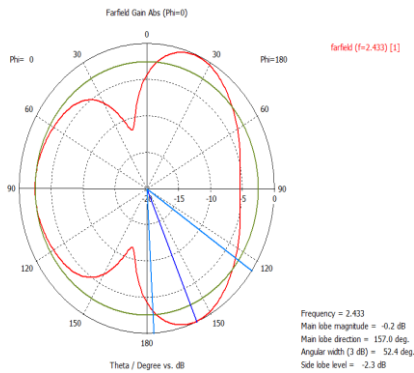


Figure 3-0-128: YOX plane in polar

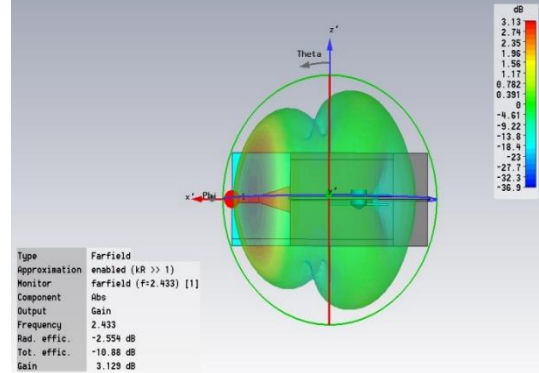


Figure 3-0-129: YOX plane in 3D

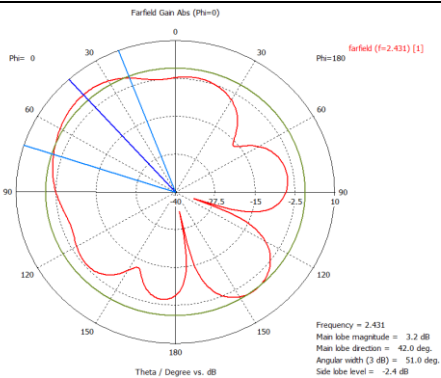


Figure 3-0-130: ZOZ plane in polar

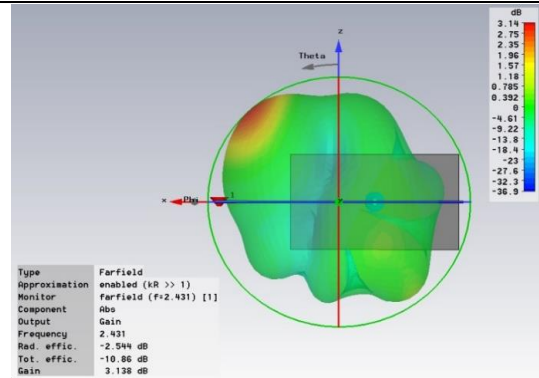


Figure 3-0-131: ZOZ plane in 3D

3.2.5 Conclusion

In this chapter, we have introduced the switching antenna with a four-direction radiation by analyzing the measurement and simulation results. Since both the measured reflection coefficient $S_{1,1}$ results and the measured far-field results are consistent with the simulation results, we can confidently conclude that this four-direction antenna can meet the design requirement. Although the dual-diode off states, all-diode off-state, and the all-diode on-state are not the standard working states of four-direction antenna, the measurement results of these three states still match the corresponding simulation results. The ideal PIN diode should not only have a large enough resistance, not less than 3000 ohms, in reverse bias state, but also have a small enough resistance, not greater than 2 ohms, in forward bias state. Therefore, the performance of PIN diode in the all-diode on-state is the determining factor of farfield pattern and gain. As the reflector wall in the four-direction antenna is only used for single slot radiation, the intrinsic coupling characteristic of dual-slot radiation will be utilized in the six-direction switch antenna which will be worked out in next chapter.

Reference

- [1] Ming-Iu Lai, Tjung-Yu Wu, Jung-Chin Hsieh, Chun-Hsiung Wang and Shyh-Kang Jeng , “Compact Switched-Beam Antenna Employing a Four-Element Slot Antenna Array for Digital Home Applications”, *IEEE Trans. Antennas Propag.*, vol. 56, no. 9, pp. 2929–2936, Sep. 2008.
- [2] Carl B. Dietrich, Jr., Kai Dietze, J. Randall Nealy, and Warren L. Stutzman “Spatial, Polarization, and Pattern Diversity for Wireless Handheld Terminals”*IEEE Trans. Antennas Propag.*, vol. 49, no. 9, pp. 1271–1281, Sep. 2001.
- [3] Nguyen Viet Anh, and Park Seong Ook, “Compact Switched and Reconfigurable 4-ports beam Antenna Array for MIMO applications”, *2011 IEEE MTT-S International Microwave Workshop Series on Intelligent Radio for Future Personal Terminals (IMWS-IRFPT)*, pp. 1–3, 2011.
- [4] Wikipedia, the free encyclopedia, (17 December 2014), “*Mathematical descriptions of opacity*”, [Online]. Available: http://en.wikipedia.org/wiki/Mathematical_descriptions_of_opacity [Accessed: 7th September 2014].

Chapter 4: Six directions switch SIW antenna

Usually, the traditional waveguide antennas only have one radiation direction. In this chapter, a six-direction waveguide antenna with reflectors is presented. Based on the four-direction waveguide antenna, this six-direction antenna is developed by utilizing the intrinsic coupling of dual-slot radiation. This novel antenna is showed as follow.

Figure 4-0-1 and Figure 4-0-2 show top plane and bottom plane of the waveguide, respectively. The white tapes at the two sides of waveguide are used to fix the DC power wires. As shown in Figure 4-0-3, the 6-direction antenna is smaller than the 4-direction one. Also, the 6-direction antenna has been improved to work at both single-diode off-state and dual-diode off-state. The dimension of the 5 GHz antenna is less than half of the dimension of 2.4 GHz antenna. Due to lack of suitable inductor, the measurement records of the 6-direction switch antenna working at 5GHz will not be shown in this thesis.

Figure 4-0-4 shows the parameters of CST simulation antenna model. Figure 4-0-5 shows the bottom plane of CST simulation antenna model. Table 4-1 summarizes the values of all parameters in the simulation antenna model. Figure 4-0-6 shows the drawing dimensions of the fabricated antenna based on the fixed reference point. Figure 4-0-7 shows the drawing dimensions of fabricated reflection wall.



Figure 4-0-1: Top surface of antenna



Figure 4-0-2: Bottom surface antenna

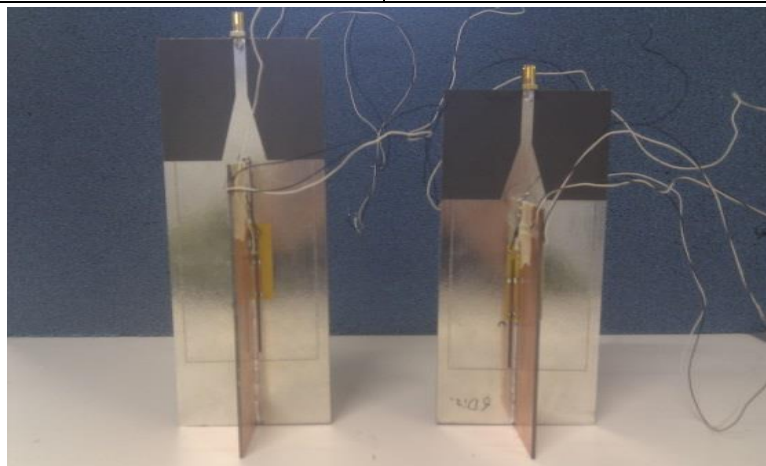


Figure 4-0-3: Left: 4-direction antenna. Right: 6-direction antenna

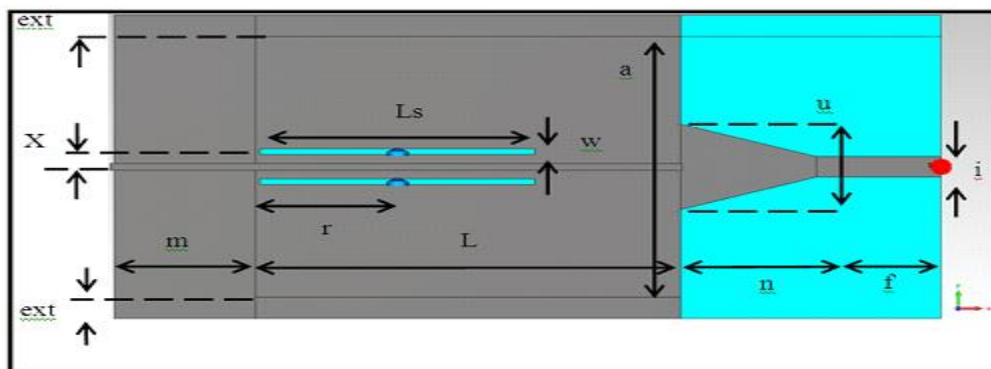


Figure 4-0-4: The top view of simulation antenna model

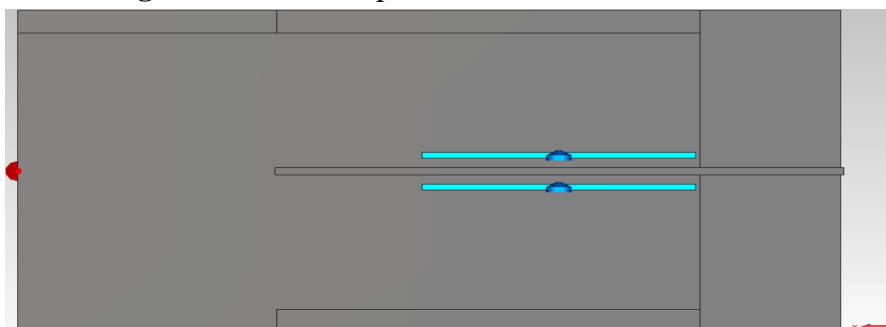


Figure 4-0-5: Bottom view of simulation antenna model

Parameters name	Length/ Unit: mm	Description
L	75	Length of waveguide antenna part= $r*3$
a	61	Waveguide width
b	1.575	Thickness of waveguide substrate
T	0.07	Thickness of surface copper
Ls	48.5	Slot length
r	25	One quarter lambda wavelength
ext	5	PEC wall width
i	4.75	Input port width
n	24	Length of Taper
u	20	Width of Taper
f	22	Length of Microstrip feedline
w	1.3	Slot width
m	25	Front PEC extension $L-r*2$
x	3.5	slot offset from waveguide center line to edge

Table 4-1: parameters sizes of simulation model

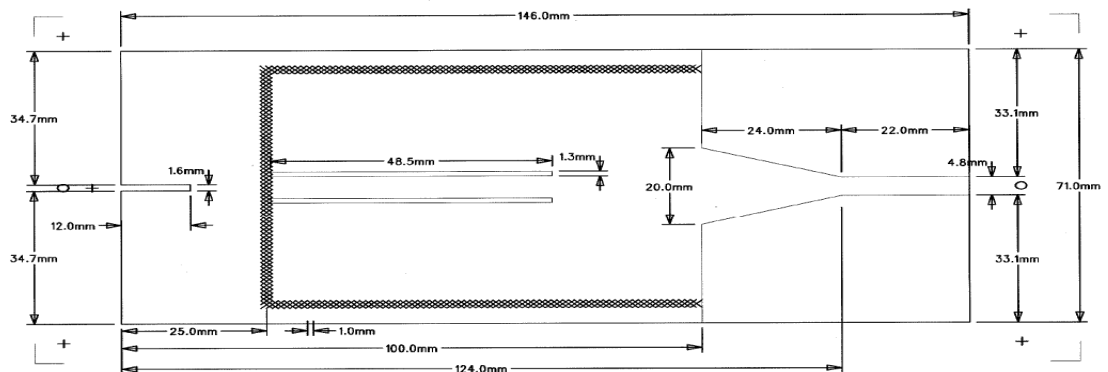


Figure 4-0-6: sizes of fabrication antenna drawn by Andy Farrel

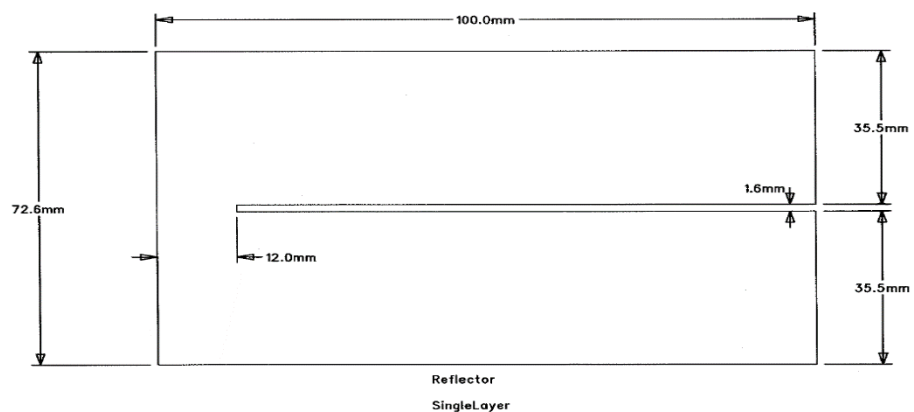


Figure 4-0-7: Reflector sizes of fabrication antenna drawn by Andy Farrel

4.1 Design idea:

Since the slot impedances are different between the off states of dual-diode and single-diode, there is a problem to make these two types of off states work at the same frequency. The slot impedance will decrease 50% when two slots are radiating simultaneously, as the equivalent circuit of these two longitudinal slots are shunt. Without changing the external structure or combining any additional electronic element, the easiest solution is to adopt the intermediate value of the impedance to make the antenna work at both types of states.

By using the Kraus formula [3.], we can easily derive the relation between the reflection coefficient $S_{1,1}$ and the load impedance, as shown in Figure 4-0-8. The equations are shown as follow:

For single-diode switch-open state:
$$\rho = \frac{Z - Z_0}{Z + Z_0} = S_{1,1}$$

For dual-diode switch-open state:
$$\rho = \frac{(Z/2 - Z_0)}{(Z/2 + Z_0)} = S_{1,1}$$

The value of load impedance Z is set between 1 ohm and 200 ohms. The characteristic impedance of the line Z_0 is set at 50 ohms, which means that the lossless line is only with pure resistance. Thus, the reflection coefficient ρ plotted in decibel unit is transformed from linear. The transformation equation is $20 \cdot \log_{10}(\text{abs}(\rho))$, where the abs. means absolute value function.

In Figure 4-0-8, the $S_{1,1}$ curve of single-diode off-state is showed by the blue line, and the $S_{1,1}$ curve of dual-diode off-state is showed by the green line.

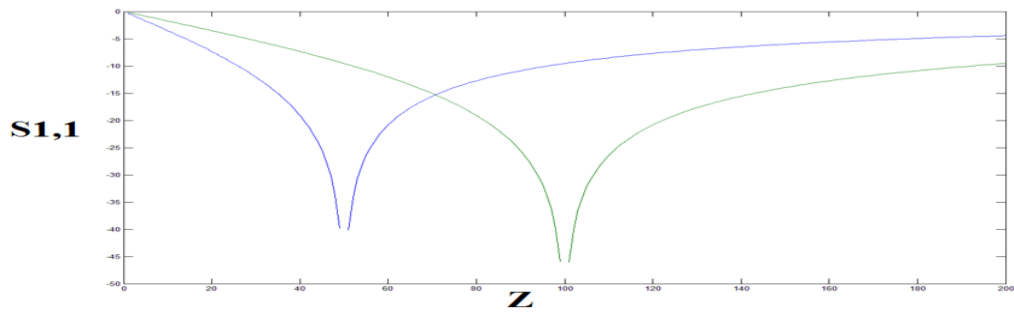


Figure 4-0-8: Deduce $S_{1,1}$ value of two diodes in off-state

For the parts of curves below the -10 dB, Figure 4-0-8 shows that most of the $S_{1,1}$ results of single-diode off-state locate at the low impedance range. But most of $S_{1,1}$ results of dual-diode off-state locate at the high impedance range. The only intersection between the two curves is at around 70-ohm with a $S_{1,1}$ value of -15 dB, which still can reach the design requirement. As this intersection point does not represent the optimum $S_{1,1}$, the evaluation criterion of slot impedance will no longer relates to the optimum value. The search method of slot impedance is demonstrated in Figure 4-0-9. The first plot in Figure 4-0-9 shows that the intersection point of $S_{1,1}$ curves must satisfy that $Z = \sqrt{2}Z_0$. The second plot shows the $S_{1,1}$ and $S_{2,1}$ curves of single-diode off-state. The intersection points between the two curves and the grey line are the $S_{1,1}$ and $S_{2,1}$ results satisfying the condition of $Z = \sqrt{2}Z_0$. The third plot shows the $S_{1,1}$ and $S_{2,1}$ curves of dual-diode off-state. Therefore, given $Z = \sqrt{2}Z_0$, the $S_{1,1}$ curves of the two states intersected.

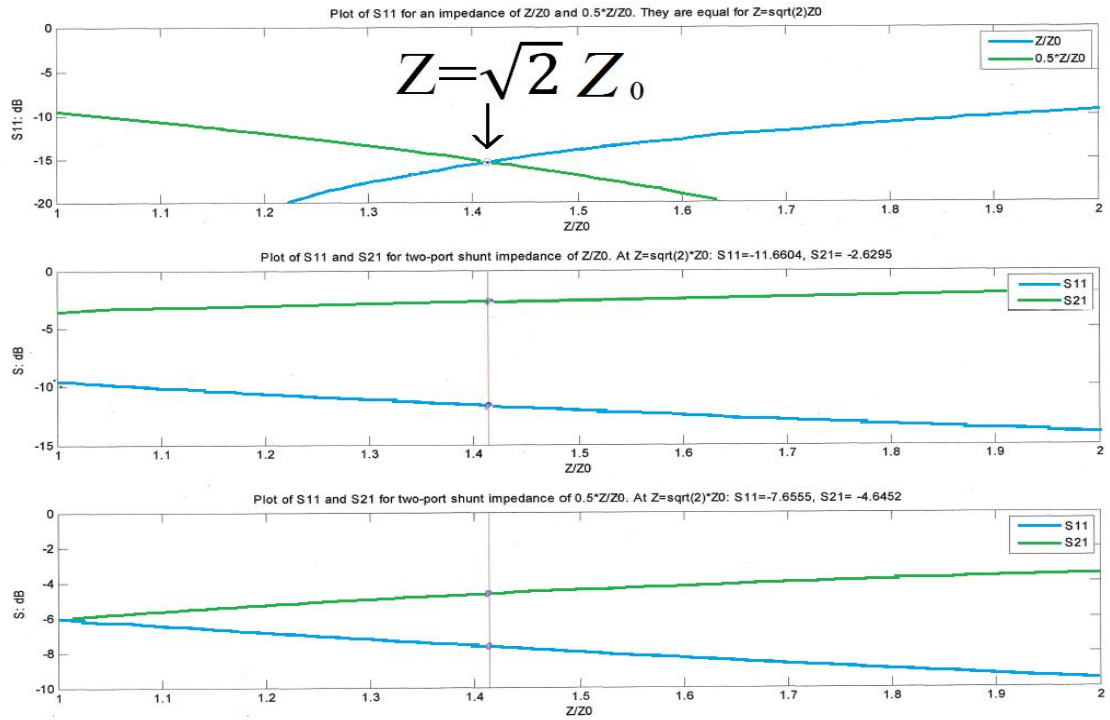


Figure 4-0-9: S1,1 intersection point of two diode-off states

4.2 The 1-D results:

Figure 4-0-10 to Figure 4-0-13 show the comparison results of measurement and simulation for the four single-diode off states. The measured reflection coefficient S1,1 in these four graphs are all below -15dB which is the S1,1 value at the intersection point. Although the measurements results seem to be better than the theoretical value, the seemingly improved S1,1 results are caused by the additional impedance of overlap circuit and wires, which, in fact, will have negative impact on slot radiation. Table 4-2 and Table 4-3 show that the off states of diode 1 and diode 4 have the same S1,1 result at -19.82 dB; the off states of diode 2 and diode 3 have similar values at -29.91 dB and -24.08 dB, respectively. As diode 1 and diode 4 locate at one side of the reflector and diode 2 and diode 3 locate at another side of the reflector, the leaky waves and radiations of slots on the same side of the reflector are in-phase, and couple with each other. Therefore, slots on

the same side of the reflector will affect each other. As a result, when calculating the impedance of a particular radiating slot, the impedance of the slot of which the leaky wave is in-phase with the radiation of the current slot should be included. The bandwidth results showed in Table 4-2 and Table 4-3 also have correspondance relationship. Therefore, the switch-open states of diode 1 and diode 4 have the same bandwidth at 70 MHz; and the switch-open states of diode 2 and diode 3 have the same bandwidth at 80 MHz.

The comparisons of the $S_{1,1}$ results of single-diode off states between 4-direction antenna and 6-direction antenna, demonstrate that the 6-direction antenna has some improvements. The first improvement is that the noise around 2.2 GHz reduces 5 dB. As the wires bonding points at metal pads of overlay do not have any shielding cover, the waveguide surface wave is guided along the DC wires. Since the wires were found to affect the noise response in the 4-direction antenna, 6-direction antenna reduces the length of wires from 676mm to 325mm. But the shortened wires will increase the difficulty in antenna installation. The second improvement is that the response frequency in the measurement of the 6-direction antenna is kept constant at 2.480 GHz, which reduces the frequency difference between simulation and measurement. For example, the 4-direction antenna has one measurement response frequency at 2.480 GHz for top slots and another at 2.470 GHz for bottom slots. The frequency difference between simulation and measurement in the 4-direction antenna is 42 MHz, but the 6-direction antenna only has 22 MHz difference. Therefore, the actual performance of 6-direction antenna is consistent with the simulation prediction. The third improvement is that the measured bandwidth of the 6-direction antenna has been increased to 80 MHz, whereas the measured bandwidth of the 4-directions antenna is 57 MHz. This is because the impacts of overlay circuit and wires are reduced in the single-diode switch-open states of six-direction antenna.

Overall, the reflection coefficient $S_{1,1}$ results of the single-diode off states of the 6-direction antenna are all improved, compared with those of the 4-direction antenna. Especially the noise problem is alleviated a lot, for no noise below -6 dB. Yet, the $S_{1,1}$ results of diode 1 state and diode 4 state have three small noises at 1.84 GHz, 2.2 GHz and 2.84GHz. Nevertheless, all these unwished resonant modes in practice can be easily filtered by the back-end system circuit. Therefore, the reflection coefficient $S_{1,1}$ results of the four single-diode states of the 6-direction antenna all meet the design requirement.

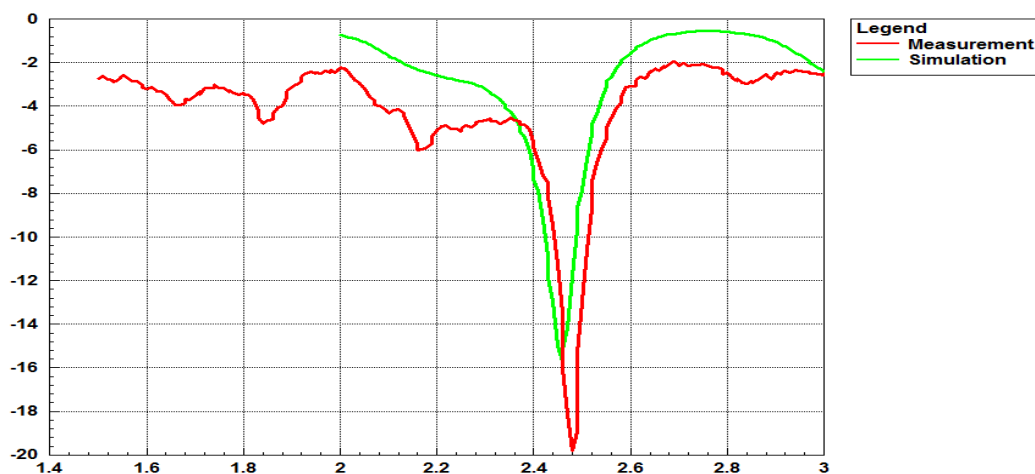


Figure 4-0-10: $S_{1,1}$ of diode 1 off-state

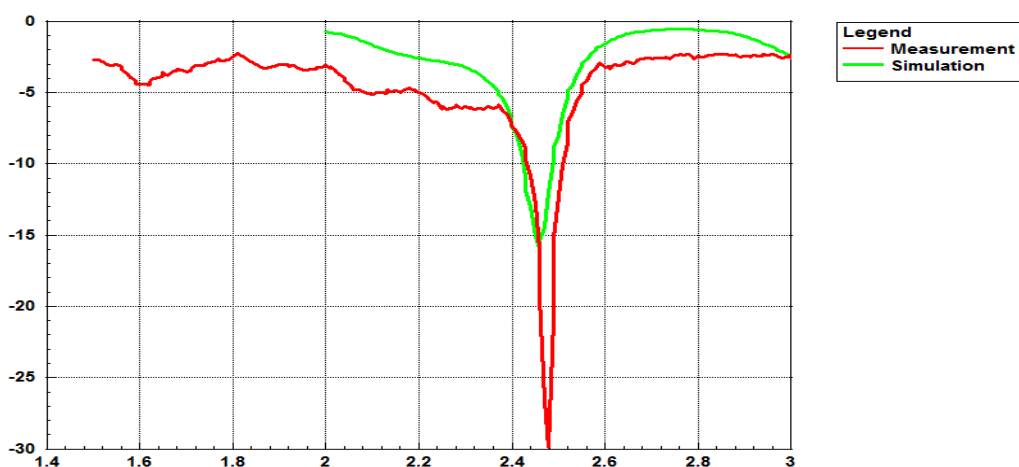


Figure 4-0-11: $S_{1,1}$ of diode 2 off-state

Top slot diode 1 off-state	Simulation results	Measurement results
Reflection coefficient	-15.76 dB	-19.82 dB
Working frequency	2.46 GHz	2.48 GHz
Bandwidth	63.1 MHz	70 MHz
Bottom slot diode 2 off-state	Simulation results	Measurement results
Reflection coefficient	-15.98 dB	-29.91 dB
Working frequency	2.46 GHz	2.48 GHz
Bandwidth	63.9 MHz	80 MHz

Table 4-2: S_{1,1} results of simulation and measurement for diode 1 and diode 2

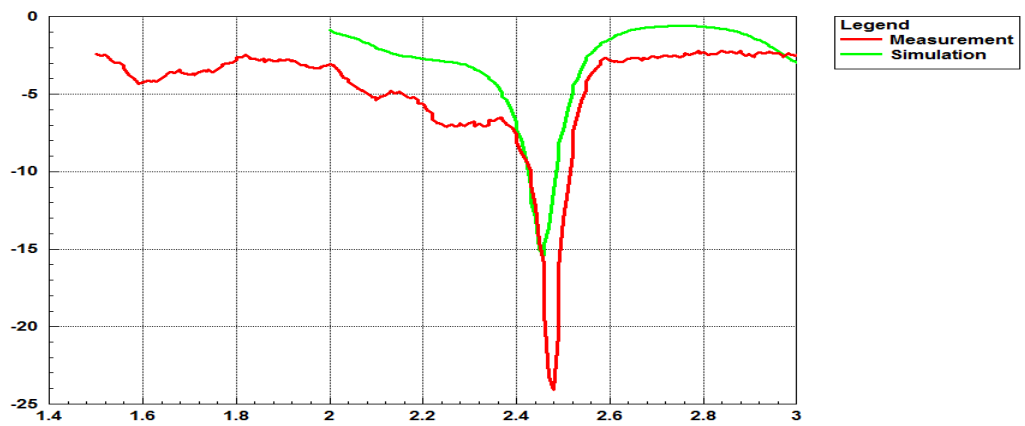


Figure 4-0-12: S_{1,1} of diode 3 off-state

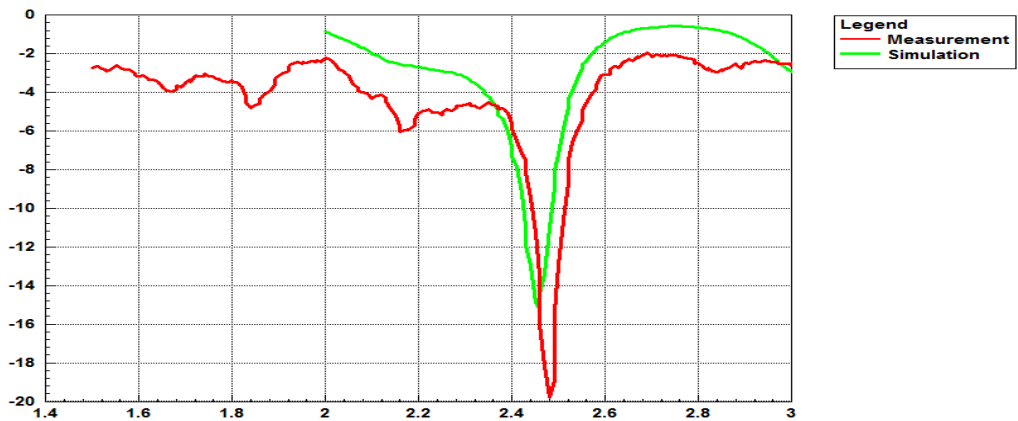


Figure 4-0-13: S_{1,1} of diode 4 off-state

Top slot diode 3 off-state	Simulation results	Measurement results
Reflection coefficient	-15.56 dB	-24.08 dB
Working frequency	2.46 GHz	2.48 GHz
Bandwidth	60.6 MHz	80 MHz
Bottom slot diode 4 off-state	Simulation results	Measurement results
Reflection coefficient	-15.34 dB	-19.82 dB
Working frequency	2.46 GHz	2.48 GHz
Bandwidth	59.8 MHz	70 MHz

Table 4-3: S1,1 results of simulation and measurement for diode 3 and diode 4

4.3 Near-field range 2-D results:

Since the single-slot radiation of 6-direction antenna is the same with the one of 4-direction antenna, here only the diode 2 off-state will be discussed. For convenience, in the following E-field explanation, the waveguide will be divided into four regions. As the slot size is unified and the slot positions are symmetric, the four regions can be sorted out into two groups by the relative position of these four slots to the reflector. One group consists of diode 2 and diode 3, both of which are at the left side of reflector; another group consists of diode 1 and diode 4, which are at the right side of the reflector, as showed in Figure 4-0-14.

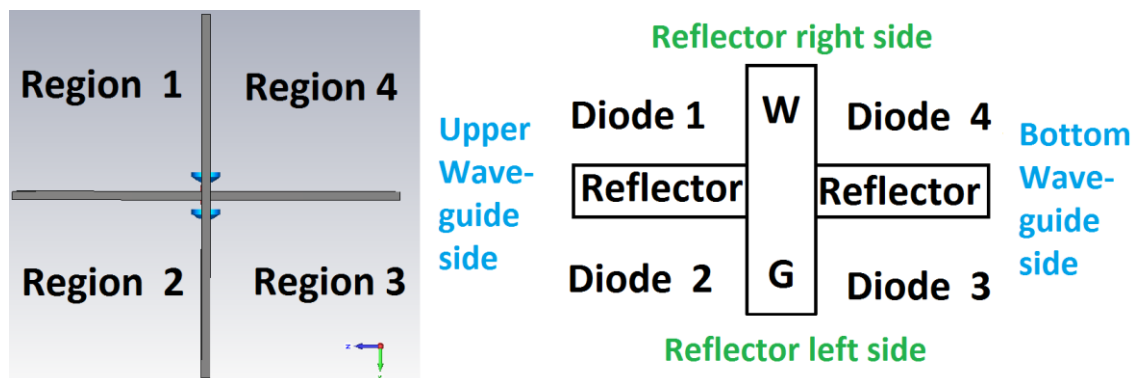


Figure 4-0-14: Definitions of region and group based on antenna installation in measurement

The common characteristic of the E-field distributions in these four single-diode off states is summarized here. When one of the slots is radiating, the short-circuited slot at the same side of the reflector, which is symmetric with the radiating slot about the waveguide plane, usually has the largest leaky wave which is anti-phase with the radiation. But the leaky E-fields from the two short-circuited slots at the opposite side of the reflector are in-phase with the radiation. This phenomenon can be easily illuminated by the vector arrow graph. For example, Figure 4-0-15 is about the diode 2 switch-open state. The logarithmic scaling of E-field strength showed in Figure 4-0-15 has been enlarged $\log_{10} 1000$ times to show the arrows. The radiation E-field of slot 2 has obvious diffractions in all of the other three short-circuited slot regions.

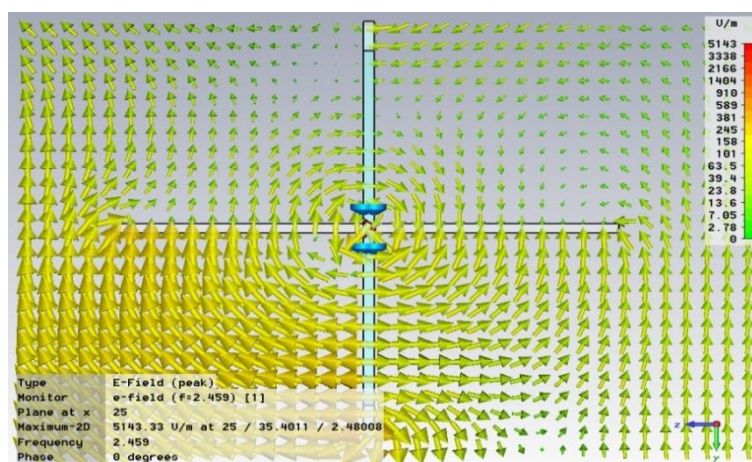


Figure 4-0-15: ZOY plane of vector arrow when diode 2 in off-state

As shown in Figure 4-0-15, the largest diffraction of slot 2 radiation trends to slot 3 region. The direction of radiation E-field arrows changes 180 degree at the waveguide surface of slot 3 region. Therefore, the diffraction and leaky wave in slot 3 region are anti-phase around the waveguide edge but in-phase around the bottom reflector edge. Compared with other leaky waves, the leaky wave in slot 3 region is the largest. As only a minor part of the diffraction is cancelled out by the leaky wave in slot 3 region, the major part of the diffraction propagates into slot 4 region. In slot 4 region, the diffraction around the bottom-plane edge of waveguide is larger than the one around the edge of bottom reflector. As the leaky wave in slot 4 is the smallest and anti-phase with diffraction, the diffraction

E-fields is able to impede the outward leaky wave from propagating along the bottom plane of waveguide and the bottom reflector surface. Therefore, the dominant E-field in slot 4 region is diffraction. The rest of the diffraction finally terminates around the top-plane edge of waveguide in slot 1 region. The leaky wave of slot 1 is anti-phase with the rest of the diffraction around the waveguide edge, but is in-phase with the diffraction around the edge of top reflector. Although the leaky wave in slot 1 is intermediate, the strong diffraction from slot 2 region enhances the in-phase leaky wave of slot 1.

4.4 Far-field measurement results for single diode open state:

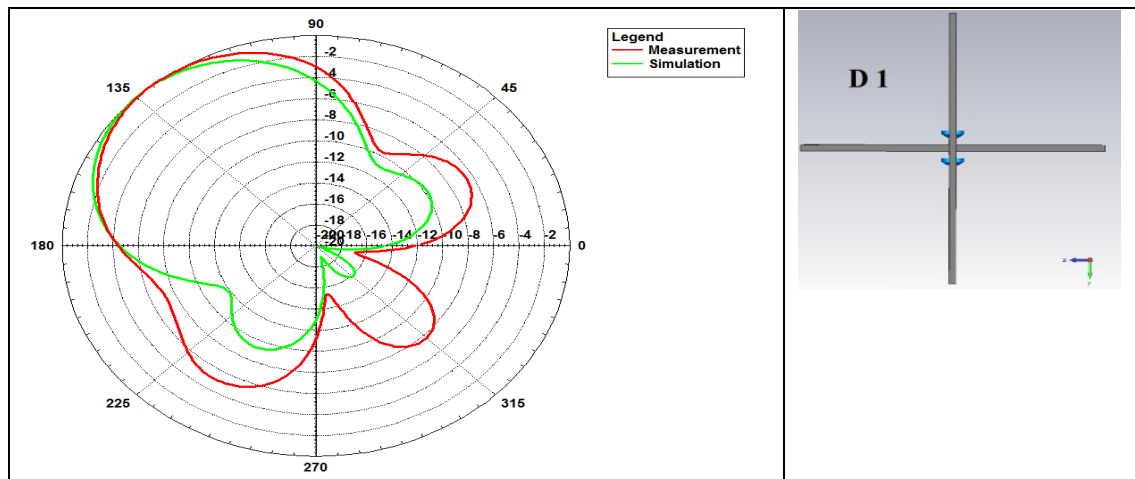


Table 4-0-4: Measurement and simulation results when diode 1 off

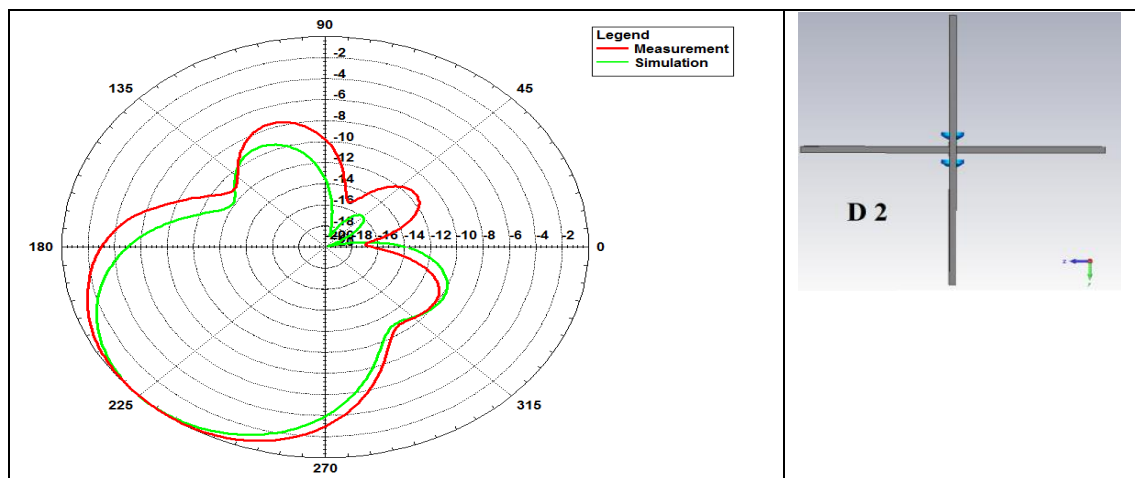


Table 4-0-5: Measurement and simulation results when diode 2 off

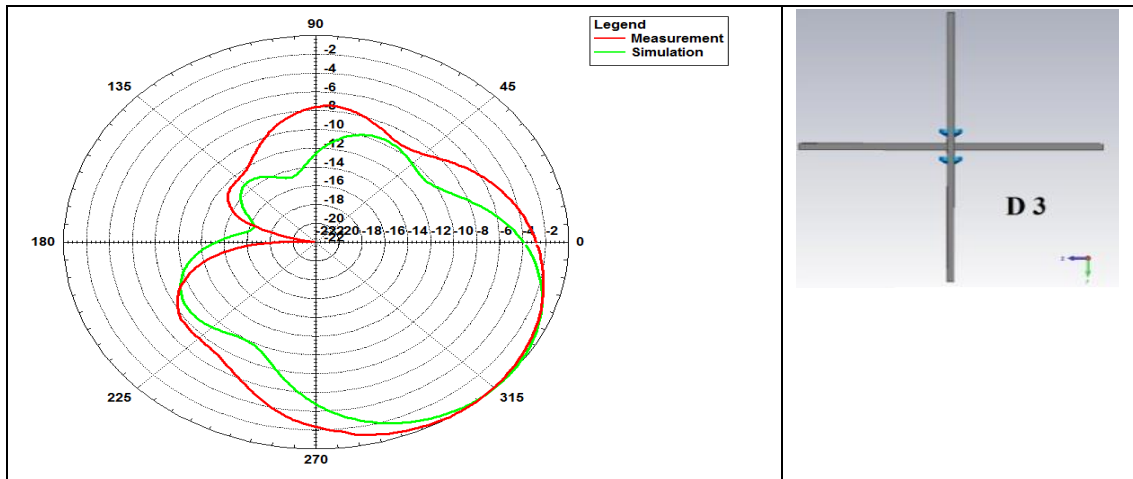


Table 4-0-6: Measurement and simulation results when diode 3 off

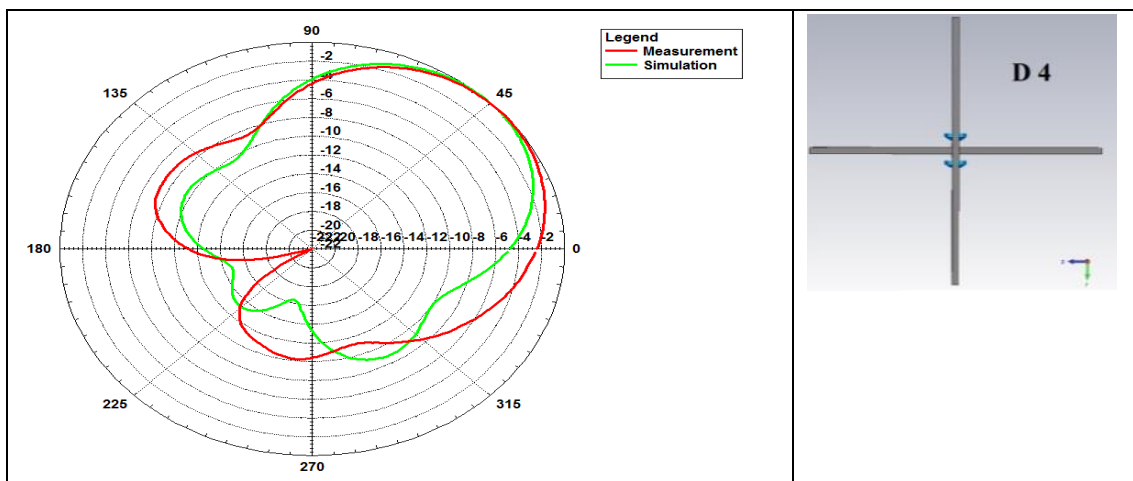


Table 4-0-7 : Measurement and simulation results when diode 4 off

All slots work at 2.48 GHz	Slot 1	Slot 2	Slot 3	Slot 4
Simulation Gain	5.6 dB	5.6 dB	5.6 dB	5.6 dB
Measurement Gain	6.0 dB	4.6 dB	3.8 dB	3.0 dB

Table 4-0-8: Measurement of gain

Table 4-0-4 to Table 4-0-7 show the comparison of farfield results between measurement and simulation for the four single-diode off states. All of the four measurement results are consistent with the corresponding simulation results. The slight differences in partial patterns are caused by the increased strength of diffraction, back lobe, and side lobes, which can dissipate radiation energy. Therefore, the measurement gains are smaller than the ones of simulation. Furthermore, the unstable performance of reverse bias diodes also affect the measured gains. The four far-field measurement patterns can be divided into

two kinds: the first kind is about the top-plane slots; and the second kind is about the bottom-plane slots. For all of the four measurement patterns, the 3 dB beamwidth is wider than the simulation result, 75.1 degree. Since part of the radiation E-field is guided along the wires, the reflector and waveguide cannot fully concentrate radiation. Furthermore, the side lobes of measurement are larger than those of simulation. As the performance of PIN diodes at such a high frequency is unstable, the actual resistance of these forward bias diodes is higher than the design resistance, 2 ohms. Moreover, as the four overlaps are manually pasted on the slots, the manual errors will bring in additional impedance.

As the farfield results of slot 1 radiation and slot 2 radiation shown in Table 4-0-4 and Table 4-0-5 are almost identical, the slot 2 radiation is used as an example to analyze the farfield measurements of top-plane slots. Since part of the radiation is conducted away by wires, the strength of diffraction observed in measurement is larger than the one of simulation. The largest side lobe, as shown in Table 4-0-5, locates at slot 1 region, where the largest diffraction also locates. Although the intensity of leaky wave in slot 1 is moderate, this leaky wave is enhanced by the in-phase diffraction. In addition, slot 3 has the largest leaky wave, which is anti-phase with diffraction. As the diffraction also increases in slot 3 region, this intensive diffraction reduces the leaky wave strength. Therefore, the measured side lobe in slot 3 region decreases a bit. As, for slot 4 region, the resistance of forward bias diode is over 2 ohms, the intensity of back lobe increases. Moreover, as waveguide ground plane does not have Microstrip fringing field, the back lobe, without being affected by coupling, can focus on one direction. As the leaky wave of slot 4 is anti-phase with diffraction, the slot 4 region has two unequal nulls, of which the shapes depend on the diffraction intensity. In theory, the main lobe direction of slot 2 should point to 225 degree, but in the simulation, the direction points to 226 degree. This is because the slot is offset from the central line of waveguide, which causes the reflection

distance at the top reflector to be longer than the one at the waveguide top plane. Therefore, the main lobe direction of slot 2 is shifted 1 degree downward to the waveguide plane.

Table 4-0-6 and Table 4-0-7 show the farfield patterns of bottom-plane slots. As the two farfield results are nearly the same, the diode 4 off-state is used as an example to analyze the measurement results. In Table 4-0-7, the only side lobe locating at slot 1 region is caused by the leaky wave anti-phase with diffraction. Though the measured side lobe has the same pattern with the simulation one, the intensity of the measured one is stronger. Therefore, the forward bias diode 1 must have a resistance over 2 ohms to counteract the diffraction. The measured back lobe in slot 2 region only has one null, which is caused by the intensive diffraction from slot 1 region. As the back lobe is in-phase with the strong diffraction from slot 3 region, the back lobe is significantly enlarged by merging with the side lobe of slot 3 region. The dominant E-field in slot 3 region is diffraction. The strong diffraction, in the measurement, changes the E-field distribution, the resulted E-field distribution, therefore, is different from the one given by the simulation prediction. As the leaky wave of slot 3 is in-phase with diffraction, the leaky wave is guided into slot 2 region by coupling with the strong diffraction. As the strong diffraction appears only when the radiating slot is a bottom-plane one, the main reason should be the impedance mismatching between feedline and bottom slots. This problem is expected, as the impedance has been compromised for the dual-slot radiation. This insufficient radiation of bottom slots causes a strong diffraction which then will be guided along wires and spread over the other slot regions. Furthermore, as the Microstrip fringing field at the waveguide top plane couples with diffraction and leaky wave, the forward bias diode 1 and diode 2 cannot effectively restrain these fields from combining. Once the forward bias diodes have a resistance over 2 ohms, the diffraction problem, in turn, will be aggravated.

4.5 The 1-D results of multi-diodes off states

For the 6-direction switch antenna, there are six possible combinations for the dual-diode off-state, and four possible combinations for the triple-diode off-state. But the design working states are dual-diode 1 and 4 off and dual-diode 2 and 3 off as summarized in Table 4-0-9. The 6-direction antenna works at both single- and dual-diode off states at the expense of sacrificing impedance matching. All $S_{1,1}$, as a result, are set to -15 dB. But, the measurement results of reflection coefficient $S_{1,1}$ and bandwidth as shown in Table 4-0-9 are better than the theoretical value. Compared with the corresponding results of 4-direction antenna, the $S_{1,1}$ results of 6-direction antenna are improved over 6 dB in simulation and maximum 8dB in measurement. Based on the fact that the $S_{1,1}$ result in measurement is better than the one in simulation, the energy efficiency in measurement presumably should be also better than the simulation efficiency which is over 80%. The bandwidth of 6-direction antenna increases about 45MHz in simulation and about 20MHz in measurement. Therefore, the intermediate-value method of reflection coefficient $S_{1,1}$ can solve the impedance matching problem.

In the single-diode off states of 6-direction antenna, the measured $S_{1,1}$ results of slot 1 and slot 4 are worse than the ones of slot 2 and slot 3. But, the measured $S_{1,1}$ result of dual-diode 1 and 4 off-state in Table 4-0-9 is -20.33 dB, which is 3.3 dB better than the one of dual-diode 2 and 3 off-state. Based on the comparisons of $S_{1,1}$ results, the diodes 1 and 4 are more suitable for working in dual-diode off-state, and the diode 2 and diode 3 are more suitable for single-diode off-state. As the parasitic effects of overlap circuit and wires bring in additional reactance to the slot impedance, all the measurement $S_{1,1}$ results, unlike the simulation ones, cannot be kept at around -15 dB. As manual installation limits the accuracy of overlap positioning, part of the slot might be covered by the metal film of

overlap. Moreover, the redundant solders at joints might affect the E-field distribution over slots. Therefore, the conditions of overlap circuit is difficult to predict in the simulation model. This empirical analysis can be verified by directly replacing the overlaps. As overlap placement inevitably has slight error, each overlap will locate at a different position. The $S_{1,1}$ results of 6-direction antenna shown here are based on the last placing overlaps and diodes. Therefore, for some particular slots, these $S_{1,1}$ results might not be the best. Since both in simulation and measurement, the differences of resonance frequency between single-diode off-state and dual-diode off-state are 20 MHz, the results between simulation and measurement are comparable, despite the fact that the resonance frequencies in simulation and measurement are different.

Table 4-0-10 summarizes the results of simulation and measurement for all-diode off-state and all-diode on-state. As the impedances are mismatched among the four slots and feed line, all the reflection coefficient $S_{1,1}$ results of simulation and measurement cannot reach the design requirement, -10 dB level. Nevertheless, these two diodes states are not of the design goal. In both simulation and measurement, the all-diode off-state shows two frequency modes. Since the impedances between top-plane and bottom-plane slots are different, the strengths of radiations on the two waveguide planes are different. Therefore, at different resonance frequencies the strongest radiation locates at different planes of waveguide. Overall, the $S_{1,1}$ curves of measurement are similar to the $S_{1,1}$ curves of simulation. Therefore, these measurement results are acceptable. In all-diode on-state, the response frequency is around 2.2 GHz, which is caused by the leaky waves. Two more frequency samples are taken. One is the resonance frequency of single-diode off-state at 2.48 GHz; another is the resonance frequency of dual-diode off-state at 2.5 GHz. For the all-diode on-state, the measurement $S_{1,1}$ curve is similar to the simulation one in shape, but the measurement results in general show larger response than the simulation ones. Actually this response is noise, which is enlarged by the wires and surface overlap. In

practice, noise response can be eliminated by the filter of the back end system. Therefore, these measurement results are acceptable.

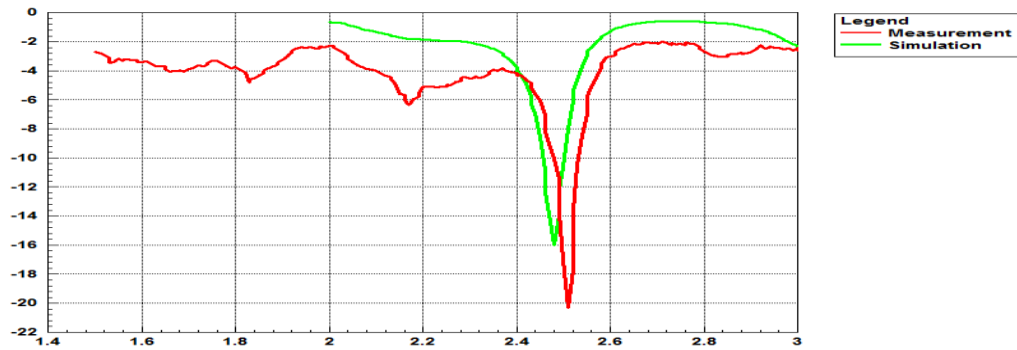


Figure 4-0-16: S1,1 of diodes 1 & 4 switched-off

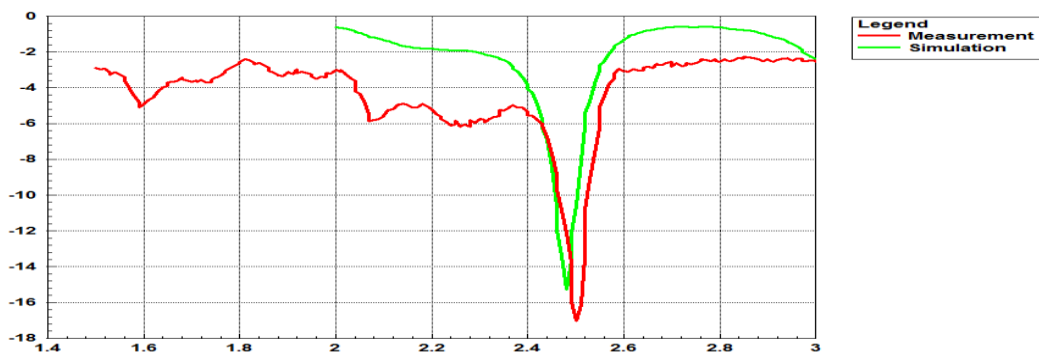


Figure 4-0-17: S1,1 of diode 2 & 3 switched-off

Diodes 1 & 4 switched-off	Simulation	Measurement
Reflection coefficient S1,1	-16.00 dB at 2.48 GHz	-20.33 dB at 2.5 GHz
Bandwidth	45.60MHz	60 MHz
Energy Balance	0.16	
Diode 2 & 3 switched-off	Simulation	Measurement
Reflection coefficient S1,1	-15.30 dB at 2.48 GHz	-17.04 dB at 2.5 GHz
Bandwidth	44.90 MHz	60 MHz
Energy Balance	0.17	

Table 4-0-9: Simulation and measurement data of diodes 1&4 off and diodes 2&3 off

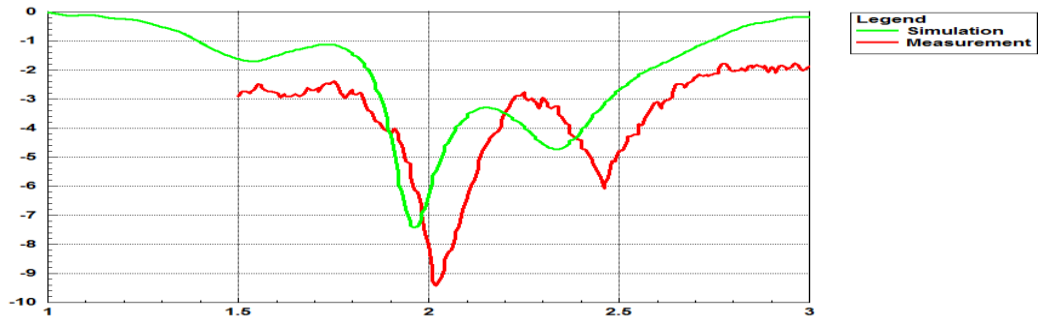


Figure 4-0-18: S1,1 of all diodes switched-off

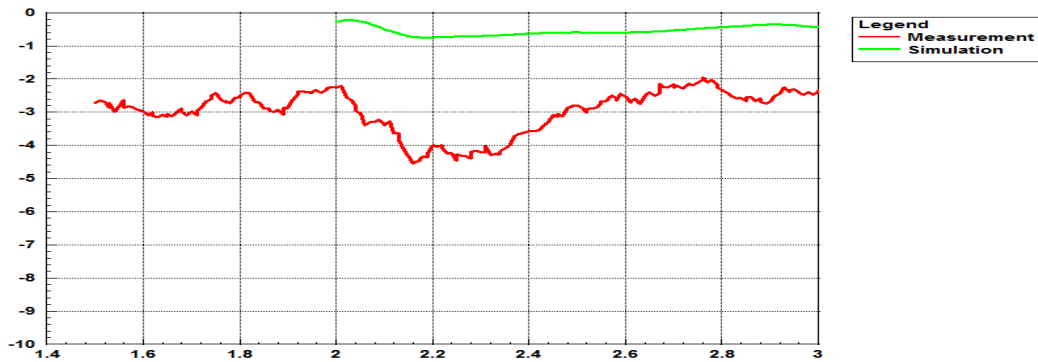


Figure 4-0-19: S1,1 of all diodes switched-on

All diodes switched-off	Simulation	Measurement
First S1,1 result with frequency	-7.439 dB at 1.964 GHz	-9.439 dB at 2.02 GHz
Energy Balance	0.427	
Second S1,1 result with frequency	-4.737 dB at 2.336 GHz	-6.079 dB at 2.455 GHz
Energy Balance	0.580	
All diodes switched-on	Simulation	Measurement
First S1,1 result with frequency	-0.746 dB at 2.192 GHz	-4.545 dB at 2.155 GHz
Energy Balance	0.918	
Second S1,1 result with frequency	-0.593 dB at 2.48 GHz	-2.853 dB at 2.485 GHz
Energy Balance	0.934	
Third S1,1 result with frequency	-0.592 dB at 2.5 GHz	-2.795 dB at 2.5 GHz
Energy Balance	0.934	

Table 4-0-10: Simulation and measurement data of all-diode off and on states

4.6 2-D near field results of multi diodes off and on states

As the all-diode off-state has been introduced in the case of 4-direction antenna and the corresponding $S_{1,1}$ results of 6-direction antenna do not reach -10dB, the all-diode off-state will not be shown here again. Figure 4-0-20 and Figure 4-0-21 show the YOZ cut-plane E-field distribution in dual-diode 1 and 4 off-state and the dual-diode 2 and 3 off-state, respectively. The E-field distributions shown in these two figures are identical. Although the intrinsic difference between the impedances of top slots and bottom slots cannot be eliminated, the intermediate-value method balances the radiation intensities of top-plane slots and bottom-plane slots. Therefore, the impedance difference between the top-plane slots and bottom-plane slots is decreased. As the coupling radiations are equalized, the diffraction at the reflector edges is much smaller than those in single-diode off states. In addition, the leaky wave of bottom slots decays slowly compared with the top slot ones. As the bottom plane of waveguide has a larger metal surface area than the top plane, the E-field of bottom slots is stronger than the one of top slots whatever in radiation or in leaking states. Figure 4-0-22 shows the YOZ cut-plane E-field in all-diode on-state at 2.48 GHz, the response frequency of single-diode off-state. The E-field strength in Figure 4-0-22 is only 5% of the intensity of single-diode off-state. Furthermore, Figure 4-0-22 has scattering only at the top reflector edge. This is because the coupling E-fields of diffraction and Microstrip fringing field enhance the scattering. Since between 2.35 GHz and 2.75 GHz, the scattering intensity decreases as the frequency increases, the leaky wave of the all-diode on-state should also decrease. Therefore, the all-diode on-state meets the design requirement.

Figure 4-0-23 and Figure 4-0-24 show the ZOY cut-plane E-fields for dual-diode 1&4 off-state and dual-diode 2&3 off-state, respectively. E-field patterns shown in the graphs are

identical. The common feature is that the radiations from top slot and bottom slot are symmetric, and the diffractions appear at the four corners of two reflectors. As the Microstrip fringing field couples with diffraction at the back corner of top reflector, the diffraction strengths are uneven at the two corners of top reflector. The radiation intensities of bottom slots in these two graphs are slightly larger than the ones of top slots. Figure 4-0-25 and Figure 4-0-26 show the ZOY cut-plane E-field in all-diode on-state at 2.48 GHz. Both graphs show that only the two corners of top reflector have weak scattering E-fields. The back corner of top reflector has a stronger scattering E-field, which is enhanced by Microstrip fringing field. These four slots only have leaky waves in higher-order mode, even the fringing field of feedline operates at higher-order mode as well.

For observing the radiation tendency at the horizontal plane, Figure 4-0-27 and Figure 4-0-28 show the YOY cut-plane E-fields of dual-diode 1 and 4 off-state, at the top surface and the bottom surface of waveguide, respectively. Figure 4-0-29 and Figure 4-0-30 show the E-field distributions of dual-diode 2 and 3 off-state at the same cut-planes. The strongest radiation in each of the four graphs always locates at the bottom slot region. This feature again proves that the radiations of bottom slots are slightly stronger than the top slots ones. Furthermore, the radiations of top slots in these four graphs all slightly backward couple with the fringing field of feedline, but the radiations of bottom slots straightly leave the waveguide. Overall, both dual-diode off states have identical E-field distributions on the top plane and the ground plane of waveguide, which are symmetric about the reflector wall. Figure 4-0-31 and Figure 4-0-32 show the YOY cut-plane E-fields of the all-diode on-state at 2.48 GHz. The Microstrip fringing field and leaky wave in Figure 4-0-31 do not couple. The scattering fields at the front corners of antenna are negligible, and the diffractions at the back corners of antenna caused by the input port are weak as well. In general, the intensities of leaky wave are much smaller than the intensity of fringing field.

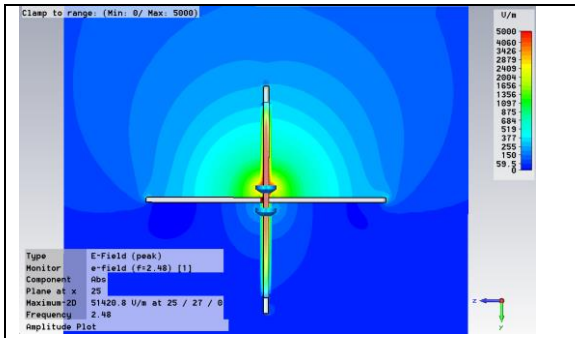


Figure 4-0-20: YOZ plane of diodes 1 & 4 off

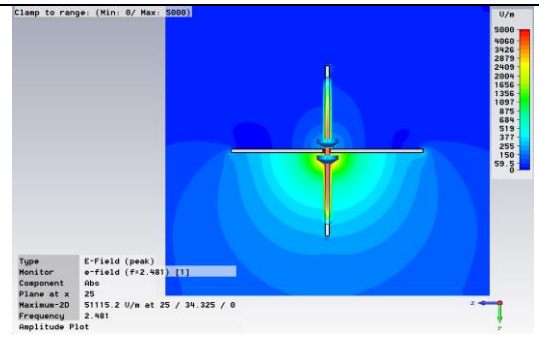


Figure 4-0-21: YOZ plane of diodes 2&3 off

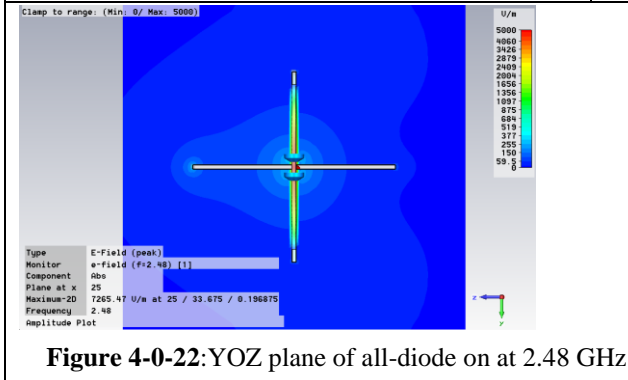


Figure 4-0-22: YOZ plane of all-diode on at 2.48 GHz

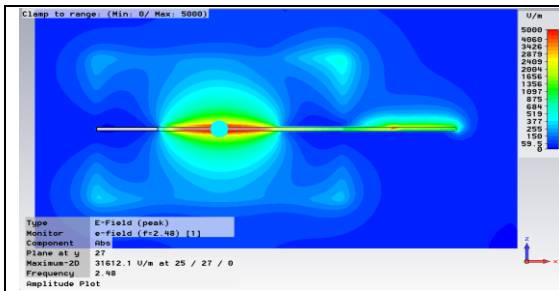


Figure 4-0-23: ZOY of diodes 1&4 off at Y=27mm

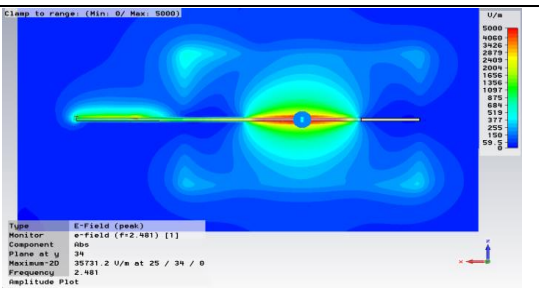


Figure 4-0-24: ZOY of diodes 2&3 at Y=34mm

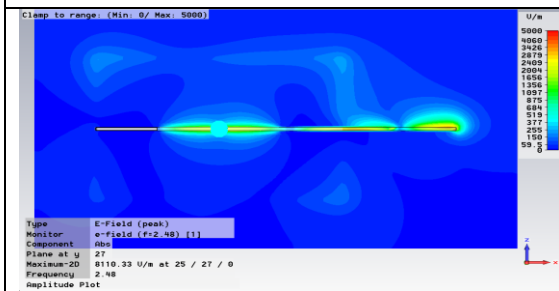


Figure 4-0-25: ZOY of all-diode on at 2.48 GHz at Y=27mm

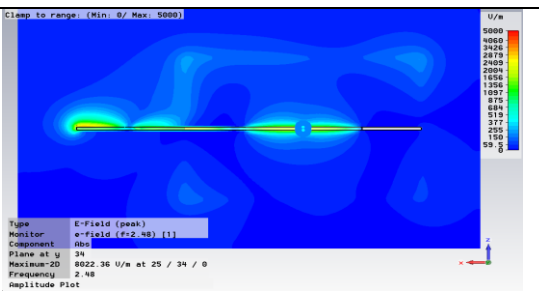
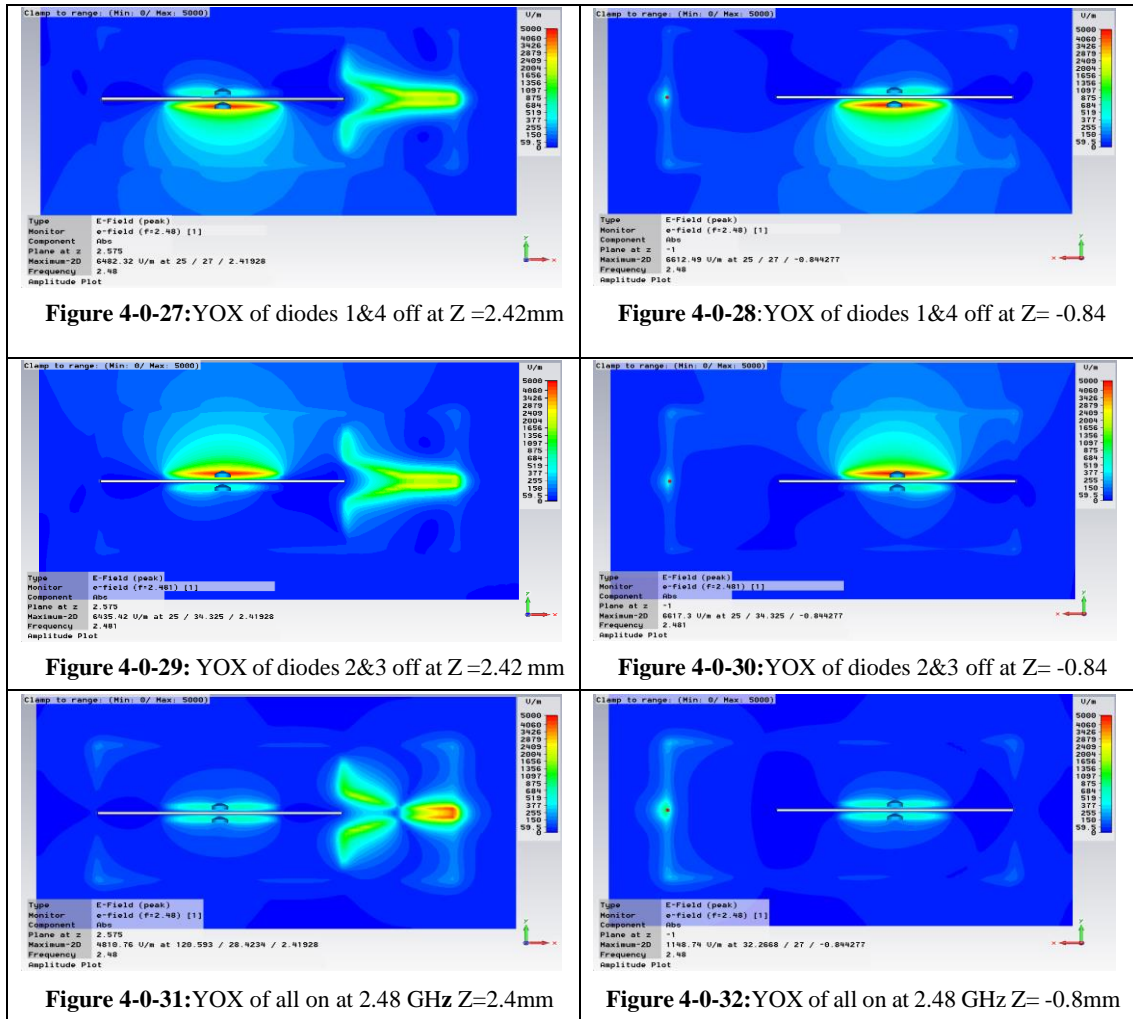


Figure 4-0-26: ZOY of all-diode on at 2.48 GHz at Y=34mm



4.7 Far-field measurement results of dual-diode off states

Figure 4-0-33 shows the comparison of farfield results between simulation and measurement of the dual-diode 1 and 4 off-state. Both main lobes in Figure 4-0-33 are in the same direction, which slightly trend towards to the waveguide top plane. The measurement pattern is the same as the simulation prediction in the top slot regions. But the farfield patterns of bottom slot regions are slightly different between simulation and measurement. This is because part of the slot 4 radiation is guided into slot 3 region due to the slight impedance mismatch. In addition, the DC control wires not only aggravate the E-field conduction into slot 3 region but also slightly attenuate the main lobe in slot 4

region. Therefore, the measurement result of diode 3 region has an obvious side lobe. As the E-fields between slot 3 region and slot 4 region are anti-phase, this side lobe does not couple with the leaky wave of slot 3. Moreover, as the forward bias diode 3 and diode 2 in practice have resistance over 2 ohms, the leaky waves of slot 2 and slot 3 increase, which in turn will enlarge back lobe. As, in slot 1 region, the diffraction is anti-phase with leaky wave, this increased diffraction cannot enlarge back lobe. As shown in Table 4-0-11, the measurement gain still reaches the simulation prediction, 4.7 dB. Figure 4-0-34 shows the comparison of farfield results between simulation and measurement of the dual-diode 2 and 3 off-state. In this graph, main lobe and back lobe have similar shapes. Both the measurement and simulation main lobes slightly trend to the waveguide top plane. Again, the farfield patterns of bottom slot regions are slightly different between simulation and measurement results. This is because the impedances of bottom slots are slightly different from the ones of top slots. As the main lobe in slot 3 region is partially guided into slot 4 region by the wires, the slot 4 region has a side lobe, which is weaker than the side lobe in dual-diode 1 and 4 off-state. Thus, the measured gain, 5 dB is larger than the simulated gain 4.7 dB, as shown in Table 4-0-11.

Overall, the measured results of dual-diode off states match with the simulation forecast, as shown in Figure 4-0-33 and Figure 4-0-34. As the impedance of bottom slots is compromised to support both single-slot and dual-slot radiations, the radiation of bottom slots is insufficient and can be easily guided along the wires. As, in practice, diodes in forward bias state have resistance over 2 ohms, the measured back lobes are slightly larger than the simulation ones for dual-diode off states. But, diodes in reverse bias state can reach the design requirement. In fact, the performances of PIN diodes can hardly be predicted accurately, as these diodes are not designed for this high frequency use, of which performance is unstable. .

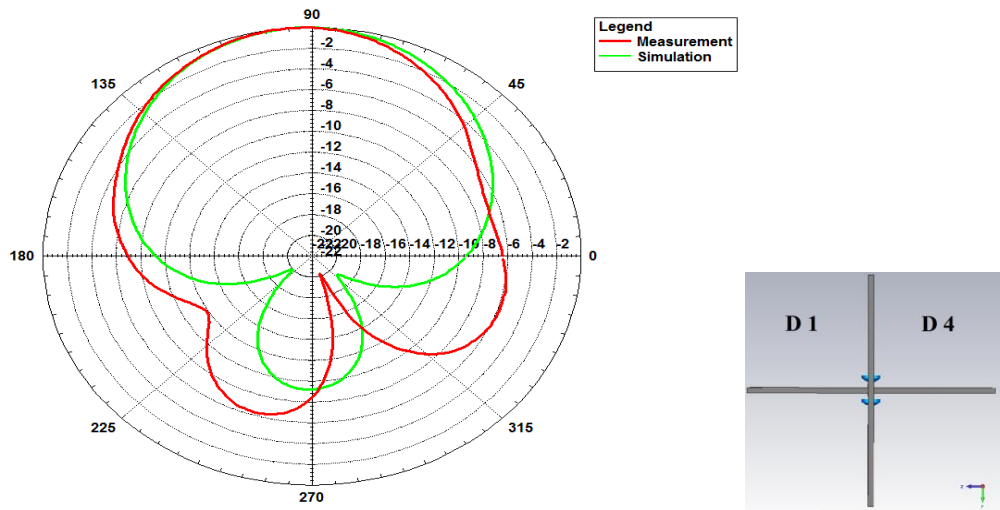


Figure 4-0-33: Measurement and simulation when diodes 1&4 off

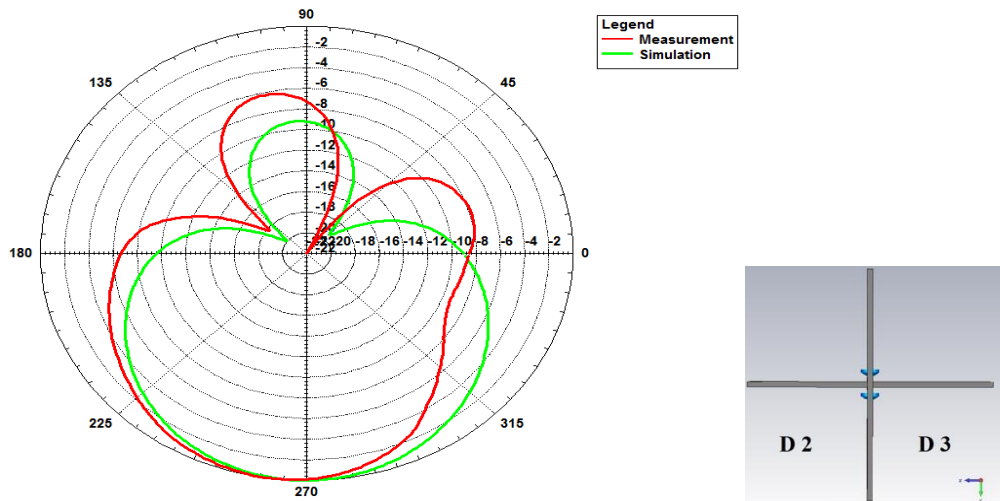


Figure 4-0-34: Measurement and simulation when diodes 2&3 off

Dual diodes off-state	Diode 1& Diode 4 off	Diode 2 & Diode 3 off
Simulation Gain	4.7 dB at 2.48 GHz	4.7 dB at 2.48 GHz
Measurement Gain	4.7 dB at 2.5 GHz	5.0 dB at 2.5 GHz

Table 4-0-11: Measurement Gain of dual diodes off-state

4.8 Far-field simulation results of multi-diodes off and on states

As the results of simulation and measurement are very close, the simulated results are used in further analysis. Figure 4-0-35 to Figure 4-0-40 show the farfield results of dual-diode 1 and 4 off-state. And Figure **4-0-41** to Figure 4-0-46 show the farfield results of dual-diode 2 and 3 off-state. As the farfield patterns of the two states are symmetric, only dual-diode 1 and 4 off-state is discussed here. Figure 4-0-35 shows the YOZ plane polar plot, and Figure 4-0-36 shows the corresponding 3D farfield pattern. The main lobe direction shown in Figure 4-0-35 slightly shifts 2 degree towards the waveguide top plane. As the impedance matching of bottom slots is slightly worse than the one of top slots, the radiation E-fields of bottom slots are susceptible to be guided away. Furthermore, the radiation intensity of bottom slots are slightly larger than the top slots one. The diffraction of slot 4 couples with the E-field of slot 1 at the waveguide top plane, when both slot 1 and slot 4 are radiating. Therefore, Figure 4-0-36 shows that the attenuation of radiation is slower in slot 1 region than in slot 4 region. This can be proved by the near field plot of YOZ cut-plane, as shown in Figure 4-0-20. Figure **4-0-37** is the XOY plane polar plot, and Figure 4-0-38 is the corresponding 3D farfield pattern. In contrast with the 5 degree shifting of main lobe direction in single-diode off states, the 1-degree shift shown in **Figure 4-0-37** means that the coupling radiations of dual slots reduce the influence of Microstrip fringing field. The near field plot of YOX plane in Figure 4-0-27 provides evidence. Figure **4-0-39** is the ZOX plane polar plot. Figure 4-0-40 shows the 3D pattern of 3 dB angular width. The local main lobe direction shown in **Figure 4-0-39** suggests that the diffraction at the back corner of top reflector still couples with fringing field but the coupling strength is 4 dB smaller than the corresponding results of single-diode off-state. In general, the 5.9 dB gain of the dual-diode off states is smaller than the 6.7 dB of the single-diode off states. The gain difference in the 6-direction antenna is 0.8 dB, but in the 4-direction antenna is 1 dB. In Figure 4-0-35 and **Figure 4-0-41**, the 3 dB

angular width of dual-diode off states is 91.7 degree which is larger than the result of single-diode states, 75.1 degree. This is because the radiation of dual-diode off states consists of two main lobes. In Figure 4-0-37 and Figure 4-0-43, the 3 dB angular width is around 69.8 degree which is very close to the result of single top-diode off-state, 70 degree. This is because the main lobes of dual-diode off states mainly locate at top slot region. Both Figure 4-0-37 and Figure 4-0-43 have a pair of unequal nulls at back lobe regions. For each pair of unequal nulls, the large null locates at the feedline region, and the small null locates around the antenna front end. This is because the radiations of top slots backward couple with fringing field at the transition region, which can be proved by Figure 4-0-27. For Figure 4-0-39 and Figure 4-0-45, the uneven nulls are caused by the same reason. The existence of the small null proves that the main lobe E-field is anti-phase with leaky wave at antenna front end.

Figure 4-0-47 to Figure 4-0-54 show the farfield results of all-diode on-state at 2.48 GHz, which is the response frequency of single diode off-state. As shown in Figure 4-0-47, the main lobe with a value of 0.3 dB is at the middle of top reflector edge. This scattering E-field is caused by the leaky waves of top slots. The farfield in YOX plane is 0 dB, as shown in Figure 4-0-49 to Figure 4-0-52. Figure 4-0-53 shows 5 side lobes and 1 local main lobe. For having a uniform frame of reference, the input port is set at zero degree and the antenna front end is set at 180 degree. Therefore, the local main lobe at 40° is caused by the coupling E-fields of minor leaky waves and major fringing field, radiating from the back corner of top reflector; the side lobes at 110° and 280° are caused by the leaky waves of top slots and bottom slots, respectively; the side lobes at 165° and 225° are caused by the diffraction from the front corners of top reflector and bottom reflector, respectively; the side lobe at 320° is caused by the diffraction from the back corner of bottom reflector. As the reflector length and the slot length are similar, the diffraction at reflector edge can produce a weak radiation below 2.4 GHz. Moreover, as the E-fields

trend to converge at the corners of reflectors, the diffraction radiates from the corners of reflectors. The leaky waves of higher-order mode from slots, show forward tendency. Although the gain is nearly 4 dB, the total efficiency is merely -10.55 dB. The reason is that the impedances between feedline and short-circuited slots mismatch, when the slots leak E-fields at higher-order mode. Overall, the all-diode on-state can be regarded as a short circuit to the single-diode off-state at 2.48 GHz.

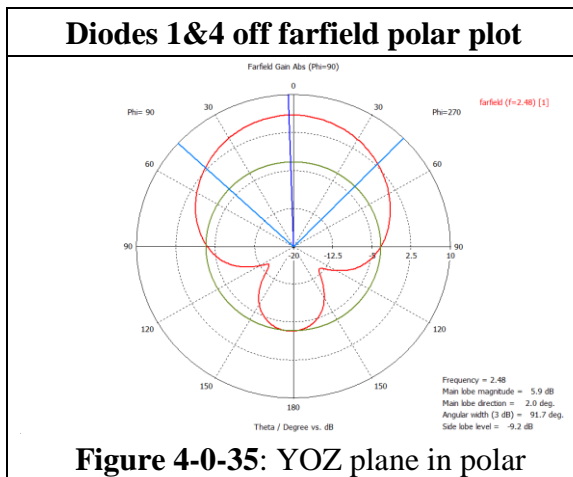


Figure 4-0-35: YOZ plane in polar

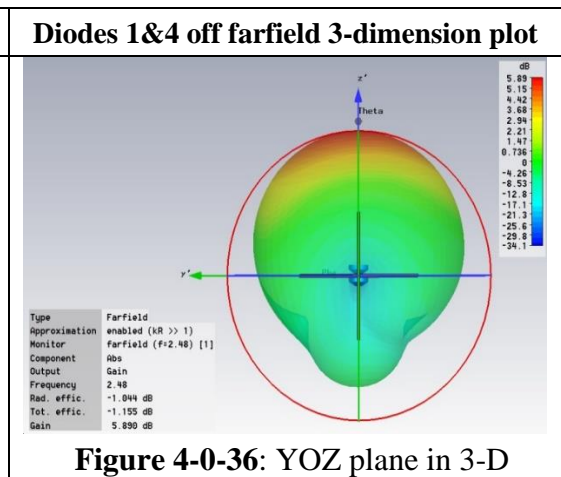


Figure 4-0-36: YOZ plane in 3-D

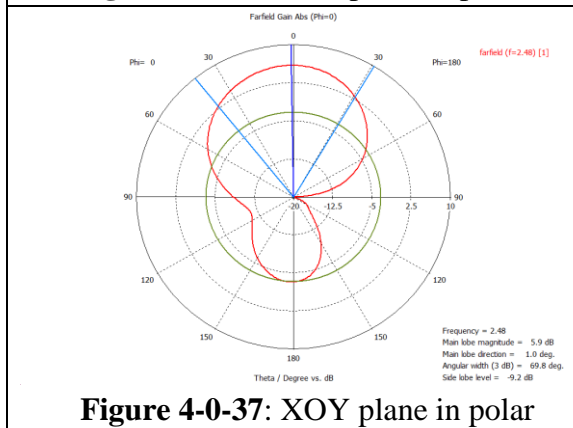


Figure 4-0-37: XOY plane in polar

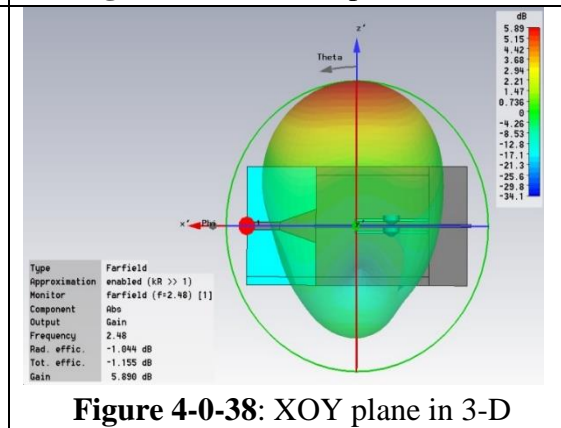


Figure 4-0-38: XOY plane in 3-D

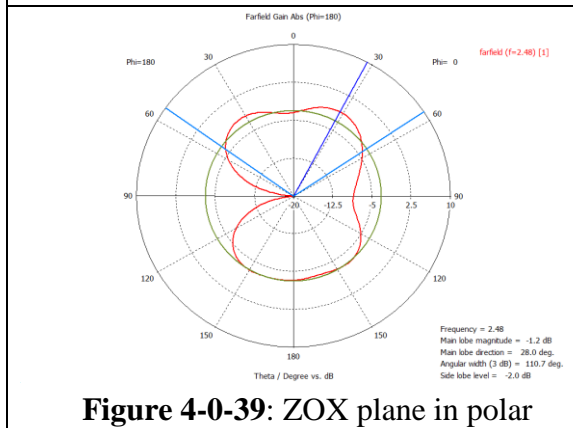


Figure 4-0-39: ZOZ plane in polar

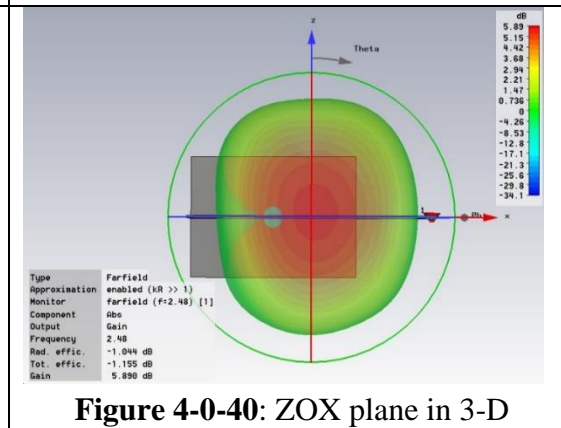


Figure 4-0-40: ZOZ plane in 3-D

Diodes 2&3 off farfield polar plot

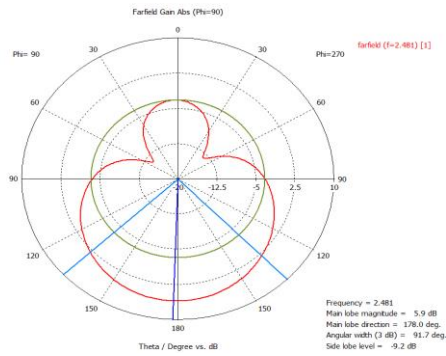


Figure 4-0-41: YOZ plane in polar

Diodes 2&3 off farfield 3-dimension plot

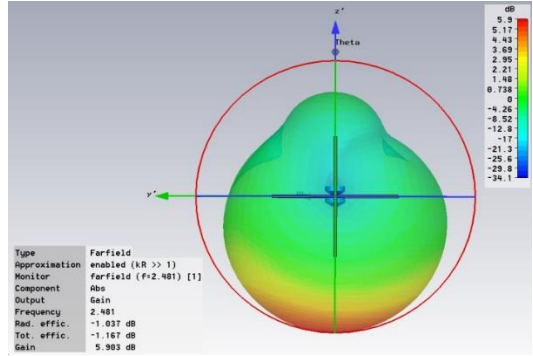


Figure 4-0-42: YOZ plane in 3-D

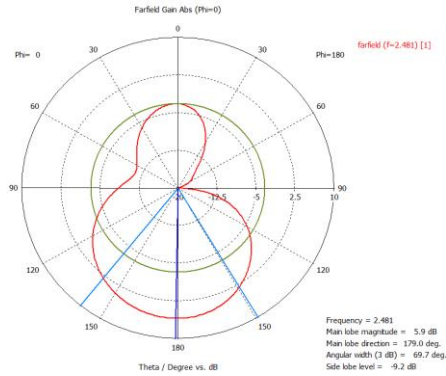


Figure 4-0-43: XOY plane in polar

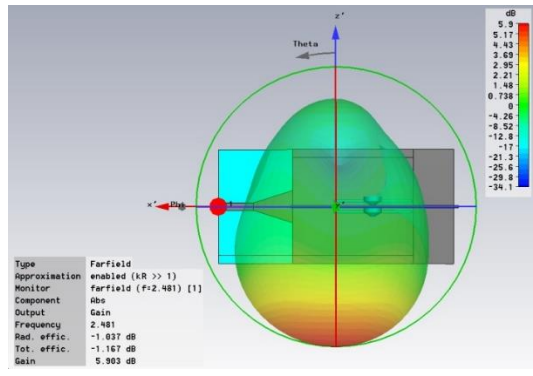


Figure 4-0-44: XOY plane in 3-D

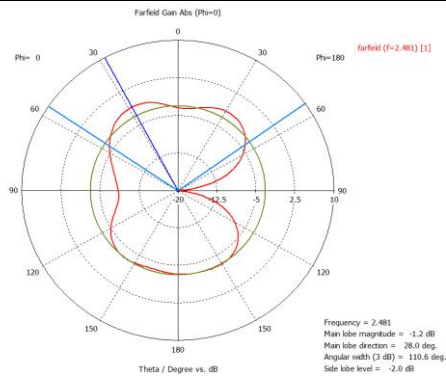


Figure 4-0-45: XOZ plane in polar

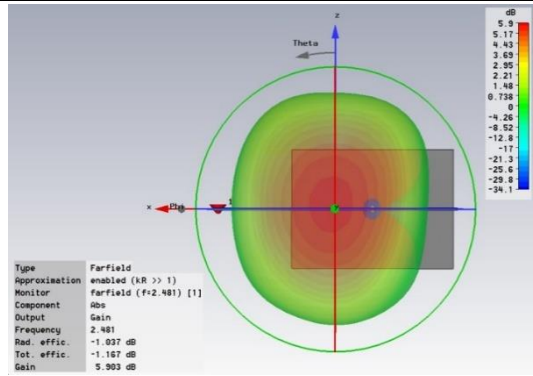


Figure 4-0-46: XOZ plane in 3-D

All diodes on polar plot at 2.48 GHz

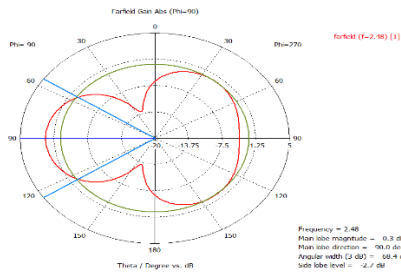


Figure 4-0-47: YOZ plane in polar plot

All diodes on 3-dimension at 2.48 GHz

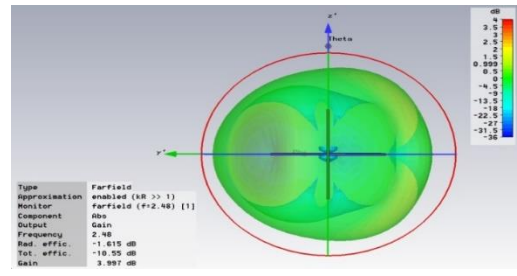


Figure 4-0-48: YOZ plane in 3-D

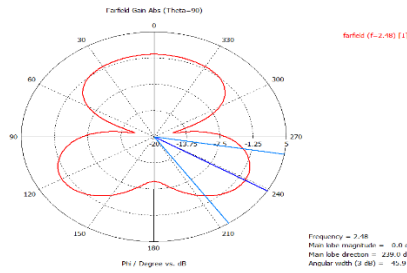


Figure 4-0-49: YOX plane in polar plot

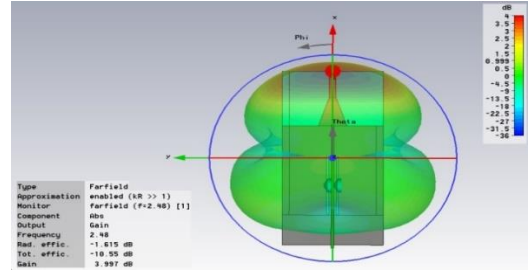


Figure 4-0-50: YOX plane in 3-D

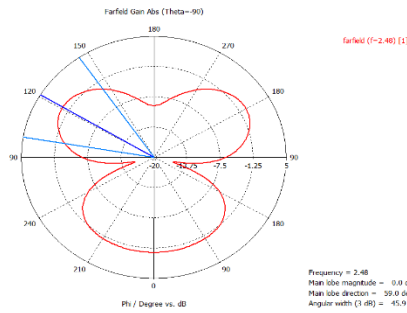


Figure 4-0-51: XOY plane in polar plot

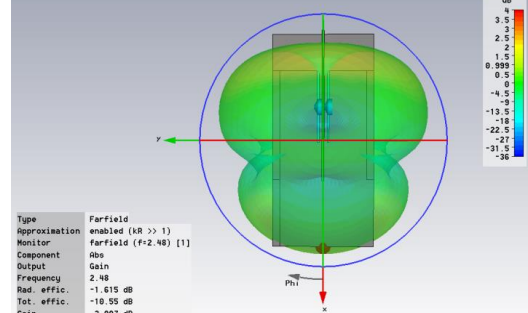


Figure 4-0-52: XOY plane in 3-D

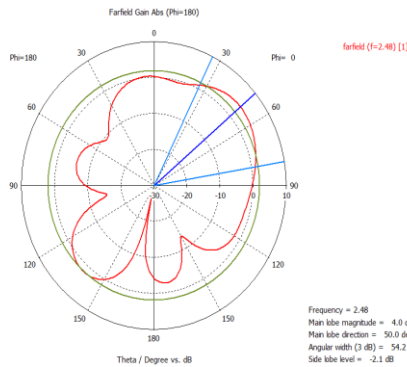


Figure 4-0-53: ZOY plane in polar plot

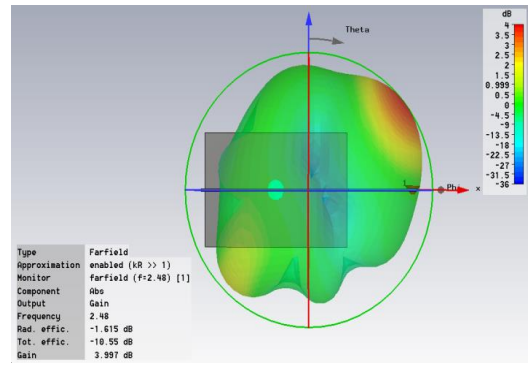


Figure 4-0-54: ZOY plane in 3-D

4.9 The others diode-off states of non-designed target:

Besides the above-mentioned work states, there are other possible combinations of slots for the dual-diode off-state which also have two main lobes. Although the results of these combinations are not good, following research can provide useful leads for the 8-direction antenna design in future. In 8-direction antenna, every two slots can radiate simultaneously by switching PIN diode and input mode. Due to the time limit, the 8-direction antenna will not be shown here.

Figure 4-0-55 shows the reflection coefficient $S_{1,1}$ results of dual-diode 1 and 2 off-state and dual-diode 3 and 4 off-state. Both states have two slots radiating on the same waveguide horizontal plane. The best reflection coefficient $S_{1,1}$ results in both states have the response frequency at around 2 GHz. As the metal surface area of the waveguide bottom plane is larger than the one of the top plane, dual-diode 3 and 4 off-state has a better impedance matching than dual-diode 1 and 2 off-state. Since the $S_{1,1}$ results of both states have two response frequencies as shown in Figure 4-0-55, the bandwidth of both states are all around 409 MHz. As both states have similar results, Table 4-12 only shows the results of dual-diode 1 and 2 off-state. According to Table 4-12 compared with the first response frequency, the second response frequency has worse $S_{1,1}$ value, total efficiency and energy balance, but better radiation efficiency and gain.

The E-field distribution of the two frequencies in near field range are showed in Figure 4-0-56 and Figure 4-0-57. The radiations from the two slots are anti-phase. Compared with the diffraction in Figure 4-0-57, the one in Figure 4-0-56 is much stronger and extends to the ground slot regions, given the antenna is working at 2.014 GHz. While

Figure 4-0-57 shows a distinctly upward wave from the top radiating slots, Figure 4-0-56 shows a strong downward diffraction. As the slot impedances match better at 2.014 GHz than at 2.306 GHz, the maximum E-field strength of top slots in Figure 4-0-56 is 103440 V/m, which is larger than the 92922 V/m of bottom slots in Figure 4-0-57. Figure 4-0-58 and Figure 4-0-59 show the farfield patterns at 2.014 GHz and 2.306 GHz, respectively. As the diffraction is in-phase with the leaky waves of ground slots, both graphs show obvious diffractions guiding into ground plane. As the leaky waves of the two ground slots are anti-phase, both graphs have two back lobes. As each back lobe is symmetric with the corresponding main lobe, Figure 4-0-58 shows four equivalent radiations. This is because leaky waves are enhanced by diffractions. Therefore, for Figure 4-0-58, there is not a clear distinction between main lobe and back lobe at 2.014 GHz. But the two top slots in Figure 4-0-59 radiate with a 5.6 dB gain, given the ground plane has two -0.5 dB back lobes. This is because the diffraction intensity in Figure 4-0-59 is obviously smaller than the one in Figure 4-0-58.

Figure 4-0-60 shows the reflection coefficient $S_{1,1}$ results of dual-diode 1 and 3 off-state and the dual-diode 2 and 4 off-state, respectively. The reflection coefficient $S_{1,1}$ results of the two states as shown in Figure 4-0-60 are totally identical. This is because both states have one top slot and one ground slot for radiation. For simplicity, only the dual-diode 2 and 4 off-state is analyzed. The reflection coefficient $S_{1,1}$ of the state has two response frequencies, but only the first response frequency at around 2 GHz is below -10 dB. Table 4-0-13 shows detailed results which are worse than those of dual-diode 1 and 2 off-state.

Figure 4-0-61 and Figure 4-0-62 show the YOZ cut-plane E-field distributions in near field range at 2.024 GHz and 2.298 GHz, respectively. In Figure 4-0-61, the E-field from slot 2 is stronger than the one from slot 4, but, in Figure 4-0-62, the opposite is true. As

the impedances of top slot and ground slot are different, top slot and ground slot respond at different frequencies. But, a strong E-field in near field range does not necessarily have a large farfield radiation, as the strong E-field has obvious diffraction at the edges of reflectors and waveguide. For example, the diffraction from slot 4 region, as shown in Figure 4-0-61, spreads over slot 1 region and slot 3 region, and cancels out the leaky waves of slot 1 and slot 3. Figure 4-0-63 and Figure 4-0-64 show the farfield patterns at 2.024 GHz and 2.298 GHz, respectively. The main lobe in Figure 4-0-63 is at slot 4 region. Although the stronger E-field in Figure 4-0-61 locates at slot 2 region, the diffraction from slot 2 region is also larger than the one from slot 4 region. Therefore, the two nulls in slot 1 region and slot 3 region are slightly close to slot 4 region. The main lobe of slot 2 is 2 dB which is 1.5 dB less than the one of slot 4. As shown in Figure 4-0-64, the main lobe is 3.1 dB and locates at slot 2 region. By comparing Figure 4-0-63 and Figure 4-0-64, the gain in Figure 4-0-63 is slightly larger than the one in Figure 4-0-64. As the metal surface area of waveguide ground plane is larger than the one of top plane, the radiation energy in bottom slot region is more intensive and can better concentrate on the main lobe direction. Therefore, the 3 dB beamwidth of slot 4 radiation in Figure 4-0-63 is only 96.5 degree which is smaller than the 107.4 degree beamwidth of slot 2 in Figure 4-0-64.

Figure 4-0-65 compares the reflection coefficient $S_{1,1}$ results of triple-diode 1, 2 and 3 and triple-diode 1, 3 and 4 off states. The reflection coefficient $S_{1,1}$ result of triple-diode 1&3&4 off-state is slightly better than the ones of triple-diode 1&2&3 off-state, as the waveguide ground plane not only has a larger metal surface area than the top plane but also does not have interference of fringing field. Since the results of both states are nearly the same, only the triple-diode 1&2&3 off-state will be analyzed here. Table 4-14 shows the detailed results of the two response frequencies in triple-diode 1&2&3 off-state. Only the reflection coefficient of the first response frequency can reach -10 dB at 2 GHz.

Figure 4-0-66 and Figure 4-0-67 show the YOZ plane E-field in near field range at two different frequencies. The strongest E-fields in both graphs are from slot 1. And in both graphs, the two diffractions in slot 1 region are strong, especially the one at the waveguide edge towards slot 4 region. Furthermore, the radiation E-field of slot 1 in both graphs is anti-phase with the radiation E-field of slot 2, but the E-fields of slot 2 region and slot 3 region are in-phase. When the coupling E-fields of slot 2 and slot 3 diffract into slot 4 region, the coupling E-fields are anti-phase with the diffraction from slot 1 region. Figure 4-0-68 and Figure 4-0-69 show the farfield results at 1.998 GHz and 2.336 GHz, respectively. The main lobes in both graphs are at the slot 1 region. As the radiation of slot 2 in Figure 4-0-68 is larger than the one of slot 3, the coupling E-fields trends to slot 3 region, which is proved by Figure 4-0-66. But the coupling E-fields in Figure 4-0-69 trends to the slot 2 region. This is because the radiation of slot 3 is larger than the one of slot 2, which is proved by Figure 4-0-67. The 4.8 dB gain in Figure 4-0-68 is smaller than the 5.8 dB gain in Figure 4-0-69. This is because the diffraction in Figure 4-0-68 is larger than the one in Figure 4-0-69. As shown in Figure 4-0-66, when the diffraction from slot 1 region is spreading over slot 2 region, the coupling E-fields of slot 2 radiation and slot 3 radiation cancel out most of the diffraction at the top reflector edge. As the radiation intensity of slot 1 and slot 2 at 1.998 GHz is stronger than the one at 2.336 GHz, the diffraction at the top reflector edge in Figure 4-0-66 is obviously larger than the one in Figure 4-0-67. Therefore, the 3 dB beamwidth in Figure 4-0-68 is larger than the one in Figure 4-0-69.

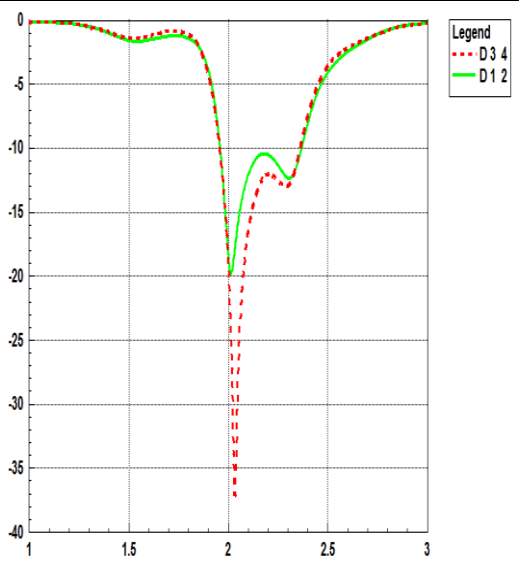


Figure 4-0-55: S1,1 comparison between diodes 1&2 off-state and diodes 3&4 off-state

Diodes 1&2 off	1st response frequency
S1,1	-19.803 dB
Frequency	2.014 GHz
Energy balance	0.102
Diodes 1&2 off	2nd response frequency
S1,1	-12.335 dB
Frequency	2.306 GHz
Bandwidth	409.24MHz-
Energy balance	0.242
	Radiation efficiency
	-0.882 dB at 2.014 GHz
	-0.7608 dB at 2.306 GHz
	Total efficiency
	-0.928 dB at 2.014 GHz
	-1.022 dB at 2.306 GHz
	Gain
	3.414 dB at 2.014 GHz
	5.605 dB at 2.306 GHz

Table 4-12: Detailed results of D1&2 off

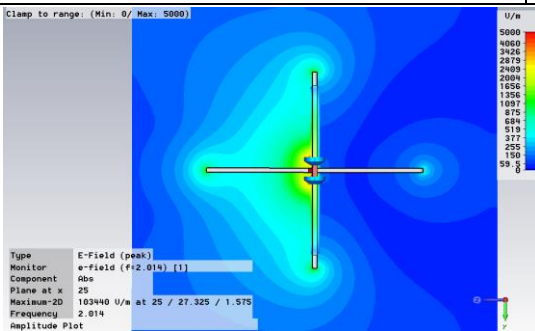


Figure 4-0-56: YOZ plane diodes 1&2 off at 2.014 GHz

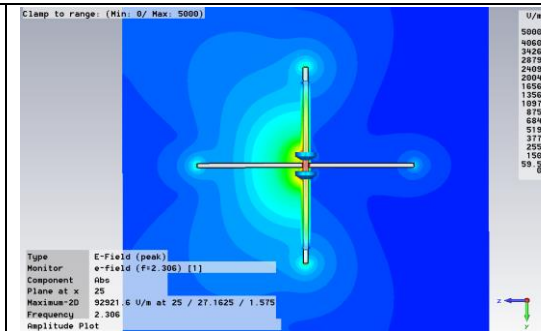


Figure 4-0-57: YOZ plane diodes 1&2 off at 2.306 GHz

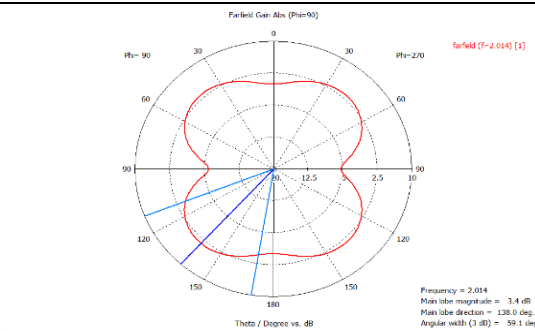


Figure 4-0-58: polar plot in YOZ plane diodes 1&2 off at 2.014 GHz

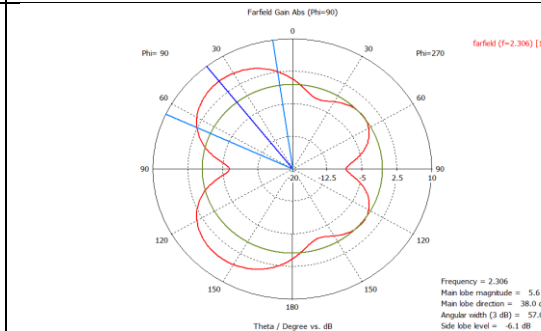


Figure 4-0-59: polar plot in YOZ plane diodes 1&2 off at 2.306 GHz

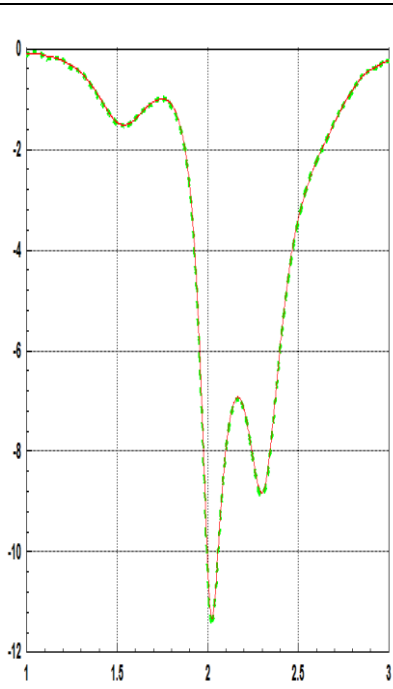


Figure 4-0-60: S1,1 comparison between diodes 2&4 off-state and diodes 1&3 off-state.

Dual diodes 2 & 4 off	1st response frequency
S1,1	- 11.324 dB
Frequency	2.024 GHz
Energy balance	0.272
Bandwidth	60.1 MHz
Dual diodes 2 & 4 off	2nd response frequency
S1,1	-8.821 dB
Frequency	2.298 GHz
Energy balance	0.362
	Radiation efficiency
	-1.155 dB at 2.024 GHz -0.972 dB at 2.298 GHz
	Total efficiency
	-1.487 dB at 2.024 GHz -1.583 dB at 2.298 GHz
	Gain
	3.540 dB at 2.024GHz
	3.218 dB at 2.298 GHz

Table 4-0-13: detailed results of dual-diode 2&4 off

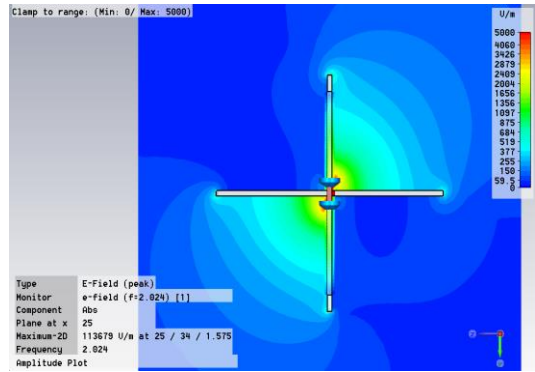


Figure 4-0-61: YOZ plane diodes 2&4 off at 2.024 GHz

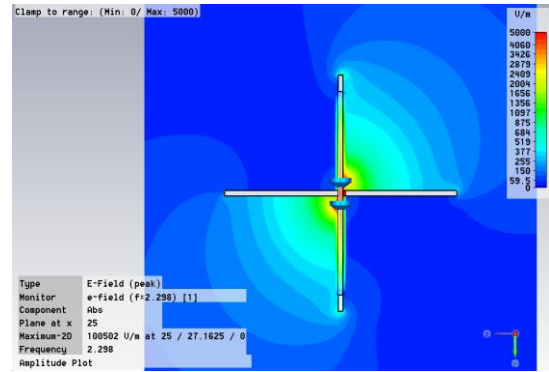


Figure 4-0-62: YOZ plane diodes 2&4 off at 2.298 GHz

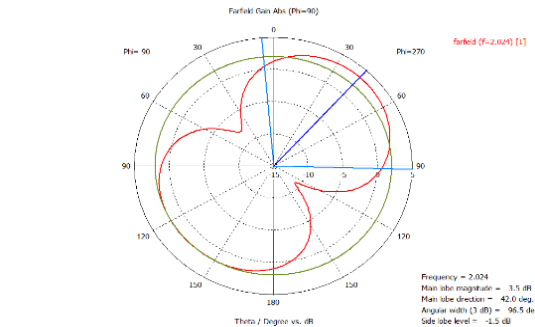


Figure 4-0-63: polar plot in YOZ plane at 2.024 GHz

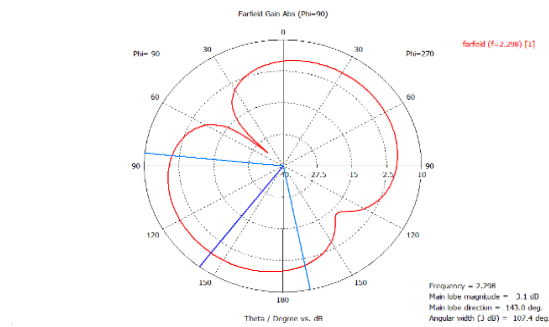


Figure 4-0-64: polar plot in YOZ plane at 2.298 GHz

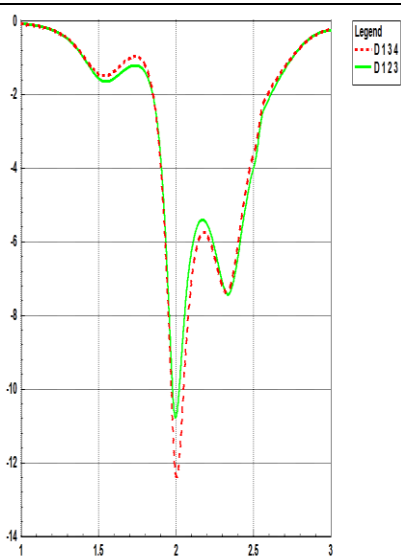


Figure 4-0-65: S1,1 comparison between diodes 1&2&3 off-state and diodes 1&3&4 off-state

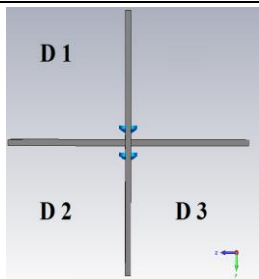
Diode 1 & 2 & 3 off	1st response frequency
Reflection coefficient	-10.774 dB
Working frequency	1.998 GHz
Bandwidth	43.304 MHz
Energy balance	0.289
Diode 1 & 3 & 4 off	2nd response frequency
Reflection coefficient	-7.427 dB
Working frequency	2.336 GHz
Energy balance	0.425
	Radiation efficiency
	-1.115 dB at 1.998 GHz -0.8609 dB at 2.336 GHz
	Total efficiency
	-1.495 dB at 1.998 GHz -1.727 dB at 2.336 GHz
	Gain
	3.652 at 1.998 GHz 4.918 dB at 2.336 GHz

Table 4-14: Detailed results of Diodes 1&2&3 off

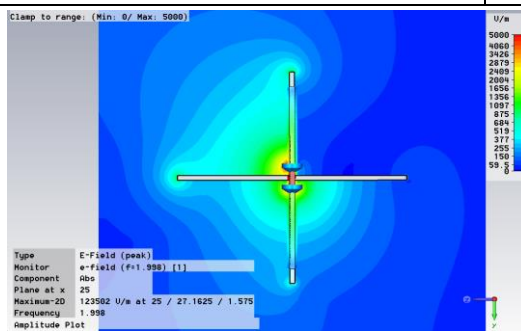


Figure 4-0-66: YOZ plane diodes 1&2&3 off-state at 1.998 GHz

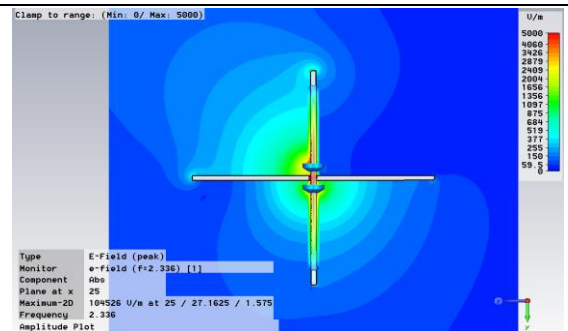


Figure 4-0-67: YOZ plane diodes 1&2&3 off-state at 2.336 GHz

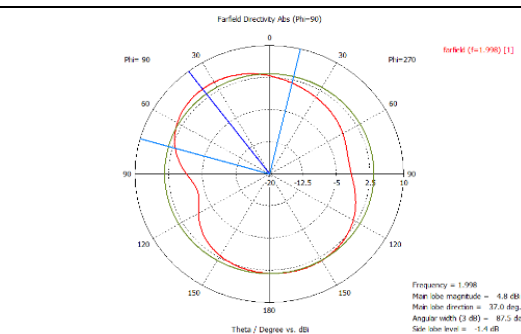


Figure 4-0-68: YOZ plane polar plot at 1.998 GHz

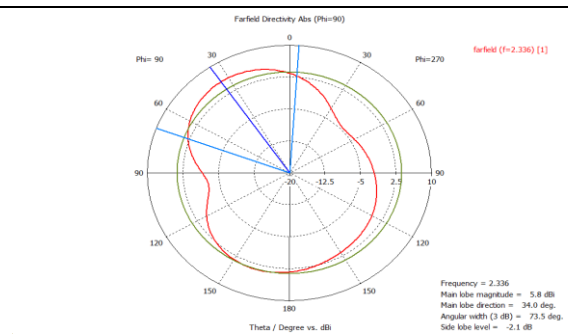


Figure 4-0-69: YOZ plane polar plot at 2.336 GHz

4.10 Further Research

The following research offers more information to support analysis above.

Tunable gain structure:

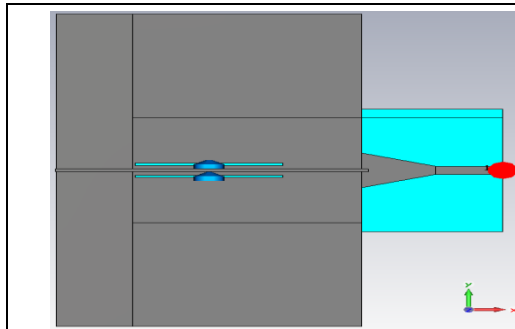


Figure 4-0-70: Antenna top view with additional 55-mm extension component

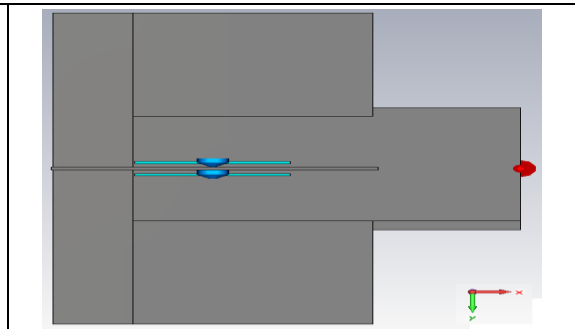


Figure 4-0-71: Bottom view of antenna structure

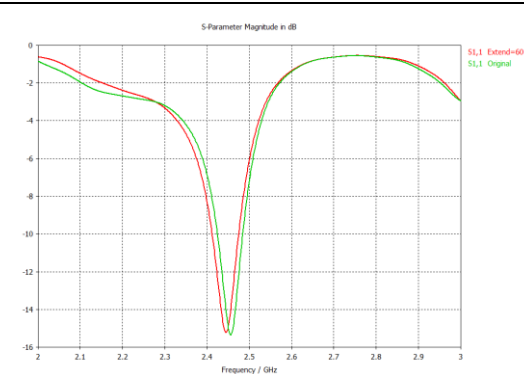


Figure 4-0-72: S1,1 of original and extension

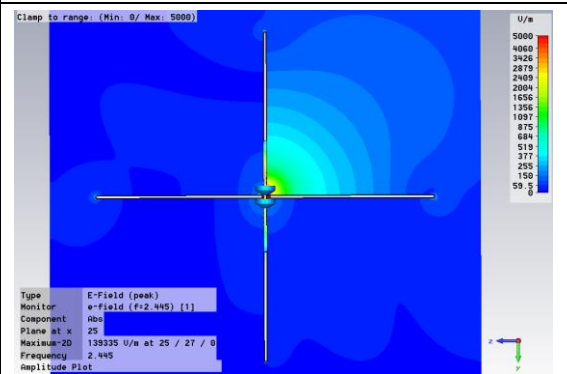


Figure 4-0-73: E-field in YOZ cut-plane

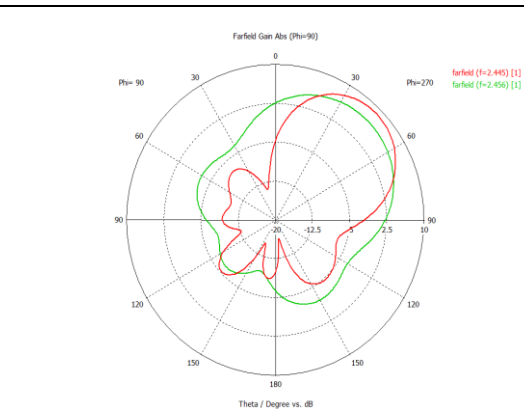


Figure 4-0-74: Polar plots of two structures

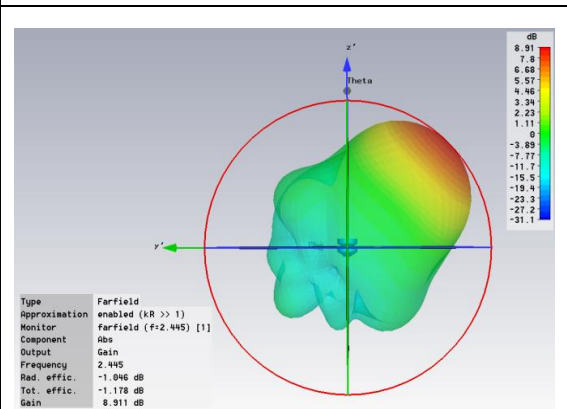


Figure 4-0-75: 3D farfield in YOZ plane

The gains in 4-direction antenna and 6-direction antenna can be easily regulated by changing both the height of reflectors and the width of waveguide. The following simulation results show improvement in gain. Based on the 6-direction antenna model, the height of reflectors are extended 55 mm and both sides of waveguide are also extended 55 mm. In this new structure, the distance between slot center and waveguide edge is 87mm, which equals 87% of the guided wavelength. Figure 4-0-70 and Figure 4-0-71 show the top plane and bottom plane of the new structure, respectively. As shown in the graphs, only the antenna part is extended. The feed line part remains intact, for avoiding the impedance mismatch problem. This is because if the feed line component was extended, the extended ground metal area of feedline would aggravate the impedance mismatching problem of ground slots. The new model is tested in the single-diode 4 off-state. As shown in Figure 4-0-72, the reflection coefficient $S_{1,1}$ results of the new structure is -15 dB at 2.445 GHz which is 11 MHz lower than the result of original structure. The bandwidth of new structure is 62.437 MHz which is 2.6 MHz larger than the one of original structure. Contrast to the strong coupling E-fields of original structure in near field range, the coupling E-fields between diffraction and leaky waves in new structure, as shown in Figure 4-0-73 are weak. Therefore, the diffraction can be greatly reduced by extending the reflectors.

Figure 4-0-74 shows two polar plots: the green pattern is for original structure; and the red pattern is for new structure. In Figure 4-0-74, the 3dB beamwidth result of original structure is 28.7 degree broader than the one of new structure. But the gain result of original structure is 2.2 dB less than the one of new structure. While the main lobe direction of original structure always inclines to 44 degree, the main lobe direction of new structure, as shown in Figure 4-0-74, exactly points to 45 degree. As the reflectors and waveguide edges in new structure are long enough to minimize the coupling of diffraction and leaky waves, the radiation in new structure concentrated on the main lobe direction

without being affected by diffraction. Although the back lobe of new structure in Figure 4-0-74 is slightly stronger than the one of original structure, the side lobes of new structure are significantly smaller than the ones of original structure. Therefore, the side lobe level of new structure, in general, is better than the one of original structure. As the diffraction in slot 1 region and slot 3 region is greatly reduced, the side lobe of new structure mainly consists of leaky waves. However, the side lobe of original structure consists of the coupling E-fields of diffraction and leaky waves.

Compared with the farfield results of original structure, the radiation efficiency and total efficiency of new structure are 0.03 dB lower. This is because the increased metal surface area of waveguide affects the matching of slot impedance. The gain of new structure is 8.9 dB which is larger than the 6.7 dB of original structure. The radiation pattern of new structure in Figure 4-0-75 is obviously narrower than the one of original structure, which means that the radiation in new structure can be better converged. Overall, the above-mentioned simulation results prove that the gain can be improved by extending reflectors and waveguide edges. The 3 dB beamwidth can also be controlled by the same way.

4.11 Relationship between reflector extension length and free space wavelength.

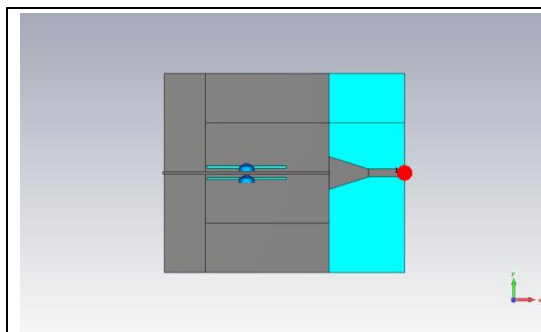


Figure 4-0-76: Another structure with additional 25 mm extension

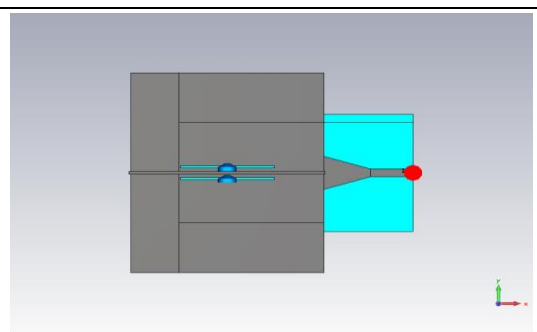


Figure 4-0-77: Adopted structure with additional 25 mm extension

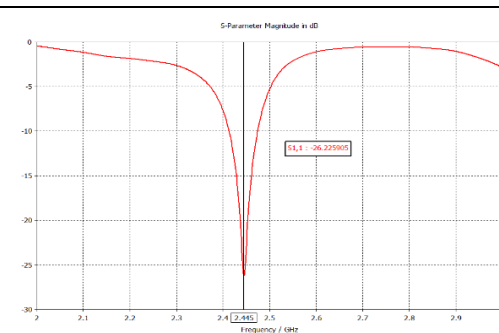


Figure 4-0-78: S_{1,1} result

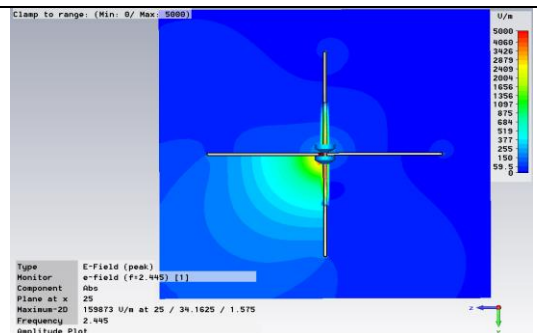


Figure 4-0-79: E-field in YOZ plane near field

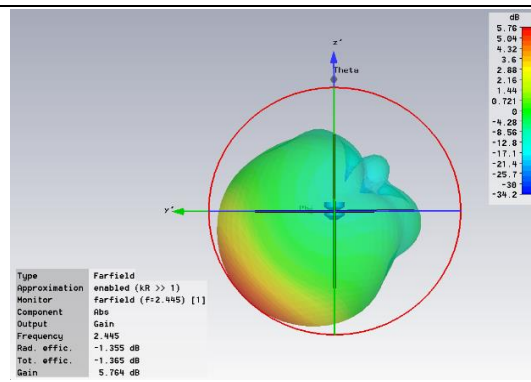


Figure 4-0-80: 3-Dimension farfield plot in YOZ

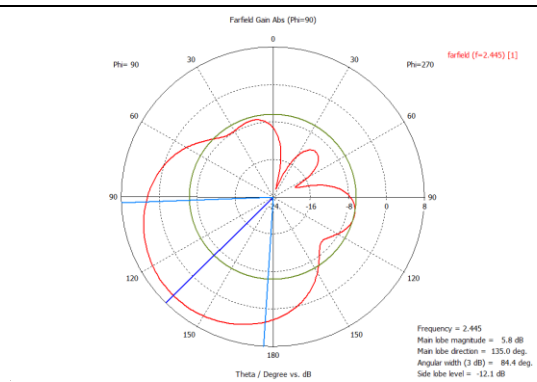


Figure 4-0-81: Polar plot in YOZ plane

Hereafter, both the height of reflectors and the width of waveguide will be uniformly called the length. The relationship between wavelength and the length of reflectors and waveguide is analyzed as follow. The 6-direction antenna model in single-diode 2 off-state is used for testing purpose. The antenna structure with extensions at both of feedline component and antenna component in Figure 4-0-76 will not be adopted, as the extended metal ground of feedline not only affects the impedance matching of bottom slots but also

produces unwanted scattering E-field which is caused by the part of input E-field guided along the ground edge. Although the ground metal surface area of the antenna shown in Figure 4-0-76 is largely increased, the bandwidth of this antenna is only slightly broader than the bandwidth of the antenna shown in Figure 4-0-77. As the part of input E-field, scattering along the ground edge of feedline, will mix with diffraction and leaky waves, the radiation energy, as a result, will be dispersed. So that, the side lobe intensity will be increased. Therefore, the antenna structure shown in Figure 4-0-77 will be adopted in the following research. For this structure, the reflectors and both sides of waveguide are all extended 25 mm. The structure adopted, hereinafter, will be called the new antenna.

Figure 4-0-78 shows that reflection coefficient $S_{1,1}$ of the new antenna is -26 dB which is improved over -10 dB compared with the $S_{1,1}$ results of the original antenna and the antenna with 55-mm extension. But the bandwidth of the new antenna is 2.6 MHz narrower compared to the result of original structure, and is 1.4 MHz narrower compared to the result of the structure with 55-mm extension. This is because the metal surface area affects the reactance of slots. The E-field of the new antenna is 16.7% stronger than the one of the original antenna, and is 14.7% stronger than the E-field of the antenna with 55-mm extension. Compared with the farfield results of original structure, the radiation efficiency and the total efficiency of the new antenna in Figure 4-0-80 decrease about 0.4 dB and 0.3 dB, respectively. Moreover, the gain of the new antenna, as shown in Figure 4-0-81, is 5.8 dB, which is 0.2 dB larger than the result of original antenna. Also, the 3 dB beamwidth of the new antenna, as shown in Figure 4-0-81, is 9.3 degree broader than the result of original antenna. Usually, if the size of extension components increases, the gain will obviously increase, but the 3 dB beamwidth will decrease. Nevertheless, the new antenna has an increased beamwidth and a slightly increased gain. However, these increases are not proportional to the extension of reflectors and waveguide. The reason is that the impact of extension on beamwidth and gain depends on whether the extension is

multiples of half wavelength. Since one-quarter wavelength in free space is about 25 mm, the length of the 55 mm extension is very close to half wavelength. As the radiation E-field has components guiding along the waveguide metal surface towards the waveguide edge, the phase variation of this surface guided E-field will affect the radiation from waveguide surface. Therefore, if the distance between slot edge and waveguide edge varies, the intensity of the superposing E-field varies as well, which, in turns, will affect the radiation. As the one-quarter-cycle phase change will cause an strong scattering E-field at waveguide edge, the increased E-field on the extension surface will be cancelled out by the scattering E-field. So that, the 25-mm extension just maintains the original radiation intensity. As the half-cycle phase change will only cause a weak scattering E-field at the waveguide edge, the increased E-field on the 55 mm extension surface will enhance the radiation intensity.

4.12 Research of diode resistance in off and on states.

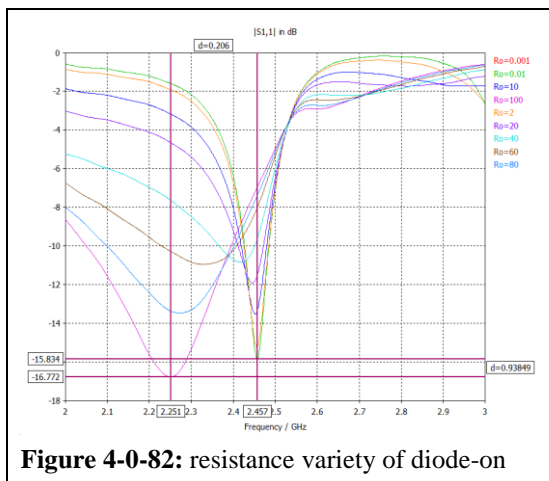


Figure 4-0-82: resistance variety of diode-on

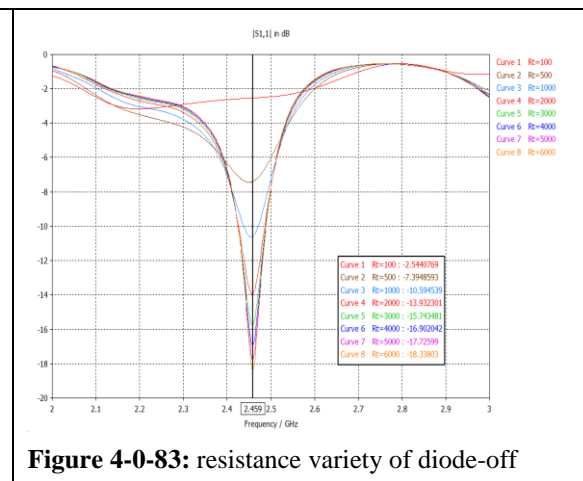


Figure 4-0-83: resistance variety of diode-off

Figure 4-0-82 shows how the variance in diode resistance will affect S1,1 result for on and off states. R_o represents the resistance value in the on-state, and R_t represents the resistance value in off-state. As shown in Figure 4-0-82, the reflection coefficient S1,1 curve with $R_o=0.001$ ohm is totally the same as the curve with $R_o=0.01$ ohm. Both S1,1

curves have the minimum value at around -15.834 dB. As the difference between the red curve with $R_o=0.001$ ohm and the green curve of $R_o=0.01$ ohm cannot be visually detected, the resistance value at 0.01 ohm can be treated as the best practical short-circuit state. The $S_{1,1}$ result of $R_o=2$ ohm is -15dB, which is 0.8 dB higher than the $S_{1,1}$ of $R_o=0.01$ ohm. As the difference of $S_{1,1}$ results between $R_o=2$ ohm and $R_o=0.01$ ohm is negligible, and $R_o=0.01$ ohm in practice is difficult to achieve, $R_o=2$ ohm is set as the practical short-circuit state in this thesis. The $S_{1,1}$ curves of $R_o=20$ ohm and $R_o=0.001$ ohm are similar. The shape of $S_{1,1}$ curves, however, starts to change when R_o reaches 40 ohm. In other words, the short-circuited slots will radiate obviously when the short-circuit resistance is between $R_o=40$ ohm and $R_o=100$ ohm. Although the $S_{1,1}$ can reach -16.772 dB when the diode is working at $R_o=100$ ohms, the resonance mode cannot generate the desired far-field pattern. So that, the forward bias resistance at 100 ohms is not suitable for the radiation in diode off-state. Overall, the diode resistance in short-circuit state should be lower than 8 ohm. Otherwise, the related $S_{1,1}$ cannot reach -15 dB.

Given that the resistance of the three forward-bias diodes is set at 2 ohms, Figure 4-0-83 shows the reflection coefficient $S_{1,1}$ results of the reverse bias diode with different resistances. Increasing the resistance of the reverse bias diode can improve both reflection coefficient $S_{1,1}$ and bandwidth. The best $S_{1,1}$ result with a value of -18.338 dB is observed when the resistance of the reverse-bias diode R_t reaches the maximum value, 6000 ohms. In order to keep the $S_{1,1}$ result lower than -15dB, the resistance of reversed diode should be 3000 ohm or higher. From $R_t=3000$ ohms to $R_t=6000$ ohms, the decreasing rate of $S_{1,1}$ drops to less than 1 dB per 1000 ohms. When the resistance R_t is 100 ohms, the radiation is deformed. Overall, the resistance of reverse-bias diode should not be less than 3000 ohms for the design requirement.

4.13 Conclusion:

For solving the impedance mismatching problem of the six-direction antenna, the intermediate-value method, for averaged impedance between single-diode off-state and dual-diode off-state, is introduced in this chapter. The measured results of reflection coefficient $S_{1,1}$ and far-field radiation pattern prove the practicability of the design and the intermediate-value method. Therefore, the impedance mismatching problem in four-direction antenna application has been solved. Due to the manual installation, the overlap circuit cannot be kept at exactly the same position, which will affect the performances of slots. Moreover, the PIN diode performance is somewhat unstable and variable, as this diode model initially is designed for 1 GHz. This is an intrinsic defect of the PIN diode. Therefore, the measured results may fluctuate above and below the simulation values. But these fabrication error are tolerable. Actually, in factory production, the overlap circuits can be placed by professional methods or machining operation, and the circuit of back-end digital communication system can be added in to filter out the noise. Therefore, this six-direction switch-beam antenna has been successfully proved to be feasible.

Reference

- [1.] Balanis, Constantine. "*Antenna Theory: Analysis and Design* ", 3rd ed., Wiley-Interscience, New York, April 4, 2005
- [2.] Robert A. Nelson. "*Antennas: The Interface with Space*", [Online]. Available: http://www.atcourses.com/antennas_tutorial.htm [Accessed 3 June 2013].
- [3.] John D. Kraus. "*Electromagnetics*", 4th ed., McGraw-Hill, New York, 1992.

Chapter 5: Substrate Integrated Waveguide (SIW)

Antenna minimization designs

5.1 Introduction

This chapter is going to present three contractible substrate integrated waveguide (SIW) antennas. All designs in this chapter are working at 5 GHz frequency, as the 5GHz frequency has a larger frequency spectrum than the 2.4 GHz one. Moreover, the SIW antennas working at 5 GHz are smaller than those working at 2.4 GHz. Traditional waveguides, as we know, have some general defects, such as large volume, heavy weight, and high cost. For the following SIW antennas, the design objective mainly focus on the size reduction. By utilizing Printed Circuit Board (PCB), these new SIW antennas have advantages in multi-layers, planar structure, and light weight.

5.2 Whole Folded Antenna

5.2.1 Introduction

As the development of RF circuit trends to planar form, the non-planar waveguides usually have large insertion loss. For reducing the cumbersome volume of traditional waveguide, some novel fabrication techniques have been introduced, such as the printed circuit board (PCB), low-temperature co-fired ceramics (LTCC) and thick film technology [1]. Due to

light weight, compact size and planar shape, all these techniques can support multi-layer structure and single-substrate integration. PCB is chosen for the proposed antennas, because PCB has apparent advantage in low cost, easy fabrication, wide application and having various integrated circuit components available in market. The substrate integrated waveguide (SIW) based on PCB manufacture method attracts the mainstream attention and is widely applied to millimeter wave antenna design [1] [2], since the prototype structure of SIW [3] kept the waveguide advantages in low loss and high isolation. Ke Wu [4] demonstrated the integration between SIW and Microstrip feedline in one substrate. As SIW is filled with dielectric, the ratio of height to width of SIW is smaller than the one of rectangular hollow waveguide. And the volume of reduction depends on the factor $\sqrt{\epsilon_r}$ which is the dielectric constant of waveguide filled material [2]. For further downsizing the SIW, the folded structure was introduced based on the experience in conventional waveguide transformation [5]. Ke Wu [6], summarized the common methods for folding SIW structure, such as the C-shape type [7][8] and T-shape type [9][10]. Both of the two folded types are used to reduce the waveguide broad-wall width. The transversely folded structure usually is suitable for transmission line. As the radiative slot is close to the edge of top plane, the C-type [8] and T-type [11] antennas without surface metal extension would have severely asymmetric farfield patterns. The effective waveguide width depended on the length of folded path [12]. As the width of unfolded SIW is set at around 0.7 wavelength depending on the operating frequency [6], the width of transversely folded SIW should be narrow when the working frequency is over X band. As the side-walls of SIW are made up of metal-plated via holes [4], the fabrication of transversely folded SIW working at high frequency band is a great challenge in practice. In general, there are two difficulties. Firstly, in order to obtain identical propagation constant of unfolded SIW and optimum bandwidth, the length of middle gap in transversely folded SIW must be half of the SIW height [13]. Secondly, even the width of SIW shrinks half, the number of via holes still keeps the same. A large amount of via holes will spend time and increase

probability of fabrication error. When SIW antenna connects to feedline, the whole length is considerably long. For reducing the total length, in this chapter, the antenna with C-shape folded front-end is proposed, which is showed in Figure 5-0-1. The front-end of this new antenna is the folded region. And the original front-end before folded is changed to the back-end of second layer. As the post wall of the short-circuited front-end is replaced by a metal tape, the number of via holes needed reduces. This proposed folded substrate integrated waveguide (FSIW) is intended for end-fire antenna. As the working mechanism of waveguide antenna is similar to the one of half-wavelength dipole antenna, the total length of SIW antenna can be reduced by folding the front-end of the antenna back to second layer by one-quarter wavelength. But the folded structure has a risk in deforming the transmission waves inside the SIW. As, contrast to unfolded SIW antenna, the folded region will increase the possibility of total reflection which means all incident waves at first layer are backward to input port. The folded SIW antenna, as a result, might not work like a half-wavelength dipole antenna, but like an end-fire leaking source. For this reason, the research focus switches to find out whether this antenna can work at fundamental mode.

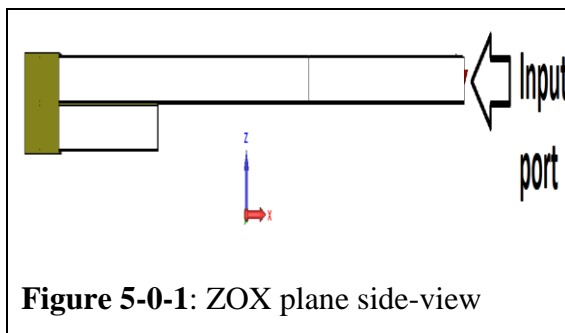


Figure 5-0-1: ZOX plane side-view

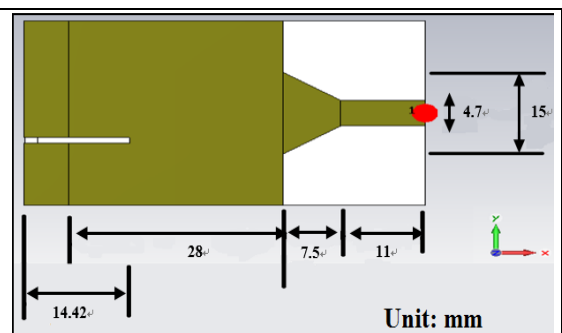


Figure 5-0-2 Top-view of antenna

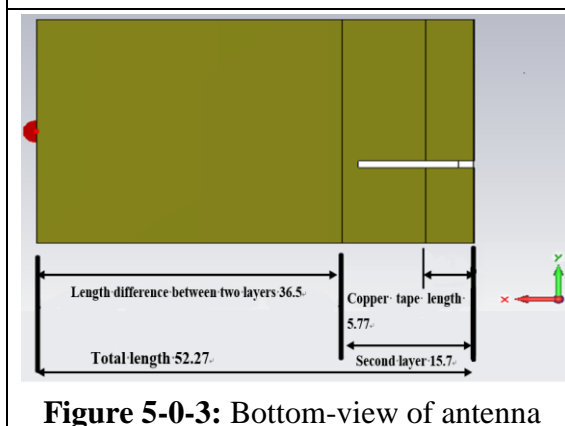


Figure 5-0-3: Bottom-view of antenna

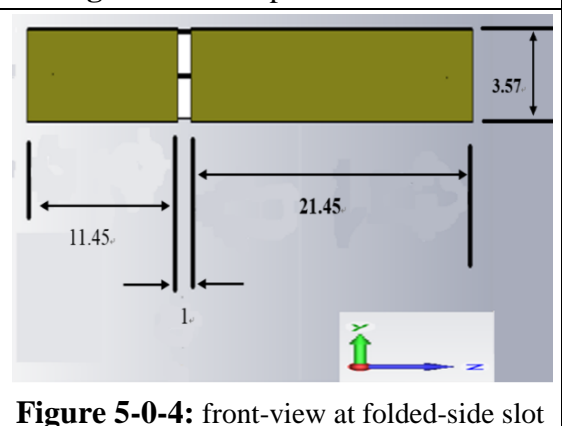
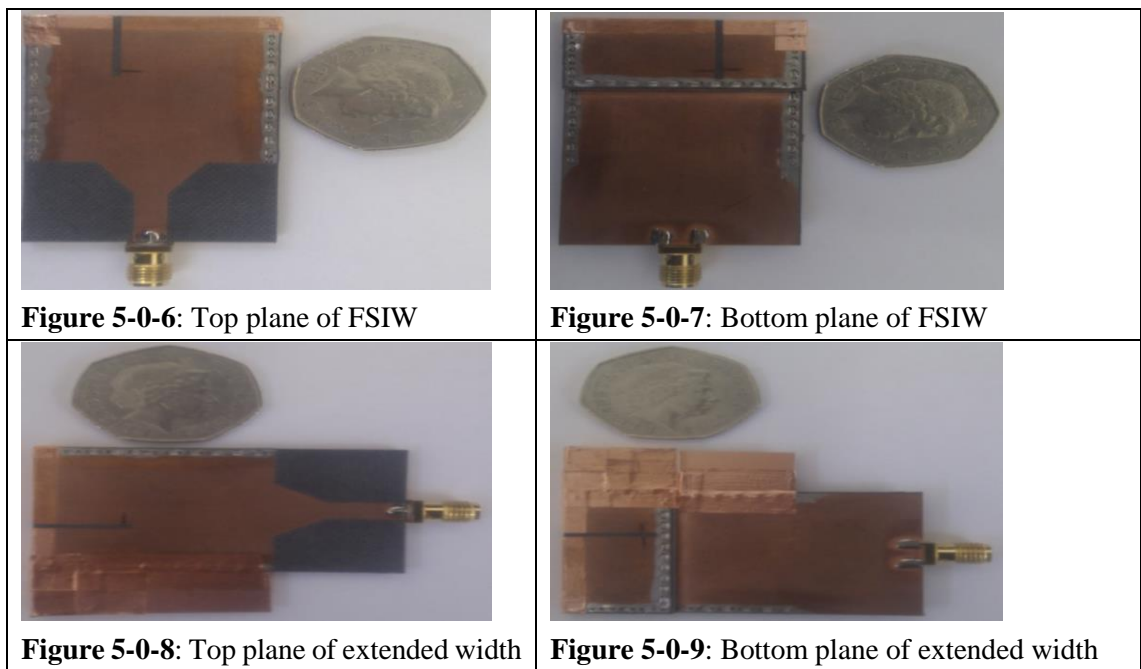


Figure 5-0-4: front-view at folded-side slot

Name	Value	Description	Type
L	45	Length of Waveguide antenna part	Length
T	0.07	Thickness of surface Copper	Length
a	31.9	Width of Waveguide antenna part	Length
b	1.575	High of substrate material	Length
f	11	Length of Microstrip feedline	Length
i	4.7	SNA input connector head	Length
ls	24	Slot length	Length
n	-1.7	Length of Dielectric middle gap	Length
r	13	one quarter lamda of wavelength	Length
v	7.5	Length of taper	Length
w	1	slot width	Length
w1	15	Width of taper	Length
x	-5	move slot from centre of waveguide to edge of waveguide	Length

Figure 5-0-5: Simulation model parameters list



5.2.2 Antenna design

This folded waveguide antenna was made by the Rogers RT/duroid high frequency laminates 5880 with a dielectric constant $\epsilon_r = 2.2$ substrate. Figure 5-0-6 and Figure 5-0-7 show the front-view and the rear-view of the waveguide structure, respectively. As the existence of via holes will affect the effective width of slot, a bended metal tape is adopted to replace the via-hole of folded side. The replacement has been proved to be valid by Sanz-Izquierdo [14]. The metal-plated via holes used for side-walls has a 0.6 mm diameter and a 1.5 mm pitch. So that the gap between each pair of via holes is 0.9 mm.

Figure 5-0-2 to Figure 5-0-4 show the dimension of the antenna. The width of the SIW antenna is 33.9 mm. The total length of the antenna is 52.27 mm, including a 33.77 mm first-layer antenna section, a 7.5mm transition, and an 11mm Microstrip line. The length of second-layer antenna section is 15.7 mm which is one-quarter wavelength of the guided wave at 5GHz. In fact, the front-end of the antenna can either be folded back by one-quarter of the wavelength or by three-quarter of the wavelength. The one-quarter wavelength folded antenna is chosen, as this structure supports a broader bandwidth, compared with the three-quarter wavelength folded one. Also, the phase shift ϕ equals to β times L, where L represents the distance between the short-circuited front end and the slot center and β is the phase constant. This equation suggests that the shorter the distance L is, the less the phase will shift. As the side-walls of the waveguide are tightly sewed by wires through via holes, the waveguide can work at the leaky wave mode to increase bandwidth [15]. Also, both layers are partially etched at the front-end, so that the dielectrics of the two layers can be connected by an air gap. Although, in simulation, the length of the air gap is set at 1.7 mm, the one in practice is less than 1.5 mm, due to the fabrication errors. This inner air gap, essentially, works like a shunt capacitance. Under ideal condition, the slot width can be set equal to the height of SIW which is 1.5 mm. However, to take the etching error into consideration, the slot width is set at 1 mm. The length of the slot is set at 24mm, which is given by the following formula [16] :

$$L_s = \frac{\lambda_{eff}}{2} = \frac{\lambda_0}{\sqrt{\frac{\epsilon_r + 1}{2}}} \quad (1)$$

Where L_s is the effective wavelength, ϵ_{eff} is the effective dielectric constant, ϵ_r is the relative permittivity and λ_0 is the wavelength in air. The slot sections etched at the metal surface of the first layer and the second layer are identical in length. The offset between the central line of waveguide and the longitudinal center of slot is 5mm. This antenna is fed by a SMA connector via a 50 Ω rectangular Microstrip line. The width of the Microstrip line is 4.7mm. The connection width between transition and antenna is 15mm.

5.2.3 Simulation results of 2-D surface current peak

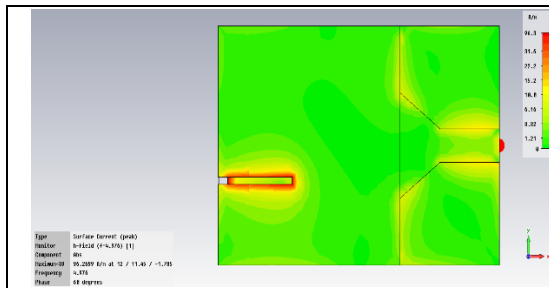


Figure 5-0-10: Current distribution of 1st layer top slot in 60 degree phase

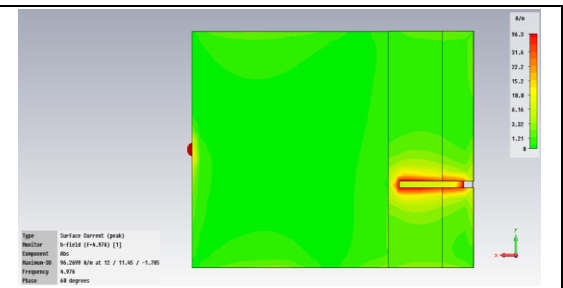


Figure 5-0-11: Current distribution of 2nd layer bottom slot in 60 degree phase

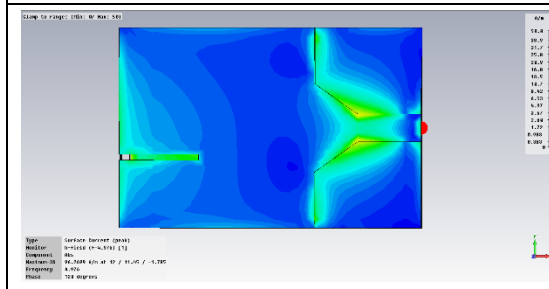


Figure 5-0-12: Current distribution of 1st layer top slot in 120 degree phase

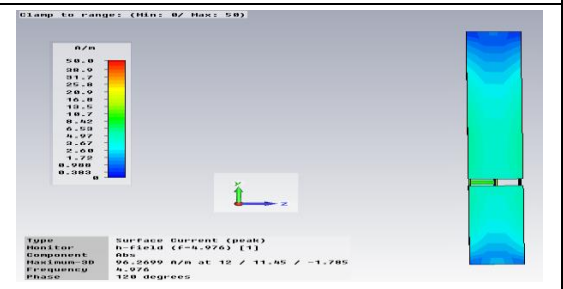


Figure 5-0-13: Current distribution of folded-side slot section in 120 degree phase

Figure 5-0-10 and Figure 5-0-11 show the current distribution of the folded slot in 60-degree phase from front-view and bottom-view, respectively. With a peak at the back-end of the slot, the current is evenly distributed at the two sides of the slot, and decays at the front-end of antenna. This current distribution accords with the fundamental mode of waveguide. But the working mode of the slot will change, when the absolute value of current with a phase at 120-degree. Figure 5-0-12 and Figure 5-0-13 show that the currents at the surface of the metal tape and the front-end edge of the antenna are strongest; while, the currents at the back ends of the top and the bottom slot sections are weakest. So that, these two sections work like two independent radiation slots. Moreover, the current distribution of feedline at this phase stage shows strong fringing field. In summary, the metal tape not only guides the inner transmission waves to the second layer, but also like a short-circuited reflector, sends part of the transmission waves back to input port. Therefore, the folded antenna slot responds at two modes, which are the fundamental mode and the second-order mode.

5.2.4 Simulation results of E-Field amplitude plot at 2D planes

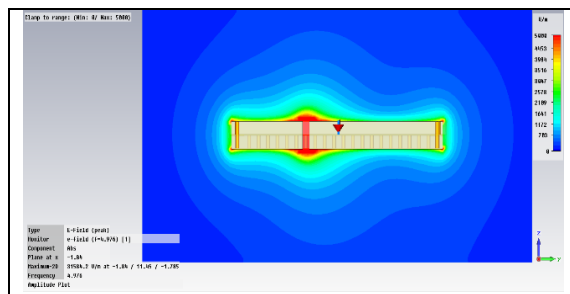


Figure 5-0-14: E-Field amplitude at ZOY plane

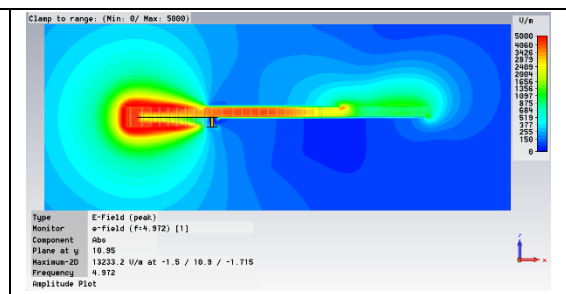


Figure 5-0-15: ZOY plane E-field distribution

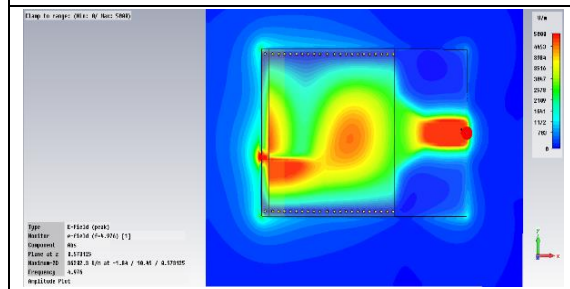


Figure 5-0-16: E-Field amplitude plot at XOY plane

Figure 5-0-14 shows the E-field distribution of the antenna when all the slot sections are radiating. There are scatterings at the four front corners of the waveguide. This is because conducting charges normally accumulate at sharp folded edges. Figure 5-0-15 shows that there is a strong fringing field spreading over the whole Microstrip feedline. And this fringing field with a forward tendency couples with the backward component of the first-layer radiation. Therefore, the backward radiations at the top and the bottom plane are unequal. The radiation E-field pattern of the folded slot can prove that this folded antenna works at the half-wavelength dipole mode. The E-fields on the first layer and the second layer are stronger than the one on the metal tape, as the two layers have a larger metal surface area than the one of the metal tape. Figure 5-0-16 shows that both the slot section of metal tape and the slot section of first layer radiate at the fundamental mode, and there are scatterings at the front corners of the antenna. So that, this folded antenna is once again proved to work at the half-wavelength dipole mode. But, the metal edge of sharp bend at the middle air gap shows the same resonance with half intensity. As these E-fields at waveguide inner does not radiate to outer space, but merely disperse the energy of

transmission wave. Therefore, the E-fields radiating at the quarter-wavelength monopole mode have a greater intensity than the one radiating at the half-wavelength dipole mode.

5.2.5 Simulation and measurement results in S1,1

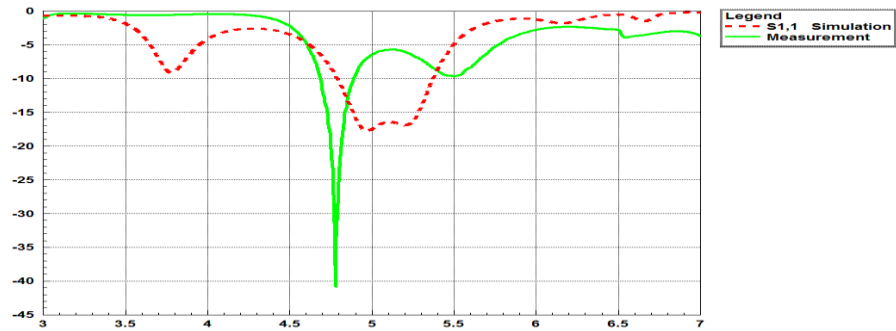


Figure 5-0-17: S1,1 results comparison of simulation and measurement

Figure 5-0-17 shows the reflection coefficient S1,1 results of simulation and measurement. The simulation S1,1 result has two resonant modes. One is -17.7 dB at 4.972 GHz; another is -16.9 dB at 5.208 GHz. As the resonant frequencies of the modes are close, the modes will couple together. Therefore, the bandwidth of simulation is about 580 MHz at -10 dB. The measured S1,1 result has two far separated resonant modes. One is -40.4 dB at 4.775 GHz; another is -9.7 dB at 5.5 GHz. The reduced air gap will increase the reflection at the first layer and only pass higher-frequency into second layer. Therefore, the two slot sections mainly respond at the quarter-wavelength monopole mode with a bandwidth of 200 MHz at 4.775 GHz. By modifying the slot size, the monopole mode can be tuned up to dipole mode at the cost of reducing bandwidth. However, as the half-wavelength dipole mode at 5.5 GHz will not contribute to the bandwidth, the loss in bandwidth cannot be compensated. The tuning, as a result, is not worthwhile.

5.2.6 Farfield simulation results at 4.976 GHz:

As shown in Figure 5-0-19, Figure 5-0-22 and Figure 5-0-23, the main lobes of the top slot section and the bottom slot section slightly slope to the positive side of Y-axis. The cause of this oblique radiation is that as the slot is offset to the negative side of Y-axis, the metal surface area at the two sides of the slot are unequal. Therefore, the metal surface area on the positive side of Y-axis is larger and can reflect more radiation energy. For the same reason, the second layer slot-section, as shown in Figure 5-0-21, has the same main lobe direction. Both the main lobes in Figure 5-0-19 and Figure 5-0-21 have a symmetric 3 dB beamwidth pattern, and show the radiation characteristic of monopole mode. As shown in Figure 5-0-18, the local main lobe of the slot-section on the metal tape also trends towards the positive side of Y-axis for the same reason. This local main lobe with 2.7 dB magnitude suggests that the antenna has a tendency to radiate at dipole mode. The side lobe level in Figure 5-0-18 is -3.1 dB. Figure 5-0-20 shows the bottom view of the antenna at YOX plane. And Figure 5-0-21 shows the corresponding farfield pattern. Figure 5-0-22, in addition, shows the polar plot of the monopole-mode radiation. The main lobe intensity of the top slot-section is slightly larger than the one of the bottom slot-section. Although the total metal surface area of the second layer and the first-layer ground plane is larger than the one of the first-layer top plane, the metal surface of the first-layer top-plane is seamless so that can concentrate more farfield reflection. Figure 5-0-23 shows that the unbroken linear radiation has two monopole-mode main lobes generated by the top and the bottom slot-sections. This linear pattern proves the existence of dipole mode. Figure 5-0-24 shows that the farfield intensity of dipole mode is weaker than the one of monopole mode. This is because the large difference in metal surface area between the two layers and the metal tape. Nevertheless, the research focus is on whether the antenna can radiate at dipole mode. The radiation intensity is not of the main concern. Although the radiation has a tendency to backward couple with the Microstrip fringing field, the dipole-mode radiation guides the whole farfield pattern forwards. As the leaky wave radiation is susceptible to any E-field distribution, this forward farfield pattern once again

proves the existence of dipole-mode radiation. Therefore, the radiation from the second layer will not be guided back to the input port. Moreover, the 3 dB angular width in Figure 5-0-24 is 295.9 degree, as the radiation consists of two resonant modes. Figure 5-0-25 shows that the radiation efficiency and total efficiency are all close to 0 dB which suggest a 100% efficiency. Both the directivity and gain in monopole-mode are 3.941 dB, as the efficiencies are very high. The gain difference between the two modes is 1.241 dB. For solving the oblique radiation problem, further research is done to analyze the working mechanism of farfield radiation.

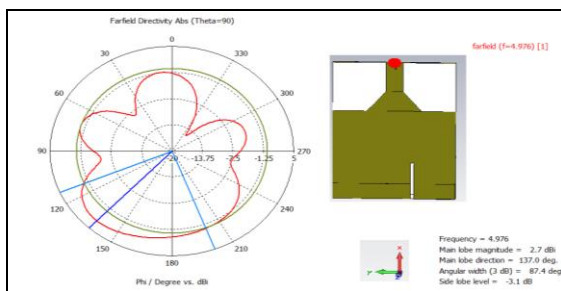


Figure 5-0-18: YOX top-plane Polar plot

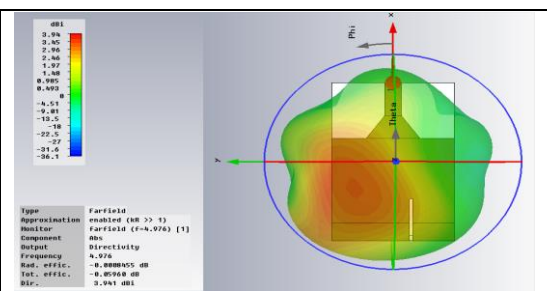


Figure 5-0-19 : YOX top-plane 3D farfield

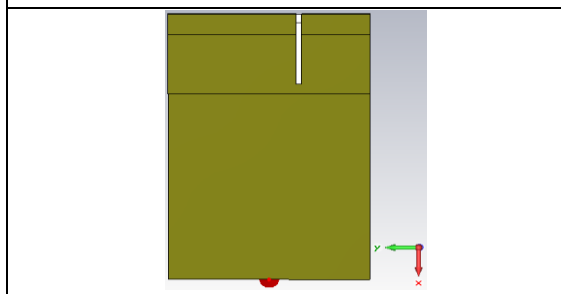


Figure 5-0-20: YOX bottom-plane of antenna

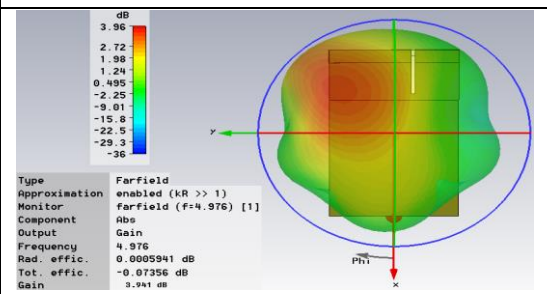


Figure 5-0-21: YOX bottom-plane 3D farfield

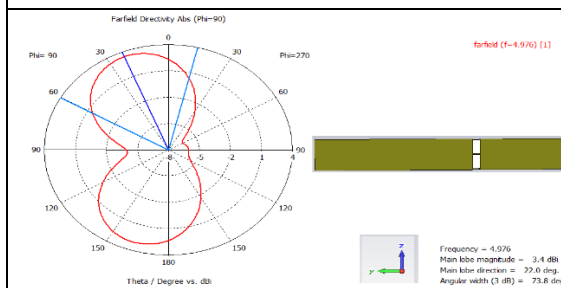


Figure 5-0-22: YOZ-plane polar plot

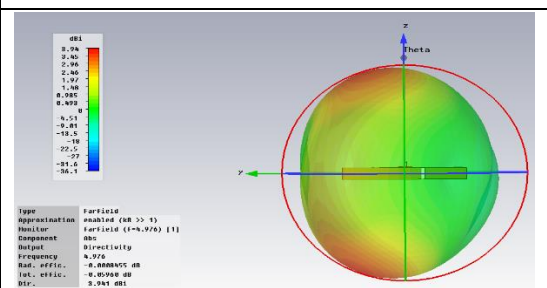


Figure 5-0-23: YOZ-plane 3D farfield

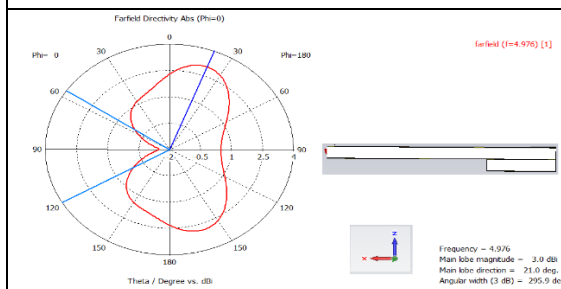


Figure 5-0-24: ZOZ-plane polar plot

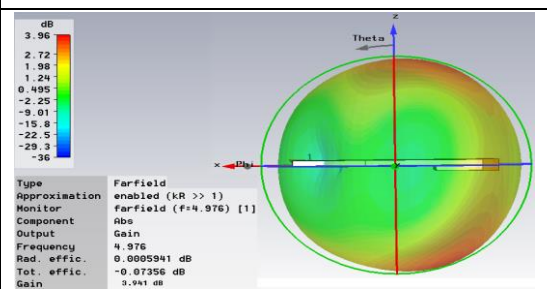
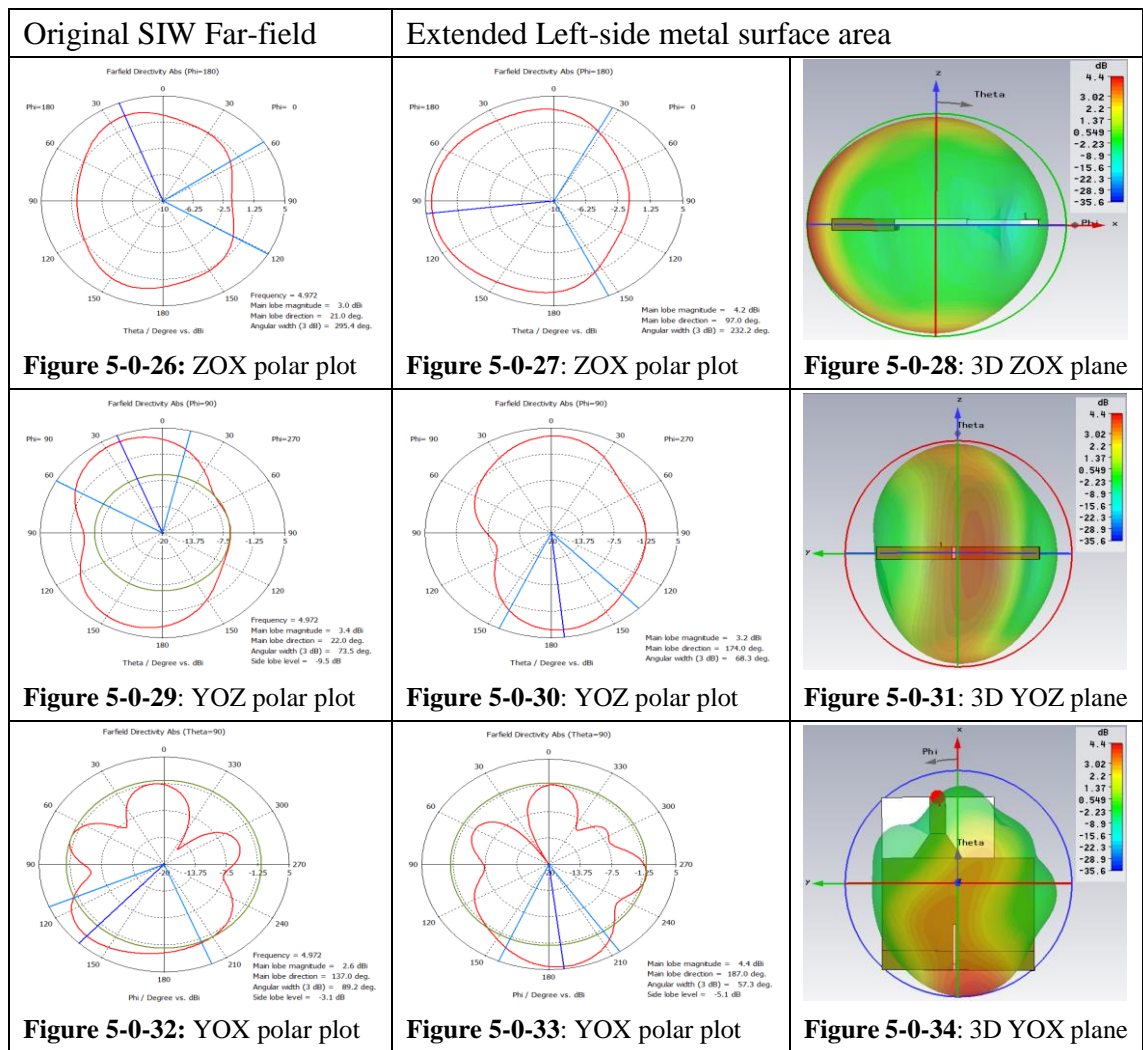


Figure 5-0-25: ZOZ-plane 3D farfield

5.2.7 Further research the antenna radiation



The extended structure shown in Figure 5-0-8 and Figure 5-0-9 is the proposed solution for improving the intensity of radiation at dipole mode. By jointing additional PCB, the waveguide left-side region is extended. The metal surface area at both sides of the slot is nearly symmetric. Although the metal surface area of waveguide is largely increased, the radiation efficiency and total efficiency still reach -0.0009598 dB and -0.1845 dB, respectively. Figure 5-0-26 shows the ZOZ plane polar plot of the original structure, of which the local main lobe is 3 dBi locating at 21 degree to the left. Figure 5-0-27 shows the corresponding polar plot of the extended structure. The local main lobe of the extended

structure is 4.2 dBi, which is 1.2 dBi larger than the one of the original structure. As shown in Figure 5-0-28, the main lobe direction of the extended structure apparently points to the front end. Moreover, the local 3dB beam width of the extended structure is 63.2 degree less than the one of the original structure. Therefore, the backward E-field component of the extended structure is smaller than the one of the original structure. Figure 5-0-29 and Figure 5-0-30 show the YOZ plane polar plots of the original structure and the extended structure, respectively. The local main lobe of the extended structure is 3.2 dBi, which is 0.2 dBi smaller than the one of the original structure. The 3 dB beamwidth of the original structure is 5 degree larger than the one of the extended structure. The local main lobe direction of the extended structure only deviates from the central axis by 6 degree, while the deviation in the original structure is 22 degree. Figure 5-0-31 clearly shows that the dominant radiation of the extended structure is at the dipole mode. Figure 5-0-32 and Figure 5-0-33 show the YOX plane polar plots of the original structure and the extended structure and the corresponding main lobe magnitudes of dipole mode. The gain of the extended structure is 4 dB which is 1.8 dB larger than the gain of the original structure. As the 3dB beamwidth of the extended structure is 57.3 degree which is 31.9 degree less than the beamwidth of the original structure, the main lobe of the extended structure is better aligned. Compared with the 43 degree deviation in the original structure, the main lobe of the extended structure only deviates from the central axis by 7 degree. The reason of the 7-degree deviation is that the PCB extension is 1.5mm wider than the design requirement due to manual error. Figure 5-0-34 shows that the radiation intensity of monopole mode is weaker than the one of dipole mode in the extended structure. Overall, the gain of the extended structure is slightly better than the one of the original structure, as the end-fire radiation of dipole mode is only affected by the metal area of metal tape.

5.3 Two symmetry slots antenna with cutting front-end

Based on the transmission line theory, at the short-circuited front end of waveguide the voltage will reach its minimum value, while the current will reach its maximum value. As current and voltage are out of phase by 90 degree, the voltage will reach its maximum at one-quarter-wavelength from the waveguide front end. This variation relation between voltage and current has been widely applied in the longitudinal slot of traditional waveguide. The following two designs are developed based on this variation relation.

5.3.1 Introduction

In this section, the design objective is to improve the radiation pattern. In general, the waveguide antenna has a relatively high gain. This feature is good for the electronically steered active phased array radar to detect in far distance. However, due to the narrow beamwidth, waveguide antenna cannot be widely used in civil products which usually prefer the wide-coverage antenna. For example, with a narrow beamwidth, waveguide antenna is not suitable for mobile phone, as the signal of antenna can be easily impeded by fingers and head. Moreover, the waveguide antenna is too big to be installed in mobile.

5.3.2 Symmetric slots structure and its parameters

To increase the beamwidth, one solution is to reduce the directivity of waveguide antenna. This section is going to present a novel waveguide antenna whose directivity is almost omnidirectional. This desirable characteristic is achieved by simply coupling the phases

of two slots without dealing with the complicated back-end system. The structure of the new antenna is shown in Figure 5-0-35. As we can see, the two slots are symmetrically located at the top and the bottom planes. However, the slots are offset to the right of the waveguide. This is distance from the slots to the right edge of the waveguide is 10.25 mm and to the left edge of the waveguide is 12.25 mm. The function of bottom slot is to cancel out the end-fire radiation and couple with the E-field at both sides of waveguide. Figure 5-0-36 and Table 5-1 together show the size of the antenna. The width of the metal side-wall is 2 mm. The overall size (Length X)*(Width Y)*(Height Z) of this antenna is 40.8*28*1.715 mm³ which includes the width of side walls and the thickness of surface copper.

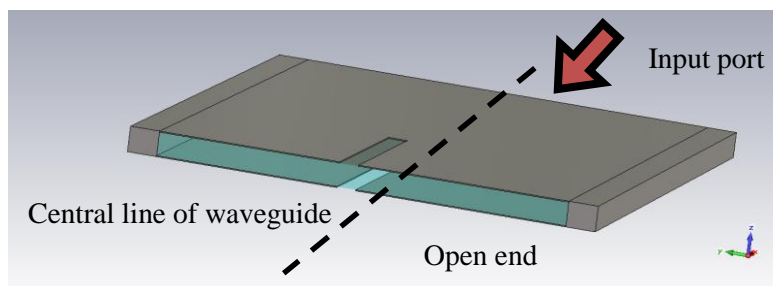


Figure 5-0-35: Perspective view (with inner dielectric transparent)

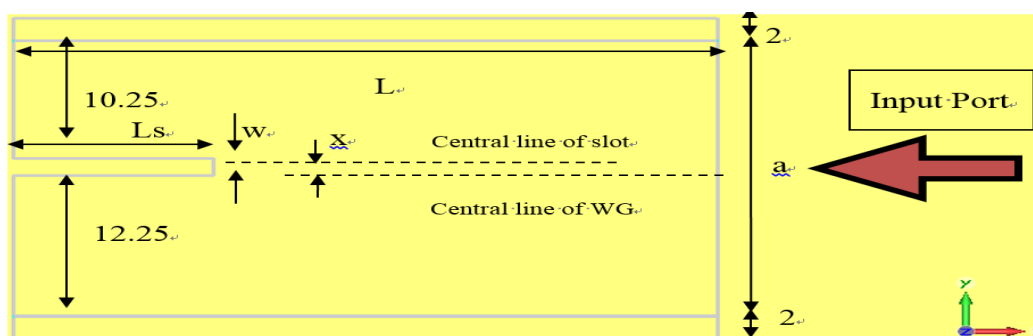


Figure 5-0-36: Parameters of structure

Parameters name	Length/Unit:mm	Description
L	$r*3= 40.8$	Length of waveguide antenna part
a	24	Waveguide width
b	1.575	Thickness of waveguide substrate
Ls	11.6	Slot length
r	13.6	One quarter lambda wavelength
w	1.5	Slot width
x	1	Offset of slot position from centre line of waveguide to edge

Table 5-1: Parameters of simulation antenna model

5.3.3 1D simulation result:

The following reflection coefficient $S_{1,1}$ are obtained by three iterations of the adaptive calculation. Although the adaptive mesh refinement requires 3-time passes, the adaptive results after two iterations are showed here. As the stop criteria have already been met, the mesh adaptation only runs for the minimum times of passes. Since the two $S_{1,1}$ curves in Figure 5-0-37 are nearly identical, the calculation results based on the two curves are convergent. Figure 5-0-38 shows that the $S_{1,1}$ result reaches -24.5 dB at 5.749 GHz and the bandwidth is 70.28 MHz at -10 dB. The energy balance in Figure 5-0-39 is around 0.06, which indicates that over 90% of the radiation energy is radiated to out space. Limited by the height of the PCB substrate, the slot width is set at 1.5 mm. If the slot width is set to be larger than the substrate height, part of the resonant E-field might be not able to cross over the slot but shorted to the waveguide inner ground. This is that though the bandwidth can be improved by increasing slot width beyond the height of substrate, the radiation efficiency will degrade. Figure 5-0-40 shows that bandwidth varies in the same direction with slot width, while the $S_{1,1}$ response varies in the reversed direction with slot width. As the thickness of PCB dielectric is 1.575mm, the slot width is set at 1.5mm.

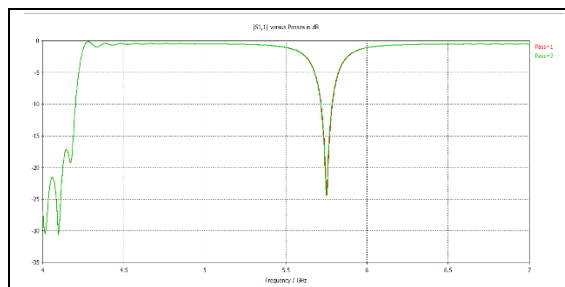


Figure 5-0-37: Adaptive calculation

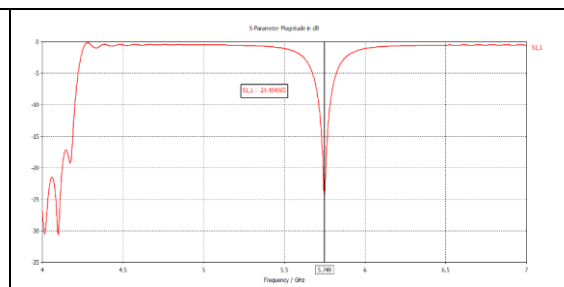


Figure 5-0-38 : S1,1 result in dB

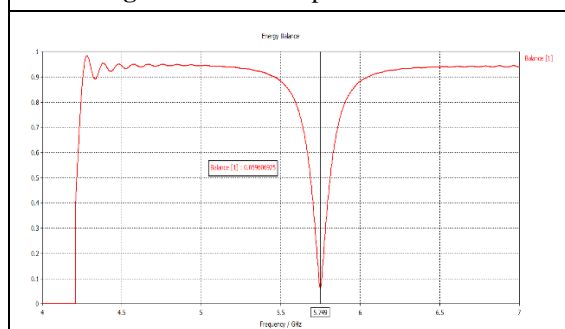


Figure 5-0-39 : Energy balance

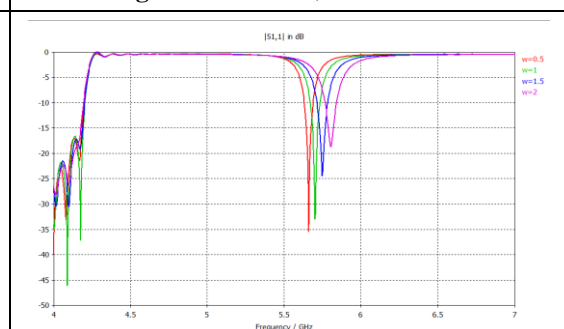


Figure 5-0-40: Slot width changing sweep results

Slot Width	Bandwidth	S1,1 result	Resonant frequency
W= 0.5	57.45 MHz	-35.393921 dB	5.659 GHz
W= 1	63.682 MHz	-33.001884 dB	5.701 GHz
W= 1.5	70.28 MHz	-24.494076 dB	5.749 GHz
W= 2	75.061 MHz	-18.783653 dB	5.803 GHz

Table 5-2: research slot width changing

5.3.4 Simulation of 2-D results: E-Field plot

The following E-field patterns in near field range are used to verify the feasibility of the design and show the working mechanism of the proposed antenna. First of all, it is important to show whether there are coupling E-fields at both sides of the antenna, and whether the E-field at the antenna front-end is cancelled out. Figure 5-0-41 clearly shows that the E-fields vectors on the top and the bottom slots are in opposite directions. Therefore, these E-fields vectors are in phase and can couple with each other at both sides of the antenna. Figure 5-0-42, as a schematic plot, shows the coupling phenomenon in Figure 5-0-41 and the direction of E-field vectors. Figure 5-0-43 clearly shows that the directions of E-field vectors between left-hand side of slots and right-hand side of slots are 180 degree out of phase in front of the antenna open-end. So that, the entire E-fields in front of slots at the open end side of waveguide are totally cancelled out. This is the main reason why this structure only has left and right side-fire radiation. Also, this reason explains why the bandwidth of this antenna is narrow. Because the longitudinal slot waveguide antenna usually has end-fire in the terminal, the E-field cancelling out in front of open side will counteract the most resonance frequencies of slot, which leaves the slot only resonating in narrow frequency range. This is the main weakness of this structure. Figure 5-0-44 simplifies the E-field cancelling phenomenon of Figure 5-0-43 .

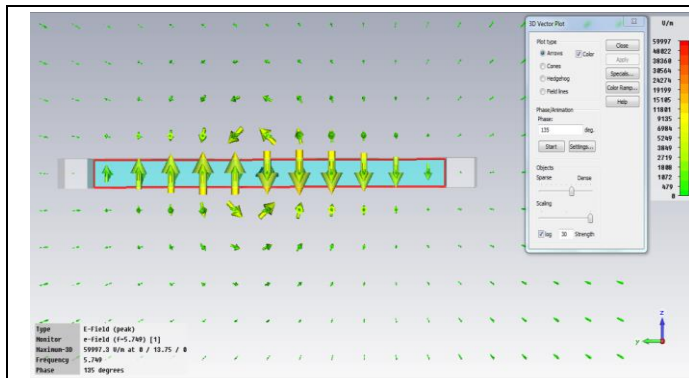


Figure 5-0-41: E-field pattern looking from the terminal side.

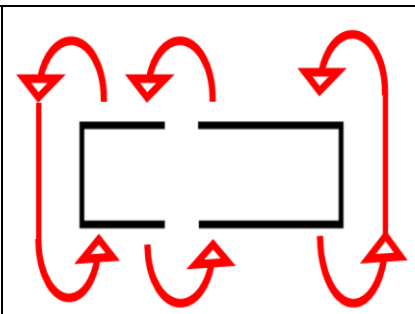


Figure 5-0-42 : Simplified diagram of E-field coupling

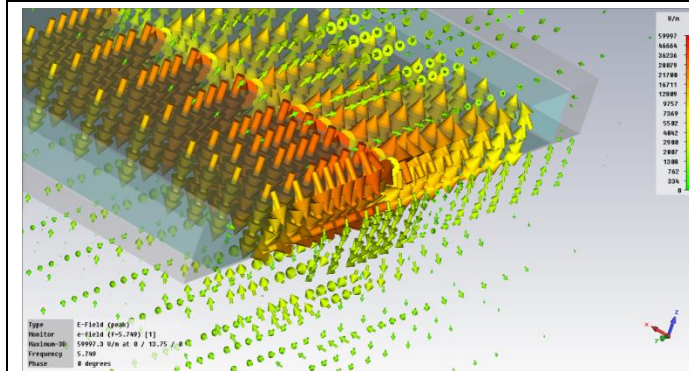


Figure 5-0-43 : Cancelling phenomenon of E-field

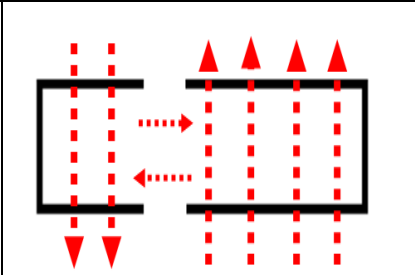


Figure 5-0-44 : Simplified diagram of E-field cancelling

As the structure has been proved to be able to work as predicted based on the theory of phase combination, we will now explore the field theory in detail. Figure 5-0-45 to Figure 5-0-48, are a series of YOX plane E-field patterns with the phase changing from 0 degree to 135 degree. These graphs reveal how the E-fields change at both sides of the slot. As the phase increases, the E-fields at both sides of the antenna gradually strengthen, and continually become a complete circle. These graphs show that the side-fire radiation is caused by the slots, but not the diffraction at the front-end corners. Theoretically, for this kind of antenna, diffraction is an inherent problem and cannot be circumvented. Also, as the length of antenna is shorter than the one of original structure, radiation energy cannot be completely emitted to outer space, the remaining radiation power will propagate along the antenna metal surface and back to the input port. This intrinsic defect always accompanies the minimized open-end antenna. However, this will not be a problem for the proposed antenna, as the antenna has a slot working at the bottom plane, which can have all the end-fire and back-fire radiation E-fields been cancelled out. So that, the

remaining power, which usually is the source of diffraction, can fully radiate at the two sides of the antenna. The aim of this design is to solve the diffraction problem by having the remaining power been sufficiently radiated. Thus, by changing the radiation direction of the antenna, we can include the diffraction into the main lobe radiation. The diffraction, as a result, can be productively utilized. Normally, the sharp edge of waveguide open-end will produce forward radiation. However, for the proposed antenna, the E-field in front of open-end couples with the radiations of slots on the waveguide left side. This is because the metal surface area on the left side of the slot is larger than the one on the right side. Hence, the E-field gradient on the right side of the slot is stronger than the one on the left side. Therefore, the radiation E-field direction of open-end trends to the waveguide left side. This principle can also be applied to the current distribution on the metal surface, which is shown in Figure 5-0-49. The slots divide the edge of open-end into two parts. As both sides of open-end have the same kind of current distribution with the ones at slots, the edge of open-end radiates the same frequency mode with the slots. As the edge of open-end at left side of slot has longer length than the one at right side of slot, the surface current at the right-side of the open-end converges stronger intensity along the edge than the one at left-side edge of the open-end. Therefore, the E-field on the right side of open-end will not be totally neutralized by the E-field on the left side. The remaining E-field energy will propagate toward the left edge of open-end, and then couple with the radiation E-field there. This progress will strengthen the E-field at the left side of slot, which is shown in Figure 5-0-46, Figure 5-0-47 and Figure 5-0-48. Figure 5-0-50 and Figure 5-0-51 show the ZOY-plane E-field pattern of the antenna. The maximum amplitude of E-field at $Y=12.25$ mm is 37168.9 V/m which is smaller than the one at $Y=13.75$ mm with a value of 51061.6 V/m. Therefore, the peak of E-field once again is proved to be at the narrow side of the waveguide.

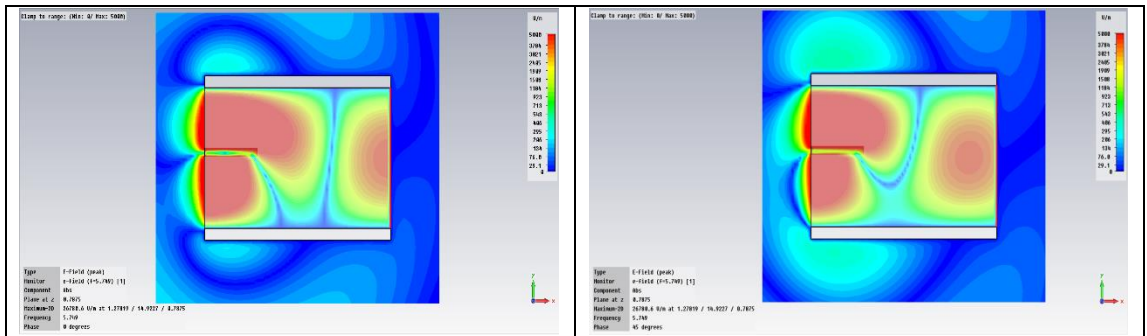


Figure 5-0-45 : 0 phase degrees in YOX plane

Figure 5-0-46 : 45 phase degrees in YOX plane

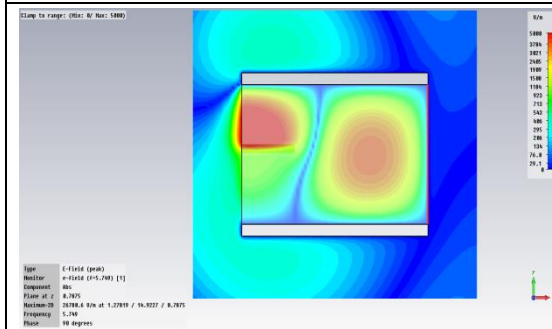


Figure 5-0-47 : 90 phase degrees in YOX plane

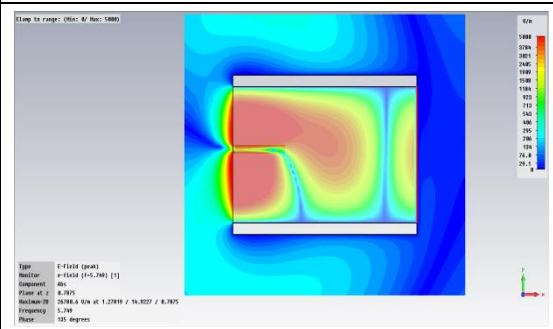


Figure 5-0-48 : 135 phase degrees in YOX plane

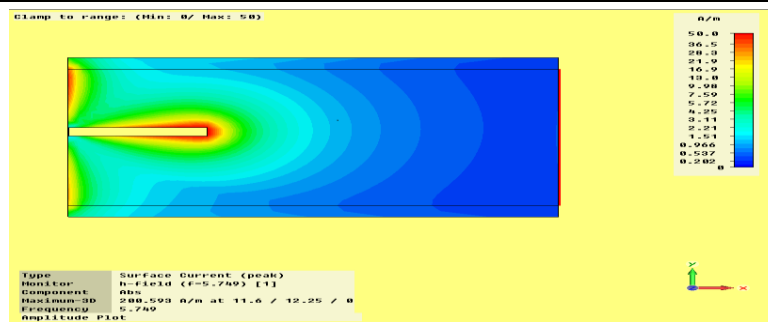


Figure 5-0-49 : Current distribution at top surface YOX plane

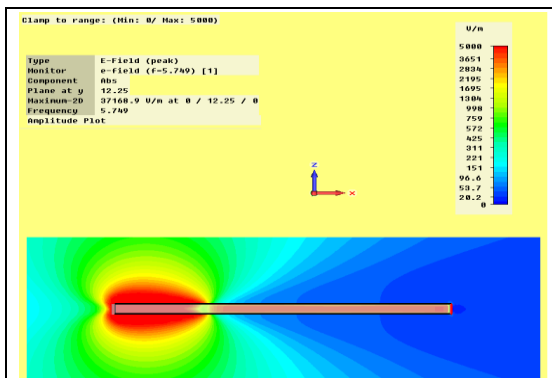


Figure 5-0-50:ZOX plane E-field at y=12.25mm

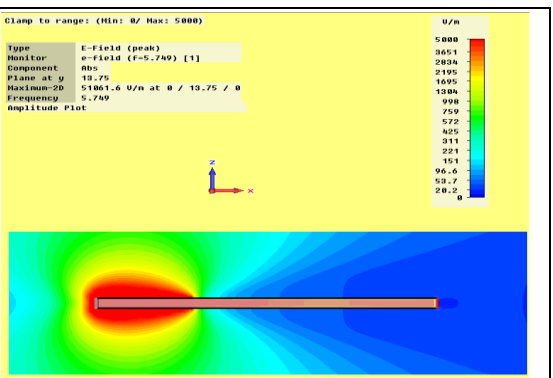


Figure 5-0-51: ZOX plane E-field at y=13.75mm

For double check, we would like to compare the E-field results in the ZOX cut plane and YOZ cut plane. Figure 5-0-52 to Figure 5-0-55 are the ZOX cut-planes at Y=13.75 mm where is the maximum amplitude of E-field can be observed. The E-fields emitted from

the top and the bottom slots are symmetric and have the same intensity. The radiation direction is vertical to the slots. And there is a diffraction propagating along the broad-wall metal surface towards the input port. However, the magnitude of diffraction is negligible relative to the radiation E-field. The tiny diffraction arises because the metal surface area of broad walls in longitudinal direction is larger than the one in transverse direction. When most of the E-field is radiated to free space in Y-axis direction, the broad walls guide the X-axis backward component of residual E-field back to input port. Figure 5-0-56 to Figure 5-0-59 are the YOZ cut-plane at X=0 mm, showing the variations of E-field at the edge of open-end. The E-field from the left side of slot will cross over the slot towards the right side, as the magnitudes of E-fields at the two sides are not uniform. Therefore, the stronger E-field on the left side will couple with the E-field on the right side when the slots mainly radiates at Y-axis. Hence, the E-field in the right side, though having a larger scope, actually is smaller than the one in the left side.

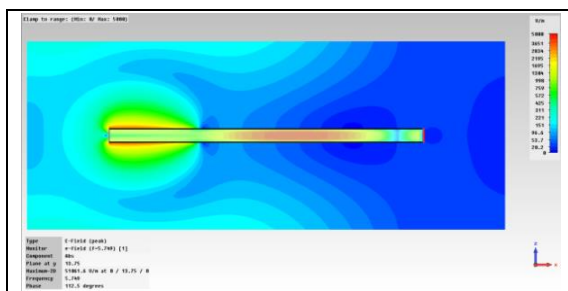


Figure 5-0-52:ZOX at Y=13.75mm Phase=112.5°

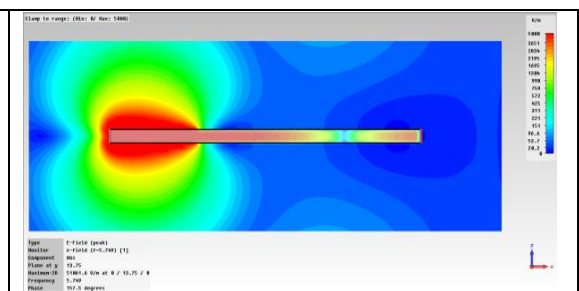


Figure 5-0-53:ZOX at Y=13.75mm Phase=157.5°

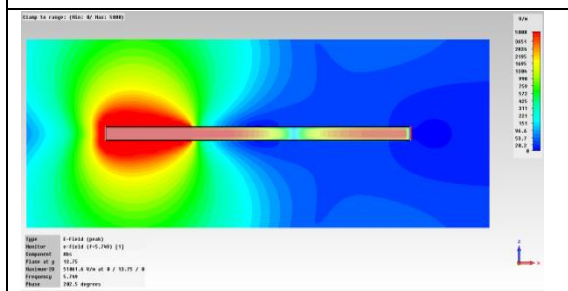


Figure 5-0-54:ZOX at Y=13.75mm Phase=202.5°

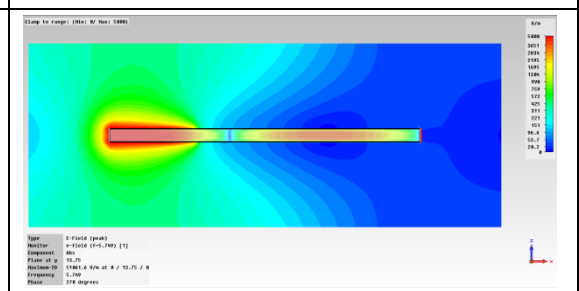


Figure 5-0-55: ZOX at Y=13.75mm Phase=270°

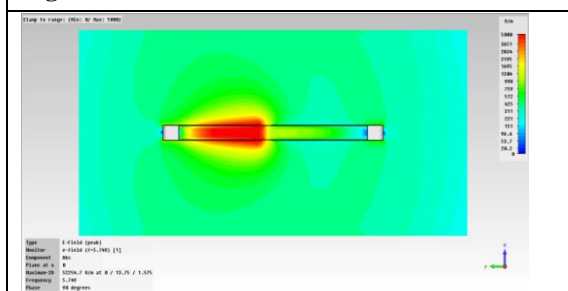


Figure 5-0-56: YOZ at X=0 mm Phase =90°

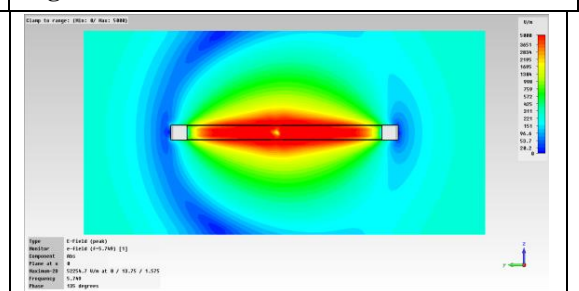
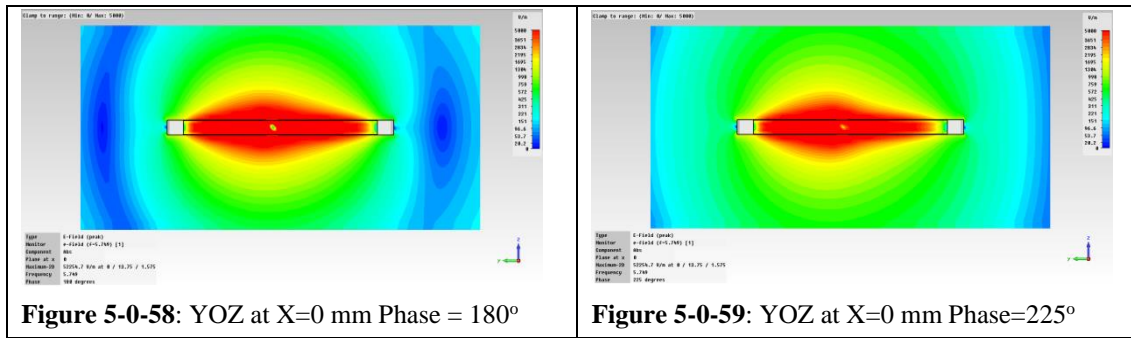


Figure 5-0-57: YOZ at X=0 mm Phase =135°



5.3.5 Simulation of 3-D results: Farfield pattern

Next, we need to study the farfield results to confirm whether the antenna can work as designed. Figure 5-0-60 to Figure 5-0-65 show a series of farfield patterns and corresponding polar plots. The radiation efficiency and total efficiency are -0.006628 dB and -0.02209 dB, respectively. The extremely small values of the efficiencies suggest that nearly 100% of the incident energy is effectively radiate to outer space. Also, the gain observed is 1.93 dBi which is slightly smaller than the one of half-wavelength dipole antenna with a value of 2.15 dBi. Therefore, the radiation of this antenna has a large coverage. Figure 5-0-60 and Figure 5-0-61 are the XOZ plane side-view of the waveguide, showing the three-dimensional pattern of 3 dB beamwidth and the intensity of radiation component at Z-axis, respectively. In Figure 5-0-60, the radiation resultant between the top and the bottom slots are vertical to the waveguide. Thus, the radiations intensity of both slots are equal. The main lobe of the polar plot, as shown in Figure 5-0-61, tilts 6-degree towards to the front end of the waveguide due to the coupling with the E-field of open-end. Figure 5-0-62 and Figure 5-0-63 are the YOZ cut-plane front view. In the graphs, the far-field has a round shape and mainly concentrates at the two sides of the antenna, of which the pattern is very similar to the radiation pattern of dipole antenna. Figure 5-0-64 and Figure 5-0-65 are the XOY cut-plane top-views. The two radiation patterns shown in Figure 5-0-64 are different in the range of 3 dB beamwidth, which means that the

attenuation of radiation energy is unequal. Moreover, the main lobe in Figure 5-0-64 also points to front open-end. Because the radiations of slots couple with the E-field of front open-end at the wide-edge side. Overall, the farfield results consistently support that the proposed antenna can work as designed. The main lobe magnitude around the circle of farfield varies between 1.1 dBi and 1.9 dBi.

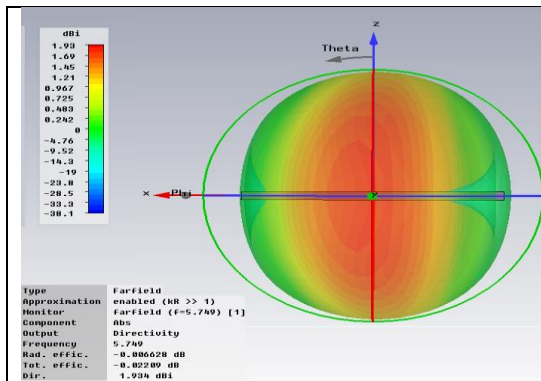


Figure 5-0-60: YOZ plane view of 3D Farfield

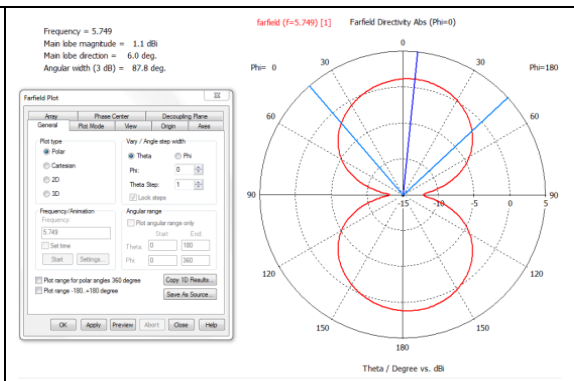


Figure 5-0-61: YOZ plane view of 2D Farfield

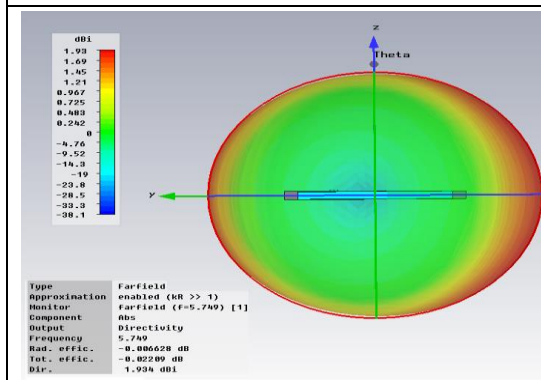


Figure 5-0-62: XOZ plane view of 3D Farfield

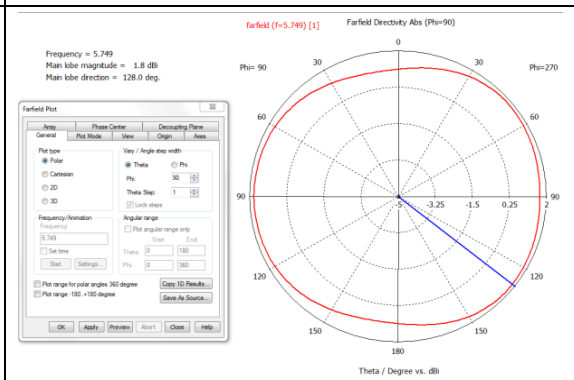


Figure 5-0-63: XOZ plane view of 2D Farfield

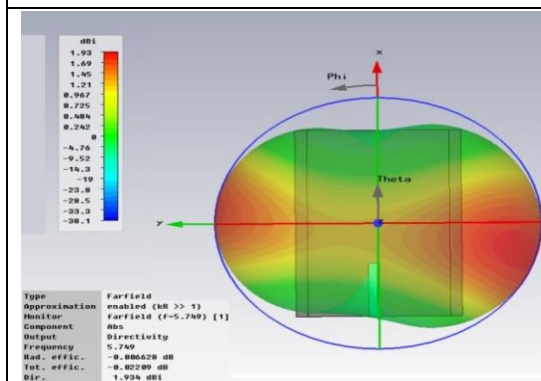


Figure 5-0-64: XOY plane view of 3DFar-field

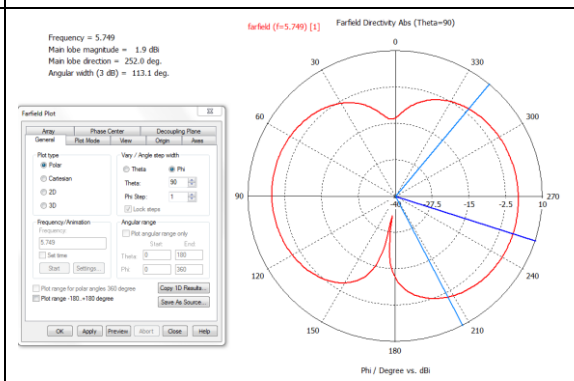


Figure 5-0-65: XOY plane view in 2D Farfield

5.4 Two non-symmetric slots antenna with cutting front-end

As we can find in the above analysis, the symmetric slot design, though, can increase radiation angle to almost 360 degree, it causes E-fields to cancel out each other at the front end of the antenna, which means that there is no end-fire radiation. Moreover, in that design, a great proportion of the radiation E-fields are neutralized, the bandwidth of the antenna, as a result, is sacrificed. Nevertheless, the symmetric slot design can be suitable for wide-angle communication. Theoretically, the symmetric slots antenna can get a wider bandwidth by fully taking the advantage of the coupling effect if the positions of the in-phase E-fields and the anti-phase E-fields are reversed. For keeping the advantages in simple fabrication and small size, the symmetric slots antenna will be modified to meet specific requirements for wide band applications. A new SIW antenna will be built with non-symmetric slots.

5.4.1 Antenna structure and its parameters

The dimension (Length X)*(Width Y)*(Height Z) of the antenna is $40.8 \times 28 \times 1.715$ mm³, where the width of side walls, 2 mm, and the thickness of copper surface, 0.07 mm, are included. Figure 5-0-66 and Figure 5-0-67 show the structure of the non-symmetric slots antenna. The light cyan part in Figure 5-0-66 represents the substrate dielectric, and the grey part represents the copper surface. Though the symmetric slot antenna and the non-symmetric slot antenna are identical in size, the positions of slots in the two antenna are different. As shown by the Figure 5-0-67, in the non-symmetric slot antenna, slots on different planes locate at the two sides of the waveguide central line. Figure 5-0-68 uses a YOZ-plane wireframe-mode view to show the parameters of the structure. To distinguish

the parameters between the two planes, dashed line with arrows are used to show the bottom plane parameters, and solid lines with arrows are for the top plane parameters.

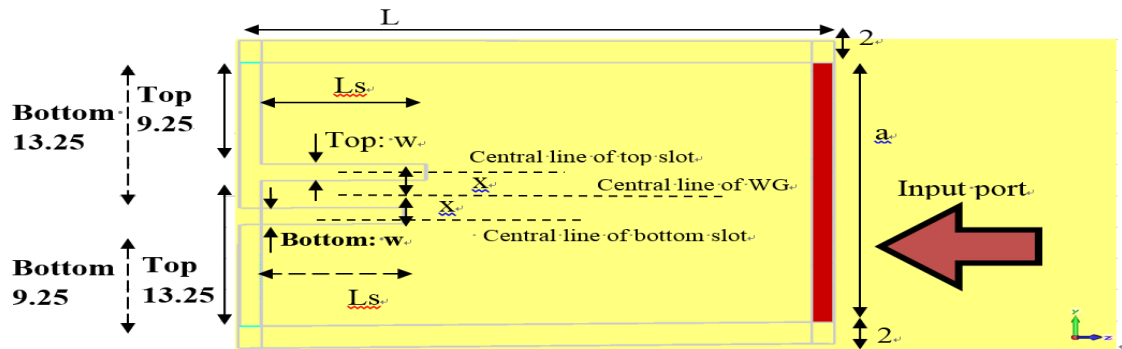
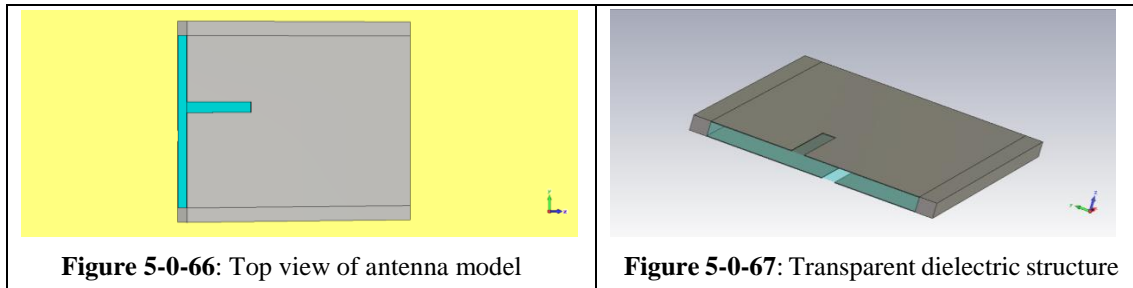


Figure 5-0-68: Parameters of structure displayed in wireframe-mode view

Parameters name	Length/Unit:mm	Description
L	$r*3= 40.8$	Length of waveguide antenna part
a	24	Waveguide width
b	1.575	Thickness of waveguide substrate
T	0.07	Thickness of surface copper
Ls	11.6	Slot length
r	13.6	One-quarter-lambda wavelength
w	1.5	Slot width
x	2	Offset of slot position from centre line of waveguide to edge

Table 5-3: parameters of simulation antenna model

5.4.2 Simulation of 1-D Result:

The following reflection coefficient $S_{1,1}$ result is obtained by three-time iterations of the adaptive calculation. As shown in Figure 5-0-69, the $S_{1,1}$ result is about -19.4775 dB at 5.416 GHz, and the bandwidth is 1.2023 GHz at -10 dB. To express this 1.2023 GHz bandwidth in fractional is around 22.199 %. With a fractional bandwidth not less than

20 %, this new antenna is a wideband antenna. The energy balance, shown in Figure 5-0-70, is about 0.1, which is slightly less than the one of the symmetric slot structure. In fabrication, the etching has a 0.07 mm tolerance. So, 1.5 mm is the maximum slot width that can be achieved. If the slot width is larger than the thickness of substrate, the slot will not only have a resonance phenomenon but also have unwanted leaking.

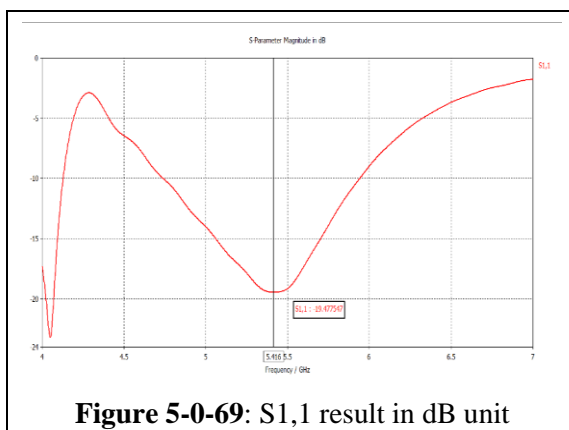


Figure 5-0-69: S1,1 result in dB unit

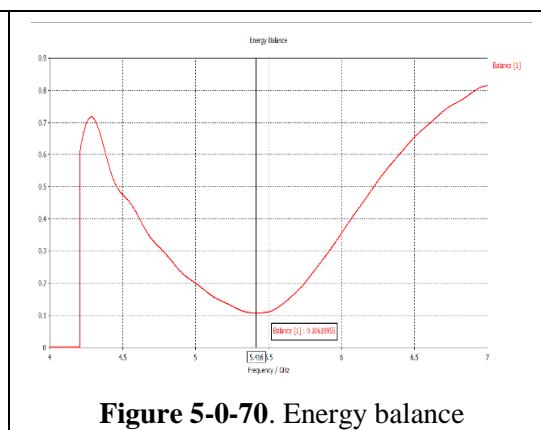


Figure 5-0-70: Energy balance

5.4.3 Simulation of 2-D results: E-Field plot

The E-field distribution in the near field range is of the main concern. Therefore, it is necessary to analyze whether the E-fields are in-phase at the front-end of the waveguide and anti-phase at the two sides. Figure 5-0-71 shows the E-field at the front-end of the waveguide in YOZ cut-plane. The E-fields on the top and bottom planes are in the same direction. Thus, these E-fields will be out of phase at the two sides of waveguide, as shown in Figure 5-0-72. But for a particular side, the intensities of the E-fields from the two slots are different depending on the relative positions of the slots to the side edge. This is because the two E-fields propagate at different distances on the metal surface. For example, at the left side of the waveguide front end, the top-slot E-field is weaker than the bottom-slot E-field, as shown in Figure 5-0-73. This is because compared with the top slot, the bottom slot is closer to the left edge of waveguide. Thus, the distance for the bottom-slot E-field to propagate to the waveguide left edge is shorter. For the same reason, at the right side of the waveguide front end, the top-slot E-field is stronger than the bottom-slot E-field, as shown in Figure 5-0-74. As the resultant E-fields on both sides of the waveguide

are composed by unequal E-fields, there is a potential to appear back-fire E-field due to the excess energy at the two sides. This potential will be tested later. Figure 5-0-75 shows the in-phase coupling phenomenon in the front end of the waveguide. Figure 5-0-76 clearly shows that the E-fields move from right to left on the waveguide. This is because E-fields, as previously mentioned, are anti-phase at the two sides of waveguide. The E-fields in front of the waveguide are in-phase, which is verified by Figure 5-0-75. Furthermore, Figure 5-0-75 also shows that the E-field in front of waveguide is stronger than those on the waveguide surface. Therefore, most of E-field energy concentrates on the waveguide front end. Figure 5-0-71 to Figure 5-0-76 prove that the antenna can work as designed. As the E-field distribution is consistent with prediction, the working mechanism of this structure will be further analyzed. Figure 5-0-77 is the YOX cut-plane at $Z=0.7875$ mm. As shown by the Figure 5-0-77, the two slots and part of the open-end of the waveguide are covered by strong E-fields, part of which propagate along the edge sections of the open-end to the corners and generate an end-fire radiation. Therefore, besides the designed frequencies, other frequencies can also be resonated at the edge sections of front open-end which produces end-fire radiation at dipole mode. But the resonant E-fields at the edge sections will increase the diffraction around the front corners of waveguide. Although the magnitude of diffraction is small compared with the one of the end-fire radiation, the diffraction still will disperse the radiation E-field back to input port and store this energy in the near field. This is the reason why the energy balance of the non-symmetric slot structure is slightly lower than the one of the symmetric slot antenna. Figure 5-0-78 is the YOZ cut-plane at $X=0$ mm. As show in this graph, there are strong scattering at the front corners of the waveguide. And the two slots upward radiate at monopole mode.

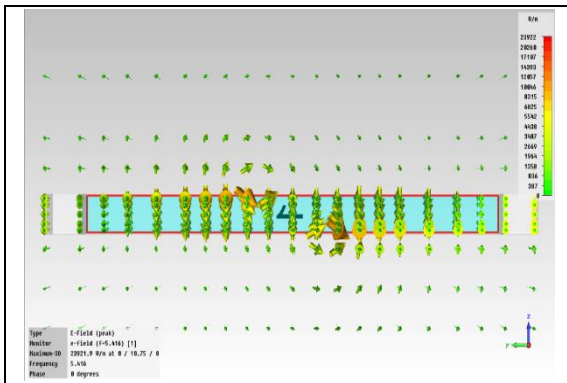


Figure 5-0-71: Cancelling phenomenon of E-field

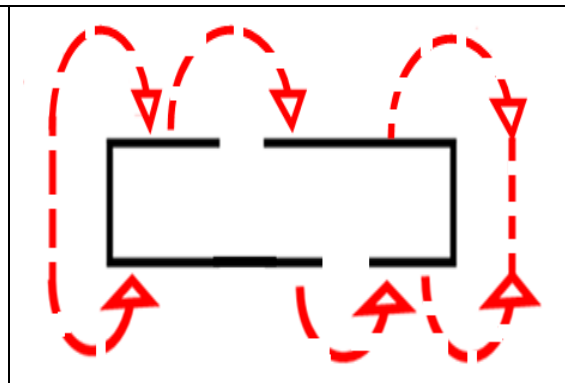


Figure 5-0-72: Simplified E-field cancelling

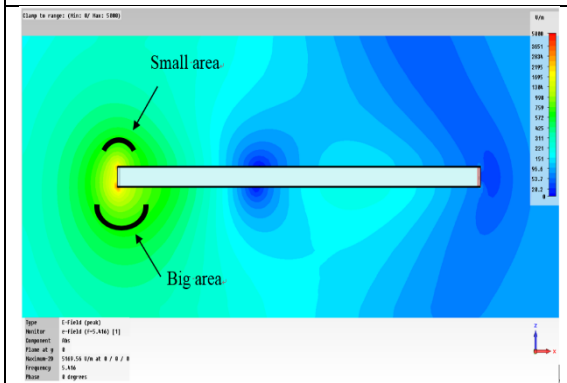


Figure 5-0-73: XOZ-plane E-field at Y=Z=0

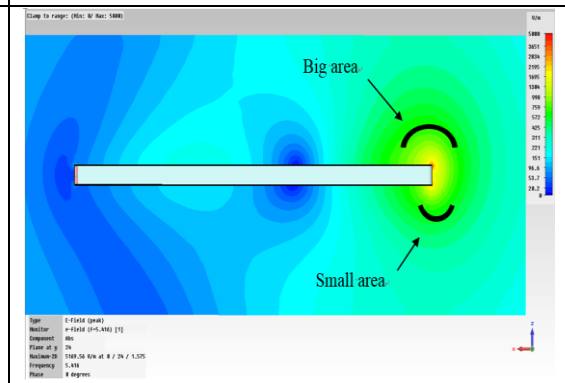


Figure 5-0-74 : XOZ-plane at Y=24 Z=1.575

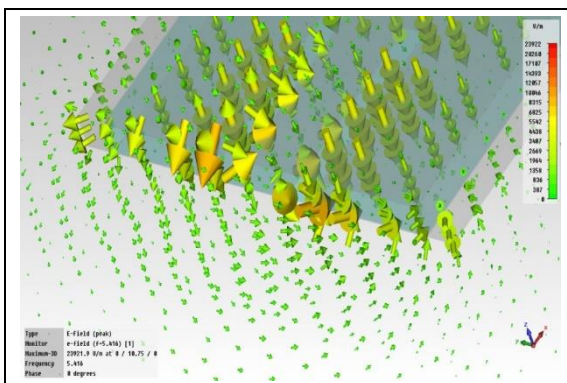


Figure 5-0-75: E-field coupling at the front end

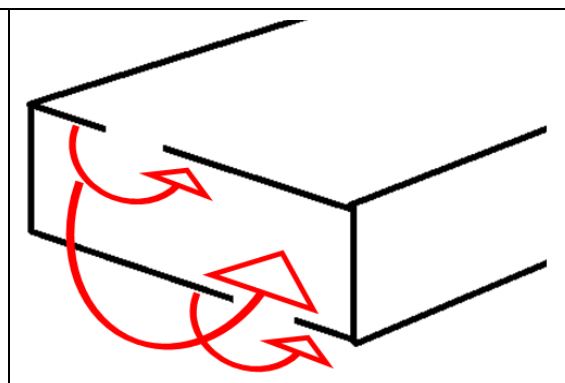


Figure 5-0-76: Simplified E-field coupling

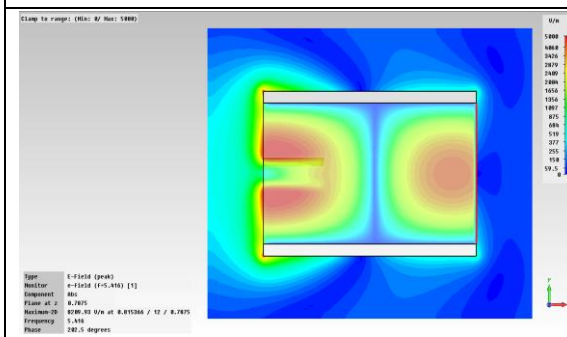


Figure 5-0-77: E-field distribution in YOX plane, Z=0.7875mm inside the waveguide.

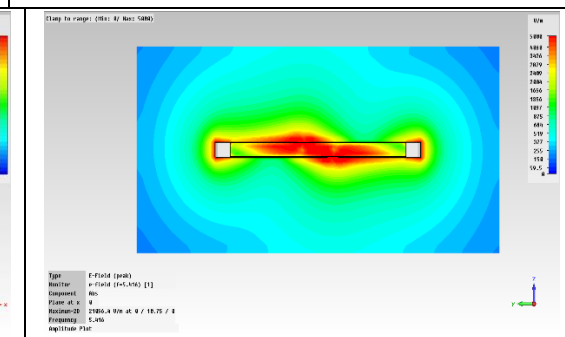


Figure 5-0-78: E-field distribution in YOZ plane, X=0 mm, at the edge of waveguide front-end.

As Figure 5-0-78 suggests that the peaks of the E-fields locate on the slots, the E-field patterns on the slots are worthwhile to further analyze. In the ZOx cut-plane of Figure 5-0-79, the peak of the top-slot E-field, with a value of 19594.7 V/m, locates at the slot edge, where $Y=14.75$ mm. The peak of the bottom slot E-field locates at $Y=9.25$ mm, as showed in Figure 5-0-81, with a value of 19594.7 V/m. The above results show that the E-fields of the two slots are symmetric with each other and locate closely to the center line of waveguide. Thus, the E-field intensity at the waveguide center line is worthy to check. As shown in Figure 5-0-80, the vast majority of E-fields symmetrically concentrate at the front end of the waveguide, and the rest of E-fields are evenly distributed on the top and the bottom surfaces. The waveguide center line, in fact, acts like a watershed. On the left side of the center line, the bottom-slot E-field dominates; while on the right side the top-slot E-field dominates. In Figure 5-0-79 to Figure 5-0-81, the amplitude of back-fire E-field is not large. Therefore, the backward component of E-fields mainly locates at the two sides of waveguide.

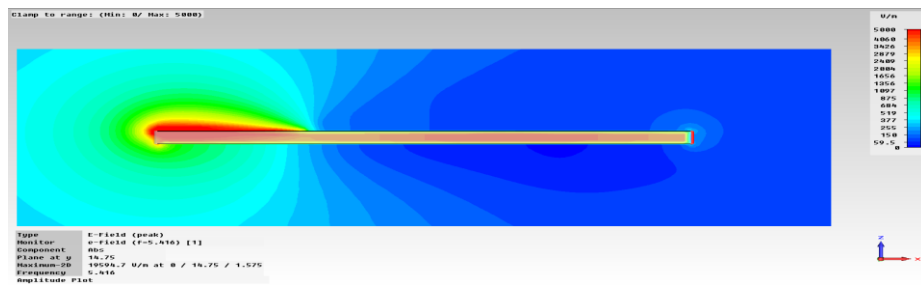


Figure 5-0-79 : ZOx plane top slot E-field at $y=14.75$ mm

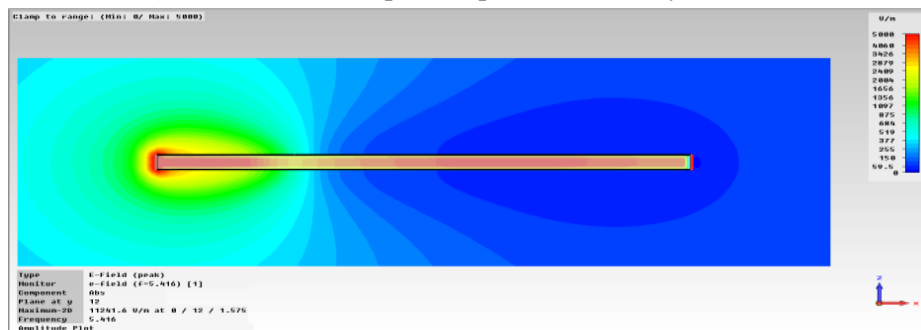


Figure 5-0-80 : ZOx plane $Y=12$ mm in middle central line of waveguide

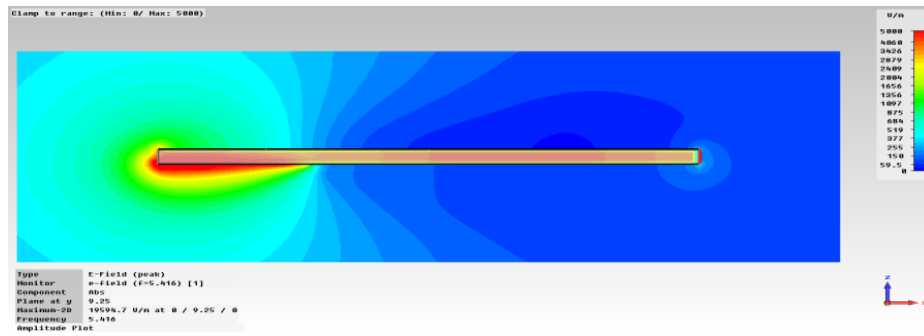


Figure 5-0-81 : ZOx plane bottom slot E-field at y=9.25 mm

5.4.4 Simulation of 3-D results: Farfield pattern

The resonance frequency of this structure is at 5.416 GHz. The radiation efficiency and the total efficiency are 0.0006421 dB and -0.04862 dB, respectively. These extremely small efficiency values suggest that nearly 100% of the energy is radiated to outer space. The gain is 3 dBi, which is slightly larger than the one of symmetric slots antenna. As showed in Figure 5-0-82, the 3 dB beamwidth of the non-symmetric slots antenna yet can reach about 309.5 degree. Figure 5-0-82 and Figure 5-0-83 show that there are two main lobes in the XOZ cut-plane. One points to 45 degree upward; another points to 45 degree downward. Also, there is an end-fire radiation between the two main lobes. Since the forward radiation is composed by the radiations from the two slots, there is a little cavern between the two main lobes which suggests that the radiation at the cavernous position is a bit weaker. Figure 5-0-84 and Figure 5-0-85 show that the farfield main lobe points straightly forward. The main lobe strength of the end-fire dipole mode is 2.5 dBi which is smaller than the 3 dBi of monopole mode in Figure 5-0-82. Therefore, the dominant radiation of this antenna is the monopole mode. At the two sides of the waveguide, E-fields from the top and the bottom slots are unequal, so that these E-fields cannot cancel out each other completely. Therefore, the excess E-field energy causes farfield side lobe at the two sides of the waveguide, as shown in Figure 5-0-84. Nevertheless, these side lobes are weak. The main lobe pattern in Figure 5-0-86 is similar to the radiation of

quarter-wavelength monopole antenna. This is because the slot length of the non-symmetric slots antenna is about one-quarter-wavelength. Also, Figure 5-0-87 show that the resultant radiation in the front of the waveguide is composed by the radiations from the top and the bottom slots.

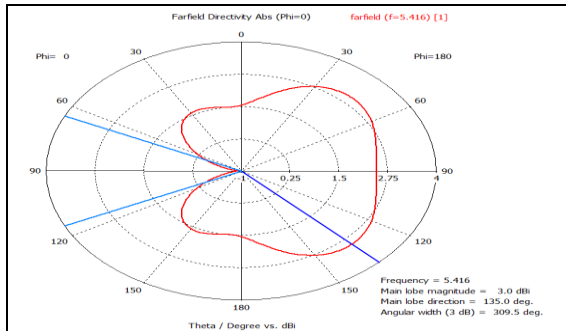


Figure 5-0-82: XOZ plane in 2D

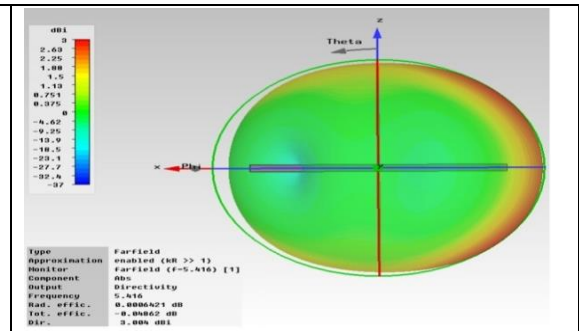


Figure 5-0-83 : XOZ plane in 3D

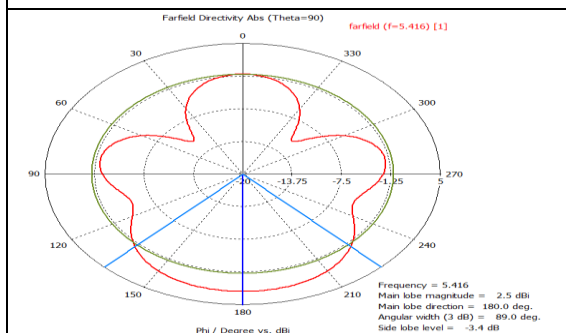


Figure 5-0-84: YOX plane in 2D

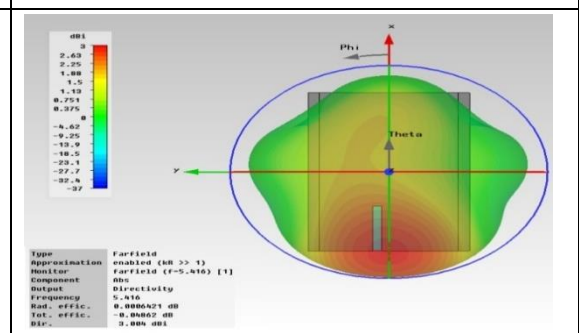


Figure 5-0-85 : YOX plane in 3D

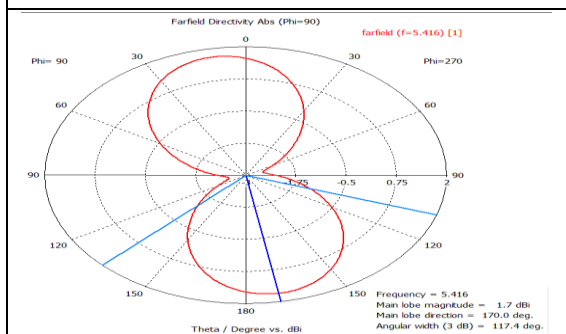


Figure 5-0-86 : YOZ plane in 2D

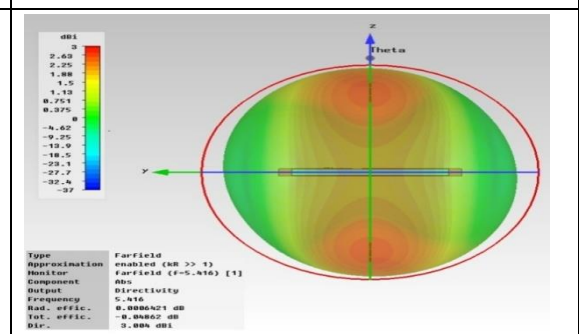


Figure 5-0-87 : YOZ plane in 3D

5.5 Conclusion

In this chapter, three antenna designs are introduced. The first is a novel SIW slot antenna with a C-type folded front-end. The length of the original SIW antenna is reduced by a length of quarter-wavelength. This new front-end folded antenna has two advantages. Firstly, the degradation in farfield pattern of new antenna is small. For symmetry farfield pattern, the new antenna just need to make both sides of slot equal. But, transversely folded antennas need to extend the metal surface area over half area of original broad-wall. Secondly, the middle air gap in front-end folded antenna only affects the bandwidth and has not limitation in half of the SIW height. Therefore, the new SIW structure is easy for fabrication.

As the size of middle air gap in fabrication is smaller than the one in simulation model, the measured bandwidth is only one half of the simulation result. But this folded SIW antenna fed by leaky wave mode still has a bandwidth of 200MHz. As the measured $S_{1,1}$ result at the dipole mode does not show any effective response below -10 dB around 5.5 GHz, the dominant radiation of this folded antenna is at the monopole mode. In order to change the dominant radiation mode, a research about the farfield pattern has been implemented. The research showed that the far-field pattern is decided by the waveguide metal surface area. By extending the waveguide metal surface, the extended structure can radiate at the dipole mode. Compared with traditional waveguide, the folded SIW antenna has a smaller metal surface perpendicular to the radiation direction. Usually, the metal surface area on the metal tape is only 13% of the metal surface area of traditional waveguide radiating at dipole mode.

The second is a symmetric slots antenna which has shorter length than the one of original antenna, as the front-end is directly cut down by one-quarter length of guided

wavelength. Moreover, the slot length of new antenna only is one half of original antenna's slot. The proposed antenna has been proved to be feasible in simulations. These symmetric slots are designed for increasing the radiation angle by composing a radiation pattern similar to dipole antenna radiation pattern. The farfield of symmetric slots antenna looks like two monopole antenna working at both sides of waveguide. The most attractive characteristic of this antenna is that a broad coverage of radiation angle in waveguide is achieved by simply utilizing the coupling effect of E-fields. Nevertheless, this waveguide antenna has advantage in compact size, simple structure and easy fabrication. However, the bandwidth of this antenna is narrow and only suitable for current Wi-Fi application.

The third is the non-symmetric slots antenna which is proposed for solving the narrow bandwidth problem in the symmetric slots antenna. The major active advantage in this structure is that this antenna can significantly improve bandwidth without losing too much coverage of radiation angle compared with the symmetric slots structure. The bandwidth of the non-symmetric antenna is 17 times larger than the one of the symmetric antenna. Although the non-symmetric slots antenna mainly works like the quarter-wavelength monopole antenna, the gain difference between dipole mode and monopole mode in this antenna is 0.5 dBi. Other advantages of this design are easy fabrication and adjustment. The reason that we keep developing the symmetric slots structure to non-symmetric slots structure is that these structures with four slots have potential to develop PIN-diode switching antenna between omnidirectional radiation and wideband radiation.

References

- [1] D. Stephens, P. R. Young, I. D. Robertson, "W-band Substrate Integrated Waveguide Slot Antenna", *Electron.Lett.*, 41, (4), pp. 165-167, February 2005.
- [2] A. J. Farrall and P. R. Young, "Integrated waveguide slot antennas," *Electron. Lett.*, vol. 40, No. 16, , pp. 974-975, 5th August 2004.
- [3] Hiroshi, U., Takeshi, T., and Fujii, M.: 'Development of a "laminated waveguide"', *Microwave Symposium Digest, 1998 IEEE MTT-S International*, Baltimore, MD, USA, vol. 3, June 1998, pp. 1811-1814.
- [4] Deslandes, D., and Wu, K.: "Integrated microstrip and rectangular waveguide in planar form", *IEEE Microw. Wirel. Compon. Lett.*, vol.11, no.2, pp. 68-70, 2001.
- [5] Barrow, W. L.; Schaevitz, H., "Hollow pipes of relatively small dimensions", *Electrical Engineering*, vol. 60, no. 3, pp.119-122, 1941.
- [6] Y. Ding and K.Wu, "Miniaturization techniques of substrate integrated waveguide circuits," in *Proc. IEEE MTT-S Int. Microw. Workshop Series on Art of Miniaturizing RF and Microw. Passive Components*, 2008, pp. 63-66.
- [7] D.-W. Kim, and J.-H. Lee, "A partial h-plane waveguide as a new type of compact waveguide", *Microwave and Optical Technology Letters*, vol.43, no. 5, pp. 426-428, 2004.
- [8] B. S. Izquierdo, P. R. Young, N. Grigoropoulos, J. C. Batchelor, and R.J. Langley, "Slot antenna on C type compact substrate integrated waveguide," in *Proc. Eur. Microw. Conf., Paris, France*, 2005, pp. 469-472.
- [9] N. Grigoropoulos and P. R. Young, "Compact Folded Waveguides," *34th European Microwave conference*, Amsterdam 2004
- [10] B. Sanz Izquierdo, N. Grigoropoulos, and P. R. Young, "Ultrawideband multilayer substrate integrated folded waveguides", *IEEE MTT-S International Microwave Symposium*, San Francisco, United States, 2006, pp. 610-612.
- [11] Izquierdo, B. S.; Young, P. R.; Grigoropoulos, N.; Batchelor, J. C.; Langley, R. J. (2005) "Substrate-integrated folded waveguide slot antenna", *Antenna Technology: Small Antennas and Novel*

Metamaterials, 2005. IWAT 2005. IEEE International Workshop on, pp. 307-309.

- [12] T. L. Owens, "Folded waveguide coupler for plasma heating in the ion cyclotron range of frequencies", *IEEE Trans. on Plasma Science*, vol.PS-14, no. 6, pp. 934-946, 1986.
- [13] Grigoropoulos, N.; Sanz-Izquierdo, B.; Young, P. R., "Substrate integrated folded waveguides (SIFW) and filters", *Microwave and Wireless Components Letters, IEEE*, vol. 15, no. 12, pp. 829-831, 2005.
- [14] Sanz-Izquierdo, B.; Wu, L.; Batchelor, J.C. ; Young, P.R. , "Textile integrated waveguide slot antenna," *IEEE Antennas and Propagation Society International Symposium (APSURSI)*, Toronto, Canada, 2010, pp.1-4.
- [15] F. Xu, and K. Wu, "Guided-wave and leakage characteristics of substrate integrated waveguide", *IEEE Trans. on Microwave Theory and Techniques*, vol. 53, no. 1, pp. 66-72, 2005.
- [16] M. Henry, C. E. Free, B. S. Izquierdo, J. Batchelor, and P. R. Young, "Millimeter Wave Substrate Integrated Waveguide Antennas: Design and Fabrication Analysis", *IEEE Trans. on Advanced Packaging*, vol.32, no.1, pp.93-100, Feb. 2009.

Chapter 6: Conclusion and future work

The main research objective of the present thesis is to provide a better solution for signal interference. The current solutions for this problem, such as adding hardware in RF frontend circuitry or installing software in digital backend system, are expensive. Our research, as a results, try to use a low-cost Substrate Integrated Waveguide (SIW) antenna as a substitute to achieve multi-directional radiation. The most attractive advantage of this switch antenna is that it can reuse a frequency channel in different directions within 360 degree. For different applications, the gain of the switch antenna can be easily adjusted by extending the reflector height and waveguide edge. Also, this new antenna can easily be upgraded to array for phased scanning. Therefore, this switch-beam SIW antenna is a promising technique to solve the problems of multipath fading, crowded band and inefficient energy utilization.

In the present thesis, the PIN-diode switch-beam antenna is applied in 2-direction, 4-direction and 6-direction. The feasibility of the two-direction switch antenna is confirmed by both CST simulation and objects measurement. Also the PIN-diode has been proved to be a suitable control for the switch-beam antenna. The two-direction switch antenna, though can be used as a point to point wireless bridge to extend the propagation distance, of which the bandwidth is limited. By inputting leaky wave mode, the slot performance in the 4-direction antenna has been significantly improved. With a compact design, the 4-direction antenna can produce a symmetric radiation pattern and has a gain higher than the dipole antenna. The 4-direction switch antenna, thus, is proposed for the WLAN application. Taking the advantage of coupling effect, the four-slot antenna, theoretically, can realize six-direction or even eight-direction radiation. However, there is an impedance

mismatching problems for multi-slot radiation. For solving the impedance mismatching problem of the six-direction antenna, the intermediate-value method is introduced. The feasibilities of the 6-direction antenna and the intermediate-value method have been proved by the measured $S_{1,1}$ results and the farfield patterns. The eight-direction antenna is only tested in CST simulation, as this antenna strictly demand the performance of PIN-diode which is expensive and lack in choice for working frequency above 2 GHz. The simulation results of this antenna are not shown in the thesis due to fragmentary data. Generally, the results obtained in simulations and measurements are consistent. However, in few cases, the measured results are slightly inferior to the simulation ones for two reasons mainly. Firstly, due to budget limitation, the circuit components chosen are of the low-cost type. The performances of PIN-diode and inductor, as a result, can be unstable. Secondly, as all of the antennas used in measurement are manually assembled, manual errors exist. In practice, the antenna performance can be improved by adopting professional circuit components and machine production.

Another research objective of the present thesis is to reduce the size of SIW antenna. Firstly, a novel SIW antenna with a C-type folded front end is introduced. The length of the SIW antenna is reduced by one-quarter wavelength. Also, as the post wall at the folded region of the antenna is replaced by a metal tape, this folded structure needs less via holes, which reduces the difficulty in fabrication. In addition, the bandwidth of the folded antenna can reach 200 MHz. Secondly, a symmetric slots antenna with open-end is introduced. This antenna is reduced one-quarter wavelength in slots length. The most attractive characteristic of this antenna is that a broad radiation angle is achieved by simply utilizing the coupling effect of E-fields. And the far-field pattern of this antenna is very similar to the one of dipole antenna. However, the bandwidth of this antenna is narrow. And this antenna does not have end-fire radiation. As a result, the non-symmetric slot

antenna is introduced. Compared with the symmetric slot structure, the non-symmetric antenna has a much broader bandwidth and an end-fire radiation.

It is noticeable that all the new SIW antennas proposed in the thesis used Printed Circuit Board (PCB) which is a mature fabrication technology. Actually, the SIW antenna is more suitable for the high RF band applications, especially for the X-band ones. However, due to time limit, the switching beam antennas working at 5 GHz have not been measured. Also, in the original designs, waveguide array would be applied to the switch antennas to achieve half-spherical radiation scanning. However, the simulations for waveguide antenna array is skipped because of budget limit. During the PhD study, another 12 designs in simulation have done. In future, we would like to perform simulations and measurements for the eight-direction switch antenna working at 2.4 GHz and continue to work on the switch antenna working at 5 GHz. Also, if the antenna anechoic chamber in the University is available, we will complete the farfield measurements for the antennas proposed in chapter 5. Except the solution of impedance mismatching used in this thesis, another method with novel slot pattern will change the slot impedance. Due to the time limit, this new method will be continued in future.

Overall, this thesis has successfully displayed six new antenna designs by using the SIW antenna. The SIW antenna not only inherits the merits of traditional waveguide antenna, but also carries forward the advantages of the PCB fabrication technique. We believe that, in future, these new multi-directional SIW antenna can perfectly replace the conventional non-planar antennas.